# DISLOCATION DYNAMICS SIMULATIONS OF STRAIN LOCALIZATION IN IRRADIATED STEELS

By

**GURURAJ KADIRI**

(Enrolment No. PHYS02200704010)

Indira Gandhi Centre for Atomic Research, Kalpakkam, India.

*A thesis submitted to the*

*Board of Studies in Physical Sciences*

*In partial fulfillment of requirements*

*For the Degree of*

**DOCTOR OF PHILOSOPHY**

of

**HOMI BHABHA NATIONAL INSTITUTE**

**November, 2013**

## Homi Bhabha National Institute

Recommendations of the Viva Voce Board

As members of the Viva Voce Board, we certify that we have read the dissertation prepared by **Mr. Gururaj Kadiri** entitled "**Dislocation Dynamics simulations of strain localization in irradiated steels**" and recommend that it may be accepted as fulfilling the dissertation requirement for the Degree of Doctor of Philosophy.

______________________ Date: 8/9/2014

(Chairman- Dr.. C.S. Sundar)

______________________ Date: 8/9/2014

(Guide/Convener- Dr.. B.K. Panigrahi)

______________________ Date: 8.9.2014

External Examiner Professor G. Ananthakrishna

M. Vijayalakshmi ______________________ Date: 8-9-14.

Member 1: Dr. M. Vijayalakshmi

______________________ Date: 8/9/2014

Member 2: Dr. G. Raghavan

Final approval and acceptance of this dissertation is contingent upon the candidate's submission of the final copies of the dissertation to HBNI.

---

I hereby certify that I have read this thesis prepared under my direction and recommend that it may be accepted as fulfilling the thesis requirement.

Date: 8/9/2014

Place: Kalpakkam

Guide

## STATEMENT BY AUTHOR

This dissertation has been submitted in partial fulfillment of requirements for an advanced degree at the Homi Bhabha National Institute (HBNI) and is deposited in the Library to be made available to borrowers under rules of the HBNI.

Brief quotations from this dissertation are allowable without special permission, provided that accurate acknowledgement of source is made. Requests for permission for extended quotation from or reproduction of this manuscript in whole or in part may be granted by the Competent Authority of HBNI when in his or her judgment the proposed use of the material is in the interests of scholarship. In all other instances, however, permission must be obtained from the author.

Date: 8th September 2014

Place: kalpakkam

**Gururaj Kadiri**

## DECLARATION

I, hereby declare that the investigation presented in the thesis has been carried out by me. The work is original and has not been submitted earlier as a whole or in part for a degree / diploma at this or any other Institution / University

KG

Gururaj Kadiri

I DEDICATE THIS DISSERTATION TO ALL THE

**DISLOCATIONS.**

YOU GUYS HAVE BEEN NICE TO ME,

EVEN THOUGH I HARDLY KNEW YOU.

---

*So long, and thanks for all the slip.*

# Publications

1. Plastic deformation of ferritic grains in presence of ODS particles and irradiation-induced defect clusters: A 3D dislocation dynamics simulation study

   C. Robertson, **K. Gururaj** Journal of Nuclear Materials **415** (2011) 167–178.

2. Plastic Deformation in ODS Ferritic Alloys: A 3D Dislocation Dynamics Investigation

   **K. Gururaj**, C. Robertson Energy Procedia **7** (2011) 279–285.

3. Channel formation in irradiated FCC metals: a 3D dislocation dynamics investigation

   **K. Gururaj,** C. Robertson, M. Fivel Phil Mag (communicated)

4. Post-irradiation plastic deformation in bcc Fe grains investigated by means of 3D dislocation dynamics simulations

   **K. Gururaj,** C. Robertson, M. Fivel Journal of Nuclear Materials (communicated)

**Manuscripts to be communicated**

1. Role of Schmid and Escaig stresses in the evolution of Split Frank-Read sources: A dislocation dynamics study

2. Dynamics of a Frank-Read source with constrictions: A nodal based dislocation-dynamics simulation.

**Publications not part of the thesis**

1. Confomational and coalescence behavior of Trialkylphosphates in various diluents

   A.S. Suneesh, G.V.S, Ashok Kumar, **K. Gururaj**, K.A. Venkatesan, M.C. Valsa Kumar, P. R. Vasudeva Rao.

   Journal of Molecular Modelling (Accepted for publication)

2. Computation of thermal conductivity: A nonequilibrium approach

   P. Anees, **K. Gururaj** and M. C. Valsakumar.

   AIP Conf. Proc. 1447, 1011 (2012)

3. Depth resolved positron annihilation studies of argon nano-bubbles in Aluminum

   R. S. Dhaka, **K. Gururaj**, S. Abhaya, S. Amirthapandian, G. Amarendra, B. K. Panigrahi, K. G. M. Nair, N. P. Lalla, and S. R. Barman

   J. of Applied Physics **105** (2009) 054304.

4. Embedded design based virtual instrument program for positron beam automation.
   J. Jayapandian, **K. Gururaj**, S. Abhaya, J. Parimala, G. Amarendra.
   Applied Surface Science **255** (2008) 104.

# Acknowledgements

Writing *Acknowledgements* is perhaps the most enjoyable aspect of this thesis writing, as it gives me an opportunity to look back at all the kindness people have displayed towards me and also because, more importantly, it indicates that the thesis writing is finally close to completion.

First and foremost, a bunch of thanks to **Dr. B.K. Panigrahi** under whose guidance this work has been carried out. He has taken great efforts to ensure that the thesis is in proper shape. I should also thank **Dr. C.S. Sundar**, Director MSG, for his valuable guidance, and his constant encouragement. He has been the driving force in motivating me to take up this difficult assignment. I also owe special thanks to **Shri M.C. Valsakumar** sir, my mentor and former division head, for training me in computational Physics. Interacting with him has always been a pleasent experience and I hope I will get more opportunities to learn from him in future too. It is also a great pleasure to acknowledge the help and kindness showed by **Dr. G. Raghavan** in all these years. I also offer many thanks to **Dr. G. Amarendra** and **Dr. B.V.R. Tata** who were instrumental in ensuring that my doctoral study goes through smoothly. I am also indebted to **IGCAR** and **DAE** management for providing me with all possible opportunities and support towards PhD. I also thank my **Doctoral Committee**, for their continuous support and encouragement.

Big thanks are also due to **Dr. C. Robertson** for introducing this fascinating subject of Dislocation Dynamics to me. His passion and obsession with dislocations is highly infectious and it has been a pleasure to interact with him and learn the tricks of this trade. Another important reason to thank him must be for introducing me to **Prof. M. Fivel**. I profusely thank both of them for hosting me at CEA and CNRS for one year. I have had a great time at France, primarily because of their company (*apart from, of course, the proximity to the fabulous city of Paris*). I should also thank Prof. Fivel and **Dr. L. Dupuy** for generously sharing with me the updates of their DD software, and for training me in proper code writing. (*I now totally agree that "Object Factory" is awesome. Also, C++ rocks. Totally*).

My heartfelt thanks to **Dr. Sharat Chandra** and **Dr. Prabhakar** for meticulously going through the thesis drafts and offering suggestions on improving its general readability.

They have also taken pain-staking efforts in keeping the volume fraction of the typos in the thesis within entropically allowed limits. I should also thank **Prabhakar** and **Satya** for their constant help, encouragement and support, particularly during those (nerve-wracking) thesis-writing days. I should also thank my friends **Anees**, **Manan**, **Gurpreet**, **Jai Ganesh**, **Radhakrishna**, and **Shilpam** for helping me at various stages of my PhD (*and also for all the tea*). I am also very thankful to **Dr. Mathijaya**, and my well-wishers **Sridhar** sir and **Kalavathi** madam for trying to keep me in good cheer and hence ensuring that my morale doesn't get too low all these years.

Last, but definitely not the least, I should thank my wife (**Sridevi**, *who now hates dislocations for understandable reasons*) and my parents (**Surekha** and **Muralidhar Rao**) for all that they have been to me. I should profusely thank them particularly for tolerating my petulant and peevish behavior of the last few months. I assure them my short-temper is temporary and purely driven by the panic of approaching deadlines. I shall, hopefully, be back to my usual pleasant demeanor once this thing is submitted to the university.

# Contents

# List of Figures

# List of Tables

# List of Algorithms

# Chapter 1

# Plastic deformation in irradiated steels

## 1.1 Motivation

Choosing materials appropriate for different components in nuclear fusion and fission reactors is a formidable challenge: these materials must withstand large spatial and temporal gradients in stresses and temperatures, resist highly corrosive chemical environment, all in the presence of intense irradiation doses, and high temperatures [Waltar & Todd 2011]. A variety of structural materials have been employed or proposed as candidates for different components in nuclear reactors, depending on the stresses and neutron irradiation doses those components are subjected to. Of these range of materials, our interest in this thesis shall be primarily confined to ferritic steels and austenitic steels.

These materials, when subjected to large neutron exposure undergo micro-structural changes that can have detrimental effect on the mechanical properties as listed by [Odette *et al.* 2008]:

> (a) hardening at lower temperatures due to the formation of dislocation loops, precipitates and cavities, (b) enhanced softening and recovery at high temperatures, (c) loss of toughness, (d) loss of ductility due to strain localization, (e) void swelling, (f) irradiation induced creep etc.

Experimentally, the effect of irradiation on the strength of the materials is examined by placing the test specimen in the irradiation environment and then by carrying out the mechanical tests like tensile tests, creep tests etc on those irradiated specimen. These tests are time-consuming and expensive, and require repetition when the irradiation conditions or other operation parameters change. Moreover, the test results have to be extrapolated for the end of lifetime of components, which can be as large as 60 years. This extrapolation is meaningful only if the underlying mechanisms are understood, reliable models based on physical insights are constructed based on available data, and predictions of the model are validated by tailored experiments. Computer simulations and modeling can complement the experimental tests in generating such phenomenological models that can explain the mechanical deformation of materials as a function of irradiation dose, temperature, stress etc. These models can then be used to design materials whose mechanical degradation remains within the tolerable limits for their whole envisaged lifetime.

This thesis presents a modeling and simulation work carried out using a computation technique called "**Dislocation Dynamics**" for understanding **strain localization** phenomena in irradiated ferritic and austenitic steels. Since dislocations are the prime carriers of plasticity, understanding their interaction with irradiation-induced defects can shed light on the process of mechanical deformation under irradiation. The focus of the thesis is three-fold: First, to understand the phenomenon of strain localization, in the presence of defects produced due to irradiation and the dispersoids added to the matrix for strengthening. A manifestation of strain localization is the formation of narrow, defect-free regions called clear-channels under the tensile loading conditions. The second part of this thesis provides a possible mechanism for understanding multiple clear-channels in austenitic steels, and factors controlling the separation of channels. The role of cross-slip in the formation of multiple clear channel is illustrated. The role of different glide and non-glide stresses on the dislocation in leading to its cross-slip in fcc materials is also studied, in more elementary

DD formalism is the third focus of this thesis.

## 1.2 Radiation damage in austenitic and ferritic steels

The primary effect of neutron irradiation on crystalline materials is the initiation of "radiation damage" through the generation of the primary knock-on atoms (PKA) [G. Was 2006]. They are those atoms to which the neutrons transfer a large fraction of their kinetic energy. These PKAs have energies of the order of several hundreds of keV, which is spent on generating a cascade of point defects by further knocking out the atoms from their lattice positions. Although most of the vacancies and interstitials so generated recombine and annihilate each other, a significant fraction of these escape the "cascade zone" through diffusion. These point defects, subsequently, agglomerate into volumetric defects like voids and cavities which can later collapse into vacancy platelets. Similarly, the self-interstitial atoms can also distribute themselves one beside the other and reduce their elastic energy. When planar interstitial clusters are big enough to be considered locally as additional (or missing) atomic planes, they have the same effect as a dislocation and, thus, they are called dislocation loops, as shown in the figure 1.1.

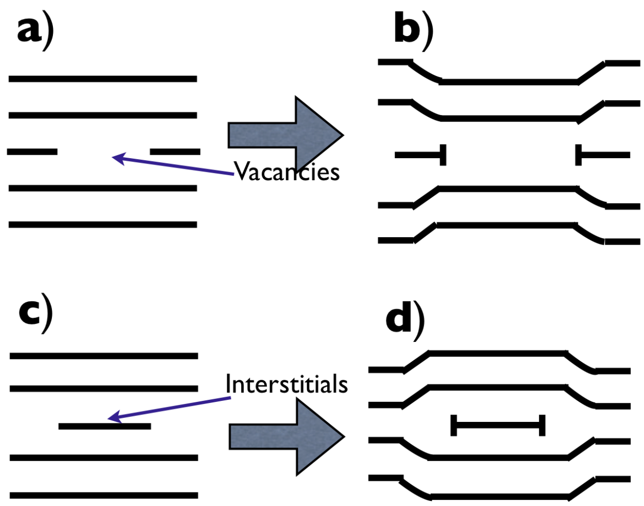


**Figure 1.1** – *Formation of irradiation induced dislocation loops. Figure a and b portray the formation of the vacancy loops, whereas figure c and d display the formation of interstitial loop.*

These loops can be glissile (i.e. perfect edge dislocation loops capable of gliding along their Burgers vector) or sessile, faulted loops (Frank loops, typical of fcc metals).

### 1.2.1 Dispersion strengthening in ferritic steels

Structural materials, under prolonged exposure to harsh irradiation environments, undergo severe degradation of their mechanical properties due to processes like void swelling, embrittlement etc. It is well-known that strength of the material and its ductility are complementary properties. Materials with high strength generally show poor ductility and vice-versa. In general, fcc metals offer higher ductility and BCC metals offer higher strength. Ferritic steels having bcc structure also show better swelling resistance as compared to fcc austenitic steels. However, these ferritic/martensitic steels in bcc structure provide poor strength at higher temperatures. Addition of oxide dispersions is seen to enhance the strength of ferritic/martensitic steels at high temperature as well as their resistances to neutron irradiations. These Oxide dispersion strengthened (ODS) steels with 0.3–1 wt% of yttrium present better mechanical behavior than the base steels up to $800K$ and still maintain good properties up to $1000K$, as shown in the figure 1.2 [Doan *et al.* 2010]. Although the ODS steels have improved tensile and creep behavior compared to their non-ODS counterparts, they also exhibit high ductile–brittle transition temperatures[De Castro *et al.* 2007]. A homogeneous dispersion of these ODS nanoparticles is also expected to strongly inhibit the formation of the **He** and **H** gas bubbles at the grain boundary, by acting as trapping sites for those gasses. Thus the sub-micron grained ODS steels are expected resist the premature failure due to the accumulation of the Helium and Hydrogen gas bubbles at the grain boundaries [Odette *et al.* 2008].

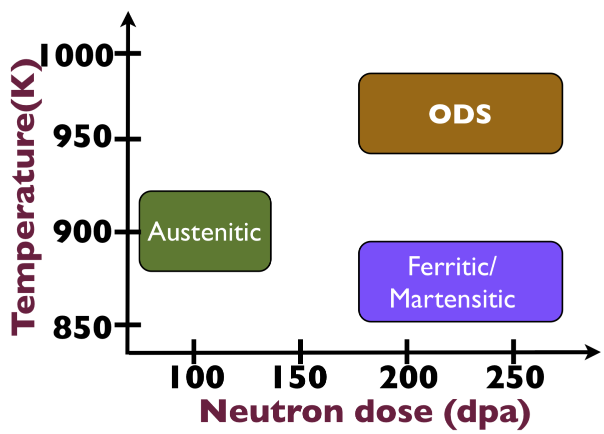


**Figure 1.2** – *Operating temperatures and irradiation doses for Ferritic, Austenitic and ODS steels.*

## 1.3 Manifestation of strain localization

Metals where the plastic deformation is spread homogeneously throughout their volume tend to be tough and malleable. Often, however, if a metal has been hardened it will no longer deform uniformly, but instead the stresses and strains tend to get confined to narrow regions of microscopic sizes. This strain localization leads to plastic instabilities, ultimately causing material failure through formation of cracks. Occurrence of strain localization can be easily recognized even by visual inspection of the strained sample: If the material is not uniformly elongated along its whole gauge length, but gets preferentially confined to some narrow zones in the length, then it is a sure sign of development of strain-localization in the sample. This visual inspection can be carried out in a better way through experiments like optical microscopy, scanning electron microscopy or by transmission electron microscopy.

The appearance of strain localization can also be studied by examining the stress-strain maps. They usually show-up in stress-strain plots as [K. Farrell & Hashimoto 2003]:

1. Drop in yield point. 2. Reduction in work-hardening rate. 3. Reduction in elongation.

Since dislocations are the primary carriers of plasticity in crystalline materials, understanding strain localization should also focus on studying the dynamics of dislocations under the applied stresses. Strain localization is the preferential confinement of dislocations in localized zones rather than being uniformly distributed throughout the volume. Dislocations will interact with other dislocations, as well as other constituents of the materials like precipitates, point-defects, irradiation induced line and surface defects etc. Understanding microscopic origins of this strain localization phenomenon in irradiated materials, hence, requires understanding the interaction of dislocations with irradiation-induced micro-structures like loops, voids, point defects etc.

### 1.3.1 Strain localization in ODS ferritic steels

It is well-known that the oxide dispersions in ODS steels strengthen the material significantly: The ultimate or yield stresses are almost doubled in comparison with non-strengthened materials. The creep strength is also considerably improved. On the other hand, the ductility slightly decreases and also ductile to brittle transition temperature increases.

The complex micro-structure of the ODS steels offers many different strengthening mechanisms that can operate concurrently. The contribution towards the increase of yield stress can come from many factors: a) the oxide dispersoids, b) Forrest type hardening, c) grain boundaries, d) solution hardening or e) lattice strengthening. Concerning oxide particles, they are usually $< 10nm$ in size but offer strong resistance to dislocation motion. Hardening of the material is due to this obstruction of the dispersoids to the dislocation motion. Figure 1.3, taken from [Kubena *et al.* 2012], illustrates the pinning of the dislocations due to these oxides dispersions.

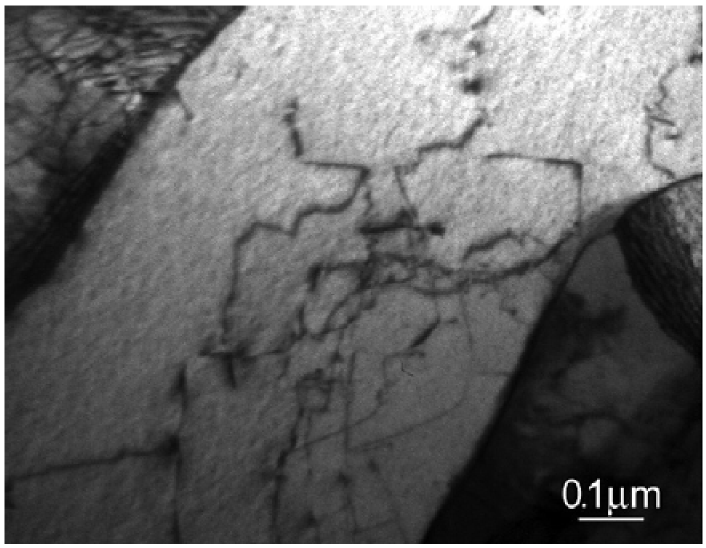


**Figure 1.3** – *Pinning of dislocations at the locations of oxide dispersions intercepting the glide plane. Image taken from [Kubena* et al. *2012].*

Dynamics of dislocations in the presence of a random three dimensional distribution of obstacles has been studied since the 1950s [see [Kocks *et al.* 1975] for a review]. This problem in fact belongs to a larger class of problems: the motion of an interfaces in a random media, of which the charge-density waves [Gruner 1988], driven flux motion in type-II superconductors[Larkin & Ovchinnikov 1973] , domain walls in random-field Ising models [Ji & Robbins 1992] etc. With this analogy, the problem of dislocation dynamics in the presence of 3D obstacles has been handled using the tools of critical phenomena, with the control parameter being the driving force and the mean velocity of the dislocation acting as the order parameter [Bakó *et al.* 2008]. These studies have indicated that indeed the depinning framework can be applied to this problem, but there were some discrepancies.

The de-pinning stress obtained from this study was found to be considerably less than the critical resolved-shear stress. This discrepancy was attributed to the collective effect of dislocations gliding in the different glide planes and hence the formation of junctions which was not accounted for in [Bakó *et al.* 2008].

### 1.3.2 Strain localization as clear channels

Clear channels are narrow defect-free regions that are seen in some irradiated materials upon deformations. See figure 1.4, for an illustration.

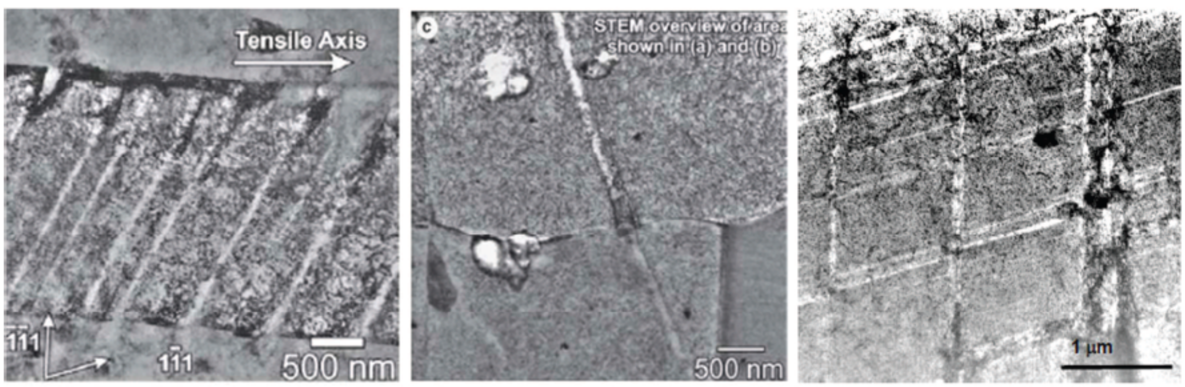


**Figure 1.4** – *Figure on the left shows the cleared channels inside an annealing twin. Middle image is the intersection point of a channel with a grain boundary in Cu irradiated (0.3 dpa)[Edwards et al. 2005]. Figure on the right shows the dislocation channels as an intertwined mesh formed in 316 stainless steel, irradiated to 0.78 dpa and strained to 32% (Figure taken from reference [K. Farrell & Hashimoto 2003]).*

These bands are narrow, but have lengths comparable to the grain size. In these clear channels the deformation can reach up to 400%, whereas the rest of the grain undergoes no significant deformation at all. This is because the clear channels are practically independent of irradiation induced defects, and dislocations glide unhindered in those regions, whereas in the rest of the grain, the radiation defects present there block the dislocation glide and multiplication and hence there is no deformation in the rest of the crystal. This inhomogeneous distribution of strain, a manifestation of plastic instability, can lead to grain decohesion, and ultimately to material failure. Clear channels are seen even in specimens irradiated only to 0.01 dpa where no yield drop was observed, and were retained even after micro-structure recovery[Edwards *et al.* 2005].

A gliding dislocation can annihilate the radiation-produced defect and subsequent dislocations will experience a relatively soft defect-free channel associated with ductility reduction and plastic instabilities. Elimination of defects is understood to be the consequence of three different phenomena : (i) pile-up effect, (ii) arm exchange, and (iii) avalanche effect (activation of a segment on a dislocation in a pile-up which can activate segments on its preceding dislocations which then activate other dislocations, and so on, leading to an avalanche of activations).

A significant drop of local shear stress in the channel occurs because of the defects getting cleared in the early stages of channel formation but, subsequently, the local stress returns quickly to a stress level as high as those in adjacent regions as the back stress builds up.

Most of the clear channels spread as long as the grain itself, and only stop when they reach the grain boundary. Thus the end points of the clear channel are effectively the grain-boundary itself. Since the channels end at the grain boundaries, all the strain accumulated within the channel are deposited there [Nishioka *et al.* 2008], leading to a significant amount of strain accumulation at the grain boundaries, in a localized fashion that produces a formation of steps on the grain boundary, as shown in the figure 1.5.Clear bands are initiated by the passage of a pile up group of dislocations [Robach *et al.* 2003].

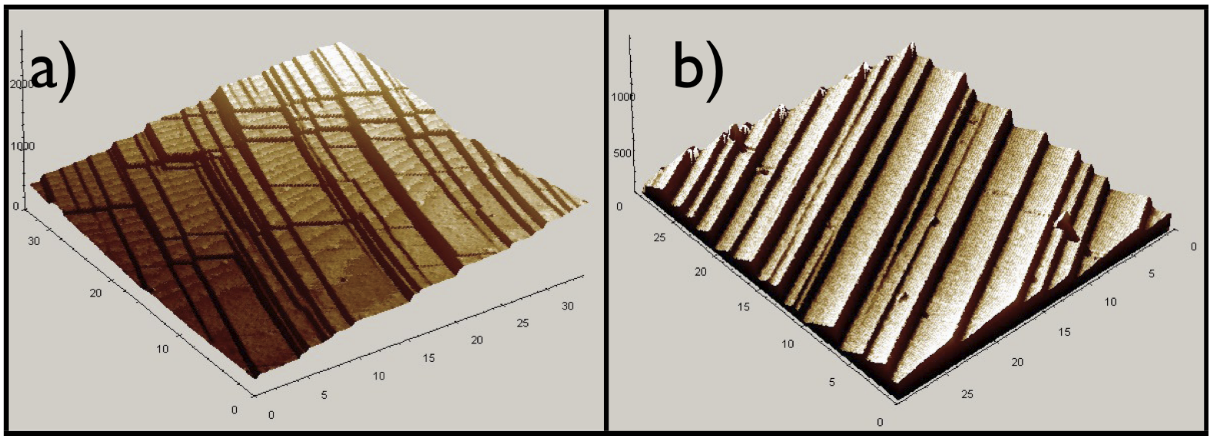


**Figure 1.5** – *AFM micrographs of 316L steel specimens strained to $e_p = 8\%$. a) 2 dpa irradiated specimen, b) as-received specimen. The z-axis represents the heights of the steps on surface, in nanometers. Slip steps are more distant, pronounced in the irradiated than in the as-received specimen. The scan size is $30\mu m \times 30\mu m$.*

Figure 1.5 shows the AFM micrographs of deformation surfaces of irradiated and un-irradiated specimens. Both the samples are deformed to the same plastic strain level. It can be seen that the slip steps are fewer in the irradiated specimen than in the as-received specimen (note that the z-axis scale is different in both the images). Fewer slip steps on the surface indicates greater slip heights, as the plastic strain is the same in both the cases. Hence slip in the irradiated sample is confined to certain narrow zones in the material, and is not uniformly spread over the whole surface. These highly localized deformations can lead to crack initiation at those points. Note that the cross-slip traces are also more pronounced the in irradiated specimen.

The effect of channeling, at the grain boundary is shown in the figure 1.6. The steps on the grain boundary surfaces can lead to cracks or act as initiation sites for clear channel formation in the neighboring grain.

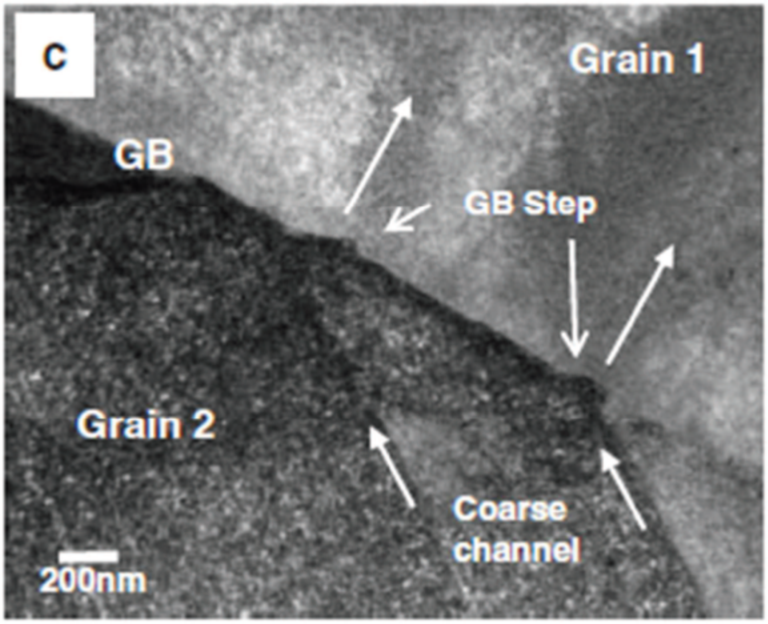


**Figure 1.6** – *Micro-structure in a grain in a 4 dpa specimen deformed at a slow strain rate [Nishioka et al. 2008].*

The main conclusions with regard to clear channel width are:

1. The greater is the applied stress, the thicker is the band.
2. The larger is the pile-up, the thicker is the band.
3. The stronger the defects, higher is the width of the band.
4. The greater the defect density, the thinner is the band.

Obtaining a more qualitative understanding of clear-channel properties and its dependence on material parameters is a complex problem owing to its multiscale nature. Even if the main mechanisms governing clear banding are broadly understood, the qualification of clear bands is difficult, because their development inside the material depends on several parameters which no single experiment can probe. The full development of a slip band takes place in less than a second. This suggests that several thousand of dislocations moved simultaneously in an instant to form such a dislocation channel that depends of the velocity of glide of dislocations. These clear channels emerge upon deformation of the irradiation materials, and are not pre-existing prior to loading, indicating that their birth and growth is due to the interaction of dislocations with irradiation induced defects. These defects are typically a few nanometers, whereas the clear channels are typically of the same length as the grain, indicating that the dislocation-loop interaction at the nanometer lengthscale controls the mesoscopic deformation behavior.

### 1.3.3 Cross-slip and Strain localization

Cross-slip is a mechanism by which a screw dislocation leaves its glide plane and glides in a conjugate “cross-slip” plane. In circumstances where climb is inhibited, it is the only available mechanism whereby a dislocation can leave its glide plane. In-fact, climb and cross-slip are complementary features that aid strain spreading in a grain, through edge and screw dislocations respectively. Cross-slip, unlike climb, can happen at any temperature and is also very sensitive to the local stresses. So, any local stress inhomogeneity can trigger cross-slip locally, leading to strain spreading. It plays an important role in phenomena like work-hardening, fatigue, creep etc, by providing the screw dislocations an extra degree of freedom for their motion [Kubin 2013]. It provides screw dislocations in close-by slip-planes a way to annihilate with each, leaving the crystal with a low-energy, multipolar edge dislocation network [Jackson 1985]. Cross-slip is also responsible for lowering the strength of the dispersion strengthened materials from their theoretical value predicted by the Orowan limit. This is because screw dislocations can bypass an obstacle just by cross-slipping, instead of forming an Orowan loop around it [Humphreys & Hirsch 1970]. Cross-slip is also responsible for the “Wall-and-Channel” structures, known as persistent slip bands (PSBs), which are formed during the cyclic deformation of fcc crystals[Sauzay & Kubin 2011].

## 1.4 Modeling and simulation of dislocations

Modeling crystal plasticity is an involved problem because the features of plasticity manifest at varied length and timescales. A useful strategy to tackle this multiscale problem is to have different simulations and modeling tools for probing different length and timescales. The timescale of physical phenomena and the corresponding modeling tools is illustrated in figure 1.7.

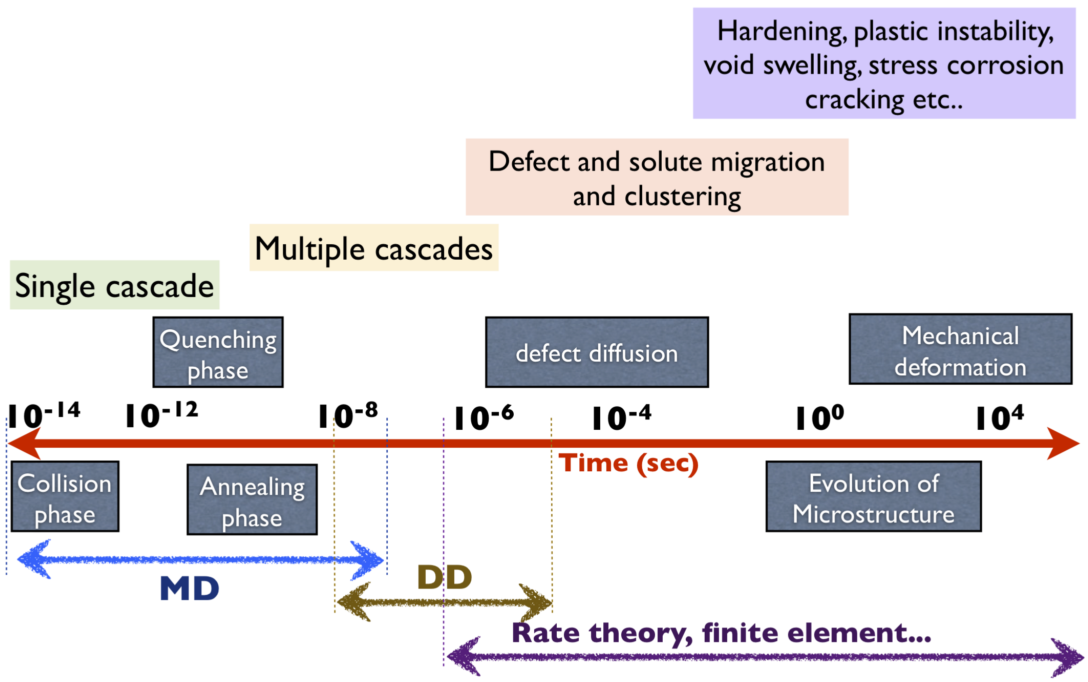


**Figure 1.7** – *Timescales at which physical phenomena manifest, along with that accessible to the various computation techniques.*

### 1.4.1 Molecular dynamics simulations of dislocations

It can be seen from figure 1.7 that molecular dynamics (MD) gives access to the smallest timescales: the timecales at which the radiation damage is initiated. In MD the elementary entities are the atoms, which interact with each other through an inter-atomic potential. At every timestep the position and velocity of each of these atoms are updated based on the force acting on it due to all other atoms, along with the external force if any. This way, the whole atomic configuration is evolved for a total-time that is long enough to capture the physical phenomenon that one intends to capture. The ability of a MD simulation to realistically capture the details of a physical phenomenon depends primarily on three things: 1. The nature of the inter-atomic potential, 2. Simulation Volume, and 3. Total simulation time. EAM potentials are widely used potentials for simulating dislocations in metals. These potentials are of the many-body type which are necessary for reproducing the elastic constants of the material. It is well-known that the simple pair-wise interaction potentials fail to compute the elastic constants of cubic crystals correctly.

Molecular Dynamics simulation of dislocations is primarily of two types: **Zero temperature modeling,** which corresponds to temperature $T = 0$, provides information on equilibrium structure under a given strain, which can be compared directly with continuum modeling of dislocations. **Finite temperature modeling**, on the other hand, corresponds to finite temperature, and allows for kinetic properties of moving dislocations to be investigated. The stress-strain curve can be obtained with both approaches and its dependence on strain rate studied in dynamics. In dynamic simulations the primary aim is to obtain the stress-strain plots corresponding to an elementary dislocation-defect interaction. From these stress-strain plots, one infers the Critical Resolved Shear Stress (CRSS), which is the measure of the strength of the individual obstacle. As an illustration, the strength of various obstacles to edge dislocation in a bcc iron matrix is shown in the figure 1.8. It can be seen that the strength of the obstacles increases with their radius, although it always remains less than the highest obstacle strength offered by the Orowan bypassing mechanism.

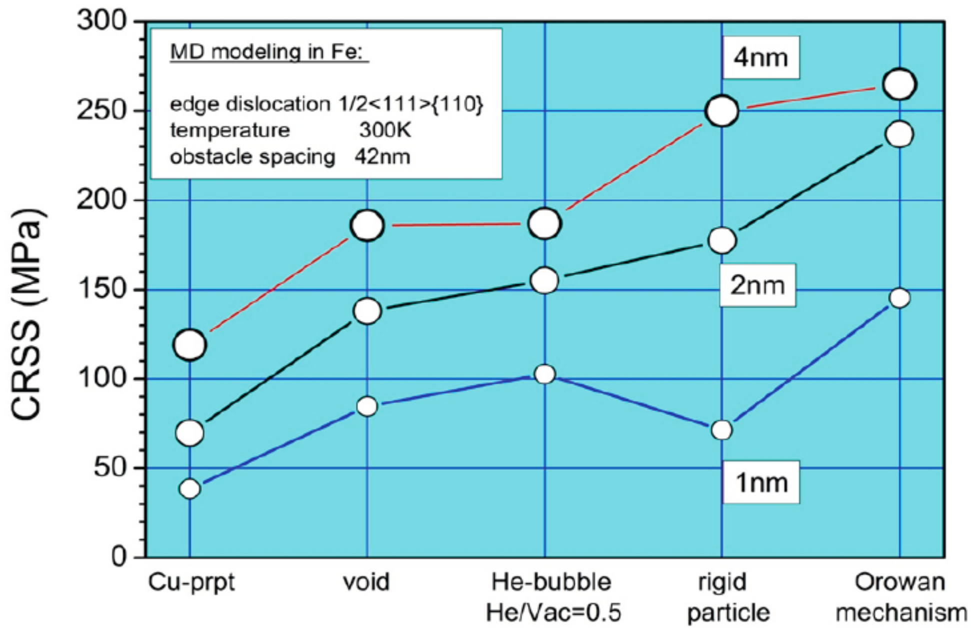


**Figure 1.8** – *Critical resolved shear stress for various defects obtained through the molecular dynamics simulations. The three plots refer to the defects of different sizes. Image from [Osetskiy & Stoller 2011].*

### 1.4.2 Dislocation-interstitial loop interactions

A dislocation whose glide plane cuts through an irradiation loop, will feel a retardation force in its glide motion. The retardation per unit length of the dislocation can be obtained by computing the stress field due to an irradiation loop at points on the dislocation line. Since these stresses fall off rapidly with distance, this retardation is appreciable only when the dislocation comes very close to the loop. But at this length scale, the elastic theory formulae for stress fields are not appropriate as the dislocation core effects come into play. MD dynamics simulations have been an invaluable tool for understanding the interaction between the interstitial loops and dislocation. This interaction is, in general, as function of the Burgers vector and line character of the incoming dislocation, the temperature of simulation, the plane of irradiation loop etc.

#### 1.4.2.1 Dislocation-loop interactions in a BCC structure

In bcc Iron, it was found that the crystallography and density of loops depends on radiation dose and temperature. At higher doses, the most visible irradiation defects are of interstitial type with vector equal to either $\frac{1}{2}\langle 111\rangle$ or $\langle 100\rangle$. At high temperature ($> 250^0C$), the fraction of $\langle 100\rangle$ loops is higher [Terentyev *et al.* 2010].

**Edge and $\langle 100\rangle$ type irradiation loop interactions** Molecular dynamics simulations of an edge dislocation with $\langle 100\rangle$ type interstitial loops, were carried out by Terentyev et al in [Terentyev *et al.* 2008]. The strain rate of $10^7 s^{-1}$ was applied in all these simulations. The volume of the box was approximately $30 \times 41 \times 20 nm^3$ and contained about $2.1$ million mobile atoms. An square-shaped interstitial dislocation loop of with sides of length $2.6nm$ was placed in different positions with respect to the dislocation.

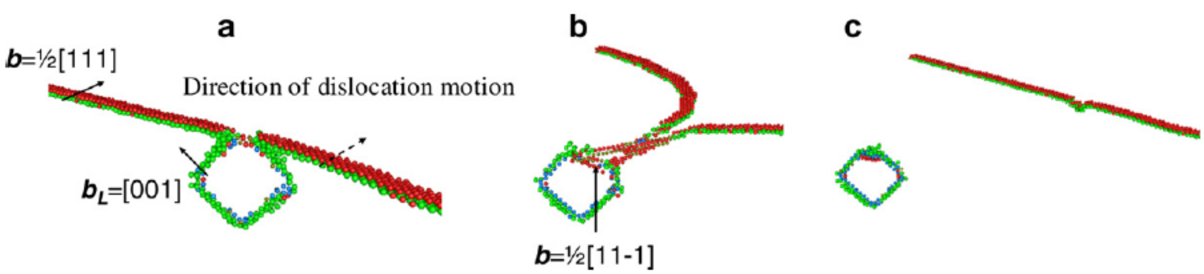


**Figure 1.9** – *One of the possible interactions of a edge dislocation with a [110] type interstitial loop, as seen in MD simulations. At the end of the simulations, it can be seen that the irradiation loop is released with the same orientation as it was before the interaction. (Image taken from reference [Terentyev et al. 2008])*

The main observations of this study were:

1. Almost all the reaction mechanisms observed can be described in terms of conventional dislocation reactions in which Burgers vector is conserved.

2. In some cases, the loop is totally absorbed on the dislocation line as a set of superjogs after conversion to $\frac{1}{2}\langle 111\rangle$ form. In others, part of the loop remains as a loop after the dislocation has broken free. The fraction of loop left behind varies from 25 to 100%.

3. Some residual loops retain their original $\langle 100\rangle$ Burgers vector, whereas others are transformed by the reaction(s) into $\frac{1}{2}\langle 111\rangle$ type.

**Screw and $\langle 100\rangle$ loop interactions** MD simulations of screw loop interaction was studied in [Terentyev *et al.* 2010]. Here, ot was found that this interaction it results in the formation of a helical turn on the screw dislocation line and breakaway from the helical turn occurs at a stress level high enough to cause turn to close on to itself so that a $\frac{1}{2}[111]$ loop is emitted back into the crystal (see figure 1.10 ) The stress required is always higher than that at which the process of loop absorption on the line is completed.

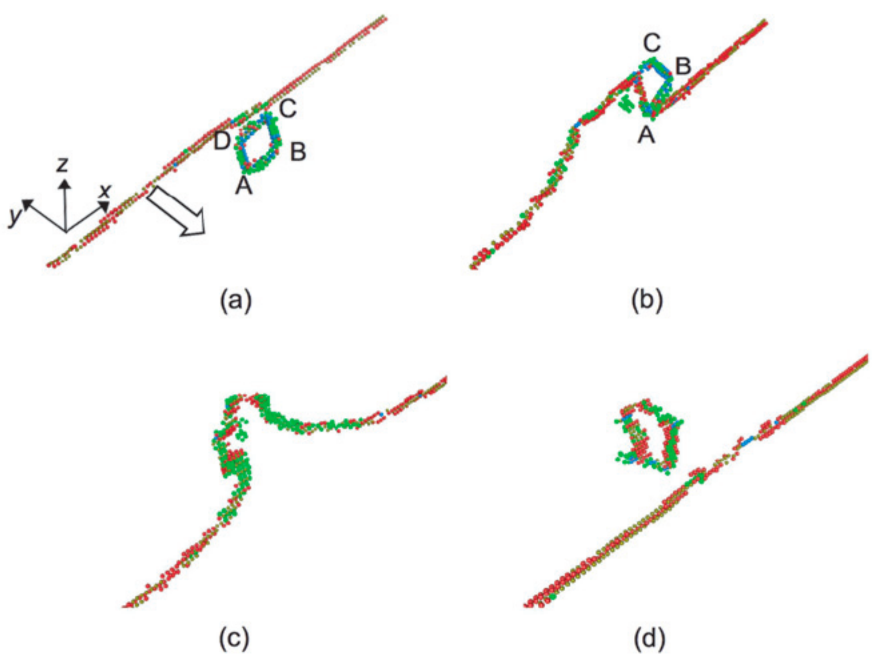


**Figure 1.10** – *Reaction of a screw dislocation and a $[100]$ interstitial loop. The dislocation glide in the direction of the arrow. It is visible that at the end of the interaction, the screw dislocation moves through the irradiation loop as if by just shearing it, and the loop, and it's Burgers vector is fully restored. (Image from reference [Terentyev et al. 2010])*

One of the most important difference between the screw-loop and the edge-loop interaction is that in case of a screw dislocation interacting with an interstitial loop, it absorbs the loop into its line as a helical turn. Since the segments with an edge component are more mobile than a pure screw dislocation and the helix expands along the direction of the dislocation line in order to decrease the total line length. However, in the simulations above, the dislocation side arms bowing forward under increasing applied stress prevent unlimited elongation of the helix. They force it to contract and, when the stress is high enough, the helical turn closes and is released as dislocation loop with the same b as the dislocation line.

#### 1.4.2.2 Dislocation-loop interactions in fcc Cu

These simulations were carried out by Nogaret et al [Nogaret 2007, Nogaret *et al.* 2007], using the EAM potential. The interaction of screw and edge dislocations with the irradiation loops, relevant in this study is as presented below:

**Screw-loop interactions** When the first dislocation comes into contact with the loop border, it progressively removes the double stacking fault of the loop (figure 1.11a) and results in the absorption of the loop in the form of a helical turn on the screw dislocation (figure 1.11b). The applied stress required to form the helical turn is low, about 40 MPa. The helical turn expands along the entire dislocation in order to minimize its length and the associated line tension energy. In this configuration, the dislocation does not belong to any specific $\langle 111 \rangle$ plane and is constricted along its entire length as seen in figure 1.11b. The helical turn is an obstacle that pins the first dislocation because it can glide only in the Y, Burgers vector direction and not the X-glide direction.

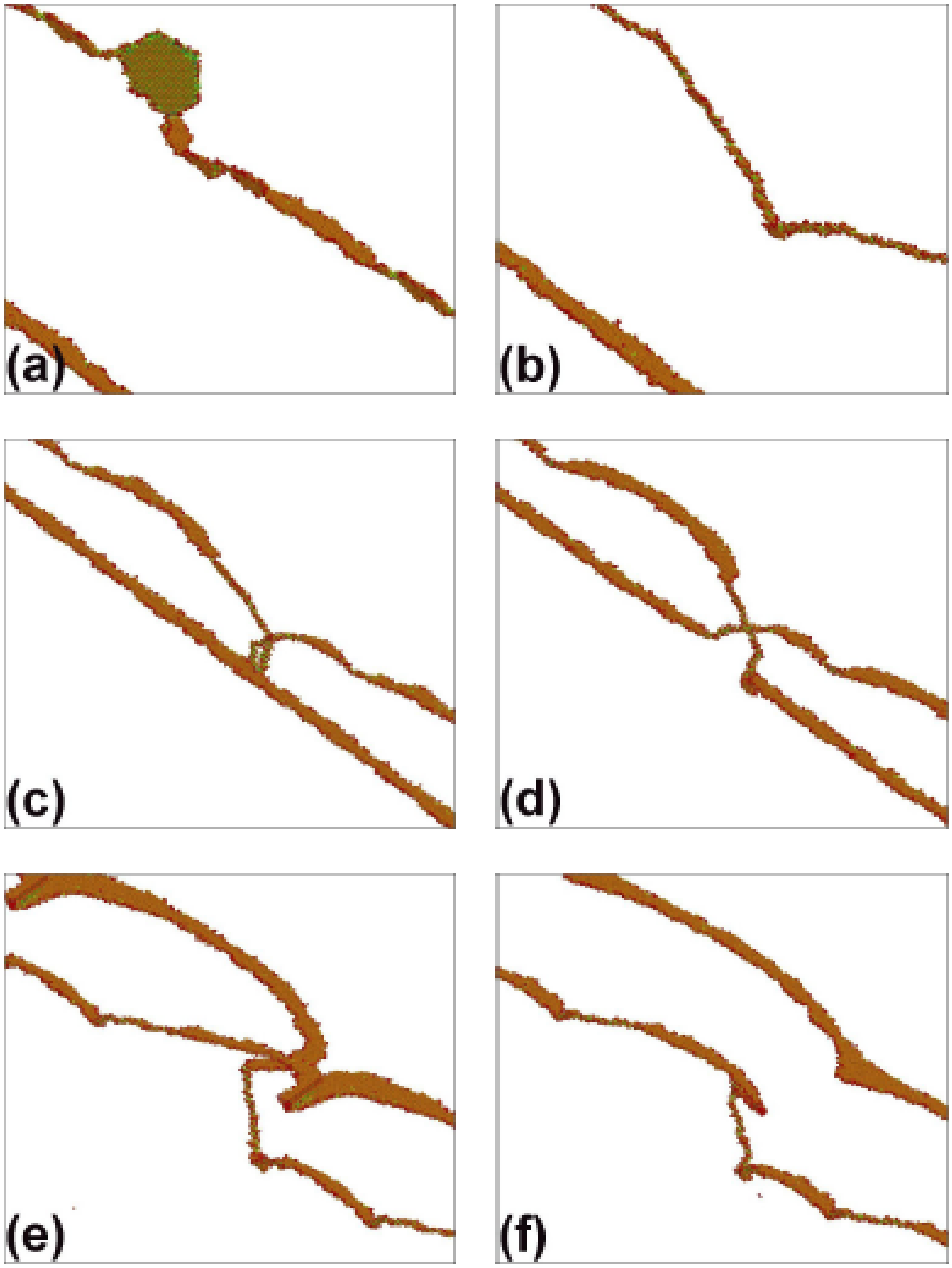


**Figure 1.11** – *MD simulation of two dislocations interacting with an irradiation loop in fcc Cu. Snapshots shown at (a) 5 MPa, 15 ps , (b) 40 MPa, 89 ps , (c) 180 MPa, 148 ps, (d) 180 MPa, 153 ps, (e) 180 MPa, 165 ps, (f) 180 MPa, 169 ps . Image obtained from [Nogaret 2007].*

As the applied stress is increased, the second dislocation approaches. The two dislocations repel each other since they have the same Burgers vector. The portion of the helical turn near the second dislocation rotates and becomes perpendicular to the latter (figure 1.11c). This configuration (with perpendicular dislocation segments) minimizes the elastic repulsion between them. The rotation of the jogs implies a contraction of the helical turn and an extension of one arm of the first dislocation in an upper $(111)$ glide plane, where it locally dissociates, as seen in the upper part of figure 1.11c. It is noted that the dissociated segment is systematically emitted from the second upper corner of the initial loop. When the second dislocation comes into contact with the helical turn, the contact is immediate. The two dislocations spontaneously exchange arms, after which the helical turn is shared by the two dislocations, as seen in figure 1.11d. Each jog now connects one segment of the first dislocation to another segment of the second dislocation. During this process, the upper dissociated arm continues to expand and bows out, being repelled by both the second dislocation and the applied stress. Then, this segment undergoes an Orowan process (figure 1.11e), unpins and leaves behind the second dislocation that now contains the helical turn (figure 1.11f). The net result is the absorption of the Frank loop into itself, followed by re-emission in an upper (111) plane.

**Edge-loop Interaction** Unlike the screw-loop interaction which results in the absorption of loops as helical jogs on the screw dislocation line, the edge-loop interaction is much simpler: the edge is just seen to shear the loop, and creating the vacancy-type step on the surface, which is mobile and annihilates on the loop border, (see figure 1.12d). Thus there is no permanent damage on the loop.

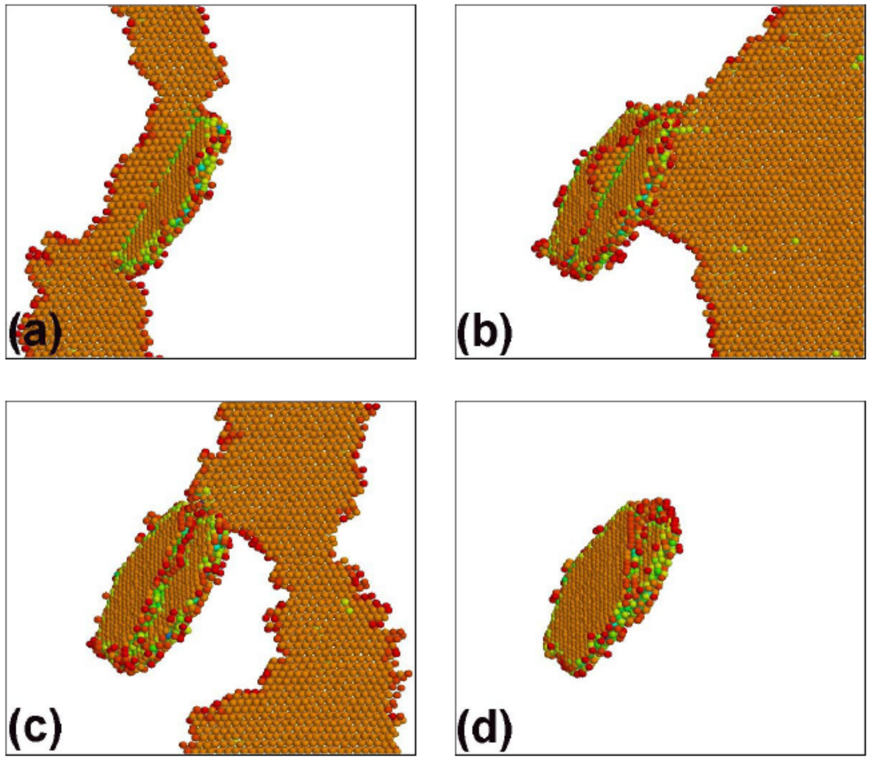


**Figure 1.12** – *An illustration of a possible interaction between an edge dislocation and the interstitial loop in fcc Cu, as seen in MD simulations. Image obtained from [Nogaret 2007].*

### 1.4.3 Dislocation-ODS precipitate interactions

ODS precipitates act as strong pinning points to dislocation motion. Overcoming these obstacles, in the absence of climb mechanism is only either by Orowan Bypassing or by shearing of the precipitates. The latter case happens only with the elastic constants of the precipitates differ from those of the matrix. The stress required for a dislocation to shear through a particle is given by[Kubena *et al.* 2012]:

$$\Delta\tau = \frac{\gamma\pi d}{2b\chi_g} \tag{1.1}$$

where $b$ is the magnitude of Burgers vector, $d$, the mean particle diameter, $\chi_g$ is the mean separation between the particles in the glide plane and $\gamma$ is the stacking fault energy (with dimensions of energy per unit area). This energy was given by Takahashi et al [Takahashi *et al.* 2011] , using atomistic simulations as $20\,mJ/m^2$. Substituting the values corresponding to the typical ODS steels, the formula 1.1 yields a stress of about $10\,GPa$. This is an unusually large stress, considering that the theoretical shear stress for iron itself is about $7.5\,GPa$. It is hence more likely that dislocations bypass the $Y_2O_3$ precipitates rather than cut through them. This is primarily because cutting through the precipitates requires breaking of the bonds between $Y$ and $O$. To summarize, according to Kubena et al [Kubena *et al.* 2012], two conclusions can be drawn:

1. The effect of oxide dispersion could theoretically explain the observed increase of strength of the ODS steels in comparison with steels without oxide.

2. The Orowan mechanism of dislocation is energetically favored to the particle cutting process.

### 1.4.4 Modeling dislocations by Dislocation Dynamics

The strength of the MD technique lies in its ability to give full access to the microscopic length and timescales at which these interactions operate, without making any distinction between core and elastic regimes. This strength of MD, however, also happens to be its biggest weakness. The phenomena of hardening, loss of ductility etc; manifest at the scale of grain size, whereas the MD techniques are efficient only at a length-scale of nanometers. This is because, in MD a dislocation is not explicitly simulated but is implicitly tracked through the arrangement of millions of atoms. It is hence practically impossible to simulate in MD a grain containing realistic dislocation and defect densities, up-to the deformation levels where the issues of hardening emerge.

The idea that plastic deformation can be microscopically analyzed by directly simulating the evolution of dislocations was first proposed by Ghoniem et al [Amodeo & Ghoniem 1990].

The premise of "Dislocation Dynamics (DD)" is that, under certain approximations, the motion of dislocations can be abstracted out of the underlying crystal structure and can be independently studied. This premise instantly reduces the complexity of the problem from simulating several millions of atoms to simulation of only a few dislocations. The effect of the underlying crystal structure would manifest itself only through the dynamics of the dislocation and in its interaction with other defects. Directly simulating dislocations themselves, instead of indirectly tracking them by simulating the dynamics of atoms comprising the crystal allows us to access length and time scales that are not traditionally accessible in classical molecular dynamics (MD) simulations. These DD simulations, however, lean heavily on the molecular dynamics technique for providing the dislocations mobility rules and rules for modeling the elementary dislocation-defect interactions. Figure 1.7 shows the timescales at which different computational techniques are effective. From the schematic, it can be seen that DD sits as a bridging tool connecting the MD and the continuum scales (FEM). This promises us that, with proper exploitation of the DD technique, an atomistically accurate model of crystal plasticity can be constructed, whose predictive power ranges in the time scales of hours and length scale of meters.

A large part of this thesis is based on the results obtained using a DD code called TRIDIS [Verdier *et al.* 1998], developed at Génie Physique et Mécanique des Matériaux (GPM2) laboratory in France, based on the framework of [Kubin *et al.* 1992]. This software has been the workhorse for understanding various dislocation mediated phenomena like indentation-induced plastic deformation[Robertson & Fivel 1999], plasticity in Fe laths [Chaussidon *et al.* 2010], fatigue in fcc single crystals [Shin *et al.* 2005], formation of persistent slip bands in AISI 316L steels [Depres *et al.* 2006], creep behavior of ice [Chevy *et al.* 2012], the phenomena of thermal fatigue [Osterstock *et al.* 2010], plasticity induced by nano-indentation [Fivel *et al.* 1997], clear channel formation [Nogaret *et al.* 2008] etc. The code is also capable of coupling to a continuum scale tool towards multiscale modeling (see reference [Chang *et al.* 2010] as one illustration).

## 1.5 Overview and organization of the thesis

The aim of this thesis is to present some new insights on how the elementary dislocation-defect-dispersoid interactions, operating at a nanometer length-scale, impact the overall plastic deformation of the material at the length scale of microns. The important players modeled and simulated in this study are a) Frank-Read sources causing dislocation multiplication, b) Irradiation induced dislocation loops modeled as prismatic loops and c) Hard impenetrable dispersoids that are opaque to the dislocations. The elementary dislocation-loop interactions are modeled based on the available molecular dynamics simulations studies. The thesis specifically aims to study:

1. **Influence of ODS particles on strain localization in irradiated ferritic steels.**

   Plastic deformation of irradiated $1\mu m$ ferritic grains is investigated here and compared with that of an irradiated ODS grain. The irradiation effect included in the simulations are the interstitial loops. These simulations were carried out using the DD code TRIDIS [Verdier *et al.* 1998], adapted for bcc materials and also enhanced with new modules for handling the dislocation-defect interactions rules specific to these studies. The code is also supplemented with external programs written in C++ for post-processing of the obtained results and also for generating the input structures. Through these simulations, it is found that in the absence of irradiation induced defect loops, ODS-grains are stronger and plastic strain is more localized than in the corresponding, particle-free grain. After irradiation however, ODS-grains become more resistant to loop-induced hardening, while plastic strain spreading is broader compared to the particle-free grain. These results are discussed in Chapter 3.

2. **The role of dislocation cross-slip in multiple clear-channel formation under tensile deformation of irradiated austenitic steels.**

   The goal of this work is to model multiple clear channel formation at the grain scale, incorporating dislocation-loop interaction rules revealed in molecular dynamics. Two types of DD simulations have been carried out based on their complementary capacities and limitations:

   In **Type-1 simulations**, irradiation-induced defect clusters are treated explicitly, in the form of prismatic loops located at random positions in the simulation volume, with a density representative of TEM observations. Dislocation evolution through this 3D random arrangement of prismatic loops is studied at different nucleation stresses. After a certain amount loop clearing, the corresponding internal stress field is analyzed in terms of the shear stress resolved on the primary and cross slip systems, and the results are understood in-terms of a closed-form 1D pile-up model.

   In **Type-II simulations**, irradiation-induced defect clusters are treated as just planar obstacles to dislocation motion. Modeling prismatic loops as planar obstacles allows for accessing larger timescales where multiple clear channels can be studied

   From these simulations it is found that the strain spreading into new shear bands depends on the interplay between clear band internal stress and the strength of the obstacle. Combination of dislocation structure and grain boundary plastic strain mapping makes it possible to locate individual band position and assess the band inter-spacing. The size of the simulated grain, the density of irradiation loops and the critical cross-slip stress are systematically varied and the separation between the bands is examined. From these sets of simulations the width of the clear channel is estimated as a function of grain size, irradiation dose as well as the stacking fault energy (SFE). It is found that the shear band spacing increases with decreasing SFE.

3. **Understanding the role of glide and Escaig stress on dislocation cross-slip in fcc materials.**

   Cross-slip is one critical phenomenon that is known to significantly affect the strain spreading in BCC and fcc materials, but whose microscopic origins are not yet well-understood [Püschl 2002]. Modeling cross-slip is particularly complicated in the case of fcc systems, as the screw dislocations there are not perfect but are split into Shockley partials that have a well-defined glide plane. Chapter 5 and Chapter 6, addresses this issue and provides some insights, albeit within the ambit of DD, on the effect of different glide and non-glide components of the applied stress tensor on the equilibrium dissociation width of split screws, and hence their role in cross-slip. These simulation involve a more realistic representation of dislocations, including partials, formation of junctions and inclusion of stacking fault contribution to the split dislocations. These simulations were carried out using the nodal based DD code NUMODIS [L. Dupuy & Coulaud 2013], under development at CEA, Saclay. Carrying out the above simulations necessitated writing new software modules for computing stacking fault area, the elastic and core-energies of dislocations and an algorithm for controlling the external stresses on the simulation volume etc. Software for generating initial dislocation configurations and for post-processing of the data is also developed as a part of this thesis.

# Chapter 2

# Methodology of Dislocation Dynamics simulations

---

*This chapter provides a brief introduction to the dislocation dynamics technique as applied in the simulations presented in the rest of the thesis. Two complementary DD techniques: the Edge-screw based dislocation dynamics and the Nodal-based dislocation dynamics, are explained along with the relevant post-processing tools.*

---

## 2.1 Introduction

The initial development of dislocation dynamics was confined to only 2D and the plane of simulation was either a) coinciding with the glide plane of the dislocation or b) parallel to the dislocation lines. Simulations carried out in the first case, hence, cannot accommodate the mechanisms that lead to change of glide plane like climb and cross-slip. The studies were mainly confined to understanding line tension effects and the equilibrium shape of dislocations under external stress [Brown 1964]. These 2D simulations have also yielded valuable insights in understanding the glide of dislocations through a random arrangement of point obstacles [Foreman & Makin 1966]. The other kind of simulations involve simulating infinitely long dislocations of the same character that pierce through the simulation plane [Lepinoux & Kubin 1987].

Three dimensional dislocation dynamics simulations allow for simulating all the features of dislocations like cross-slip, climb, formation of junctions etc [Canova & Kubin 1991]. Within 3D dislocation dynamics, there are different models for representing the dislocations of arbitrary orientation and Burgers vector. These models can be broadly divided into two classes: The Edge-Screw model and the Nodal-model. In the edge-screw model of dislocation dynamics, a dislocation of arbitrary character is represented as a collection of interconnected edge and screw dislocation *segments*. The dynamics of dislocations is obtained through the evolution of the constituent dislocation segments. In the nodal based representation a dislocation line is parameterized into a collection of nodes and the dynamics laws are applied to these nodes. This representation allows for greater precision in dislocation topology but is computationally intensive compared to the edge-screw based DD. The nodal based DD is more appropriate when studying the dislocation splitting and complex topological changes involving multiple junction formation (see references [Shenoy *et al.* 2000, Weygand *et al.* 2001, Schwarz 1999, Ghoniem *et al.* 2000]). The edge-screw based DD, on the other hand, is appropriate to study the collective effects of dislocations and for predicting phenomena at the length-scales of up to microns. The rest of the chapter discusses in detail these two dislocation dynamics models.

## 2.2 Edge-screw based dislocation dynamics

In this model, a dislocation of arbitrary line shape is discretized into a series of perpendicular segments. This leaves only two types of dislocations in the simulation volume: screws and edges, as shown in the figure (2.1).

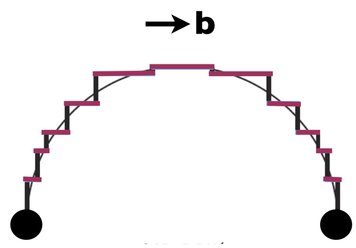


**Figure 2.1** – *Edge-Screw modeling of a dislocation of mixed character. Since the Burgers vector is along the horizontal direction, the dislocation segments represented as thick black lines are edge dislocation segments whereas the dislocation segments represented in brown are the screw dislocation segments.*

Distinction is made between the dislocation line and the dislocation segment. Consider the figure (2.1). This figure depicts a single dislocation line, which is represented through a series of connected dislocation segments.

A dislocation segment is characterized by its

1. Length, 2. Center, 3. Line direction, 4. Burgers vector, 5. Glide direction, 6. ***previous*** and ***next*** pointers.

The maximum length of a dislocation segment is fixed by a parameter of the model called the discretization parameter $d_{desc}$, which sets the accuracy of the representing dislocation lines as a series of segments. The smaller the discretization length, the greater is the accuracy in approximating the mixed dislocations in terms of edges and screws. In the course of the dynamics, if the length of a dislocation segment exceeds the discretization length, the segment is split to two segments, one with length $d_{desc}$, and the next segment with the rest of the length. Similarly if the sum of the two dislocation segments having the same line direction are such that the sum of their lengths is less than or equal to $d_{desc}$, the two segments are merged into one. Thus the number of dislocation segments in the simulation volume keeps varying with the number of time-steps, although in a typical simulation, under tensile loading conditions, on average this number increases. This marks an important distinction between an MD simulation and a DD simulation. In a typical MD simulation, the time it takes for evolving the system through $N$ time-steps is same whether the first $N$ time-steps are considered or the last N time-steps, whereas in a typical DD simulation the time taken for evolving $N$ time-steps is different for first $N$ compared to the last.

The beginning and the end positions of the dislocation segment change as it evolves in time, but one can store only the center of the segment in the memory. The start and end points can be constructed from the information about the line direction and the length of the segment.

Similarly the glide direction of the dislocation can be obtained from the cross-product of the line direction and the Burgers vector direction unless the dislocation segment is a screw segment, in which these two directions coincide. The glide direction of a screw segment is hence hand-put and needs to be updated whenever cross-slip has to be activated for that segment.

The ***next*** and ***previous*** are pointers to the next and previous dislocation segments. This information also needs to be updated at each time-step, since as the dislocation segments evolve their neighborhood connections also change. A dislocation segment can have one or both its neighbors to be ***null***. A dislocation segment whose ***previous*** neighbor is ***null*** represents the beginning of a dislocation line, whereas a segment whose ***next*** neighbour link is ***null*** represents the last segment of a dislocation line.

### 2.2.1 Enforcing segment connectivity

Consider a dislocation configuration, pinned at AB shown in figure (2.2). Here the dislocation line AB is initially (at $t = 0$, say) is split into three dislocation segments $S_{prev}$, $S_0$, $S_{next}$. Under the evolution, these segments will always move perpendicular to their own line direction, as shown in the figure (2.2b). Since the dislocation is pinned at A and B, as the segments $S_{prev}$ and $S_{next}$ evolve, they generate two dislocation segments to ensure line connectivity at A and B. These segments are of opposite type: If $S_{prev}$ and $S_{next}$ are edge type, the new segments connecting $A$ with $S_{prev}$ and $S_{next}$ with $B$ will be screw dislocations, and vice versa.

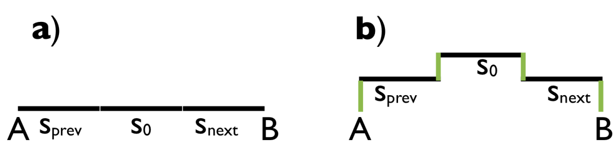


**Figure 2.2** – *The dislocation, pinned at points AB, is initially consisting of three segments. b) After evolution of a time-step $\Delta t$, the segments are connected by adding new segments of opposite type, shown in green.*

Similarly, if the segment $S_0$ acquires greater velocity and hence evolves further than $S_{prev}$ and $S_{next}$, again two new segments are generated to connect $S_0$ with $S_{prev}$ and $S_{next}$. These two new segments have opposing line directions, and hence are attractive.

### 2.2.2 Strain induced by dislocation motion

The strain induced by a collection of dislocations in the simulation volume is obtained by summing up the slipped area in each slip system, which is computed as

$$\gamma_i = \frac{|\mathbf{b}|\, A_i}{V} \tag{2.1}$$

where $\gamma_i$ is the slip induced in the $i^{th}$ slip system, $\mathbf{b}$ is the Burgers vector, $V$ is the simulation volume, and $A_i$ is the area swept by the mobile dislocations in the $i^{th}$ slip system:

$$A_i = \sum_j L_j v_j \triangle t \tag{2.2}$$

where the summation runs over all the dislocation segments in the $i^{th}$ slip systems. From the slip, the strain is computed as

$$\epsilon_{ij} = \sum_{s=1}^{N_s} \frac{1}{2} \left( n_i^{(s)} b_j^{(s)} + n_j^{(s)} b_i^{(s)} \right) \gamma_s \tag{2.3}$$

where $n_i^{(s)}$ and $b_j^{(s)}$ are the slip plane normal and Burgers vector component in the $i^{th}$ and $j^{th}$ direction.

### 2.2.3 Stresses acting on dislocation Segments

In MD, atoms are treated as point particles which respond to the forces, and themselves exerting forces on other atoms. Similarly, in DD dislocations are treated as lines responding to external stresses and themselves act as source of stresses. The dynamics of a dislocation hence depends on the net stress acting on it which is the sum total of :

1. The stress due to all other dislocations in the simulation volume, excepting its two neighbors. This stress is termed as the internal stress.

2. The external applied stress.

3. The line tension stress that tends to minimize the dislocation length.

4. The Peirerls stress, due to the atomic nature of the lattice.

The contribution of each of the four stresses are explained below

#### 2.2.3.1 Internal stress on a dislocation

Of these four contributions, computing of internal stress is the most computationally intensive aspect of a dislocation dynamics simulation. The stress field of a dislocation at an arbitrary point $\mathbf{r}$ in the simulation volume depends on the character of the dislocation of the dislocation and its length. In this section, formulae for the stress field due to infinitely long edge and screw dislocations are presented, and subsequently the procedure for obtaining the stresses produced by finite dislocations is given.

#### 2.2.3.2 Stress Field of finite dislocation segments

Consider a semi-infinite dislocation oriented along the z-axis, and whose Burgers vector is $\mathbf{b} = (b_x, b_y, b_z)$. The stress field at an arbitrary point $(x, y, z)$ due to this dislocation is given by:

$$\sigma_{xx}(\mathbf{r}) = \frac{-b_x y - b_y x}{r(r-z)} - \frac{x^2(b_x y - b_y x)(2r-z)}{r^3(r-z)^2} \tag{2.4}$$

$$\sigma_{yy}(\mathbf{r}) = \frac{b_x y + b_y x}{r(r-z)} - \frac{y^2(b_x y - b_y x)(2r-z)}{r^3(r-z)^2} \tag{2.5}$$

$$\sigma_{zz}(\mathbf{r}) = \frac{z(b_x y - b_y x)}{r(r-z)} - \frac{2\nu(b_x y - b_y x)}{r(r-z)} \tag{2.6}$$

$$\sigma_{yz}(\mathbf{r}) = \frac{y(b_x y - b_y x)}{r^3} - \frac{\nu b_x}{r} + \frac{(1-\nu)b_z x}{r(r-z)} \tag{2.7}$$

$$\sigma_{xz}(\mathbf{r}) = \frac{x(b_x y - b_y x)}{r^3} + \frac{\nu b_y}{r} + \frac{(1-\nu)b_z y}{r(r-z)} \tag{2.8}$$

$$\sigma_{zz}(\mathbf{r}) = \frac{y(b_x x - b_y y)}{r(r-z)} - \frac{xy(b_x y - b_y x)(2r-z)}{r^3(r-z)^2} \tag{2.9}$$

Where $r$ is the perpendicular distance between the point $(x, y, z)$ and the dislocation line . These stresses are in units of $\frac{\mu}{4\pi(1-\nu)}$, where $\mu$ and $\nu$ are the shear modulus and Poisson ratio of the material respectively.

These formulae are applicable in the case of an infinitely long dislocation, located the origin. The stress formula allows us to compute the stress due to finite dislocation segments as follows. The stress field due to a dislocation of finite extent located along $z_1$ to $z_2$ on the $z$ axis, is equal to the difference between the stress fields produced by two semi-infinite dislocations oriented along from $z_1$ to $\infty$ and $z_2$ to $\infty$ on the z-axis.

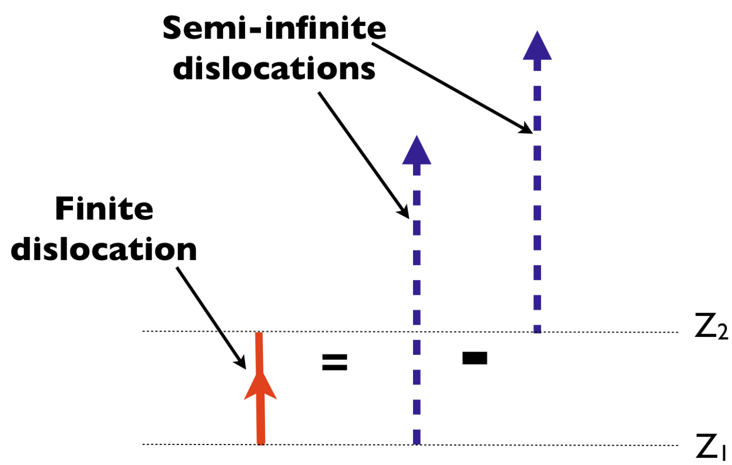


**Figure 2.3** – *Obtaining Stress-Field due to a finite dislocation, from the difference of the stress fields produced by two semi-infinite dislocations. The stress field due to a finite dislocation segment extending from $Z_1$ to $Z_2$ is computed by taking the difference due to the stress due to two semi-infinite dislocation segments ranging from $Z_1$ to $\infty$ and $Z_2$ to $\infty$ respectively.*

The stress field of a semi-infinite dislocation located at $z_1$ instead of at the origin is simply obtained by replacing $z$ in equations (2.4-2.9) by $z - z_1$, and similarly from the other dislocation lying at $z_2$. Hence we have

$$\sigma_{ij}(\mathbf{r}) = \sigma_{ij}(\mathbf{r})|_{z=z-z_1} - \sigma_{ij}(\mathbf{r})|_{z=z-z_2} \tag{2.10}$$

This formula is applicable only if the finite dislocation is aligned along the $z$-axis. If the dislocation is along any other direction, these formula are to be be treated with a co-ordinate transformation to align dislocation along the $z - axis$. A coordinate independent way of expressing the stress field is given by Devincre in [Devincre 1995, Shin 2004].

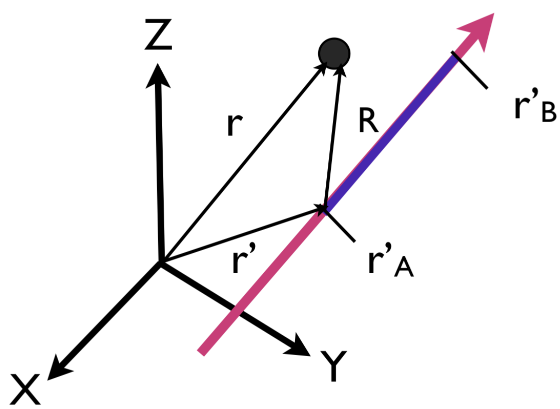


**Figure 2.4** – *Geometry of the configuration considered in formula 2.11. The dislocation is located along the direction of pink arrow and extends from $\mathbf{r}'_\mathbf{A}$ to $\mathbf{r}'_\mathbf{B}$. The stress due to this dislocation of length $L$ is computed at the point $\mathbf{r}$. The line direction $\mathbf{t}$ is the unit vector along $\mathbf{r}'_\mathbf{A}$ to $\mathbf{r}'_\mathbf{B}$.*

Consider a semi-infinite dislocation located at $\mathbf{r}'$, having a Burgers vector as $\mathbf{b}$, and oriented along an arbitrary direction $\mathbf{t}$ as shown in figure 2.4. The stress field due to this dislocation at an arbitrary point $\mathbf{r}$ is given by Devincre [Devincre 1995] as :

$$\sigma_{ij}(\mathbf{r}) = \frac{\mu}{\pi Y^2}\left[[\mathbf{bYt}]^s_{ij} - \frac{1}{1-\nu}[\mathbf{btY}]^s_{ij} - \frac{(\mathbf{b},\mathbf{Y},\mathbf{t})}{2(1-\nu)}\left(\delta_{ij} + t_i t_j + \frac{2}{Y^2}\left(\rho_i Y_j + \rho_j Y_i + \frac{L}{R} Y_i Y_j\right)\right)\right] \tag{2.11}$$

Where $R = \mathbf{r} - \mathbf{r}'$, $L = \mathbf{R}.\mathbf{t}$, $\rho = \mathbf{R} - L\mathbf{t}$ and $\mathbf{Y} = \mathbf{R} + R\mathbf{t}$, $(\mathbf{b}, \mathbf{Y}, \mathbf{t})$ is the triple product, and $[\mathbf{bYt}]^s_{ij}$ stands for the component $\frac{1}{2}((\mathbf{b} \times \mathbf{Y})_i \mathbf{t}_j + (\mathbf{b} \times \mathbf{Y})_j \mathbf{t}_i))$.

From the stress formula Eq (2.11) the stress field due to a dislocation of finite length lying between $\mathbf{r_A}$ and $\mathbf{r}_B$ is determined by substituting $\mathbf{r}_A$ and $\mathbf{r}_B$ for $\mathbf{r}'$ in Eq (2.11) and then taking the difference between those two stresses. All these stress formulae breakdown at the very close to the dislocation line. This is because these are derived within the domain of the Hooke's Law of linear stress-strain dependence.

#### 2.2.3.3 External Applied Stresses

Apart from the internal stress generated by other dislocations, a dislocation will also couple to the external stresses acting on the simulation volume. The form of this external stress is specific to the loading conditions that one wants to mimic. All the simulations presented here are carried out in the tensile loading scheme, and the applied stress is homogeneous throughout the simulation volume. This implies all dislocations in the simulation volume experience the same external stress. Although the stress is homogeneous in space, it can be varying in time depending on the experiment being simulated. The three prominent stress-control schemes used in DD calculations are a) Constant stress simulations, b) Constant stress rate simulations and c) Constant strain-rate simulations. The cases a) and b) are easy to understand, where the stress is held constant and varied linearly with time respectively. Constant strain-rate simulations, on the other hand, stand on a different footing compared to the other two. In here, the stress acting is manipulated such that the strain deformation in the system proceeds at a constant pre-defined rate. This means that the stress acting on the system is a function of the current deformation level. This loading scheme is the closest to the experimental tensile loading conditions. The simulations presented in chapters 3 and 4 are carried out in the constant strain rate conditions, and the procedure employed is illustrated in algorithm 2.1.

**Algorithm 2.1** Algorithm for constant strain rate simulations employed in chapters 3 and 4.

- First, the strain at any instant of time in the edge-screw model is computed as

$$\epsilon_{ij} = \sum_{s=1}^{N_s} \frac{1}{2} \left( n_i^{(s)} b_j^{(s)} + n_j^{(s)} b_i^{(s)} \right) \gamma_s \tag{2.12}$$

where $n_i^{(s)}$ and $b_j^{(s)}$ are the slip plane normal and Burgers vector component in the $i^{th}$ and $j^{th}$ direction, and $s$ refers to different slip systems, and $\gamma$ is the slipped area (see equation 2.1).

- At any time step $n$, the applied stress magnitude depends on the difference between the desired strain rate $\dot{\epsilon}_{ij}^{imp}$, and the actual strain rate calculated over a certain number of timesteps $n_{avg}$:

- $$\sigma_{app}(n) = \sigma_{app}(n-1) - C\left[\left(\epsilon_{ij}^{n} - \epsilon_{ij}^{n-n_{avg}}\right) - n_{avg}\delta t \dot{\epsilon}_{ij}^{imp}\right] \tag{2.13}$$

  where C is the elastic compliance tensor.

### 2.2.4 Line tension stress acting on a dislocation

In the absence of any external stresses, the energy of a dislocation that is constrained to pass through two points is minimum when it is straight. Upon application of an external shear stress to this dislocation, it bows out to a curved shape such that the increased line energy balances exactly the work done by the external stress (see figure 2.5). If the external stress is subsequently withdrawn, the dislocation line returns to the original straight configuration. This propensity of a dislocation to acquire a linear shape when the external stress is withdrawn can be conceived of as a line tension force which acts on the end-points of any curved dislocation, tangentially and opposes the forces that make the dislocation bow.

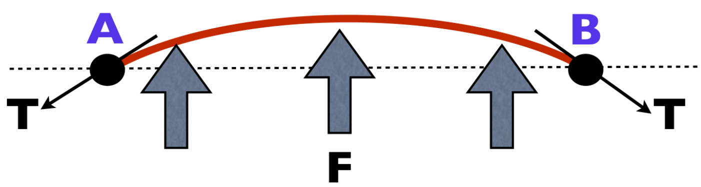


**Figure 2.5** – *A dislocation bowed at its end-points A and B, upon the action of a glide force $F$ perpendicular to the line joining the pinning points. The line tension forces $T$ operates at the ends of the pinning points tangential to the local line direction at those points.*

Even though screws and edge have different energies, in the context of line tension computation, all dislocations are assumed to have same energy per unit length, and hence the line tension is

$$T = \alpha \mu b^2 \tag{2.14}$$

Where $\mu$ is the shear modulus, and $b$ is the magnitude of the Burgers vector, and $\alpha$ is a scaling factor. If R is the radius of curvature of the dislocation arc, the line tension creates a force on the dislocation

$$\tau_{lt} = \frac{T}{bR} \tag{2.15}$$

So, if a dislocation is bent in the shape of arc, its line tension will be given by

$$\tau_{lt} = \frac{\alpha \mu b}{R} \tag{2.16}$$

A straight dislocation segment has a radius of curvature $R \to \infty$, so it experiences no line tension force.

Since the edge and screw dislocations don't have identical energies, the formula in equation (2.14) is not quite appropriate. Incorporating edge screw energy differences, the line tension force is given by [Foreman 1967, Shin 2004]:

$$\tau_{lt} = \frac{\mu b}{4\pi(1-\nu)R}(1 - 2\nu + 3\nu cos^2\theta)\left(ln\left(\frac{L}{2b}\right) - \nu cos(2\theta)\right) \tag{2.17}$$

where $\mu$ and $\nu$ stand for the shear modulus and the Poisson ratio respectively. $R$ is the radius of curvature, $L$ is the length of a segment and $\theta$ is the angle between the Burgers vector $b$ and the dislocation line vector.

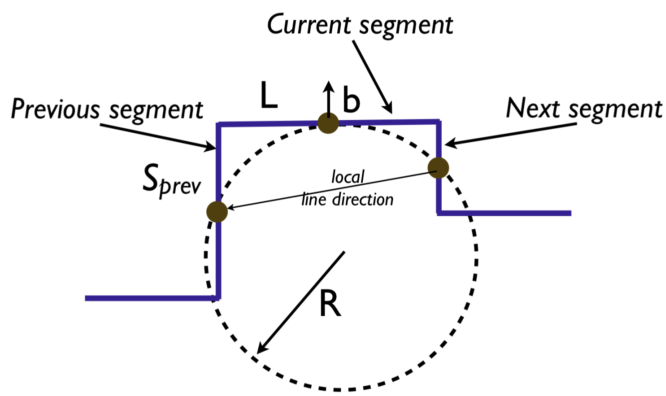


**Figure 2.6** – *Procedure for calculating the line tension on a given segment (labeled "Current segment"). The blobs on the segments indicate their midpoints. The dotted circle is the one that passes through all these three midpoints.*

In TRIDIS, the local line direction is defined as the line joining the mid-points of the neighboring segments. $R$ is the radius of the circle passing the midpoints of the current segment and the two neighboring segments, as illustrated in Fig. 2.6. The information about the next and previous neighbors of a dislocation segment is available, since they are always stored, as explained in the introduction section. Note the stress contribution of the two neighboring segments was not included during the internal stress computation. They contribute only through the line tension.

### 2.2.5 The Peierls Stress

Peierls stress is defined as the minimum resolved shear stress required to initiate glide motion in a dislocation residing in a crystal.

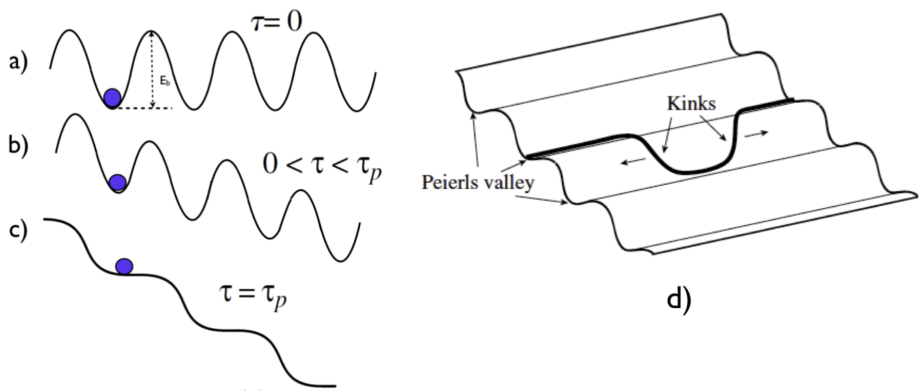


**Figure 2.7** – *Origin of Peierls stress. Figure taken from [Bulatov & Cai 2006]. The images on the left are viewed along the dislocation line, which is as a filled circle. a) In the absence of external stress, $E_b$ is the energy barrier that the dislocation sees. b) The energy barrier decreases with the increasing stress $\tau$. c) At $\tau = \tau_p$, the energy barrier disappears completely. d) The three dimensional view of mechanism nucleation of kink-pair, at $\tau = \tau_p$.*

This stress arises because the preferred dislocation position in a crystal is at the minimum of the potential offered by the crystal lattice (see figure 2.7). This potential is, by symmetry, periodic with the same period as the crystal. So, if a dislocation has to glide from one energy minima to the next, it has to do so by crossing the potential barrier presented by the atoms on the lattice. The energy barrier per unit length that a dislocation has to surmount to glide from one energy minima to the next at zero stress is termed as the Peierls barrier, $E_p$. Now, the presence of an external stress adds a constant slope to the potential landscape offered by the crystal, which effectively reduces the energy barrier that a dislocation sees. The critical value of the applied shear stress at which the Peierls barrier vanishes altogether is termed as the Peierls stress $\tau_p$. At stresses less than this Peierls stress, the dislocation cannot move unless aided by thermal fluctuations. This thermal-fluctuation assisted dislocation motion happens through the formation of kink-pairs and proceeds segment by segment rather than all at once. Hence the dislocation motion is distinctly different between resolved shear stress less than $\tau_p$ and when it is greater than $\tau_p$.

In case of fcc metals, the Peierls stress $\tau_p \sim 10^{-5}\mu$, where $\mu$ is the shear modulus of the materials. Since it is so small, ignoring its contributing in the simulation would not have much impact on the results. In bcc materials, however, the glide of screw dislocation is heavily influenced by the presence of Peierls barriers, and happens only through the formation of double kink-pairs. Details about handling glide of a screw dislocation in a bcc system is provided in Chapter 3 (see page 62).

### 2.2.6 Forces acting on a dislocation

If the stress field at the center of a dislocation segment is $\sigma$ and its Burgers vector $\mathbf{b}$, the magnitude of force per unit length acting on this dislocation is given by the Peach-Koehler (PK) formula [Hirth & Lothe 1982]:

$$f = |\overleftrightarrow{\sigma}.\mathbf{b} \times \xi| \tag{2.18}$$

where $\xi$ is the local line direction. The stress $\overleftrightarrow{\sigma}$ is net total of the stresses acting: external as well as internal stresses due to other dislocations and defects. From equation (2.18) it can be inferred that the force acting on a dislocation always acts in a direction normal to the local direction, and the magnitude of this force is always the stress tensor resolved in the direction of it's Burgers vector. In the absence of climb, the scalar version of equation (2.18) can be written as

$$f = \overleftrightarrow{\sigma}.\mathbf{n}.\mathbf{b} \tag{2.19}$$

Where $\mathbf{n}$ is indicates normal to the glide plane of the dislocation. From equation (2.19), it can be seen that the component of the stress that leads to the evolution of the dislocation is the one that acts in the glide plane $\mathbf{n}$ and in the direction of the Burgers vector $\mathbf{b}$ (see figure 2.8).

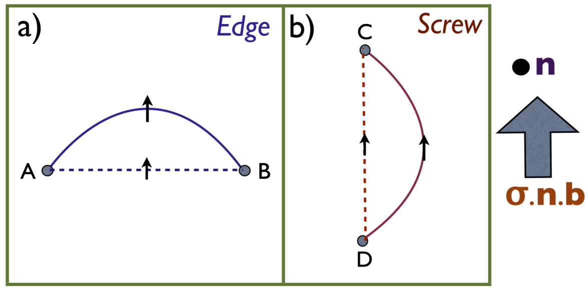


**Figure 2.8** – *The deformation of a) edge and b) screw dislocations under the glide stress of magnitude $\sigma.\mathbf{n}\mathbf{b}$. Since the two dislocations have the same Burgers vectors, the stress force acting on the two dislocations will always be the same in magnitude but in a direction perpendicular to the local line direction.*

The bowing of the screw dislocation in a direction orthogonal to the direction of the applied stress, as shown in figure 2.8 is counter-intuitive at first. The arrangement of atomic planes which leads to this type of motion for a screw dislocation is illustrated in figure 5b of Chapter 88 of book [Hirth & Kubin 2009]. It can also be understood by examining a typical screw dislocation in the simple cubic crystal structure as shown in the figure 2.9.

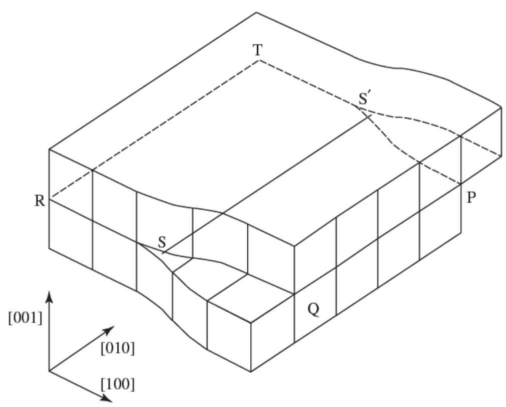


**Figure 2.9** – *A typical screw dislocation in a simple cubic structure. The screw dislocation here is $SS'$, oriented along the $[010]$ direction. Image from [Kelly & Knowles 2012]*

The dislocation here is $SS'$ oriented along the $[010]$ direction, and gliding in the $[001]$ plane. Now, under a stress in the plane $[001]$ and along the direction $[010]$ will shear the crystal further, causing the dislocation $SS'$ to move towards RT, along the direction $[\bar{1}00]$. This illustrates that a dislocation can bow in a direction different from the direction in which the shear is applied. Hence it can be concluded that in the case of conservative motion, the shear plane is the glide plane of the dislocation, and the shear direction direction is the Burgers vector **b** and that this is independent of the line character of the dislocation. Only the direction of the force depends on the local line character (see figure 2.10).

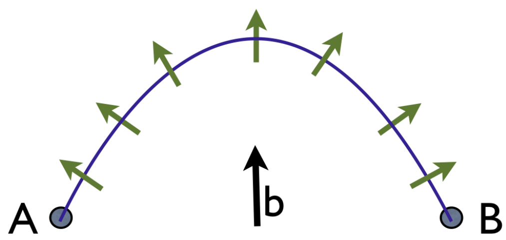


**Figure 2.10** – *Direction of forces acting on an arbitrary curved dislocation. The arrows in green indicate the direction of the force, whereas the arrow in black is the direction of Burgers vector of the line. The force direction matches the Burgers vector direction only if the dislocation is locally an edge.*

### 2.2.7 Velocity of a dislocation

The dependence of velocity of a dislocation segment on the force acting on it is a complex function depending upon the dislocation character, the temperature and the stress itself. It also, of course, depends on the material composite and its crystal structure. In the case of closely-packed structures, at 300K, the velocity of the dislocation segment is found to be directly proportional to the force acting on it. In this regime the velocity of the dislocations is governed by the thermal vibrations of the lattice. The dislocation will move in a drag field provided by the phonons of the crystal lattice and hence the dislocation is termed over-damped, where the velocity is given by

$$\nu_d = \frac{f}{B} \tag{2.20}$$

where $B$ is termed the phonon drag coefficient. In principle, $B$ itself can be different for edge and screw dislocations, and it is also a function of the dislocation velocity through

$$B(\nu_d) = \frac{B}{(1 - \frac{v_d^2}{c^2})} \tag{2.21}$$

Where $c$ is the velocity of the sound. But in the current simulations, for computational simplicity, the dependence of B on the dislocation velocity is not considered. Instead, the maximum velocity of a dislocation is capped at $v_{max}$ such that the denominator of equation (2.21) is always close to unity. In these simulations, $B$ is taken constant, independent of the line orientation.

### 2.2.8 Dislocation-Dislocation interactions

A dislocation interacts with other dislocations as will as other entities in the simulation volume like the precipitates, irradiation loops etc as it glides in its glide-plane. In handling dislocation-dislocation interactions, the following distinction is made[Shin 2004]:

- **Co-planar interactions:** Here the two dislocations are gliding on the same plane.
- **Non-coplanar interactions:** Where the two dislocations two dislocations are gliding on different planes.

Co-planar interactions are handled very easily: If the two segments have opposite line-directions, the intersecting portion is deleted and rest of the dislocations is re-constructed. If the dislocations are of same direction, the segments are not annihilated but are arrested next to each other, as shown in figure 2.11.

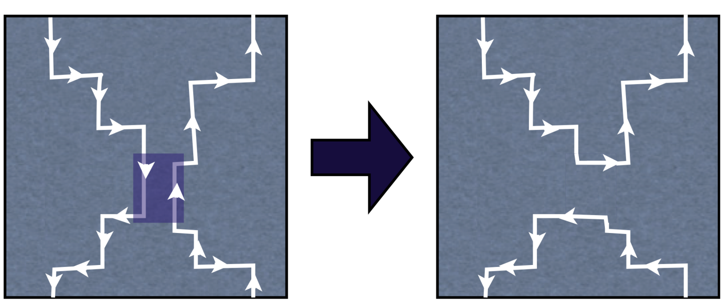

**Figure 2.11** – *Annihilation of co-planar dislocations of opposite line characters.*

Non-coplanar interactions lead to the formation of junctions and is handled through the hardening theory, with the hardening parameters depending upon the kind of junctions[Shenoy *et al.* 2000

**Case 1** Dislocations with the **same** Burgers vectors but gliding on different slip planes.

**Case 2** Dislocations with **different** Burgers vectors, and gliding on different slip planes.

**Case 3** The Burgers vectors are other **orthogonal** to each other and the dislocations are gliding in different glide planes.

**Case 4** Dislocations are such that the **sum** of their Burgers vectors **is** a possible Burgers vectors for that crystal structure.

**Case 5** Dislocations are such that the **sum** of their Burgers vectors **is not** a possible Burgers vectors for that crystal structure.

**Case 1** corresponds to the usual cross-slip configuration, and this is handled just by changing the neighborhood of the segments. Cases **2** and **5** correspond to the Hirth and Lomer-Cortell locks which are handled by implementing the hardening coefficients. **Case 4** is handled by examining the energetics and checking the Frank-energy criteria. The hardening parameters are obtained in [Shin *et al.* 2001].

### 2.2.9 Computing displacement fields

The computation of the displacement field of dislocations is very useful in analyzing surface deformation induced by dislocations. The displacement produced by any closed dislocation configuration, at a point $\mathbf{r}$ is given by the Burgers formula:

$$\mathbf{u}(\mathbf{r}) = -\frac{\mathbf{b}}{4\pi}\Omega - \frac{1}{4\pi}\oint \frac{\mathbf{b} \times dl'}{R} + \frac{1}{8\pi(1-\nu)}\nabla \oint \frac{(\mathbf{b} \times \mathbf{R})dl'}{R} \tag{2.22}$$

where $\mathbf{b}$ is the Burgers vector, $\nu$ is the Poisson's ratio, and $\Omega$ is the solid angle through which the dislocation loop is seen:

$$\Omega = -\oint_A \frac{\mathbf{R}.d\mathbf{A}}{R^3} \tag{2.23}$$

The methodology for obtaining a displacement field for a triangular loops is provided by [Hirth & Lothe 1982], and it is an involved problem to obtain analytical solutions for arbitrary dislocation configurations. Hence, the general way to compute the displacement field due to an arbitrary dislocation loop is to decompose the dislocation loop into a collection of triangulated loops, as shown in figure 2.12.

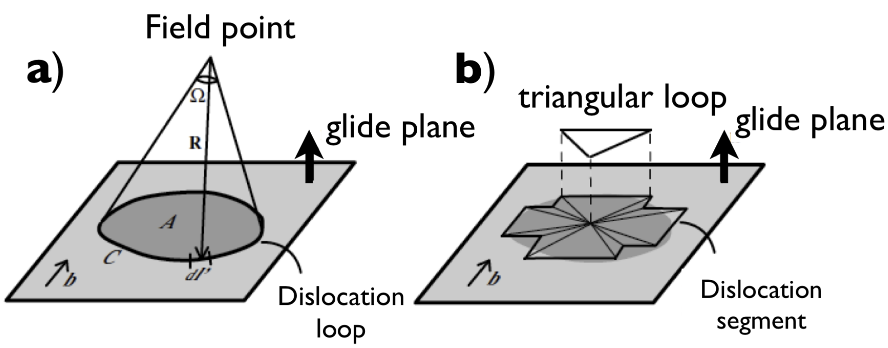


**Figure 2.12** – *Barnett triangulation scheme [Barnett 1985]. The dislocation loop of b) is divided into a collection of triangles. The displacement at the field point due to the loop in figure a is computed by summing the vectorial displacements due to the the triangles shown in the figure b. Image taken from [Shin 2004].*

The displacement field at a computation point P($\mathbf{r}$) due to a triangular dislocation loop with points $A(\mathbf{r}_A)$, $B(\mathbf{r}_B)$ and $C(\mathbf{r}_C)$ is given by

$$\mathbf{u}(\mathbf{r}) = -\frac{\mathbf{b}}{4\pi}\Omega + \mathbf{F}_{AB} + \mathbf{F}_{BC} + \mathbf{F}_{CA} \tag{2.24}$$

where

$$\Omega = -sign(\mathbf{R}_i.\mathbf{n})\left[4\arctan\left(\sqrt{tan\left(\frac{s}{2}\right)tan\left(\frac{s-a}{2}\right)tan\left(\frac{s-b}{2}\right)tan\left(\frac{s-c}{2}\right)}\right)\right] \tag{2.25}$$

and

$$\mathbf{F}_{ij} = -\frac{1-2\nu}{8\pi(1-\nu)}(\mathbf{b}\times\mathbf{t}_{ij})ln\frac{R_j+\mathbf{R}_j.\mathbf{t}_{ij}}{R_i+\mathbf{R}_i.\mathbf{t}_{ij}} + \frac{1}{8\pi(1-\nu)}(\mathbf{b}.\mathbf{n}_{ij})\left(\frac{\mathbf{R}_j}{R_j}-\frac{\mathbf{R}_i}{R_i}\right)\times\mathbf{n}_{ij} \quad (2.26)$$

where the vectors are indicated in figure 2.13, and $s$ is the semi-perimeter of the triangle.

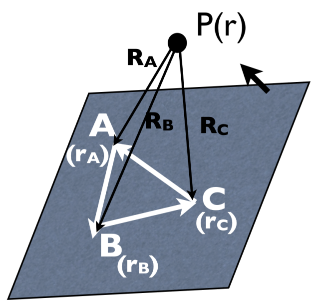


**Figure 2.13** – *Parameters for Barnett's triangulation formula.*

### 2.2.10 Algorithm of Edge-Screw Dislocation Dynamics

Once the computation parameters like the time-step $\Delta t$, the total simulation time $T_{tot}$, stress increment scheme etc are chosen, an elementary dislocation dynamics simulation is carried out as described in the algorithm 2.2.

**Algorithm 2.2** Edge-Screw Dislocation Dynamics.

1. Initialize $t = 0$.
2. Compute the forces acting on the dislocation segments, and then compute their velocities. Advance the position of the all segments, by one time step corresponding to their velocities. Increment time $t = t + \Delta t$.
3. Re-establish segment connectivity by creating new dislocation segments, if necessary.
4. Merge or split dislocation segments depending upon the current length.
5. Compute strains and dislocation densities corresponding to this time-step.
6. Update external stress, if needed, depending on the current strain level or other parameters.
7. Return to step 2, unless $t \geq T_{tot}$, or deformation is equal to the desired value or other such termination condition is met.

### 2.2.11 Typical outputs of a DD simulation

Output of a Dislocation Dynamics simulations is usually in terms of stress-strain plots and dislocation densities. One can also monitor the spread of dislocations into different slip-planes, whereby obtaining the distribution of strain into different slip-systems. It is also possible to get access to the velocity profile of the dislocation segments and the number of cross-slip events registered per unit time through which one can estimate the role of physical parameters like temperature etc as well as effect of irradiation, precipitates etc on cross-slip process.

### 2.2.12 Limitations of Edge-Screw based DD

The Edge-Screw based dislocation dynamics code TRIDIS is not equipped to handle dislocation junction formation. It also cannot incorporate partial dislocations and the stacking faults enclosed by those partials. The stress-strain plots obtained by these DD simulations are also not comparable to those obtained through conventional experiments. This is because of the high-strain rate employed in the simulations, as well as the initial dislocation densities chosen. The present DD simulations are carried out only on a single grain, so influence of poly-crystallinity cannot be obtained from these simulations. Also, the accuracy of this code is controlled by the discretization length specified in the code and all the dislocations, of arbitrary line character, are represented as edges or screws of this minimum length scale. In the next section, a new way of doing dislocation dynamics is introduced which can overcome the above limitations.

Another limitation of conventional dislocation dynamics as well as molecular dynamics simulations, concerning the loading conditions, is in the strain rates that are possible (see section 2.2.3.3 on page 36 for discussion on constant strain rate controlled simulation). Typical elongation experiments are carried out at a strain rate of $10^{-4}s^{-1}$

to $10^{-2}s^{-1}$ [Onimus & Béchade 2009, Onimus *et al.* 2004, Dunlop *et al.* 2007], whereas in MD and DD simulations, the strain rates are typically $10^{5}s^{-1}$ to $10^{8}s^{-1}$ [Zbib *et al.* 2000, Hatano & Matsui 2005]. A systematic study of role of strain rate on the dislocation interaction has been recently presented in [Liu *et al.* 2008] and [Fan *et al.* 2013]. Within the context of this thesis, the sensitivity of our results to the strain rate is explained in the corresponding chapters.

## 2.3 Nodal based Dislocation Dynamics

### 2.3.1 Representing dislocations as collection of nodes

In the nodal formalism, the dynamic variables are the so-called nodes as shown in the figure (2.14). The dislocation segments are just straight line segments that connect a pair of these nodes. Each dislocation line connecting nodes $\mathbf{r}_i$ and $\mathbf{r}_j$ can have an arbitrary Burgers vector $\mathbf{b}_{ij}$. This readily demonstrates that the nodal based representation of dislocations allows us to represent the dislocation junctions where two or more dislocations meet, as shown in the figure (2.15), which is not possible in the Edge-Screw representation. At every nodal point $i$, the conservation of Burgers vector demands $\sum\limits_{j}\mathbf{b}_{ij} = 0$, where the summing is carried out over all nodes $j$ that connect to the node $i$.

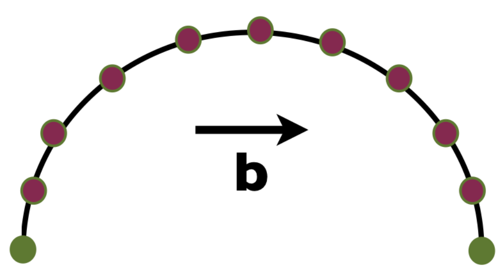


**Figure 2.14** – *Node based discretization of an arbitrary dislocation line. Compare this figure with the figure of Edge-Screw modeling of the same dislocation configuration. Figure (2.1) The nodes represented in green are pinned and have no degree of freedom, whereas the nodes in brown have two degrees of freedom, spanning the entire glide plane of the dislocation.*

A dislocation node can also belong to more than one dislocation line, as illustrated in figure (2.15).

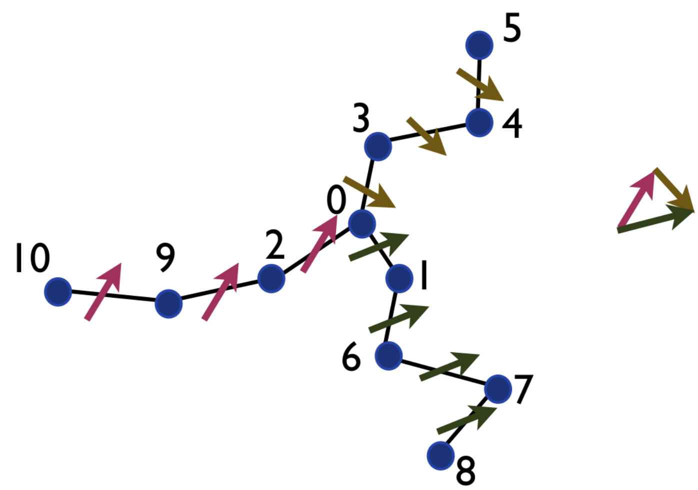


**Figure 2.15** – *An arbitrary network of dislocation segments. Node 0 is connected to three arms, having three different Burgers vectors. The vectorial sum of these Burgers vectors must become zero at every such node.*

At every instant in time, the set of all nodes and the Burgers vectors of all the segments connecting the nodes: $\{\mathbf{r}_i, \mathbf{b}_{ij}\}$ represents the complete configuration of the system. The energy of the dislocation configuration can hence written as $E_{tot}(\{\mathbf{r}_i, \mathbf{b}_{ij}\})$. The force acting on the node $i$ is then defined as the negative derivative of the total energy with respect to its position $\mathbf{r}_i$, i.e.,

$$\mathbf{f}_i = -\frac{\partial E_{tot}(\{\mathbf{r}_i, \mathbf{b}_{ij}\})}{\partial \mathbf{r}_i}. \tag{2.27}$$

### 2.3.2 Non-singular stress formalism

The non-singular stress formalism provides a non-singular expressions for energies of arbitrary dislocation configurations, and for stresses at arbitrary distances. Consider, for example, the elastic energy of an arbitrary dislocation :

$$E = \frac{1}{2}\int S_{ijkl}\sigma_{ij}(\mathbf{x})\sigma_{kl}(\mathbf{x})d(\mathbf{x}) \tag{2.28}$$

where the matrix **S** is the elastic compliance tensor. Now, since $\sigma_{ij}(\mathbf{x})$ falls off as $1/R$, the volume integral diverges. The appearance of this divergence should come as no surprise. It, actually, portends to the breakdown of the linear elastic theory at very close distances to the dislocation line, as well as on the dislocation line itself. In the **Non-singular stress formalism** [Cai *et al.* 2006], this singularity is removed by smearing the Burgers vector along the whole dislocation line. This Burgers vector density is represented by $\mathbf{g}(\mathbf{x})$ and the normalization condition requires

$$\mathbf{b} = \int \mathbf{g}(\mathbf{x})d^3(\mathbf{x}) \tag{2.29}$$

This $\mathbf{g}(\mathbf{x})$ was taken of the form

$$\mathbf{g}(\mathbf{x}) = \mathbf{b}\widetilde{w}(\mathbf{x}) = \mathbf{b}\widetilde{w}(r) \tag{2.30}$$

where $\widetilde{w}(\mathbf{x})$ is chosen such that $w(\mathbf{x}) \equiv \widetilde{w}(\mathbf{x}) * \widetilde{w}(\mathbf{x})$ ,where $w(\mathbf{x})$ satisfies the condition

$$R_a(\mathbf{x}) = R(\mathbf{x}) * w(\mathbf{x}) = \sqrt{R(\mathbf{x})^2 + a^2} = \sqrt{x^2 + y^2 + z^2 + a^2} \tag{2.31}$$

where $a$ is a free parameter in the model, called the "core width". The functional form $R_a(\mathbf{x})$ was chosen such that it has the similar functional form as $R(\mathbf{x}) = \sqrt{x^2 + y^2 + z^2}$, but remains finite even when $R(\mathbf{x})$ becomes zero. The functional form for $w(\mathbf{x})$ that gives the above $R_a(\mathbf{x})$ is given by

$$w(\mathbf{x}) = \frac{15}{8\pi a^3 \left[(\frac{r}{a})^2 + 1\right]^{\frac{7}{2}}} \tag{2.32}$$

where $r = \|\mathbf{x}\|$.

### 2.3.3 Energy of a dislocation

A solid with dislocations is always of higher energy compared to the solid without such dislocations. The line energy of the dislocation in an isotropic elastic medium is given by [Argon 2008]:

$$\mathcal{F}_e = \frac{\mu b^2}{4\pi(1-\nu)} ln\left(\frac{\alpha R}{b}\right), \quad \mathcal{F}_s = \frac{\mu b^2}{4\pi} ln\left(\frac{\alpha R}{b}\right) \tag{2.33}$$

Where $\mathcal{F}_e$ and $\mathcal{F}_s$ are the line energies per unit length of screw and edge dislocations, within a range R of the outer field. The term $\alpha$ is there to ensure the core energy contribution, and is of the order of $1$ to $4$. The contribution of the core energy is of the order of $10-15\%$ of the total energy of the dislocation. Under certain assumptions on $R$ and $\alpha$, and ignoring the parameter $\nu$, it is possible to simplify the expressions of equation (2.33) as

$$\mathcal{F} \approx \mathcal{F}_e \approx \mathcal{F}_s \approx \frac{\mu b^2}{2} \tag{2.34}$$

The non-singular stress formalism is self-consistent, in the sense of the force obtained by taking the derivative of elastic energy with respect to a nodal position and the force obtained by the usual Peach-Koehler formula.

In this stress formalism, the total energy per unit length of a dislocation configuration is composed of two components: an elastic energy contribution $\epsilon_{self}$ and a core energy contribution $\epsilon_{core}$. The elastic energy of a dislocation segment of length $L$, Burgers vector $\mathbf{b}$, and line direction $\mathbf{t}$ is given as

$$\epsilon_{self} = \frac{\mu}{4\pi(1-\nu)} \left\{ \left[\mathbf{b}.\mathbf{b} - \nu(\mathbf{b}.\mathbf{t})^2\right] Lln\left[\frac{L_a + L}{a}\right] - \frac{3-\nu}{2}(\mathbf{b}.\mathbf{t})^2 \left(L_a - a\right) \right\} \tag{2.35}$$

where $L_a = \sqrt{L^2 + a^2}$.

To this energy, the core-energy contribution $\epsilon_{core}$ is to be added such that the total energy matches that obtained by the atomistic simulation. The core energy per unit length is given by [Shishvan *et al.* 2008]:

$$\epsilon_{core} = \frac{\mu}{4\pi} ln \frac{a}{\bar{a}} \left[ (\mathbf{b}.\mathbf{t})^2 + \frac{|\mathbf{b}\times\mathbf{t}|^{\mathbf{2}}}{1-\nu} \right] \tag{2.36}$$

where $\bar{a}$ is another free parameter, which is used to match total energy with that obtained by the atomistic studies. If the core-radius parameter $a$ is itself taken as $\bar{a}$, then the core contribution to the dislocation total energy will be zero, and the elastic energy will directly match the atomistic energy.

#### 2.3.3.1 Interaction energy of two dislocations

Given two parallel dislocations $(\mathbf{x}_1, \mathbf{x}_2, \mathbf{b})$ and $(\mathbf{x}_3, \mathbf{x}_4, \mathbf{b}')$, in the non-singluar stress formalism, their interaction energy is given by [Cai *et al.* 2006]:

$$E_{int} = W(\mathbf{x}_4 - \mathbf{x}_2) + W(\mathbf{x}_3 - \mathbf{x}_1) - W(\mathbf{x}_4 - \mathbf{x}_1) - W(\mathbf{x}_3 - \mathbf{x}_2) \tag{2.37}$$

where $W(\mathbf{R})$ is given by

$$\begin{aligned}
\frac{W(\mathbf{R})}{W_0} &= \{(\mathbf{b}.\mathbf{t})(\mathbf{b}'.\mathbf{R}) + (\mathbf{b}'.\mathbf{t})(\mathbf{b}.\mathbf{R}) \\
&- [(2-\nu)(\mathbf{b}.\mathbf{t})(\mathbf{b}'.\mathbf{t}) + \mathbf{b}.\mathbf{b}']\mathbf{R}.\mathbf{t}\} ln[R_a + \mathbf{R}.\mathbf{t}] \\
&+ [(1-\nu)(\mathbf{b}.\mathbf{t})(\mathbf{b}'.\mathbf{t}) + \mathbf{b}.\mathbf{b}']R_a \\
&- \frac{[\mathbf{b}.\mathbf{R} - (\mathbf{R}.\mathbf{t})(\mathbf{b}.\mathbf{t})][\mathbf{b}'.\mathbf{R} - (\mathbf{R}.\mathbf{t})(\mathbf{b}'.\mathbf{t})]}{R_a^2 - (\mathbf{R}.\mathbf{t})^2} R_a \\
&+ \frac{a^2[(1+\nu)(\mathbf{b}.\mathbf{t})(\mathbf{b}'.\mathbf{t}) - 2(\mathbf{b}.\mathbf{b}')]}{2(R_a^2 - (\mathbf{R}.\mathbf{t})^2)} R_a
\end{aligned} \tag{2.38}$$

where

$$W_0 = \frac{\mu}{4\pi(1-\nu)} \tag{2.39}$$

$$R = \|\mathbf{R}\| \tag{2.40}$$

$$R_a = \sqrt{R^2 + a^2} \tag{2.41}$$

$$\mathrm{t} = \frac{\mathrm{x}_2 - \mathrm{x}_1}{\|\mathrm{x}_2 - \mathrm{x}_1\|} \tag{2.42}$$

For a collection of dislocations, the total energy is given by the sum of 1. Elastic self energy, that includes the core-energy contribution. 2. Elastic interaction energy for every pair of dislocations in the configuration, and 3. Energy configuration due to the stacking fault. The pair-wise interaction energy in the non-singular stress formalism is given in [Cai *et al.* 2006], whereas the stacking fault energy is taken as proportional to the area of the enclosed faulted region [Martinez *et al.* 2008].

A systematic study of variation of the total energy with line character and other physical parameters is carried out in Chapter 5.

### 2.3.4 Algorithm of nodal based dislocation dynamics

Discretize each dislocation line into nodes such that the distance between two adjacent nodes is less than or equal to a predefined value. Note that in this model the dislocation line is assumed to remain straight between the discretization nodes.

The stress at any arbitrary point due to the dislocations connecting these discretization nodes is given by [Cai *et al.* 2006]:

$$\sigma^{int}(\mathbf{x}) = \sum_{(k-l)} \sigma^{int}(\mathbf{x}; k-l) \tag{2.43}$$

where $\sigma^{int}(\mathbf{x}; k-l)$ is the stress at $\mathbf{x}$ due to the dislocation segment joining nodes $k$ and $l$, and the summation is over all such connected nodes. The stress at a point $\mathbf{x}$ is due to all the internal stresses due to the dislocations, as well as the applied stress.

$$\sigma(\mathbf{x}) = \sigma^{int}(\mathbf{x}) + \sigma^{app} \tag{2.44}$$

where $\sigma^{app}$ is the external applied stress. From the stress acting at $\mathbf{x}$, the force per unit length at that point is given by the familiar Peach-Koehler formula [Cai *et al.* 2006]:

$$\mathbf{f}^{\mathbf{PK}}(\mathbf{x}) = (\sigma(\mathbf{x}).\mathbf{b}) \times \xi(\mathbf{x}) \tag{2.45}$$

where $\xi(\mathbf{x})$ is the local line direction at **x.** The PK force, hence, acts in a plane that contains both the Burgers vector and the line direction and is perpendicular to the local line direction. The PK force is converted into the nodal force by weighing it by a shape function. This step is necessary for ensuring that the pinning points do not respond to any force acting on them. The discretization nodes are evolved for a time-step $\delta t$ with a velocity proportional to the nodal force acting on them. Once the nodes evolve, the nodes that are closer than a predefined value are merged, and if the nodes are farther than a predefined value, new nodes are inserted. This process is repeated until the total time of the simulation equals the desired time. At every certain number of time-steps, the nodal configurations, the energies, the instantaneous dislocation lengths are recorded for processing of the results.

**Algorithm 2.3** Algorithm for Nodal based dislocation dynamics

1. Initialize time t := 0.
2. Compute nodal forces and velocities, and to advance nodal positions by one time step. Increment time $t := t + \Delta t$.
3. For each multi-arm node, compute the rates of energy dissipation for all of its possible dissociation outcomes and split the nodes if required.
4. For all pairs of unconnected segments, find the minimum separation $d$. For pairs with $d < r_a$, introduce new nodes at the locations of closest approach.
5. Merge all pairs of nodes within $r_a$ of each other.
6. Split every node with more than three neighbors into two nodes if this increases the local energy dissipation rate.
7. Re-mesh the entire dislocation network.
8. Return to step 2, unless the total number of cycles is reached.

## 2.4 An illustration of split dislocation simulation

The nodal based DD is able to handle dislocation features like junction formation, dislocation splitting into partials, formation of stacking faults etc which are not possible in the conventional Edge-Screw dislocation modeling. As an illustration of strength of this technique in modeling dislocation behavior, some elementary examples are considered below. These simulations are carried out using NUMODIS [L. Dupuy & Coulaud 2013].

### 2.4.1 Equilibrium dissociation width

Consider a split screw dislocation, constructed as shown in the figure 2.16 a below. The nodes in red are the computation nodes with two degrees of freedom and the nodes in blue are the pinned with no degrees of freedom. The two lines connecting two sets of nodes are the two partial dislocation and the arrows indicated over them point in the direction of the Burgers vector. The area in brown is the stacking fault enclosed by the partials.

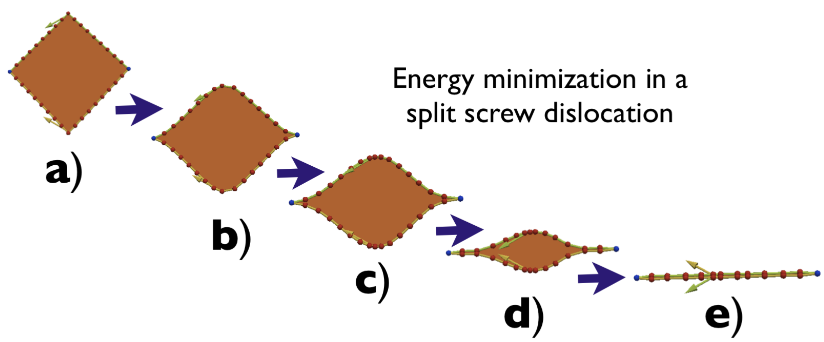


**Figure 2.16** – *Equilibrium dissociation of split FR source. Frame a) shows the initial configuration, with the brown region indicating faulted region, with the green lines being the partial dislocations. The red dots are the nodal points where the PK forces are evaluated.*

### 2.4.2 Evolution of a split FR source

The snapshots in the evolution of a split Frank-Read source, under a shear stress greater than its activation stress is shown in the figure 2.17. The initial configuration for this simulation is the equilibrium configuration under zero stress, that is figure e of 2.16. Distances between the pinning points in all the snapshots of figure 2.17, are of the same length, although they are scaled differently here.

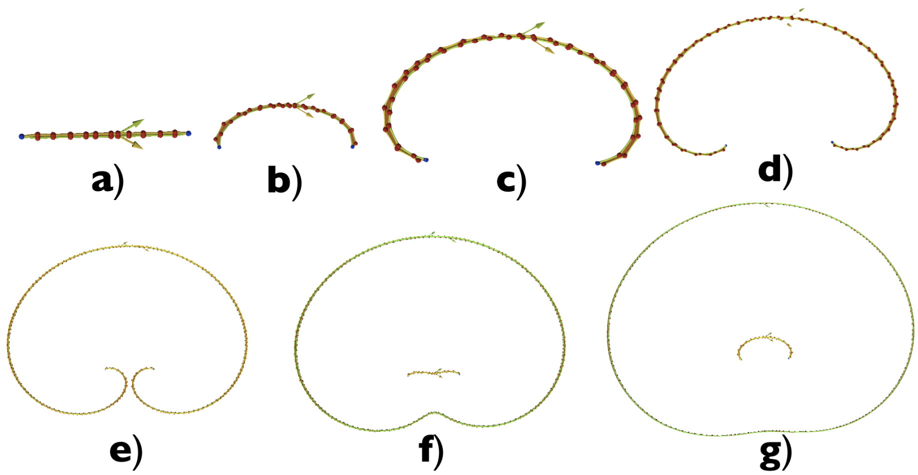


**Figure 2.17** – *Evolution of a split FR source. Image a) represents the initial configuration, and images b) to g) show various stages of FR evolution under a shear stress. The distance between the pinning points (blue nodes), is the same for all the images.*

### 2.4.3 Evolution of a Stacking Fault Tetrahedron

Stacking fault tetrahedra (SFTs) are a type of three dimensional defects, which are produced along with other defects like Frank loops etc during irradiation[Kiritani 1997]. These are the most common vacancy type defect cluster in materials with low stacking fault energy. These defects have the shape of four equilateral vacancy type stacking faults on {111} planes intersecting along $\langle 110 \rangle$ edges to form a perfect tetrahedron. Consider the Frank loop formed as shown in the figure 2.18.

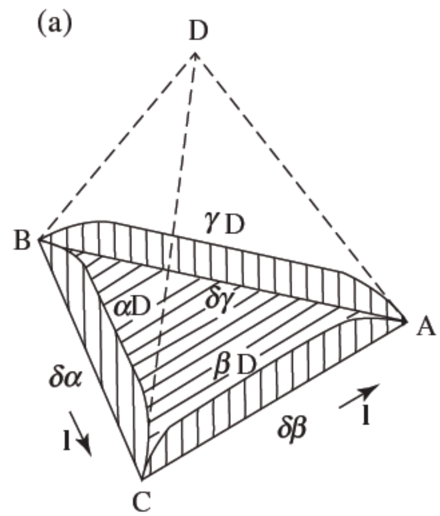


**Figure 2.18** – *The triangular Frank loop, the starting configuration for the formation of the stacking fault tetrahedron.*

The Frank-loop considered in figure 2.18 is a triangular loop with sides along the $\langle 110 \rangle$ directions AB, BC, and CA. The Shockley partials of this dissociated Frank-loop react at the intersection of the $\{111\}$ planes and form stair-rod dislocations. The final configuration is shown in the figure 2.19.

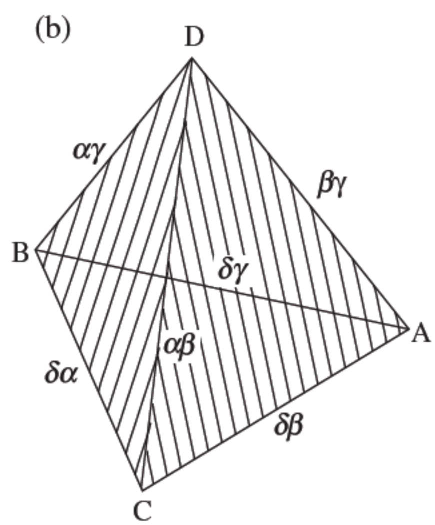


**Figure 2.19** – *Formation of stacking fault tetrahedron from a triangular Frank loop.*

The evolution of stacking fault tetrahedron from triangular Frank-loop, as seen in Nodal based dislocation dynamics simulation is shown in the figure 2.20. The configurations on the foreground of the graph are instantaneous snapshots of the formation of the SFT, and the time-evolution is indicated by the arrows, starting from top-left to bottom-right. The graph in the figure shows the variation of elastic energy, stacking fault energy and the total energy as the Frank loop evolves into the stacking fault tetrahedron. The stacking fault energy is taken as $45mJ/m^2$.

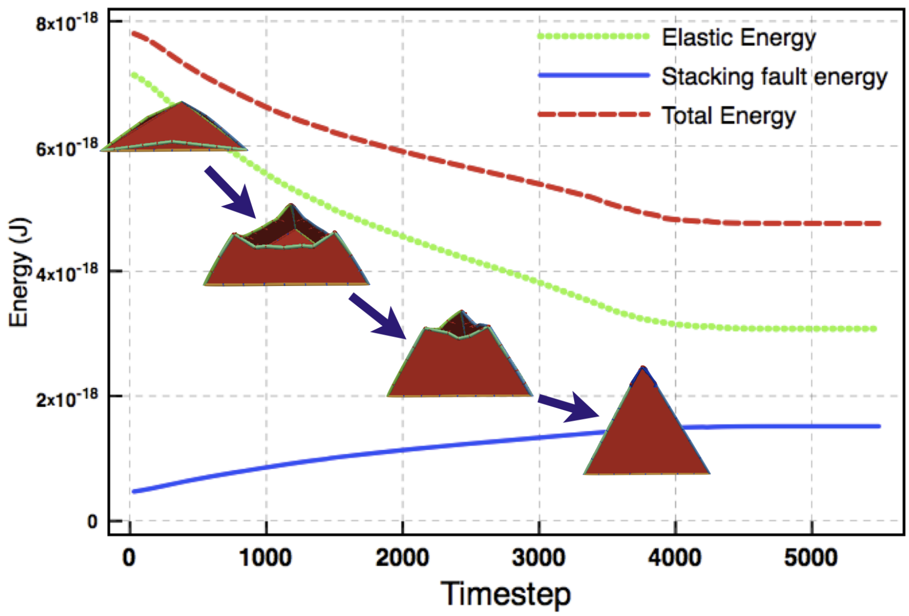


**Figure 2.20** – *Change in energetics of the system as the stacking fault tetrahedron is formed from a Frank-loop in an fcc matrix. The x-axis indicates the number of time-steps, each timestep corresponds to* $0.000015$ *ns.*

# Chapter 3

# Effect of oxide dispersions in strain localization of irradiated ferritic steels

*This chapter discusses the results obtained in DD simulations of strain localization studies in irradiated ODS steels. The interplay of dislocations, irradiation-induced defects and dispersoids in affecting the stress-strain behavior and strain localization in one micron grain is investigated in detail. The chapter is primarily divided into three sections:*

***Dislocation dynamics in bcc systems****: Here, the mobility and cross-slip rules required for carrying out the dislocation dynamics simulations in bcc are discussed, along with the implementation details as applicable to the subsequent sections.*

***Dislocation evolution in the presence of loops and ODS precipitates****: Results obtained by performing three-dimensional discrete dislocation dynamics simulations of ODS steels are presented and the effect of irradiation on strain localization and hardening is compared between ODS steels and pure $\alpha$ Iron.*

***Effect of irradiation loop density on plastic deformation in RPV steels****: The previous study of irradiation in bcc iron is here extended to understand the role of loop density, temperature, and loading in irradiation-induced hardening, with loop densities appropriate for Reactor Pressure Vessel (RPV) steels.*

## 3.1 Dislocation dynamics in bcc systems

The shortest lattice vector in bcc is of the type $\frac{1}{2}\langle 111\rangle$ and hence this defines the Burgers vector in a bcc crystal. The slip planes over which the glide happens is more complex to define. Slip is seen to happen in three different crystallographic slip planes: $\{110\}, \{112\}$ and $\{123\}$. It is important to note that each of these slip planes contains the $\langle 111\rangle$ direction. In fact, three $\{110\}$ three $\{112\}$ and six $\{123\}$ planes intersect along the same $\langle 111\rangle$ direction. Thus it is possible for a screw dislocation in the $\langle 111\rangle$ direction can glide in any of these planes and can also, for instance, randomly change its glide plane from one of the $\{110\}$ type planes to another, even to one of $\{112\}$ or $\{123\}$ type leading to wavy dislocation motion. The ease of cross-slip in bcc compared to fcc indicates perhaps that the stacking faults are of very high energy. Molecular Dynamics simulations performed by deliberately creating the stacking faults in low-index planes have revealed that stacking faults are unlikely to form in bcc.

The DD code used in this study is based on the discrete edge–screw model [Verdier *et al.* 1998] introduced earlier (section 2.2 on page 29), but adapted to the bcc crystalline structure, including 12 $a/2110\,\langle 111\rangle$ slip systems. The dislocation glide on the other planes is not considered in this study.

### 3.1.1 Dislocation mobility rules

Dislocations motion in bcc materials is a much involved process compared to that in fcc structures. This complexity in bcc is attributed to its unusual core structure. The edge dislocations are found to move with a velocity proportional to the force acting on them, but the glide of screw dislocations is an activated phenomenon, occurring through the thermal assisted formation of kink-pairs.

Ferritic materials undergo a smooth but well defined brittle to ductile transition in the 50–300 K temperature range. For this reason, it is essential to develop mobility rules covering this temperature range. Screw segments velocity is taken proportional to $exp(\Delta G/kBT)$, as per thermal activation theory (see also expressions (3.2) and (3.3) ). In the adopted framework, $\Delta G$ is the activation energy barrier to move a given screw dislocation at a given temperature T and a given effective resolved shear stress $\tau^*$ [Caillard *et al.* 2003]. Here, we assume the stress dependence of $\Delta G$ as given by Kocks expression [Kocks *et al.* 1975]:

$$\Delta G(\tau*) = \Delta H_0 \left(1 - \left[\frac{\tau*}{\tau_p}\right]^p\right)^q \tag{3.1}$$

where $\Delta H_o$ is the thermal activation barrier at $0K$, whereas $\tau_p$, $p$ and $q$ are fitting parameters, determined from the evolution of $Fe$ crystal yield stress with temperature. All three parameters were estimated during various tests, made prior to this investigation [Libert 2007]. These and other important simulation parameters are listed in Table 3.1 below.

**Table 3.1** – *Mechanical and microscopic parameters of bcc Fe matrix.*

| $\Delta H_0$(eV) | $p$ | $q$ | B($10^{-5}Pa.s$) | b ($10^{-10}m$) | Young's modulus E (GPa) | Poisson's ratio $\nu$ |
|---|---|---|---|---|---|---|
| 0.76 | 0.593 | 1.223 | 10.5 | 2.5 | 210 | 0.3 |

From a physical point of view, mobility laws implemented so far in DD simulations were based on the nucleation of isolated double kinks. This approach breaks down at intermediate temperature regimes (near 300 K) and leads to computational instabilities (sharp velocity changes for little stress increments). A possible improvement consists in accounting for the mean free path of kink pairs. An extensive presentation of such a model can be found in reference [Hirth & Lothe 1982].

The specific features used in this DD model are the following:

1. In calculating the screw dislocation velocities, we consider the average distance $X_0$ along a screw dislocation swept out by a kink before its annihilation at another kink or, if not, at the end of the screw segment. This new rule naturally accounts for the possibility to nucleate simultaneously several double-kinks along a screw dislocation of finite length (see figure (3.1)).

2. Stress dependence is accounted for by critical kink pair formation.

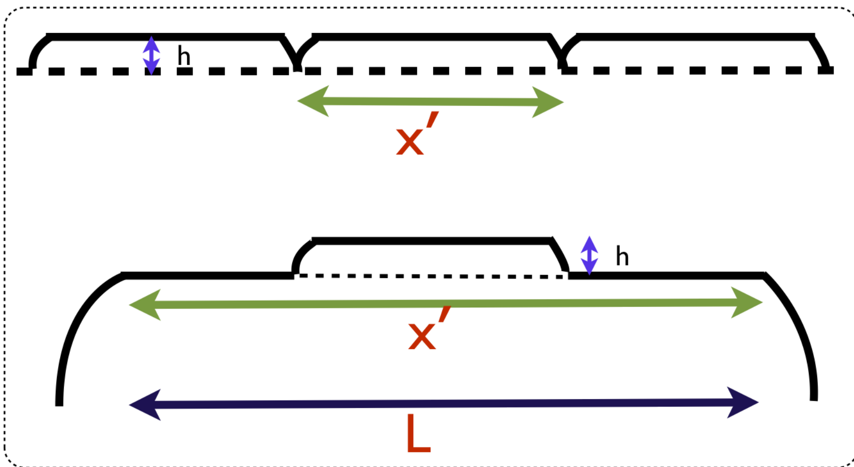


**Figure 3.1** – *Multiple kink-pair formation along a screw dislocation in Dislocation Dynamics simulations. The average distance $X'$ is swept out by a given kink pair before annihilation, along a screw dislocation of finite length L. Distance $X'$ can apply to kinks annihilating on opposite kinks (first scheme) or if not, on two ends of the screw dislocation.*

The screw dislocation velocity corresponding to rules (i) and (ii) is expressed by:

$$v_{Screw} = hX^{'}J \tag{3.2}$$

where $h$ is the distance between two consecutive Peierls barriers, $X^{'}$ being the average annihilation distance for a kink pair through a $L$ long screw dislocation (see also figure 3.1), whereas $J$ is the double-kink nucleation rate per unit length. Quantities $J$ and $X^{'}$ are calculated according to the following expressions [Garcia-Rodriguez 2011b]:

$$J = \frac{8\pi\tau^*}{\mu B h} exp(-\frac{\Delta G}{k_B T}) \tag{3.3}$$

and

$$X' = \frac{X_\infty L}{X_\infty + L} \tag{3.4}$$

here $\mu$ is the shear modulus, B is the phonon drag coefficient, $k_B$ the Boltzmann's constant and $T$ the simulation temperature (while $\Delta G$ is derived from expression (3.1)). The term $\tau^*$ in pre-factor of expression (3.3) implicitly accounts for the stress dependence for critical kink pair formation. Quantity $X_\infty$ is the average distance swept by a kink pair before annihilation with another kink pair, along an infinitely long screw dislocation:

$$X_\infty = 2\left(\frac{v_k}{J}\right)^{\frac{1}{2}} \tag{3.5}$$

where the kink velocity $v_k$ is assumed to be equal to edge dislocation velocity $v_{edge}$. The screw dislocation velocity calculated using expressions (3.1)–(3.5) with the parameters listed in Table 3.1 is fully consistent with experimental measurements made in Fe single crystals, in the whole 4–300 K temperature range [Urabe & Weertman 1975].

It can be seen that the velocity of edge dislocations is at least an order of magnitude higher than the screw dislocations. This strong anisotropy between edge and screw velocities can induce strong slip instabilities in simulations. Consider, for illustration, figure 3.2, showing an edge dislocation segment evolving under stress.

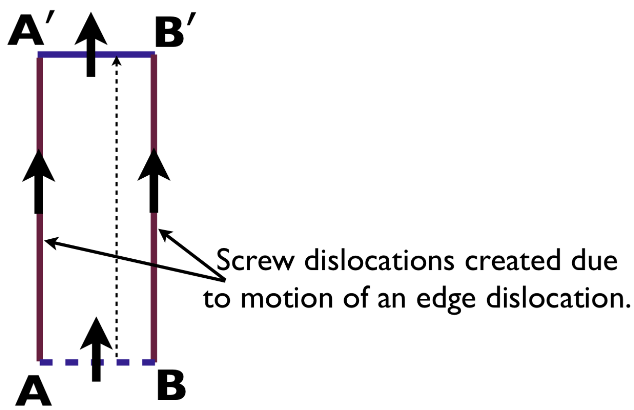


**Figure 3.2** – *The evolution of a pinned edge dislocation from $AB$ to $A'B'$ creates two long screw dislocations, $AA'$ and $BB'$. The arrows on the lines indicates their Burgers vectors.*

As the velocity of edge dislocations is independent of their length, evolution of a small edge dislocation $AB$ to $A'B'$ will create long parallel screw dislocations $AA'$ and $BB'$, very close to each other. These screws, having the same line direction, strongly repel each other and this leads to unrealistically large displacements in the screw dislocations in the subsequent timestep. This instability in the dynamics can be avoided by decoupling the edge and screw evolutions from each other. That is achieved by setting the timestep of edge dislocation as $N$ times the timestep of a screw dislocation, where $N$ is temperature and strain rate dependent.

### 3.1.2 Cross-slip Algorithm

Implementing cross-slip phenomenon into dislocation dynamics is a difficult task: A realistic, averaged cross-slip probability computed in the DD framework has to be representative of numerous single cross-slip events, each one taking place at the atomic scale and during very short characteristic periods of time. In MD simulations for instance, the glide plane is found to fluctuate within the time scale of a few tens of picoseconds and length scale of one b, whereas in a DD simulation, the typical time and space scale are rather of the order of 1000 ps and 10 b [Chaussidon *et al.* 2008]. An accurate cross-slip scheme must hence provide a coarse-grained approximation of this atomistic cross-slip phenomenon at the length and timescale of dislocation dynamics. Also, recall that the Burgers vector of the $\frac{1}{2}\langle 111\rangle$ type can glide on any of the three $\{110\}$ planes, and hence for every primary plane, there is a choice of two cross-slip planes to which the screw dislocation can cross-slip.

#### 3.1.2.1 Choice of cross-slip plane

The Thompson tetrahedron for the bcc structure is given in figure 3.3.

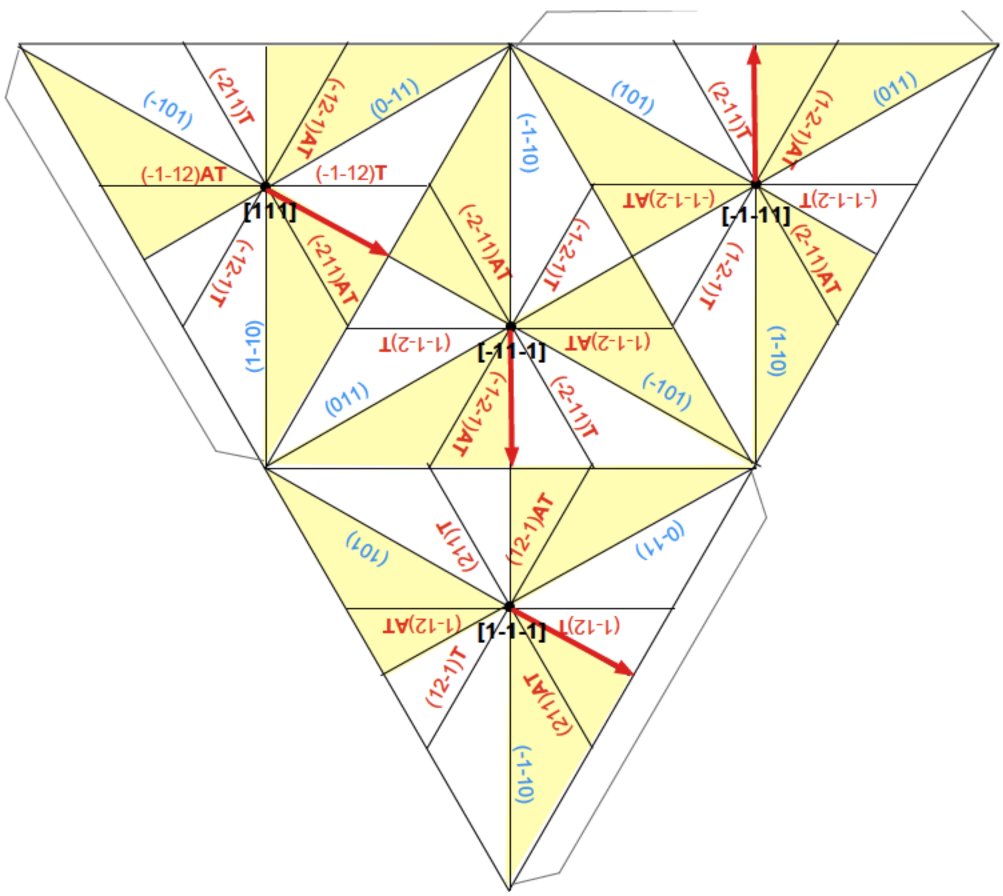


**Figure 3.3** – *Thompson tetrahedron in bcc crystal structure. On each side of $\langle 111\rangle$ type normal traces of {110} and {112} planes are shown. The bright areas correspond to twinning whereas dark areas correspond to the anti-twinning.*

An important complication in bcc not present in fcc crystals is the so-called "Slip Asymmetry". Consider a dislocation living in a particular slip-plane. It has been found experimentally that the shear stress required to move this dislocation in one direction is not the same as the stress required to move it in the opposite direction. This asymmetry in the context of choice of cross-slip plane, illustrated in figure 3.3, is based on the observations seen in prior molecular dynamics (MD) simulation results of bcc systems: Nucleation of kink pairs never takes place in the anti-twin planes, regardless of the applied loading conditions. The above asymmetry is implemented in the current DD technique as shown in the algorithm 3.1.

**Algorithm 3.1** Implementation of twin-anti-twin asymmetry in TRIDIS for bcc systems.

- First, the maximum resolved shear stress plane (MRSSP) orientation, characterized by the angle it makes with respect to the $(101)$ glide plane taken as a reference, is determined (see figure below).

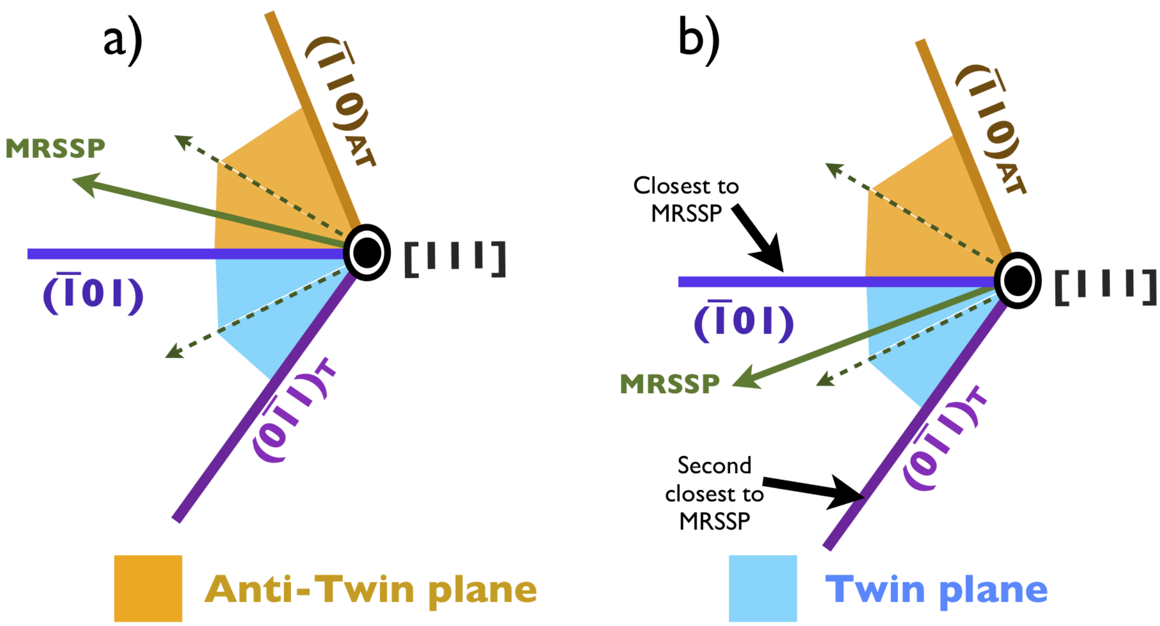


- The primary slip plane is then the closest $110$ slip plane to the MRSSP. The cross-slip plane is defined as the second closest slip plane from the location of the MRSSP.
- If the angle falls in an anti-twin zone (see case 'a' in figure), cross-slip is inhibited and the screw dislocation continues to glide in the primary slip plane only.
- If the angle falls in a twin zone, the screw dislocation can glide on either the primary or cross-slip planes (see case 'b' in the figure), depending on a cross-slip probability at each step.

#### 3.1.2.2 Algorithm of cross-slip

The cross-slip algorithm is implemented as suggested in [Chaussidon *et al.* 2008]. Let $p_1$ and $p_2$ be the rates of gliding in slip plane 1 and slip plane 2 at the atomic scale. If $d$ is the average distance between the two consecutive Peierls valleys, then the average velocity on the plane $1$ is $v_1 = p_1 d$ and similarly for the average velocity in plane 2. Now the average time between any two of these events taking place is

$$\langle t \rangle = \frac{1}{p_1 + p_2} \tag{3.6}$$

During the DD simulation timestep $\Delta t$, the number of atomic jumps will be

$$n = \Delta t.(p_1 + p_2) \tag{3.7}$$

The average velocity during the time $\Delta t$ is

$$\langle v \rangle = \frac{n.d}{\Delta t} = (p_1 + p_2).d = v_1 + v_2 \tag{3.8}$$

So, at each time step $\Delta t$, the glide plane of each screw segment is chosen according to the relative probability of glide in slip planes 1 and 2.

The normalized probability $p_1$ for a given screw dislocation to glide in the primary slip plane 1 is:

$$p_1 = \frac{v_1}{v_1 + v_2} \tag{3.9}$$

where $v_1$ (respectively $v_2$) is computed using equations (1)–(5) for each screw dislocation segment. Similarly, the normalized probability $p_2$ for the same screw dislocation to glide in the cross-slip plane 2 is:

$$p_2 = 1 - p_1 = \frac{v_2}{v_1 + v_2} \tag{3.10}$$

The probability for gliding in the primary plane is then obtained as

$$P_1 = \frac{p_1}{p_1 + p_2} = \frac{v_1}{v_1 + v_2} \tag{3.11}$$

and the probability of gliding in the corresponding cross-slip plane is given by

$$P_2 = \frac{p_2}{p_1 + p_2} = \frac{v_2}{v_1 + v_2} \tag{3.12}$$

The velocities $v_1$ and $v_2$ are obtained from the resolved shear stress in the primary and cross-slip stresses respectively, in conjugation with equation 3.2. With these velocities, the probability $P_1$ is calculated. A random number $P_r$ between $0$ and $1$ is then drawn and compared with $P_1$. If $P_1 > P_r$, the dislocation continues to glide in the primary plane, other wise it glides in the cross-slip plane[1].

It must be pointed out that this method is not adapted to predict single (atomic scale) cross-slip events, for which minimum energy or maximum entropy criteria are, in principle, better suited. Rather, this method is dedicated to the mesoscale typical for DD modeling, both in terms of space (minimum glide distance is $10b$) and time (typical DD time step is $10^{-10}s$ ). This approach is very robust and correctly describes 3D dislocation populations spreading in bcc Fe crystals, in the whole 50–300 K temperature range and for an arbitrary applied stress tensor (in single or multiple slip). The results are consistent with observations regardless of the simulation volume geometry, including thin laths and equi-axial grains [Chaussidon *et al.* 2010, Garcia-Rodriguez 2011a].

[1] The cross-slip algorithm for the fcc case is explained in section 4.5 on page 134.

## 3.2 Dislocation evolution in the presence of loops and ODS precipitates.

Poly-crystalline ferritic steels strengthened by oxide particle dispersions (ODS steels) are prime candidates for future nuclear applications, involving high irradiation doses and temperatures [Oksiuta *et al.* 2009, De Carlan *et al.* 2009]. Plastic flow and strain accumulation in crystalline materials are carried out by dislocation motion. Therefore, particles or irradiation-induced defect clusters can strongly influence material mechanical response, by obstructing dislocation motion and multiplication. In particular, certain Oxide Dispersion Strengthening (ODS) alloys exhibit better post-irradiation ductility and hardening characteristics, by comparison with their single phased counterparts [McClintock *et al.* 2009, Schaeublin *et al.* 2002, Alamo *et al.* 2004, Baluc *et al.* 2004, Ramar *et al.* 2007]. So far, beneficial effects of ODS particles are not completely explained, in terms of dislocation based mechanisms [Kimura 2007]. In this work, plastic deformation of 1 $\mu m$ grains (with and without ODS particles) is investigated in more details, by means of 3D dislocation dynamics (DD) numerical simulations[Verdier *et al.* 1998]. Recent papers focused on the hardening effect of precipitates in bcc ODS systems, using DD simulations with specific dislocation mobility rules and boundary conditions [Bako *et al.* 2007, Bakó *et al.* 2008, Bakó *et al.* 2009]. The hardening effect of irradiation-induced He bubbles [Bakó *et al.* 2009, Schäublin *et al.* 2008] has also been investigated.

In this work three-dimensional discrete dislocation dynamics simulations were carried out to analyze pre and post-irradiation plastic deformation in ferritic grains, with and without ODS particles. The edge-screw based DD [see section 2.2 on page 29] simulations are performed in a representative of small ($1 \mu m$) bulk grains, embedded in a poly-crystalline matrix. This technique is valid not only for analyzing hardening due to dispersoids and defect loops, but also for describing 3D evolutions of the dislocations structures that can be compared with microscopic observations (TEM micrographs, for example).

This section is structured as follows: The following subsection 3.2.1 provides a detailed description of the assumption, features and methodologies used in this chapter. Subsection 3.2.2 illustrates the various configurations used here, including impenetrable ODS particles, irradiation-induced defect loops and a combination of ODS particles and defect loops. In subsection 3.2.3, simulation results obtained with these different obstacle configurations are presented. Corresponding results are analyzed in terms of strain localization and stress–strain characteristics, using specially developed post-treatment tools. Subsection 3.2.4 is a discussion based on the aforesaid results.

### 3.2.1 DD adapted to ferritic ODS systems: model description

#### 3.2.1.1 Simulation volume, boundary conditions and initial dislocation microstructure

The adopted simulation volume (dodecahedral grain) morphology and size ($1\mu m$) is shown in figure 3.6. Outer interfaces are taken as impenetrable obstacles to dislocation motion, as if for highly disordered grain boundaries. Unlike periodic boundary conditions, the chosen conditions allow for a realistic description of intra-granular stress and associated deformation mechanisms (strain localization, for example), assuming stress heterogeneities due to grain dis-orientations are neglected. In real ODS systems, precipitates have different sizes and are distributed at random positions in the grain. In our simulations however, precipitates (and irradiation-induced defect clusters) are regularly spaced, in the form of a three-dimensional array. With this simpler arrangement, strain localization in lower particle density regions is avoided and hence, comparison between different simulated systems (see Section 3.2.2) mainly depends on the implemented facet properties. Irradiation loops formed at high temperature in bcc Fe alloys are sessile due to their specific Burgers vector

[Jenkins *et al.* 2009, Marian *et al.* 2002]. Such defects can therefore be introduced in the form of immobile facets, as shown in figure 3.4b. Unlike precipitate-facets, loop-facets are (conditionally) crossed by mobile dislocations. In this work, the loop-facet strength is taken as per DD [K. Gururaj 2010] and MD calculation results[Terentyev *et al.* 2010, Terentyev *et al.* 2008] and depends on the character of the incoming dislocation (edge or screw, see also section 3.2.3.5).

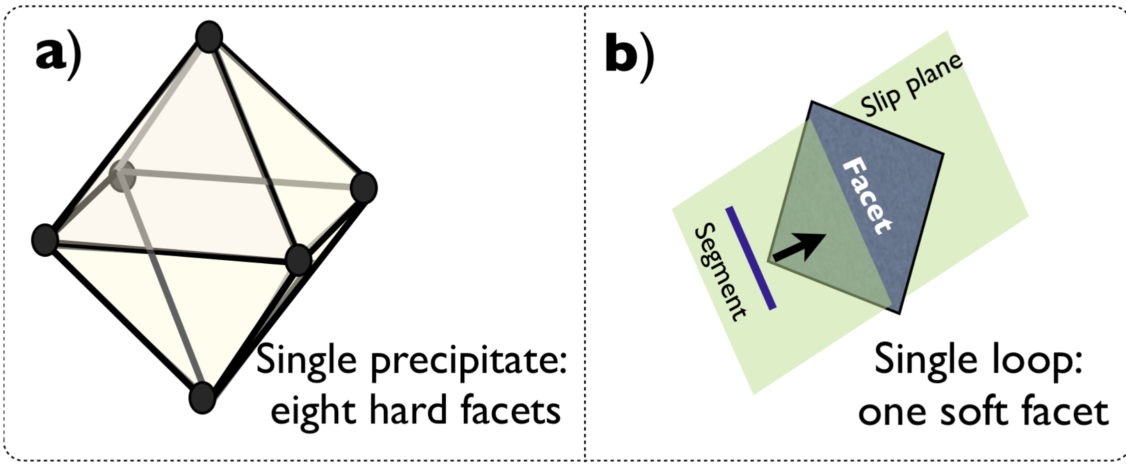


**Figure 3.4** – *Intra-granular obstacles to dislocation motion are introduced in simulation volume as planar interfaces called facets: (a) impenetrable or "hard" facets are used to simulate the presence of incoherent ODS particles, and (b) shear-able or "soft" facets are used to simulate the presence of irradiation induced defect clusters, in the form of sessile (immobile) dislocation loops. Dislocation can penetrate these facets provided a local stress criterion is satisfied.*

MD results (see section 1.4.2.1 on page 16 ) have revealed that dislocations tend to absorb the loops as helical jogs and release them at higher stress [Terentyev *et al.* 2010]. Complementary DD calculations were performed using loops made of four glissile segments. These simulations are carried out with much smaller length and time step than the conventional DD simulations. It was possible to observe the formation of helical loops and their subsequent detachment from the dislocation line for both edge and screw dislocations. Figure 3.5 shows the interaction of a screw dislocation line with six equidistant loops.

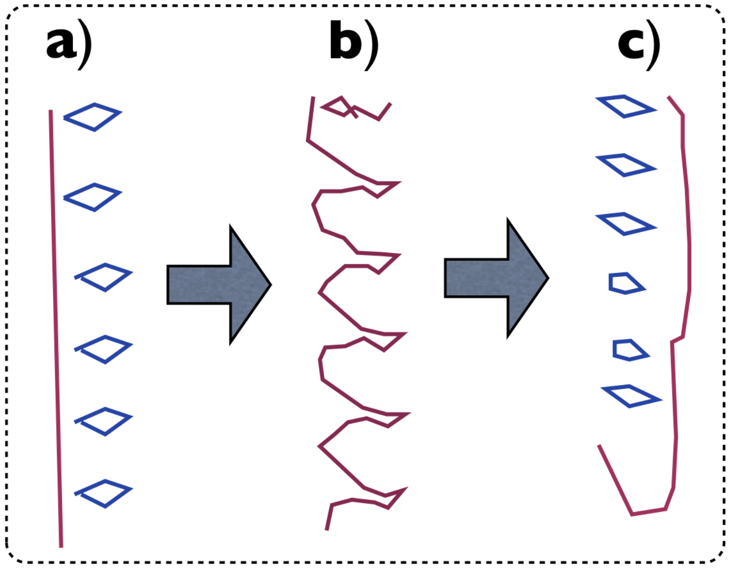


**Figure 3.5** – *Elementary dislocation dynamics simulations of a screw dislocation with six interstitial loops. a) represents the initial configuration. b) is an intermediate configuration where the loops are absorbed as jogs on the dislocation line. c) is the configuration where the irradiation loops are restored from the dislocation line.*

Since these simulations gave exactly the same mechanical response and dislocation microstructure (helical turns in bcc Fe are compact and unstable), it was decided to use the facet representation mainly to save computation time. Indeed, this method allows using a time step as high as $10^{-10}s$ compared to $10^{-12}s$ for the dislocation loop case.

### 3.2.2 Simulated cases

The DD simulations were performed at room temperature (300 K), under fixed plastic strain rate conditions. This means that the applied stress is feedback controlled, in order to keep the (plastic) deformation rate at a constant, pre-selected level. Stress correction magnitude at a given time depends on current accumulation of plastic strain. Four different cases were investigated, for analysis and comparison purposes:

**Case-1:** One ferritic grain, without particle-facets or loop-facets. This case represents a non-irradiated conventional grain.

**Case-2:** One ferritic grain including a mono-modal distribution of $0.5\%$ volume fraction of hard D = 20 nm particles. This case represents a non-irradiated ODS grain.

**Case-3:** One ferritic grain including a mono-modal distribution of $10^{20}m^2$ density of soft $20nm$ loop-facets. This case represents an irradiated, conventional ferritic grain.

**Case-4:** One ferritic grain containing a combined distribution of 0.5% volume fraction of hard $20nm$ particles and $10^{20}m^2$ density of soft D = 20 nm facets. This case represents an irradiated ODS grain.

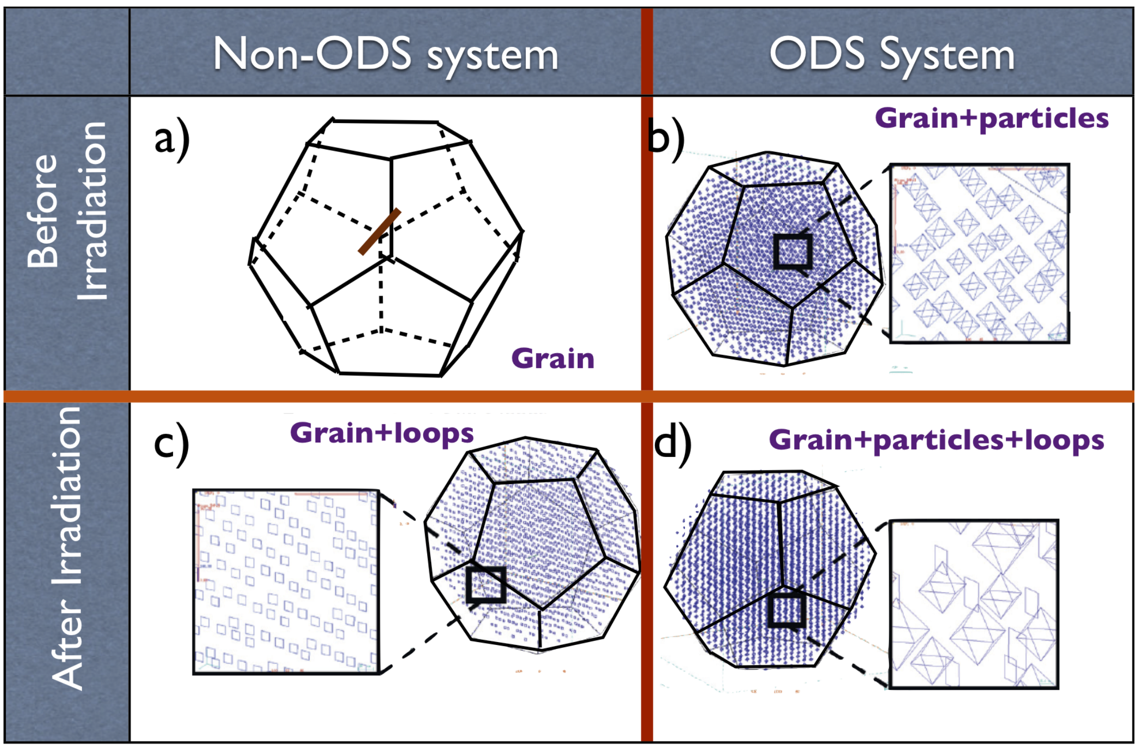


**Figure 3.6** – *The different simulated cases investigated in this paper. Analysis of more complex particle and irradiation loop effects is facilitated by comparison between the different cases.*

All simulated grains are loaded in uni-axial tension along the $(001)$ axis and initially contain 2 edge dislocation sources, with L = 500 nm. One source belong to the $a/2(101)[111]$ slip system, taken as the primary slip system (cross-slip systems associated with that source are: $a/2(011)[111]$ and $a/2(110)[111]$). The selected loading direction yields the same resolved shear stress in each slip system (Schmid factor = 0.41), a condition that also maximizes the time-dependent probability for cross-slip. Positions of the initial sources are exactly the same in all 4 cases, with a view to facilitate analysis of the results. In particular, stress–strain curves corresponding to different cases can more easily be compared to each other, to analyze certain test setup characteristics. In general however, stress–strain data in Section 3.2.3 should not be directly compared to experimental results, obtained on macroscopic, poly-crystalline specimens. Such comparison needs averaging over many different calculations, where initial dislocation configurations, grain sizes and applied stress tensor are systematically varied. This particular point therefore needs a separate investigation, which is beyond the scope of this work.

### 3.2.3 Results

#### 3.2.3.1 Plastic deformation before irradiation

#### 3.2.3.2 Case 1: Ferritic grain

When the applied loading is switched on, familiar glide characteristics of bcc crystals are rendered by our DD model, including: random cross-slip, pencil glide and edge–screw mobility anisotropy [Caillard *et al.* 2003, Louchet & Saka 2003, Lagow *et al.* 2001]. Dislocation density increases linearly throughout the simulated time, attaining $10^{13}m^{-2}$ for $\epsilon_p = 2 \times 10^{-4}$. The same type (and rate) of evolution is observed in all 4 tested cases described in section 3.2.2. In the stress–strain curve displayed in Fig. 3.7, a transient high stress regime is first noticed, before steady state is achieved.

This transition is an artifact, associated with the chosen initial dislocation configuration and can be totally suppressed by using a larger number of initial dislocation sources (>10 initial sources). The chosen initial configuration is nevertheless kept the same, for simplicity and analysis purposes.

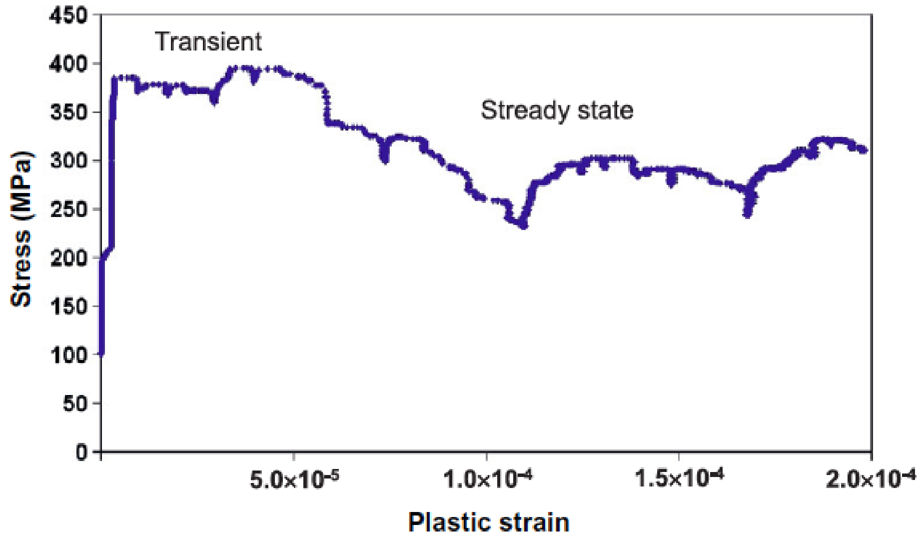


**Figure 3.7** – *Stress–strain response of an un-irradiated ferritic grain. The initial high stress regime is transient and associated with spontaneous dislocation multiplication (see main text). This transition regime is followed up by a lower stress, steady state regime.*

In this case as well as for case 2 reported in subsection 3.2.3.3, the initial applied stress increases spontaneously to produce new sources: first, by cross-kink wandering [Louchet & Saka 2003] and later on, by double cross-slip mechanism [Depres *et al.* 2004]. Spontaneous source formation and subsequent multiplication lead to stress level and dislocation velocities stabilization (see Fig. 3.8).

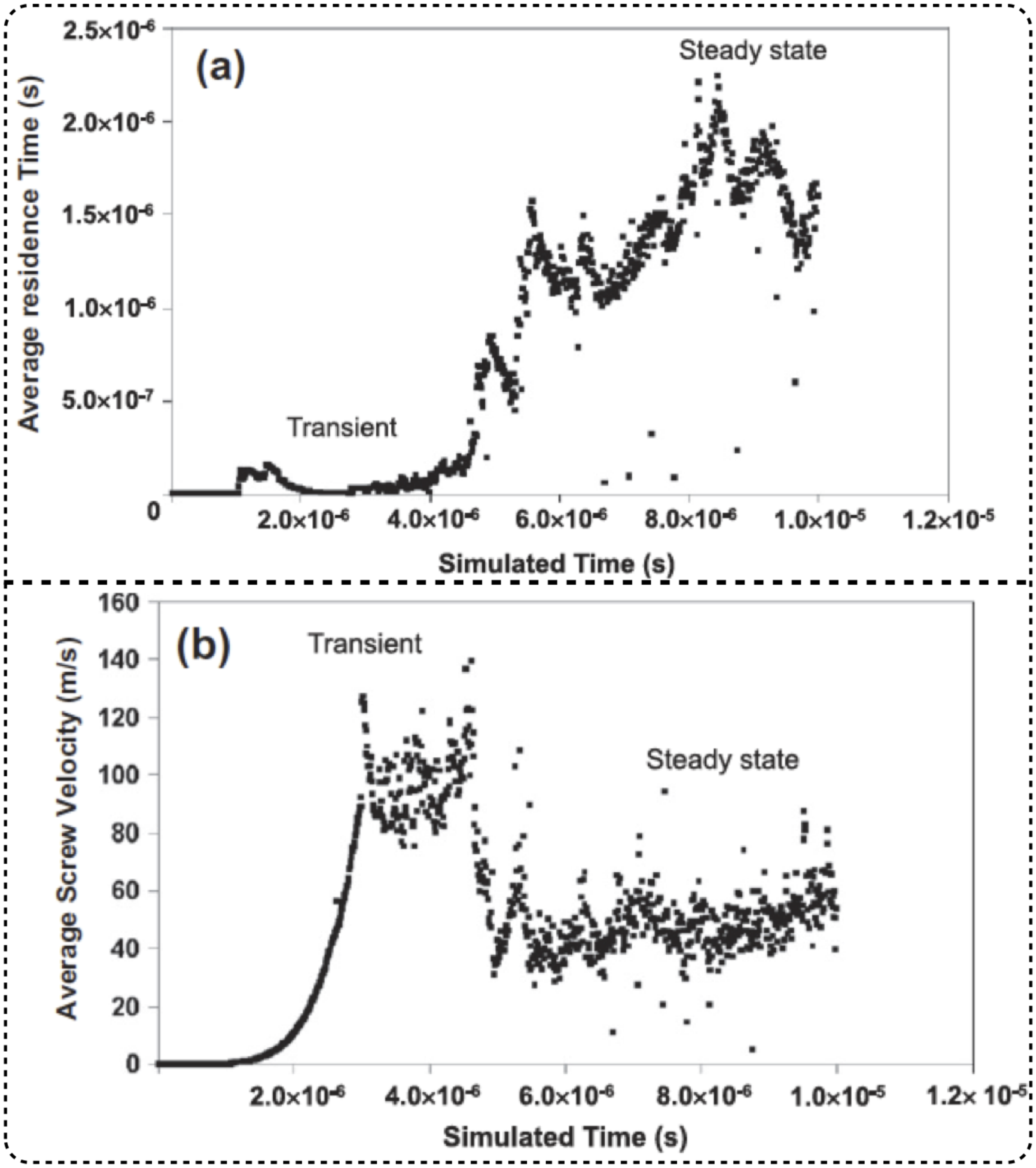


**Figure 3.8** – *Dislocation kinetics in an un-irradiated ferritic grain: (a) residence time calculated from screw dislocation velocities, using expressions (3.13)–(3.15). Lower initial residence time is associated with a stress–strain transition regime, and (b) average screw dislocation velocities evolutions.*

It is important to note that the same stabilized stress level is achieved (300 MPa, in figure 3.7 ), regardless of the initial number of initial dislocation sources (at least, up to 20 initial sources). In steady state, the number of immobile dislocation far exceeds that of mobile dislocation (estimated ratio 1:40), which is a well know character of plastic deformation, in metallic systems. With our initial dislocation configuration, none of the above processes are imposed and emerge as a natural outcome of the simulations.

Thermally activated glide and cross-slip for screw dislocations are time-dependent processes. This means a given microstructure containing mobile screw dislocation can be associated with a definite "dwell time". For this reason, the time step of DD simulations generally need not coincide with the actual, physical time of atomic events such as cross-slip. Hence, if the dwell time of a given dislocation configuration is larger than the numerical time step used to calculate the next configuration, the actual strain rate is larger than the apparent strain rate[2] and vice versa. The actual dwell time depends on many different factors including the applied stress, size of the system, temperature, etc. From [Chaussidon *et al.* 2008], the dwell time the of a mobile screw segment at a given time step corresponds to equation 3.6:

$$\langle t \rangle = \frac{1}{p_1 + p_2} \tag{3.13}$$

where $p_1$ is the glide frequency in primary slip system "1" and $p_2$ is the glide frequency in cross-slip system "2". Unlike expressions (3.9) and (3.10) in subsection 3.1.1, quantities $p_1$ and $p_2$ have $s^{-1}$ units and relate to instantaneous dislocation velocities $v_1$ and $v_2$ through:

$$(p_1 + p_2).d = v_1 + v_2 \tag{3.14}$$

where velocities $v_1$ and $v_2$ are computed using expressions (3.1)–(3.5) in subsection 3.2.1.1. The magnitude of parameter $d$ is set to one Burgers vector. For a dislocation microstructure comprising $N = N_{screw}$ screw dislocations, the dwell time T associated with time step-i is simply:

[2] Apparent strain rate = (cumulated plastic strain/cumulated numerical time).

$$T_i = \sum_{j=1}^{N_{Screw}} \langle t_j \rangle \tag{3.15}$$

Calculating the period $T_i$ associated to each time step allows determining the "actual" strain rate achieved during our simulations. In the present case, plastic strain $\epsilon_p = 2 \times 10^{-4}$ is completed after $20,000$ time steps of $\Delta t = 5 \times 10^{-10} s$, i.e. after $10^5 s$ of simulated time. The corresponding apparent strain rate is thus $2 \times 10^{-4}/10^{-5} s = 20 s^{-1}$.

Computing the dwell time using expression (3.13)–(3.15) yields $T_i \sim 1.5 \times 10^{-6} s$, in the steady state regime (see figure 3.8 a and b). The estimated actual strain rate is therefore equal to $\epsilon_p/[1.5 \times 10^{-6} s/\Delta t] \sim 7 \times 10^{-3} s^{-1}$, which is reasonably close to usual tensile testing conditions, given the actual strain rate sensitivity of poly-crystalline Fe at room temperature [Nakada & Keh 1968].

Whenever possible, simulation parameters for different simulations are adjusted to obtain exactly the same, average steady-state dislocation velocity. This precaution ensures that in all the cases, exactly the same actual strain rate and mobile dislocation densities are obtained. In this manner, differences in stress–strain behavior can be genuinely attributed to the adopted simulation setup, i.e. loops, particles, grain boundaries, forest dislocations or any combination of the above.

#### 3.2.3.3 Case 2: Ferritic grain including a mono-modal distribution of ODS particles

Mechanical behavior of ODS steels is determined by interactions between lattice dislocations and particles which lead to dislocation pinning and thus to an increased flow stress of the material. Grain deformation simulations made in this section include a 0.5% volume fraction mono-modal distribution of hard $D = 20nm$ particles, yielding an average inter-particle spacing $L = 80nm$. The dislocation/precipitate interaction methodology introduced in subsection 3.2.1.1 on page 72 is first tested here with a simple configuration, including one dislocation line and two hard precipitates, as shown in figure 3.9. Precipitates are by-passed by mobile dislocations, whereby residual "Orowan" loops are left around each by-passed precipitate.

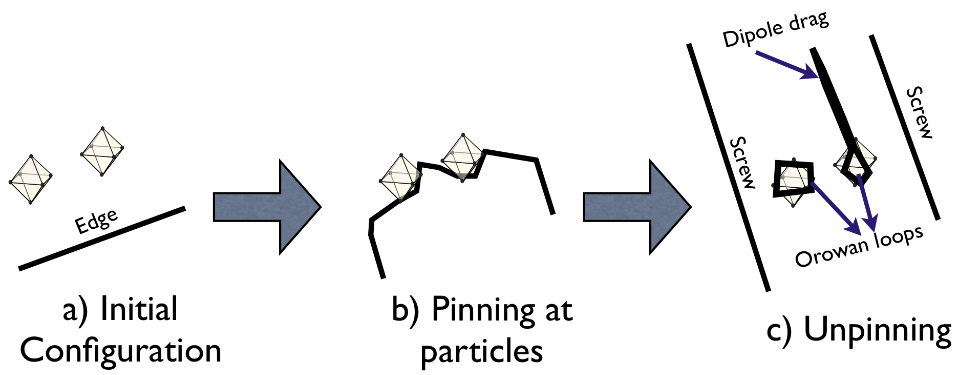


**Figure 3.9** – *Interaction between one edge dislocation and two impenetrable D = 20 nm particles. (a) Interaction configuration evolutions, under controlled plastic strain rate loading conditions, in uni-axial (0 0 1) tension. Center to center particle inter-spacing is 80 nm. The 150 nm long initial edge source is pinned at its extremities and belongs to the a/2(1 0 1)[1 1 1] slip system. An Orowan loop first formed around the particle positioned to the left-hand side. Dipole drag is visible at the end of the interaction, just before its annihilation and the formation of a second Orowan loop, around the right-hand particle. Interaction asymmetry between the two particles comes from the (deliberately) slightly asymmetric position of the initial pinning points, with respect to particle center positions. Particle-induced hardening corresponding to this configuration is* $\Delta\tau = 89MPa$.

The critical stress of this mechanism is called the Orowan stress, which is given by the following expression[3], based on (elastic) line tension theory [Bacon *et al.* 1973]:

$$\frac{\sigma}{\mu} = \frac{1}{4\pi(1-\nu)}\frac{b}{L}\left[-ln(\frac{b}{D}+\frac{b}{L})+0.615\right] \tag{3.16}$$

where $\mu$ is the material shear modulus, $\nu$ the Poisson coefficient, $b$ is the Burgers vector magnitude, $L$ distance between hard particles and $D$, the particle diameter. Using the above-mentioned $D$ and $L$ values together with $b = 2.5 \times 10^{-10}m$, $\mu = 55GPa$ and $\nu = 0.3$ in expression (3.16) yields $\Delta\tau = 95MPa$. Hardening corresponding to figure 3.9 is $\Delta\sigma =$

[3]This particular expression applies for edge dislocations, assuming $\mu_{particle} = \mu_{matrix}$.

$220MPa$ i.e. $\Delta\tau \sim 95MPa$, which is fairly consistent with expression (3.16). This result is also comparable to independent DD simulation results reported in [Shin *et al.* 2005]. This means that at room temperature, line tension controls the hardening response of precipitates in both bcc and fcc crystals.

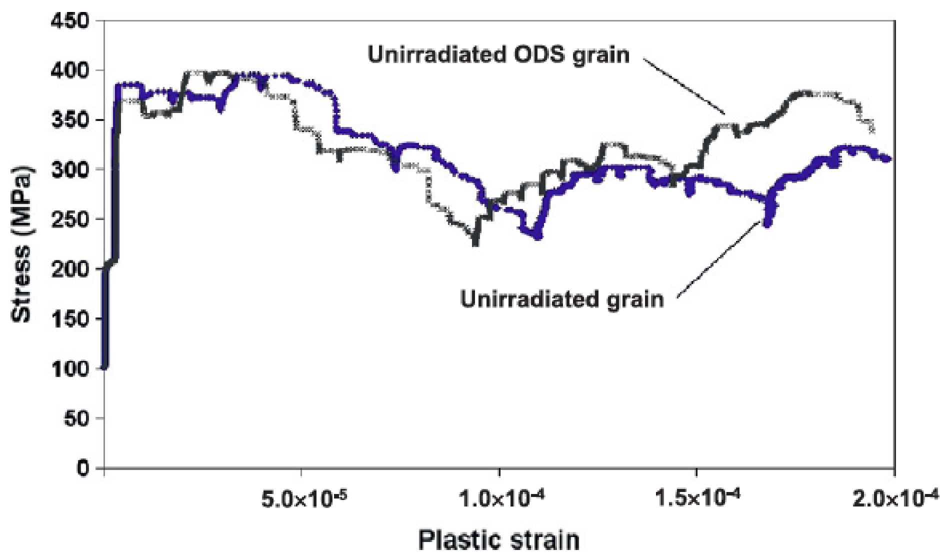


**Figure 3.10** – *Comparative stress–strain response of un-irradiated ODS grain (with particles) with an un-irradiated reference grain (without particles). Averaged dislocation velocities achieve a steady state in both simulations for $\epsilon_p > 10^{-4}$, where hardening due to precipitates can be estimated with better accuracy (see main text).*

When the external loading is applied, initial dislocation sources are activated and give rise to a similar stress–strain behavior as observed in the previous case (see figure 3.10 and subsection 3.2.3.2 on page 76). Shear loops are emitted until dislocations are stopped by the hard precipitates and grain boundaries. Orowan loop (typically 1 or 2 loops) accumulation around the particles generates high internal stress, giving rise to further cross-slip activation (see subsection 3.2.4 on page 88). Repetition of this process can generate high density dislocation tangles which are three dimensional random arrangements of dislocations with no characteristic polarity. Illustration of such tangles in the presence of precipitates is also provided in [Shin *et al.* 2007]. Such tangles then act as pinning point for incoming mobile dislocations, effectively increasing the capture cross-section of the precipitate around which they are formed.

During the simulations, processes of dislocation accumulation, unpinning and tangle destruction is time (or plastic strain level) dependent. In other words, new sources are either shorter or longer than the previous ones, depending on instantaneous configurations involved. This leads to the steady state regime (for $\epsilon_p > 10^{-4}$ in figure 3.10), where corresponding hardening level $\Delta\sigma$ is comprised between $+20$ and $+80$ MPa. These values correspond to $\Delta\tau \sim 7.8 \times 10^{-5}$–$3.1 \times 10^{-4}\mu$, which is fairly comparable (though somewhat smaller) to dislocation depinning transition stress obtained elsewhere ($\tau_c \sim 3\ to\ 6 \times 10^{-4}\mu$, see [Bakó *et al.* 2008]), using $2\mu m$ simulation volumes[4]. The smaller hardening obtained herein is a consequence of cross-slip activation, providing an additional degree of freedom that facilitates dislocation unpinning (see also caption of figure 3.9). In the scope of this thesis hardening, unless mentioned otherwise, refers to the increase of the yield point. The slope of the stress strain curve is referred as the work-hardening.

#### 3.2.3.4 Plastic deformation after irradiation

#### 3.2.3.5 Case 3: Ferritic grain including a mono-modal loop distribution

Irradiation effects on plastic deformation is examined here, by introducing defect clusters in the form of dislocation loops, a feature common to a wide range of irradiation doses and temperatures, in metallic materials. MD calculations show that defect loop resistance to dislocation motion ("loop strength") generally depends on the character of the incoming dislocation. In particular, screw dislocations can absorb [0 0 1] loops in the form of helix jogs, producing a strong pinning effect [Terentyev *et al.* 2010]. In the edge/loop interaction case, loops are simply sheared-off, yielding lower interaction strength. In MD calculations, maximal loop strength is 2.26 times the Orowan stress

[4] They used random size particle distributions with a mean radius of 26 nm and 0.5% volume fraction.

for screw dislocations [Terentyev *et al.* 2010] and 0.7 times the Orowan stress for edge dislocations[Terentyev *et al.* 2008]. Grain deformation simulations made in this section include a mono-modal $10^{20}m^{-2}$ density of soft 20 nm loop-facets with, with irradiation doses of $0.5$–$1$ dpa (estimated), performed at $T = 400°C$ [Porollo *et al.* 1998]. This setup yields $L = 80$ nm and a critical Orowan shear stress $\Delta\tau = 95\ MPa$ (for edge dislocations). Hence, we set the loop-facet strength at $\Delta\tau = 2.26 \times 95\ MPa = 215\ MPa$ for screw/loop interactions and at $\Delta\tau = 0.70 \times 95\ MPa = 67\ MPa$ for edge/loop interactions (see subsection 3.2.1.1). Adopted loop interaction methodology and simulation parameters are tested using the simple DD simulation setup as shown in figure 3.11.

When tensile loading is applied to the irradiated ferritic grain, initial sources are activated and shear loops are emitted in their respective, initial glide planes. Mobile dislocations then interact with loop-facets and grain boundaries. Unlike in the previous two cases (see subsections 3.2.3.2 and 3.2.3.3), the applied stress level achieved here is quite stable with cumulated plastic strain $\epsilon_p > 10^{-5}$ (see figure 3.12). In other words, the initial transient regime is much less pronounced than before.

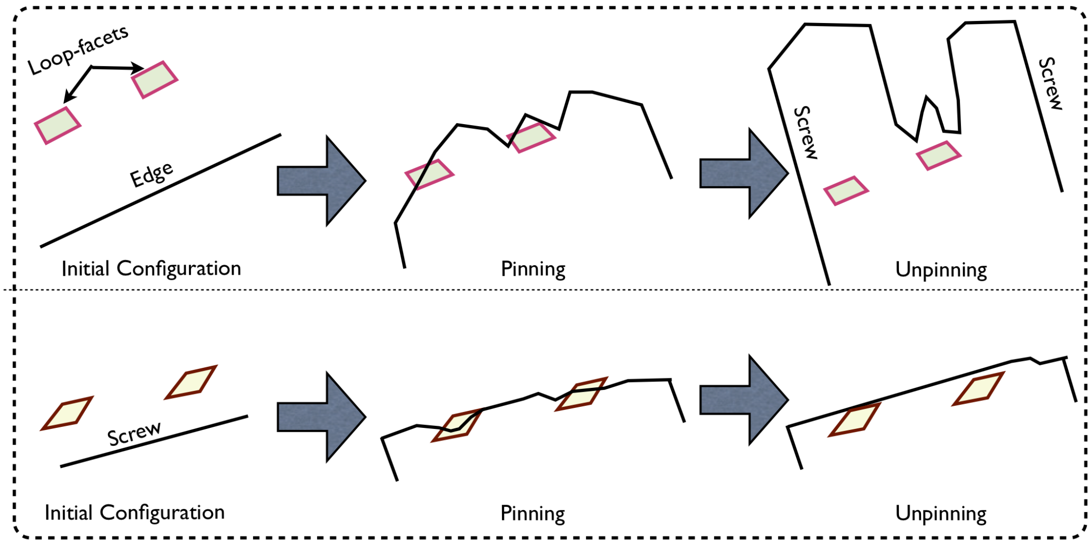


**Figure 3.11** – *Interaction between one dislocation and 2 loop-facets. Calculations are performed under controlled plastic strain rate loading conditions, in* $(001)$ *uni-axial tension. Loop diameter is* $D = 20nm$ *and center-to center loop inter-spacing is* $80nm$*. The initial* $L = 150nm$ *long segment is pinned at its extremities and belongs to the* $a/2(101)[111]$ *slip system: (a) edge-loop case. Corresponding hardening is* $\Delta\tau = 58MPa$ *and (b) screw-loop case. Corresponding hardening is* $\Delta\tau = 88MPa$*. In both cases, loops are simply sheared-off, no debris is left after dislocation–loop interaction completion.*

The hardening numbers referred in the figure 3.11 are obtained as the difference between the yield points in simulations carried out with loops and without loops for edge and screw dislocations respectively.

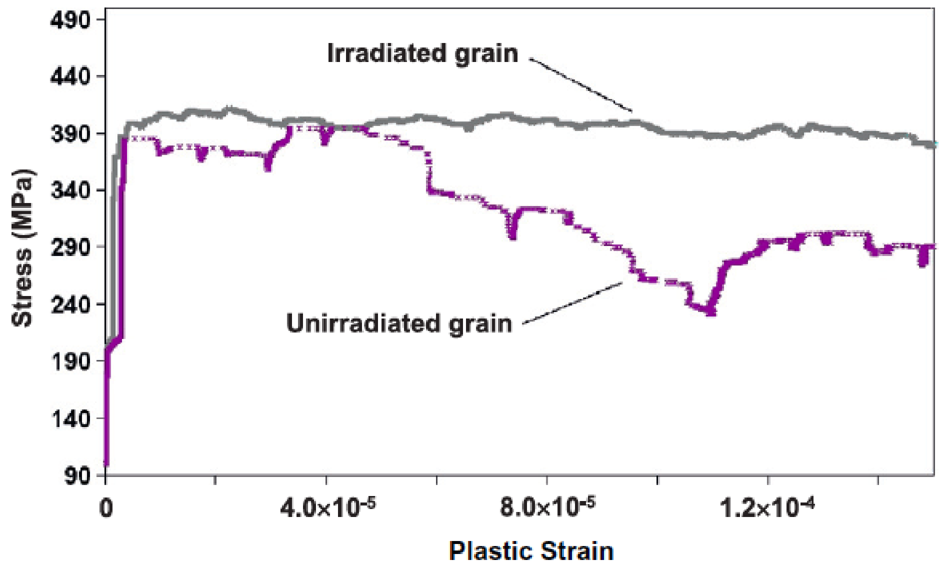


**Figure 3.12** – *Comparative stress–strain response of an irradiated grain (with loops) with a non-irradiated ferritic grain (without loops). Averaged dislocation velocities achieve steady state for $\epsilon_p > 10^{-4}$, in both simulations. Hardening due to irradiation-induced loops is estimated during the steady state (see main text).*

The average screw dislocation velocity is very stable during the whole simulated time since very few new sources were generated; indicating that generation of new sources is difficult, due to strong screw–loop interactions. Hardening induced by loop population is estimated to be around $\Delta\tau = 41\ MPa$[5] or $\Delta\tau = 3.9 \times 10^{-4}\mu$, i.e. significantly smaller than in figure 3.11. This effect is ascribed to the time (or strain) dependent dislocation configurations generated during tensile deformation of the grain. In usual MD calculations for instance, dislocation pinning points are located far away from the loops, where interactions are more active. In the present DD simulations, dislocation pinning points are located at arbitrary distance relative to the irradiation loop positions. When that distance is comparable to the loop diameter, impinging screw dislocations are strongly bowed-out at the time of contact, instead of in a straight line. And so, the mix of straight and bowed out segments yields smaller hardening. Changing the facet strength by $\pm 50$ affects the hardening amplitude in the same proportion. Decreasing the loop density by a factor of 5 also changes loop-induced

[5]see figure 3.12, for $\epsilon_p > 6 \times 10^{-5}$

hardening in the same, proportional way. Increasing the loop density from to $10^{21} - 10^{22} m^{-3}$ yields hardening saturation, which is again in agreement with well know experimental trends [Matijasevic *et al.* 2008, Kohyama *et al.* 1994, Baluc *et al.* 2007, Miller *et al.* 2009]. Sharp plastic instabilities[6] however develop for higher loop densities, whenever a very high initial stress is involved, either by using a shorter initial source or by increasing the actual applied strain rate (100 times faster, for example).

#### 3.2.3.6 Case 4: Ferritic grain including a combined distribution of loops and particles

Simulations carried out in this section include a combined distribution of $10^{20}\ m^{-2}$ density of soft $D = 20nm$ loop-facets and a 0.5% volume fraction of hard $D = 20\ nm$ particles. This configuration is consistent with 0.75 dpa irradiations performed at 400 C, in ferritic ODS system having similar characteristics as in our investigation (0.5% volume fraction of $28 \pm 8\ nm\ Y_2O_3$ particles) [Chen *et al.* 2008]. When the external loading is applied, tangles develop between precipitates as described in subsection 3.2.3.3. This scenario also holds for larger particles sizes, at least up to $D = 30\ nm$. Unlike case 3, additional stresses coming from the tangles allow formation of distant or dispersed sources, by double cross-slip and wandering mechanisms. These substructures generate internal stress that help shearing irradiation loops which otherwise, would have obstructed dislocation motion [Nogaret *et al.* 2008][7]. This mechanism is further discussed in the next section. As a (beneficial) result, hardening due to defect loops is significantly reduced (see figure 3.13) and plastic deformation spreading in the grain is much more homogeneous (see also figure 3.16, in subsection 3.2.4). Resistance to irradiation-induced hardening is also consistent with experimental data on several ODS alloys [Kishimoto *et al.* 2006].

[6] Strong hardening followed by sharp softening.

[7] A similar effect was observed in fatigue simulations using bi-modal particle distribution where the presence of small precipitates helped concentrating plastic strain, until larger precipitates are sheared-off [Shin *et al.* 2007].

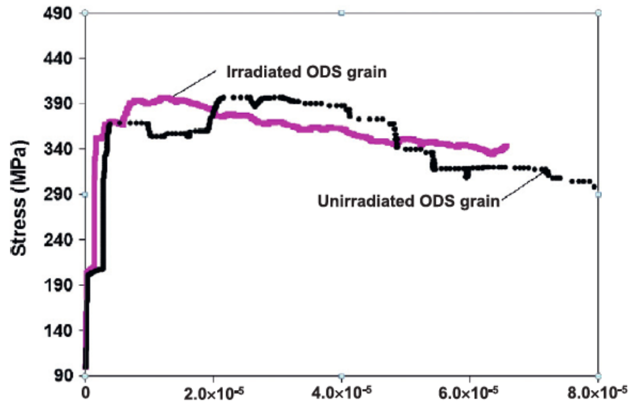


**Figure 3.13** – *Comparative stress–strain response of an irradiated ODS grain and a non-irradiated ODS grain. Average dislocation velocities achieve steady state for $\epsilon_p > 10^{-5}$ in ODS grain (see Fig. 3.12) and for $\epsilon_p > 10^{-4}$ in un-irradiated ODS grain, while stress stabilizes 400 MPa (see Fig. 3.10). This means the as-tested ODS grain configuration is actually softer after irradiation (with loops) than before irradiation (without loops). No matters how qualitative, this comparison shows ODS particles provide resistance to loop-induced hardening (compare with figure 3.12).*

### 3.2.4 Discussion

In subsection 3.2.3.3 on page 80, it was shown that introduction of a mono-modal distribution of $D = 20\,nm$ particles (0.5% volume fraction) yielded significant hardening ($\Delta\tau \sim +3.9 \times 10^{-4}\,\mu$). The irradiation effect in ODS grains was also examined by adding a $10^{20} m^{-3}$ density of $D = 20\,nm$ loop-facets having specific interaction characteristics (see subsection 3.2.3.5). The loop spacing and size are kept exactly the same as the particle spacing and size. Hence, the slight difference of stress–strain behavior between case 2 (subsection 3.2.3.3) and case 3 (subsection 3.2.3.5) can be directly ascribed to screw–loop interactions[8].

Edge–screw dislocation mobility anisotropy at low temperature is a well-known characteristic of bcc systems. Experimentally, this effect vanishes at the onset of the so-called a-thermal regime, i.e. above room temperature in (un-irradiated) bcc Fe. The presence

[8] See figure 3.12 on page 86 and figure 3.13

of irradiation- induced loops in the crystal augments the edge/screw mobility anisotropy at, and presumably beyond, room temperature. This characteristic can significantly affect the material engineering characteristics, including fracture toughness. Indeed, it is known since many years that fracture toughness measured at a fixed irradiation dose for $\Phi = \phi$ and temperature $T$ corresponds to fracture toughness of the same material at $\Phi = 0$ and $T = T - \Delta T$. In other words, decreasing temperature by $\Delta T$ possibly has the same effect as irradiating up to $\Phi = \phi$, in terms of edge–screw mobility anisotropy.

In the above section, resistance to irradiation-induced hardening is pointed out as a beneficial material characteristic. The effect of ODS particles on the hardening characteristics can be emphasized by plotting the stress–strain curves of irradiated (non-ODS) grain and irradiated ODS grain side by side. In figure 3.14, the irradiated ODS grain exhibit good resistance to loop-induced hardening.

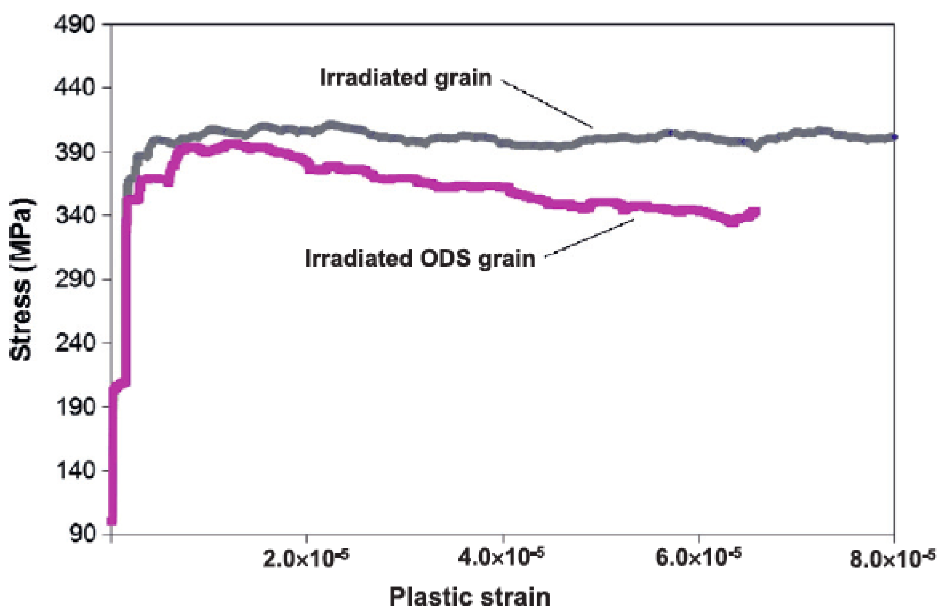


**Figure 3.14** – *Comparative stress–strain behavior of irradiated ODS and non-ODS grains. Averaged dislocation velocities achieve steady state for $\epsilon_p > 10^{-5}$ in both simulations. Obviously, grains with ODS particles are resistant to loop-induced hardening.*

Interestingly, this characteristic totally disappears using periodic boundary conditions, representative of single crystals. This means that resistance to loop-induced hardening observed here possibly relates to internal stress generated at the grain boundaries (due to dislocation pile-ups, for example). In grains containing ODS particles, internal stress–strain also relates to dislocation accumulation around the precipitates (see figures 3.15 a and b ).

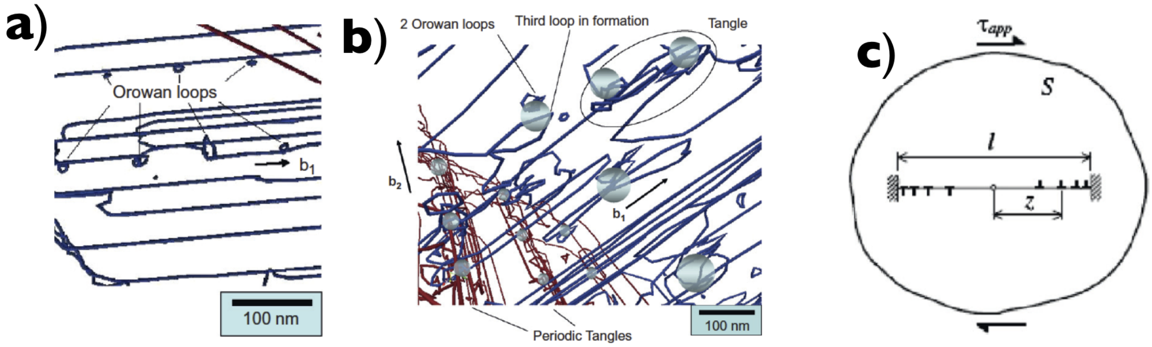


**Figure 3.15** – *Dislocation structures in the presence of ODS precipitates: (a) at low plastic strain ($< 10^{-4}$), only a few particles are decorated by Orowan dislocation loops (debris loop). Particles are not displayed for clarity, (b) at higher plastic strain ($> 4 \times 10^{-4}$), most of the precipitates are decorated by loops and/or dislocation tangles. Tangle positions have the same periodicity as the particle network, and (c) 1D pile-up model of inter-precipitate dislocation structures. The dislocation source is positioned at the middle point $z = 0$. Shear loops emitted from the source pile-up at obstacles, after gliding $-\frac{1}{2}l$ and $\frac{1}{2}l$. In this analysis, l = 80 nm, the inter precipitate distance (see subsection 3.2.2).*

This effect can be further examined by using an analytical 1D pile-up model [Hirth & Lothe 1982]. In figure 3.15c configuration, the total number of dislocations $n_d^{PU}$ simply writes:

$$n_d^{PU} = 2\int_0^{\frac{l}{2}} n(z)dz = \frac{2(1-\nu)}{\mu b} l\tau_{app} \tag{3.17}$$

where the dislocation density n(z) expression used in expression (3.17) is:

$$n(z) = \frac{2(1-\nu)}{\mu b} \frac{z}{\sqrt{\left(\frac{l}{2}\right) - z^2}} \tau_{app} \tag{3.18}$$

where $l$ is the pile-up of length and $\tau_{app}$ is the resolved shear applied to the crystal. From figure 3.15a and b, it is readily seen that $n_d^{PU}$ lies between 1 and 3.

Taking $l = 80\,nm$ for the inter-particle spacing, expression (3.18) prediction is consistent with $\tau_{app} = 2.2 \times 10^{-3}\mu\ -\ 6.7 \times 10^{-3}\mu$. This represents the local or internal stress needed to overcome ODS particles, after plastic strain accumulation. The minimal stress amplification factor is therefore $2.2 \times 10^{-3}/3.9 \times 10^{-4} \sim 6$. For this reason, local stress around particles exceeds irradiation loop strength, for both edge and screw mobile dislocations. Such a stress level is sufficient to activate deformation in cross-slip system over relatively large distances, from initial pile-up plane. Stress in cross-slip plane associated with a pile-up like in figure 3.15c decays with distance normal to the reference glide plane as:

$$\sigma = -\tau exp(-k(z)\frac{|x|}{l}) \tag{3.19}$$

The closed form expression (3.19) is actually a fit to the stress field for a single dislocation pile-up, generated by an ad-hoc DD simulation [Depres *et al.* 2004, Depres 2004]. Dependence of $r$ on the non-dimensional quantity $|x|/l$ means the stress range of pile-up in direction $x$ is essentially proportional to its size $n_d^{PU}$ (see expression (3.17)). For screw-type pileups, maximum values are $k(z) \sim 5$, where $z = \pm l/2$. In this way, stress from configurations shown in figure 3.15b falls down to the average stress level ($\sigma = +3.9 \times 10^{-4}\,\mu$) at $x = 0.32$ times the inter-precipitate distance, i.e. at $l = 26\,nm$ from individual precipitates. Hence, both primary and cross-slipped dislocations can then go through local loop populations, in spite of the loop obstacle strength. Tendency to strain localization is avoided and plastic strain easily spreads across the whole grain.

Though it is clearly beyond the scope of this work to predict ductility for actual polycrystals, comparative degrees of strain localization between different cases can be examined quantitatively at the grain scale. To achieve this investigation, simulation volumes are first divided into N sub-regions, parallel to the primary slip plane (see figure 3.16a). The $i^{th}$

region is considered as being active if dislocation density is non-vanishing. The spatial coordinate of the $i^{th}$ plane region, $x_i$ (in nm), is the distance of the plane i taken from a reference grain boundary along a reference axis normal to slip planes. This axis is divided into finite spatial intervals $\Delta x \sim 10\,nm$, and results are displayed in the form of dislocation population versus position histograms (see figure 3.16). Localization effects presently reported thus refer to the spatial extent of plastic strain spreading, in one simulation setup relative to another. For example, if plastic deformation $\epsilon_p$ in setup-A is partitioned between $N_A$ regions and $\epsilon_p$ in setup-B is partitioned between $N_B$ regions, then, plastic strain is more localized in setup-A relative to setup-B, if $N_A < N_B$.

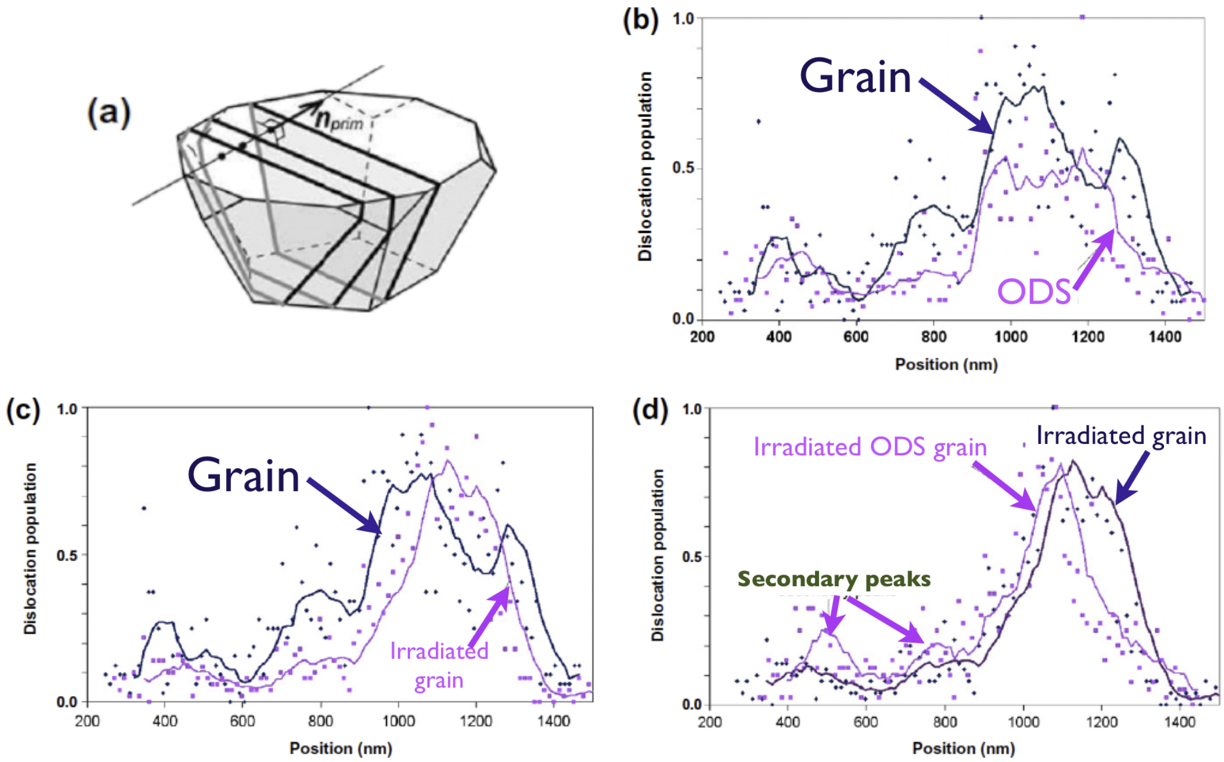


**Figure 3.16** – *Spatial distribution of intra-granular plastic strain: comparison between the different simulation cases, at exactly the same plastic strain level ($\epsilon_p = 2 \times 10^{-4}$). (a) The plastic strain distribution assessment method (see also in the main text). Dislocation population of the most populated slice is set to 1. Populations in all other slices are relative, with respect to this reference quantity. (b–d) Comparison between the various cases of investigated in this work. Presence of secondary peaks in d) witnesses plastic strain spreading at long distance from the initial dislocation source slip plane. Solid, running average curves (calculated from the as-displayed discrete values) are also plotted for clarity.*

In the absence of irradiation loops, plastic strain in an ODS-grain is more localized than in its particle-free counterpart (see figure 3.16b). The present simulation results are consistent with experimental trends obtained with early ODS steel fabrications, having 20 nm particles. In Ref. [Schaeublin *et al.* 2002] indeed, room temperature ductility is lower[9] in ODS alloys than in their precipitate-free counterpart. In presence of the irradiation loops however, our calculations predict an opposite trend. Namely, strain is more localized in irradiated particle- free grains than in irradiated ODS-grains (see Fig. 3.16c and 3.16d). This model thus predicts a beneficial role of ODS particles, on post-irradiation ductility [McClintock *et al.* 2009, Alamo *et al.* 2004]. The relation between strain localization effects reported above and macroscopic stress–strain behavior is not clear yet; this point would need a separate study.

### 3.2.5 Conclusions

Full three dimensional DD simulations of plastic deformation in $1\mu m$ Fe grains have been performed at room temperature, accounting for thermally activated glide and cross-slip for screw dislocations relevant to bcc crystallography. A tensile load has been applied under multiple glide symmetric conditions, up to plastic strain of $\epsilon_p = 10^{-3}$. Systematic comparisons between grains containing various types of internal obstacles have been presented including: 20 nm hard ODS-like precipitates, 20 nm soft loop-facets and a joint distribution of 20 nm ODS-like precipitates and loop-facets. Loop-facet strength introduced herein is as per MD simulation predictions of irradiation-induced dislocation loop defect clusters. DD simulation analysis shows that, in absence of loop-facets, ODS particles reduce the dislocation mean free path and hence lead to both material hardening and further strain localization. In the presence of irradiation-induced loop-facets however, the co-presence of particles yields an opposite trend. This beneficial effect is especially

[9] Reduction of ductility and increased strain localization are related quantities.

active in small grains and explained in terms of particle/loop interplay. During tensile deformation, dislocations accumulate around the precipitates, generating high internal stresses. Subsequent plastic strain then spreads on account of cross-slip activation. With the help of internal stresses, cross-slipped dislocations then overcome irradiation defect cluster barriers. As a result, irradiation-induced strain localization and hardening are reduced altogether. The present work describes dislocation-based mechanisms explaining the beneficial role of ODS precipitates. The available computational power however imposes limitations both on the amount of simulated plastic strain and on the particle distribution examined.

## 3.3 Effect of irradiation loop density on plastic deformation in RPV steels

### 3.3.1 Background

The ductile to brittle transition temperature regime (DBTT) of 16MND5 RPV steel occurs between 150K and 300K. In this regime, material toughness (and its scattering) markedly increases with temperature and brittle fracture initiates, after a definite amount plastic deformation accumulation. Description of local plastic deformation in function of the macroscopic strain, temperature and dose can therefore help to improve the existing tools and their predicting capabilities. At the grain (or bainitic lath) scale, dislocation dynamics (DD) simulations have been developed in the past few years and adapted to treat irradiated metallic materials. At the continuum mechanics scale, Finite Element crystalline plasticity models have been recently presented in [G. Monnet 2011], where stress-strain evolution in irradiated alpha-Fe also depends on irradiation defect density evolution. In that case, it is believed that the irradiation defect population gradually decreases with strain, due to the glide of dislocations on slip planes intersecting the defects. Our goal in this work is to describe the interaction of the irradiation defect population with dislocations, using detailed three-dimensional DD simulations adapted to alpha-Fe grain plasticity.

### 3.3.2 Model Description

This work carries forward the “loops-as-facets” prescription introduced in section 1, to correlate the number of irradiation loops interacting with the dislocations and the overall plastic deformation the grain undergoes. Although the distribution of irradiation loops can be assumed to be homogeneous across the grain, the actual number of loops interacting with a dislocation can be confined to only a certain regions of grains, depending upon the distribution of dislocation sources and their suitability of loading conditions for dislocation glide and cross-slip. Our goal in this work is to describe the interaction of irradiation defect population with dislocations, using detailed three-dimensional DD simulations explained earlier.

A realistic representation of an irradiation loop is to construct it as a collection of co-planar edge type dislocations. This description, apart from being computationally intensive, also has another drawback: the distinction between the dislocations making up the irradiation loop and the dislocations available for glide (FR source, for example) is no longer available. Since in our simulations, irradiation loops are implemented as just planar obstacles and not as a collection of co-planar edge-type dislocations, it becomes possible to track the status of each of the irradiation defect as a function of time or stress. Here the status refers to whether the loop is pierced by the dislocation or not. Getting this information will help in understanding the strain localization phenomenon and the effect of the loading conditions etc on it.

Since the glide of screw dislocations is thermal-assisted, the interacting loop population also becomes a function of temperature. In the current study our interest is to explore the loop-dislocation interaction in the temperature window of 150K-300K which the ductile to brittle transition temperature regime (DBTT) of low-carbon ferritic steels, like 16MND5 bainitic steel, for example. In the DBTT regime, material toughness markedly increases with temperature and brittle fracture initiates after a definite amount of plastic deformation accumulation. Description of local plastic deformation in function of the macroscopic strain, temperature and dose can therefore help to improve the existing tools and their predicting capabilities. At the scale of continuum mechanics, stress-strain evolutions in irradiated $\alpha - Fe$ also depend on irradiation defect density evolution [G. Monnet 2011]. It is believed that the irradiation defect population gradually decreases with strain, due to the glide of dislocations on slip planes intersecting the defects.

### 3.3.3 Simulation Setup

The adopted simulation volume morphology (cubical grain) and size ($1\mu m$) is shown in figure 3.17. Outer cube interfaces are taken as impenetrable obstacles to dislocation motion, as for highly disordered grain or lath boundaries decorated by a high density of small carbide particles.

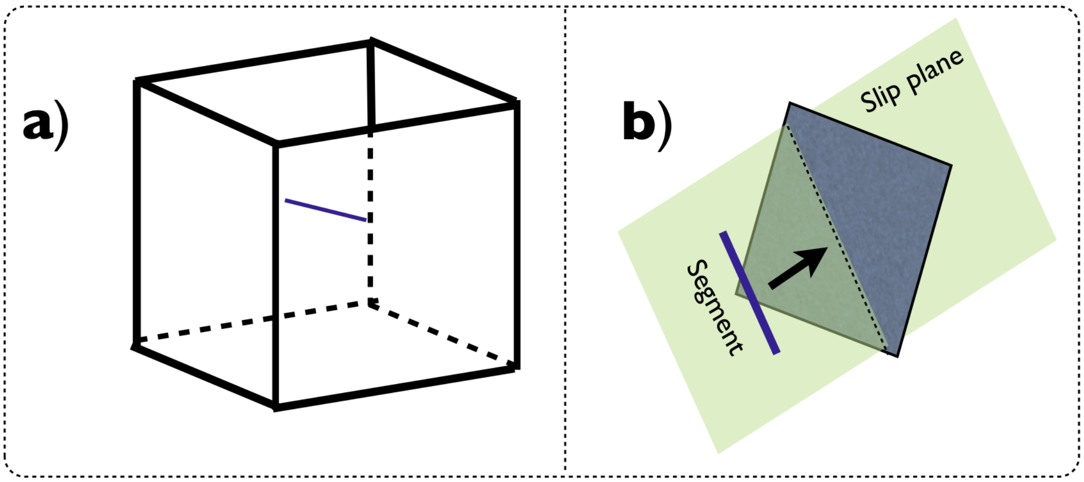


**Figure 3.17** – *DD simulation setup. (a) The simulation volume containing one initial dislocation source. b) Intra-granular obstacles to dislocation motion are taken as planar interfaces called facets.*

Unlike periodic boundary conditions, the chosen setup allows for a realistic description of intra-granular stress and associated deformation mechanisms (strain localization, for example), assuming stress heterogeneities due to adjacent grain plastic deformation are neglected.

### 3.3.4 Simulated Cases

Our DD simulations are performed at $300K$ and $100K$, under fixed plastic strain rate conditions, in multiple slip (uni-axial tension along the $(001)$axis) and single slip applied stress tensors (pure shear stress). The applied stress magnitude is feedback controlled in order to keep the plastic deformation rate at a constant, pre-selected level and the stress correction magnitude at a given time depends on current accumulation increment of plastic strain as explained in algorithm 2.1 on page 37. Runs with non-irradiated grain (without particle-facets) are first performed, as reference cases. Then, up to 4 different mono-modal 20 nm (diameter) loops densities are tested: $5 \times 10^{20}$, $10^{21}$, $2 \times 10^{21}$ and $5 \times 10^{21} m^{-3}$ (see Figure 3.18). The selected densities are representative of different experimental conditions [Hernandez-Mayoral & Gomew-Briceno 2010], as shown in Table 3.2.

**Table 3.2** – *Loop features in Fe versus dose (from [Hernandez-Mayoral & Gomew-Briceno 2010]). In RPV steel, loop diameters can be up to 50% larger and loop densities 50% lower than in pure Fe [C. Robertson 2010].*

| Dose (dpa) | Mean diameter (nm) | Max. Diameter (nm) | Density ($\times 10^{20} m^{-3}$) |
|---|---|---|---|
| 0.026 | 2 | 4 | 3.4 |
| 0.051 | 4.9 | 15 | 8.6 |
| 0.1 | 7.1 | 21 | 12.8 |
| 0.19 | 10.2 | 49 | 39.1 |

In actual irradiated grains, defect clusters have different sizes and are distributed at random positions in the crystal. In the present simulations however, loop-facet clusters are regularly spaced, making up a three-dimensional array. With this simpler arrangement, strain localization in lower particle density regions is avoided and hence, comparison between different simulated systems (see section 3.3.5.2) will mainly depend on implemented loop-facet densities and properties. All simulated grains initially contain one $L = 500nm$ dislocation source, in the $a/2(101)[\bar{1}\bar{1}1]$ slip system, taken as the primary slip system (cross-slip systems associated with the initial source are: $a/2(011)[\bar{1}\bar{1}1]$and $a/2(1\bar{1}0)[\bar{1}\bar{1}1]$). The position of the initial source is exactly the same in all the cases, with a view to facilitate analysis of the results.

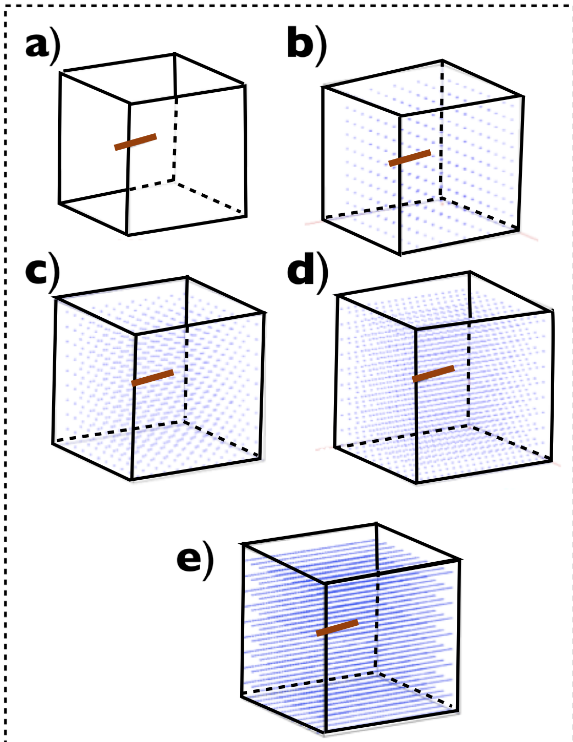


**Figure 3.18** – *Initial meso-scale DD simulation setups. a) Un-irradiated reference alpha-Fe grain, (b) Irradiated alpha-Fe grain containing* $5 \times 10^{20} loops/m^3$ *c)* $10^{21} loops/m^3$ *d)* $2 \times 10^{21} loops/m^3$ *e)* $5 \times 10^{21} loops/m^3$*.*

In general, stress-strain data to be presented in section 3.3.5 should not be directly compared to experimental results obtained on macroscopic, poly-crystalline specimens, as was the case with the earlier section.

### 3.3.5 Results

#### 3.3.5.1 Plastic deformation before irradiation: reference alpha-Fe grain

The dislocation density increases linearly throughout the simulated time, attaining for example $10^{13}\ m^{-2}$ at $\epsilon_p = 2 \times 10^{-4}$. The same type (and rate) of dislocation density evolution is observed in all the simulations herein. In the present case, applied stress increases until new dislocation sources are generated spontaneously: first, by cross-kink wandering and later on, by a double cross-slip mechanism. Spontaneous source generation and subsequent dislocation multiplication lead to stress level and dislocation velocity stabilization. It is important to note that the same stabilized stress level is achieved, regardless of the initial number of initial dislocation sources (at least, up to 20 initial sources). Beyond the transient regime, the number of immobile dislocation far exceeds that of mobile dislocation (estimated ratio 1:40), which is a well know character of plastic deformation, in metallic crystals.

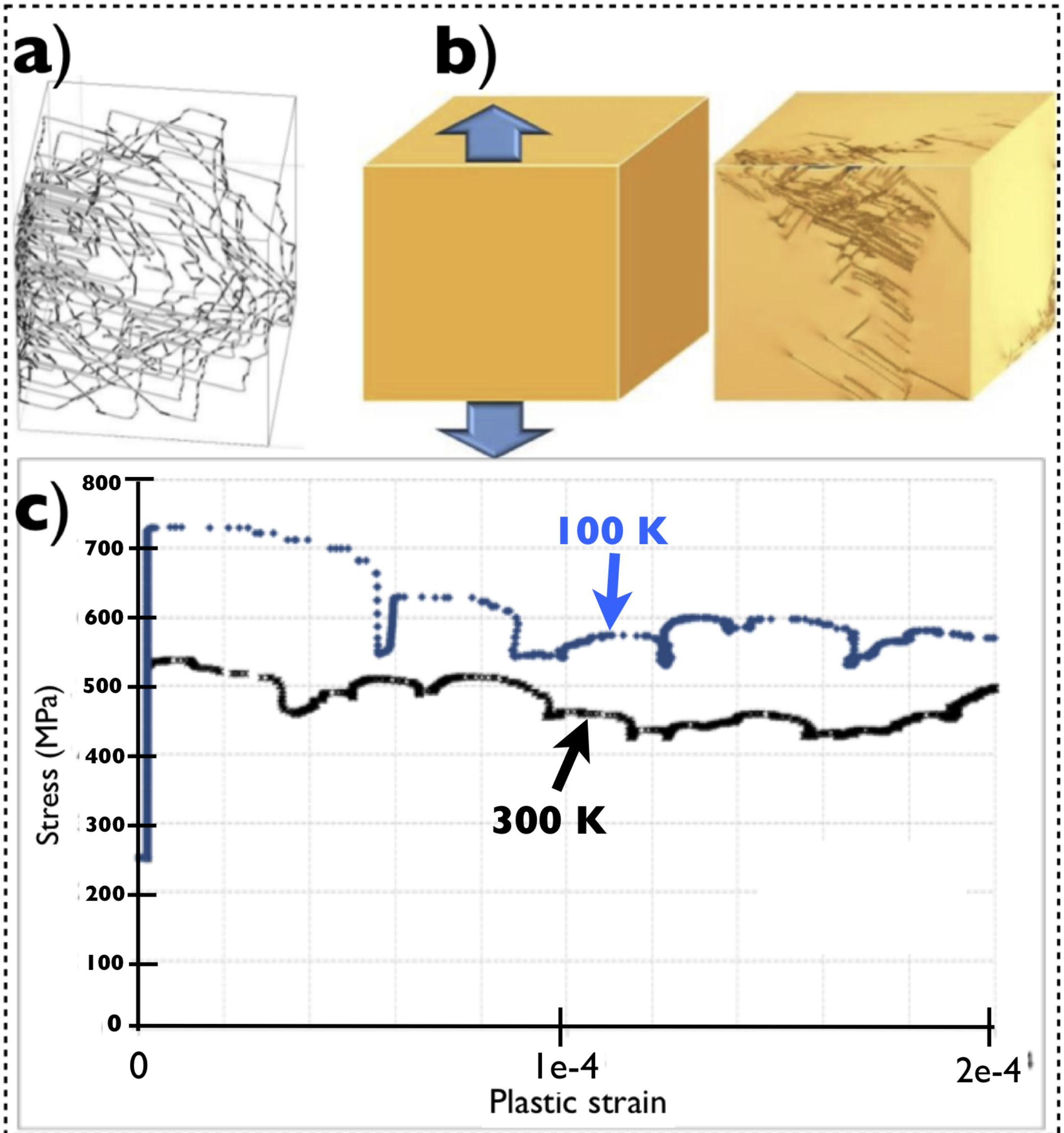


**Figure 3.19** – *Effect of plastic strain in an un-irradiated alpha-Fe grain. a) 3D dislocation structure for* $2 \times 10^{-4}$ *plastic strain, b) corresponding 3D deformation map. c) Equivalent stress-strain curves at 100K and 300K.*

Careful examination of gamma-tau plot (not shown) show an absence of forest type hardening: the tau level in primary slip system is not influenced by a high density of dislocations in the secondary slip system, i.e. tau-primary remains the same (about 250 MPa) in both single and multiple slip, at both 100K and 300K. Flow stress increase with decreasing temperature, in multiple and single slip, reflects the temperature dependent evolution of quantity $\Delta G/k_B T$ with temperature (see expression 3.1).

#### 3.3.5.2 Plastic strain after irradiation: effect of mono-modal loop density

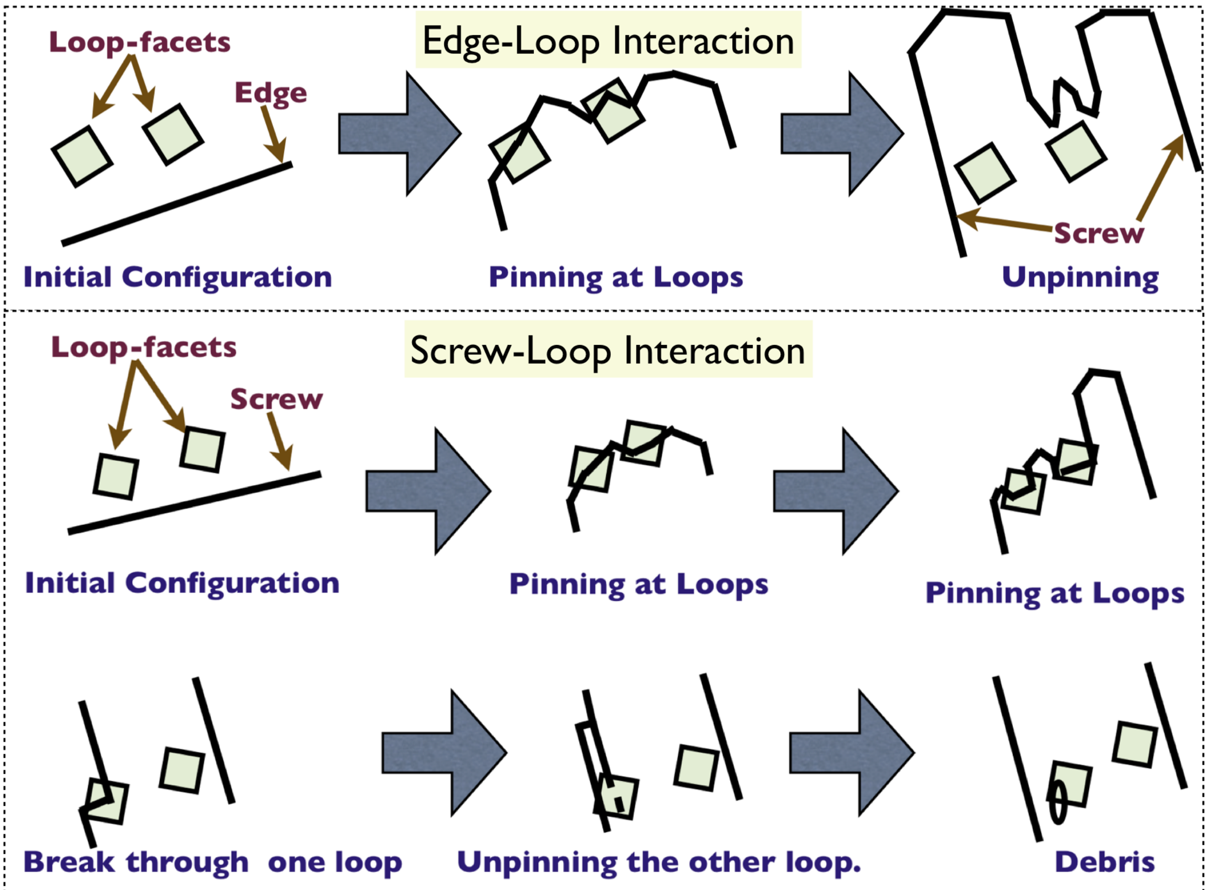


**Figure 3.20** – *Interaction between one dislocation and 2 loop-facets using test DD simulations. Calculations are performed under controlled plastic strain rate loading conditions, in (001) uni-axial tension. The loop diameter is D =20 nm and center-to center loop inter-spacing is 80 nm. The initial L = 150 nm long segment is pinned at its extremities and belongs to the* $a/2(101)[\bar{1}\bar{1}1]$ *slip system. a) Edge-loop case. b) Screw-loop case.*

The irradiation loops are again implemented as shearable facets, as explained earlier (3.2.1.1). The elementary loop-dislocation interaction is as shown in the figure 3.20. The simulation parameters of the different runs (in section 3.3.5) are adjusted to obtain exactly the same, average steady-state dislocation velocity. This precaution ensures that exactly the same actual strain rate and mobile dislocation densities are obtained in each case. Then, differences in stress-strain behaviors genuinely come from the adopted simulation setup, i.e. loops, particles, grain boundaries, dislocation-dislocation interactions or any combination of the above.

### 3.3.6 Meso-scale simulations

Simulations presented in this section include different, mono-modal densities of soft loop-facets, consistent with irradiation doses of $0.05 - 0.2$ dpa (estimation based on Table 3.2 data). When tensile loading is applied to the irradiated alpha-Fe grain, initial sources are activated and shear loops are emitted in their respective, initial glide planes. Mobile dislocations then interact with loop-facets and grain boundaries and cross-slip spreads out plasticity across the entire simulated space. The average screw dislocation velocity is stable during the whole simulated time; indicating that generation of new sources is more difficult, due to loop-dislocation interactions.

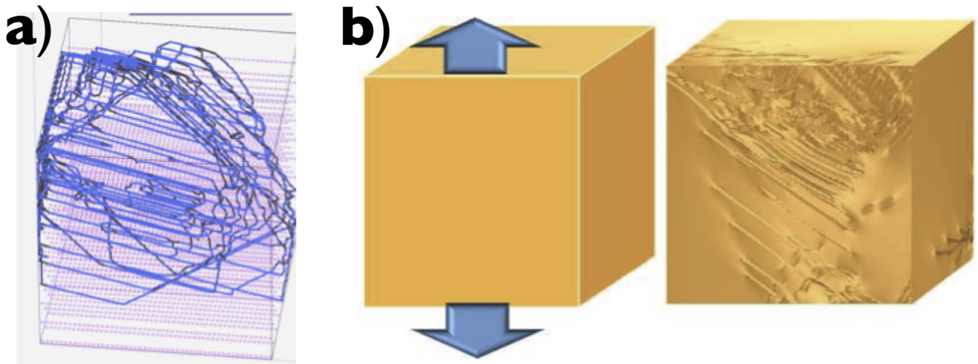


**Figure 3.21** – *Effect of plastic deformation on irradiated alpha-Fe grain containing* $5 \times 10^{21} loops/m^3$. *(a) 3D dislocation and loop structures, (b) corresponding 3D plastic strain map.*

Interestingly, the presence of up to $5 \times 10^{21} loops/m^3$ do not affect the meso-scale plastic deformation significantly (compare Figures 3.21 to Figures 3.19). In other words, there is no evidence of sharp strain localization, up to irradiation doses representative of the tested irradiation conditions. Homogeneous plastic deformation is one important condition for continuum-scale modelling applicability. Hardening induced by the different loop populations is around $t = 50MPa$ in single slip (see Figure 3.22b, for $\epsilon_p > 2 \times 10^{-4}$). Loop-induced hardening has a weak temperature-dependence, between 100K and 300K (compare Figures 3.22a to 3.22b).

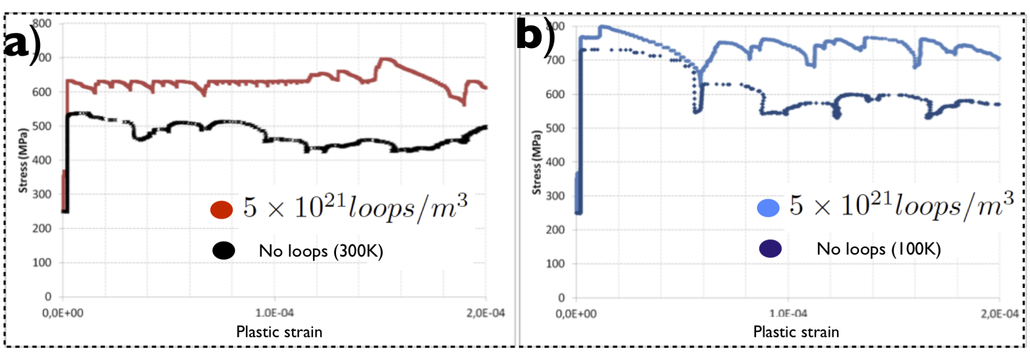


**Figure 3.22** – *Stress-strain data in an un-irradiated and irradiated* $\alpha - Fe$ *grain including* $5 \times 10^{21} loops/m^3$ *. Stress-strain curves obtained: a) at* $300K$*, b) at* $100K$*.*

Increasing the loop density from $5 \times 10^{21}$ to $5 \times 10^{22}$ $m^{-3}$ does not significantly affect the hardening magnitude significantly (not shown). Hardening saturation for those loop densities variation is consistent with well known experimental trends [Matijasevic *et al.* 2008, Miller *et al.* 2009]. All 3 available slip systems (one primary and two cross-slip planes corresponding to it) get activated during all the simulations. Dislocation populations in those different slip systems and corresponding hardening amplitude strongly depend on the applied stress tensor. Dislocation population partition between the different slip systems is, on the other hand, weakly dependent on temperature.

### 3.3.7 Quantitative evaluation of interacting loop population

The nature of the irradiation defects generating strain hardening in RPV steels is still a matter of debate. Continuum scale models assume that irradiation defects in Fe can be treated like local obstacles, namely considering only their density and average strength, regardless of the defect type involved. Irradiation defect population intersecting one family of slip planes gradually decrease with cumulative dislocation glide, due to dislocation-defect interaction. For this reason, plastic strain tends to localize on initially active slip planes, at least until dislocation density accumulation yields an augmentation of the Critical Resolved Shear Stress. At the continuum level [G. Monnet 2011], the equation describing corresponding total irradiation defect population $\rho_L$ is:

$$\dot{\rho}_L = -\xi \rho_L \dot{\gamma} \tag{3.20}$$

where $\xi$ is the elimination yield of loop-defects as obstacle to dislocation motion and $\dot{\gamma}$, the (plastic) shear deformation rate (in $s^{-1}$). This means

$$\rho_L = \rho_L^0 exp(-\xi \gamma) \tag{3.21}$$

Also,

$$\rho_L = \rho_L^0 - \rho_{LV} \tag{3.22}$$

where $\rho_{LV}$ is the interacting loop population whose evolution with plastic strain is finally given by:

$$\rho_{LV} = \rho_L^0 (1 - exp(-\xi\gamma)) \tag{3.23}$$

Here, we will compare prediction of expression 3.23 with the interacting loop population directly calculated during DD simulation, as explained in Figure 3.23. The interacting loop count is incremented each time mobile dislocations interact and then, go through a loop-facet, regardless of the incoming dislocation character. The curves shown in Figure 3.24 and 3.25 thus indicate the maximum possible number of interactions, as a function of equivalent plastic strain.

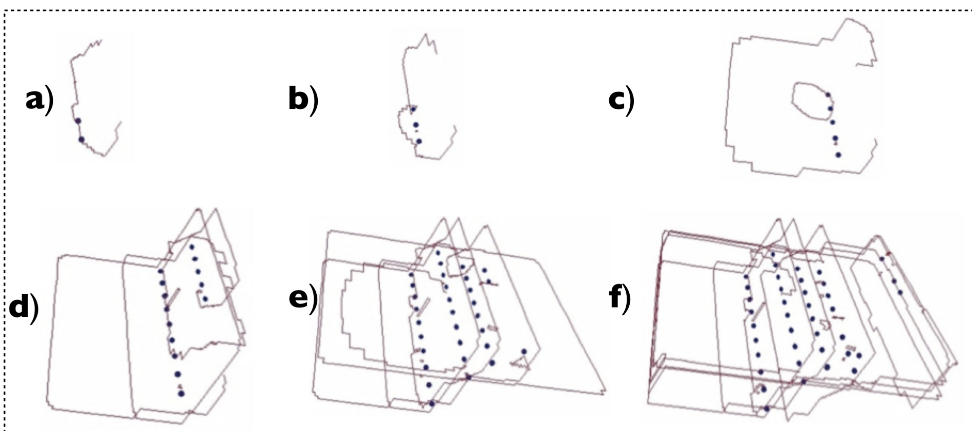


**Figure 3.23** – *Progressive development of plastic deformation and interaction with loop population. In this example, loop count associated with images (a) through (f) reads: 2, 3, 5, 14, 31, 40, etc. Loop density is* $5 \times 10^{21} loops/m^3$ *. Only the interacting loops are represented.*

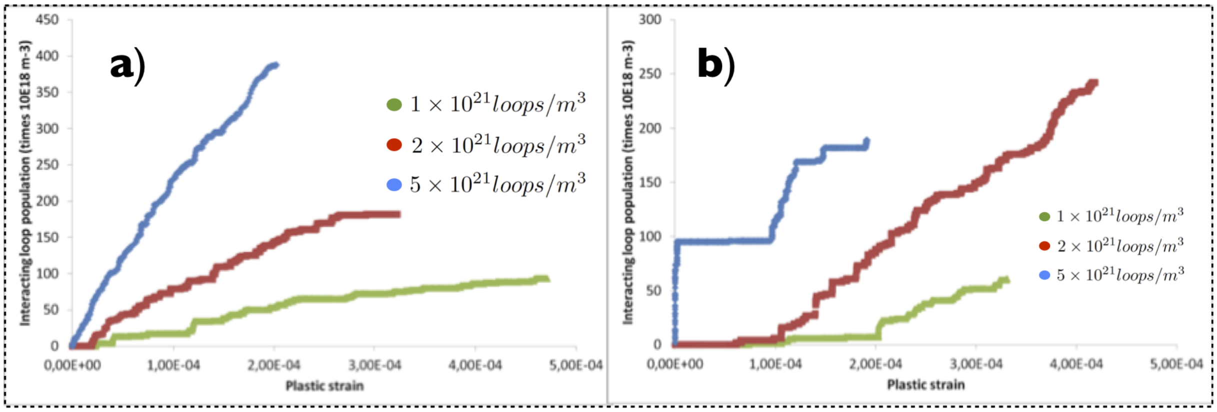


**Figure 3.24** – *Interacting loop population assessment at 300K, using DD simulations. a) Multiple slip b) single slip.*

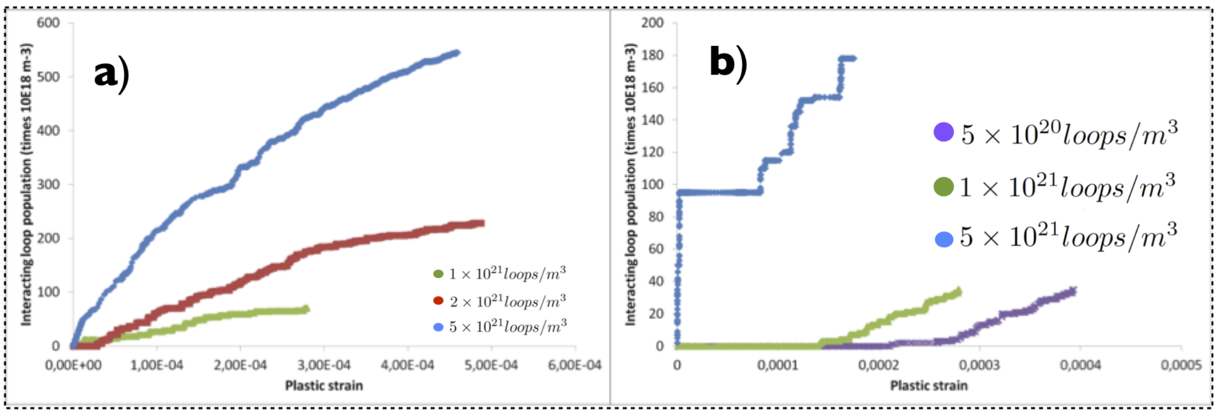


**Figure 3.25** – *Interacting loop population assessment at 100K, using DD simulations. a) Multiple slip b) single slip.*

Interestingly, it is possible to fit all the curves from 3.24 and 3.25 using expression 3.23 using a narrow range of the parameter $\xi = 100 - 120$ with corresponding initial loop densities. This means equivalent plastic strain is the main factor controlling interacting loop population evolutions, regardless of the selected applied stress tensor or temperature. Under controlled strain rate conditions, interacting loop population is thus independent of the active slip system number and of screw dislocation mobility evolutions with temperature.

The quantity $\xi$ derived from Figures 3.24 and 3.25 data assumes a loop sweeping yield of 100%, regardless of the nature of the interacting dislocation (edge or screw). In reality, loop removal mainly takes place due to screw-loop interactions.

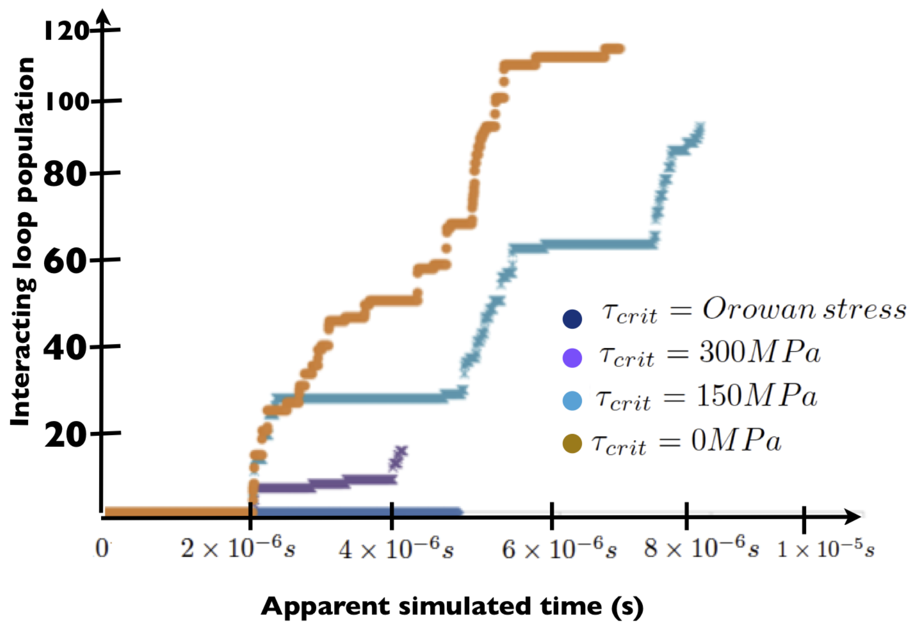


**Figure 3.26** – *Effect of loop-facet strength on the interacting loop population. Plastic strain is proportional to simulated time, since the runs are made under controlled plastic strain rate conditions.*

Incidentally, the number of interactions at a certain plastic deformation level directly depends on the obstacle strength, at least up to $300\,MPa$(see Figure 3.26). This means loop count due to edge-loop interaction (strength = $215\ MPa$) should be about 3 times as large as loop count due to screw-loop interaction (roughly: $215/67 \approx 3$, see section 3.2.1.1), assuming identical edge and screw dislocation densities. Accounting for screw-loop interaction only, the quantity x should therefore be in the range $25-30$ (instead of $100-120$). In reference [G. Monnet 2011] however, best consistency with stress-strain evolutions observed at the macro-scale is obtained with x = 1-10. This is apparent discrepancy which we analyze in the following way: Unlike in fcc, loops in bcc are re-emitted after interaction completion, whereby the loop is displaced over a distance comparable to the loop diameter. This means that a given loop can interact many times with new coming mobile dislocation, as plastic deformation accumulates, as long as it is present in the crystal. So the average number of interactions is the crystal diameter divided by the half loop diameter. Here we have $0.5\mu/0.02\mu = 25$. Our data is compatible with both macro-data and well-known dislocation-loop interaction mechanisms, provided 5-10 screw-loop reactions take place, on average, before a given loop is dragged sufficiently far to cease interacting with mobile dislocations. The total loop displacement (from its initial position) is then about 5 to 10 times the loop diameter, i.e. 100 to 200 nm.

### 3.3.8 Conclusions

Full three dimensional DD simulations of plastic deformation in $1\mu$ alpha-Fe grains have been performed at $100^\circ\ K$ and $300^\circ\ K$, accounting for thermally activated glide and cross-slip for screw dislocations. A tensile load has been applied under single and multiple glide conditions. Glide characteristics of bcc Fe-crystals are observed during all the runs, including: random cross-slip, pencil or wavy glide. At the grain scale, the present DD simulations show that:

1. Flow stress variations with temperature reflect corresponding evolutions of the quantity $\Delta G/k_BT$ used to calculate the screw dislocation velocity.

2. Unlike fcc crystals, Fe grains exhibit very little forest-type strain hardening: this means deformation mechanisms at low plastic strain are more or less independent of the plastic strain levels. In other words, it is possible to extrapolate the evolutions observed herein to larger plastic deformation.

3. Dislocation population evolution in the different systems strongly depend on the applied stress tensor.

Irradiation induced loops are introduced in the form of immobile internal obstacles called facets. During the runs, loop-facets are crossed by mobile dislocations, depending on whether a local stress criterion is satisfied. The loop-facet strength introduced herein is as per MD simulation results and depends on the mobile dislocation type. Systematic comparisons between grains containing various loop densities are then performed. The analyzed post-irradiation features include: dislocation micro-structures, cross-slip frequency and dislocation/facet interaction frequency and grain boundary plastic displacements. The main conclusions from that investigation are:

- The addition of up to $5 \times 10^{21} loop/m^3$ loop-facets does not induce significant strain localization, based on 3D plastic strain mapping of the simulation volume.
- Loop-induced hardening is significant and stable with increasing plastic strain. Its magnitude is weakly dependent on temperature ($100^\circ\ K - 300^\circ\ K$ range) and loop density, within $5 \times 10^{20} - 5 \times 10^{21} loops/m^3$ density range.
- The loop interaction frequency is independent of the nature and the number of active slip systems and of screw dislocation mobility evolutions with temperature ($100^\circ\ K - 300^\circ\ K$ range).
- The interacting loop population is directly proportional to loop strength (at least up to a strength of 300 MPa) and density.
- Macro and DD scale evolutions of loop population with plastic strain are compatible, assuming 5-10 screw-loop interactions (absorption and subsequent re-emission) take place before a given loop cease interacting with mobile dislocations.

# Chapter 4

# Role of primary and cross-slip stresses on the multiple clear channel formation in irradiated austenitic steels

---

*In this chapter, the collective effects of interaction between dislocation and interstitial loops in leading to clear channel formation, is studied through 3D DD simulations. More specifically, this is an attempt to predict the number of shear bands affecting (deforming) the grain boundaries, in presence of the representative irradiation defect cluster populations.*

---

## 4.1 Introduction

*This chapter examines a different manifestation of strain localization: the clear channel formation, discussed in section 1.3.2 on page 8.* Here, two types of DD simulations have been carried out based on their complementary capacities and limitations:

In **Type-I simulations**, irradiation-induced defect clusters are treated explicitly, in the form of prismatic loops. These simulations are an extension of the work performed by Nogaret et al [Nogaret *et al.* 2008], in understanding the single clear channel. Through these simulations, the collective phenomena obtained by Nogaret are reproduced, and then those results are analyzed in terms of stresses in the primary and cross-slip planes to predict the characteristics of multiple clear channels.

In **Type-II simulations**, the Type-I configuration is coarse-grained both in space and time. Here, the irradiation-induced defect clusters are treated as planar obstacles to dislocation motion. This description has reduced computational load and unlike Type-I modeling, includes thermally activated cross-slip mechanism, as required for simulating the formation of multiple slip bands. Experimentally new clear bands initiate from existing ones by germination of secondary channels in cross-slip planes. This means strain spreading into new shear bands is a deterministic process, depending on interplay between clear band internal stress and obstacle strength. Shear band spacing and plastic strain spreading obtained in Type-II simulations is documented and analyzed, in terms of a pile-up model.

## 4.2 Type 1 DD simulations: loop defect clusters as prismatic loops

### 4.2.1 Simulation setup and dislocation-loop interaction modeling

**DD simulation parameters** The 3D dislocation dynamics code used for the study is the edge-screw model [Verdier *et al.* 1998] introduced in chapter 1, section 2.2 on page 29. Elastic constants of a copper crystal are selected. Copper was chosen because its lattice parameters and are close to that of Fe, and also because the elementary MD results for elementary dislocation-loop interactions are available for it [Nogaret *et al.* 2007]. The cross-slip threshold $\tau_{III}$, stacking fault energy and other material parameters correspond to that of fcc iron. The materials parameters used in this work are listed in the Table 4.1. No thermally-activated cross-slip is implemented in Type-I simulations.

| Poisson ratio | Young's modulus E (GPa) | Density $\rho$ ($kg.m^{-3}$) | Viscous drag coef. B ($10^{-5}Pa.s$) | Cross-slip threshold stress $\tau_{III}(MPa)$ | Burgers vector b ($10^{-10}m$) |
|---|---|---|---|---|---|
| 0.324 | 42 | 8940 | 1.06 | 32 | 2.54 |

**Table 4.1** – *Mechanical and microscopic properties of copper at T=300 K*

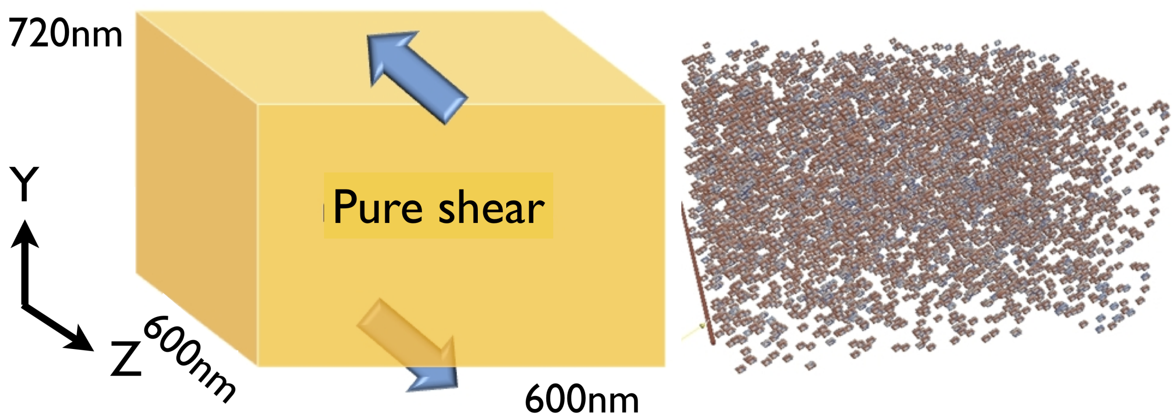


**Figure 4.1** – *a) Type-I DD simulation cell dimensions. b) Random loop positions.* $D = 10nm$, $L = 50nm$, $\delta t = 5 \times 10^{-14}s$. *Lattice spacing* $= 0.08b$, $Lmax = 11nm$, $\tau_{nuc} < \tau_{edge}$. *The blue arrows indicate the shear direction. Thermally activated cross-slip is switched off.*

**Loading and boundary conditions** The $0.60 \times 0.60 \times 0.72\ \mu m^3$ simulation cell is shown in the figure 4.1. Cell borders act as impenetrable grain boundaries, with respect to dislocation motion. Horizontal planes are Y = (111) glide planes, while the Z axis is along the $\frac{1}{2}[10\bar{1}]$ Burgers vector direction. The applied stress tensor shear component $\sigma_{yz}$ is feedback controlled in order to impose a constant strain-rate $d\sigma_{yz}/dt = 3.0 \times 10^2 s^{-1}$. A dislocation source is placed along one of the simulation cell border, to model dislocation emission from heterogeneities.

A simple criterion is used for dislocation emission: the source emits a new dislocation (one half-loop) when the applied stress $\sigma_{yz}$ reaches a critical value, called the nucleation stress $\tau_{nucl}$. Dislocations emitted by the grain boundary source belong to the ½ $\langle 10\bar{1} \rangle$ 111 system, to be called the primary slip system.

**Implementation of MD observations in DD modeling** The atomistic mechanisms observed in the MD simulations of Nogaret, discussed in section 1.4.2.2, are implemented in the current DD simulations, in the following way: Loops are initially introduced as a set of perfect prismatic loops with the Burgers vector of the dislocation source. Each prismatic loop consists of 4 edge segments, two on the primary slip system and the other two on the cross-slip system (see figure 4.2). Segment length (and thus the loop size) is set to $D = 10nm$. The loops are located at random positions in the simulation volume, with a density $N = 3.7 \times 10^{22} m^{-3}$, in agreement with TEM observations (dose < 1 dpa, [Pokor *et al.* 2004]). The mean corresponding inter-loop distance in glide planes is $L = 1/\sqrt{(N \times D)} = 52nm$, which is equal to the distance considered in reference MD simulations [Nogaret *et al.* 2007]. Frank loops are modeled as "frozen" $\frac{1}{2}[10\bar{1}]$ interstitial prismatic loops, as the $\frac{1}{3}\langle 111\rangle$ Burgers vectors are not valid Burgers vectors in fcc (see figure 5.2 on page 151). Initially, these prismatic loops are "frozen", i.e. they are fixed and not allowed to recombine with mobile dislocation segments, because they model Frank loops that are sessile loops.

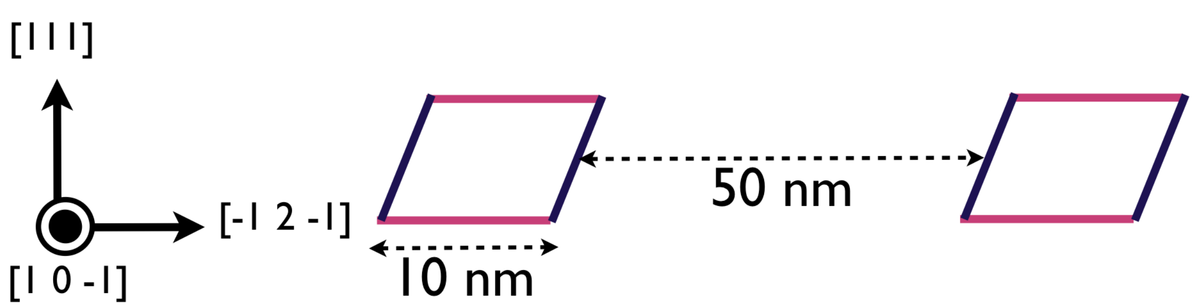


**Figure 4.2** – *Modeling of Frank-Loops in fcc. Each loop is constructed such that two of its edges are in the primary slip plane and two of them are in the cross-slip plane. The Normal of these loops is in the direction of the Burgers vector corresponding to those two planes. The density of the loops is so chosen such that the the average separation between the loops is about 50 nm.*

The interaction rules of this prismatic loop with edge and screw dislocations is explained in figure 4.3:

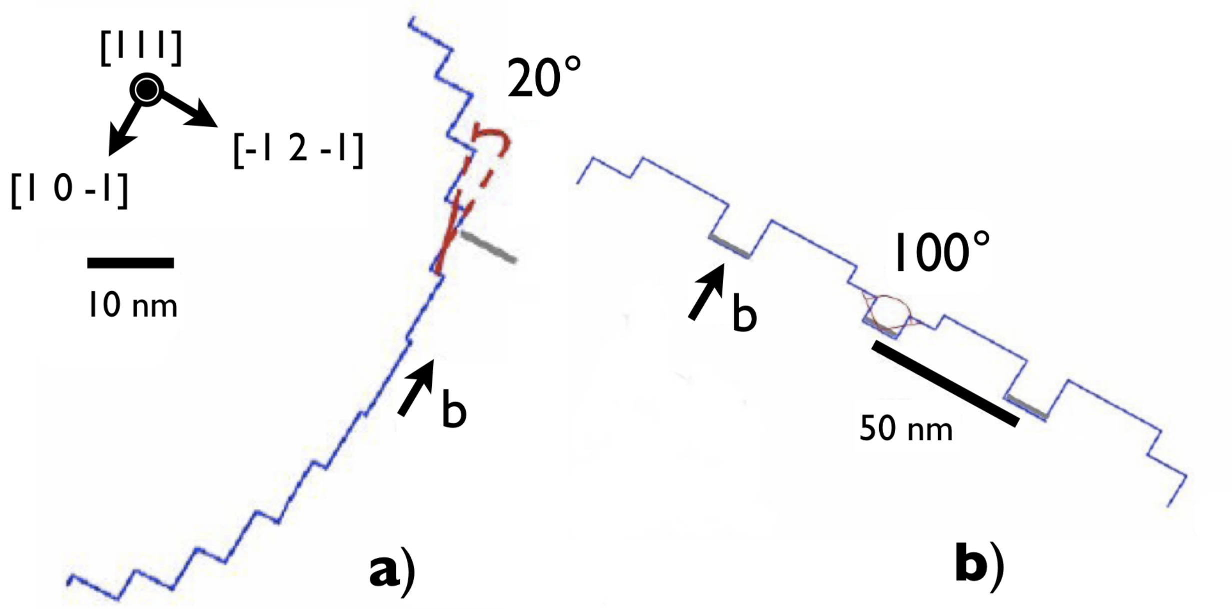


**Figure 4.3** – *Illustration of interaction rules for a) Screw and b) Edge dislocation with a prismatic loop. The edge-screw segmentations of these dislocations are shown here. The dislocations are located in the* $[111]$ *plane and have Burgers vector of the type* $[10\bar{1}]$.

When a dislocation meets a loop, if the dislocation is locally screw at $20°$(see figure 4.3a), the loop is unfaulted and is freed : thus the contacting dislocation segment can react with the loop to form spontaneously a helical turn. In the other cases, the loop is sheared and remains "frozen" : the contacting dislocation segment cannot react with the loop and remains blocked until the two dislocation arms pinned on the loop reach a critical angle equal to $100°$ (see figure 4.3b), which gives a shear stress in agreement with MD simulations.

The values for XL (lattice parameter), $L_{max}$ (maximal length of dislocation segments), $dt$ (time step) are taken as $0.08b$, $11nm$, $5 \times 10^{-14}s$ respectively. Thus, $XL$ is less than the inter-atomic distance, but in practice, the dislocation segments have a size greater than some tens of $XL$, i.e. greater than b. The use of $XL$ less than b permits a good description of Frank loops. Since the lattice parameter XL was decreased, the time step was also decreased down to $5 \times 10^{-14}s$ in order to insure the stability of the integration algorithm.

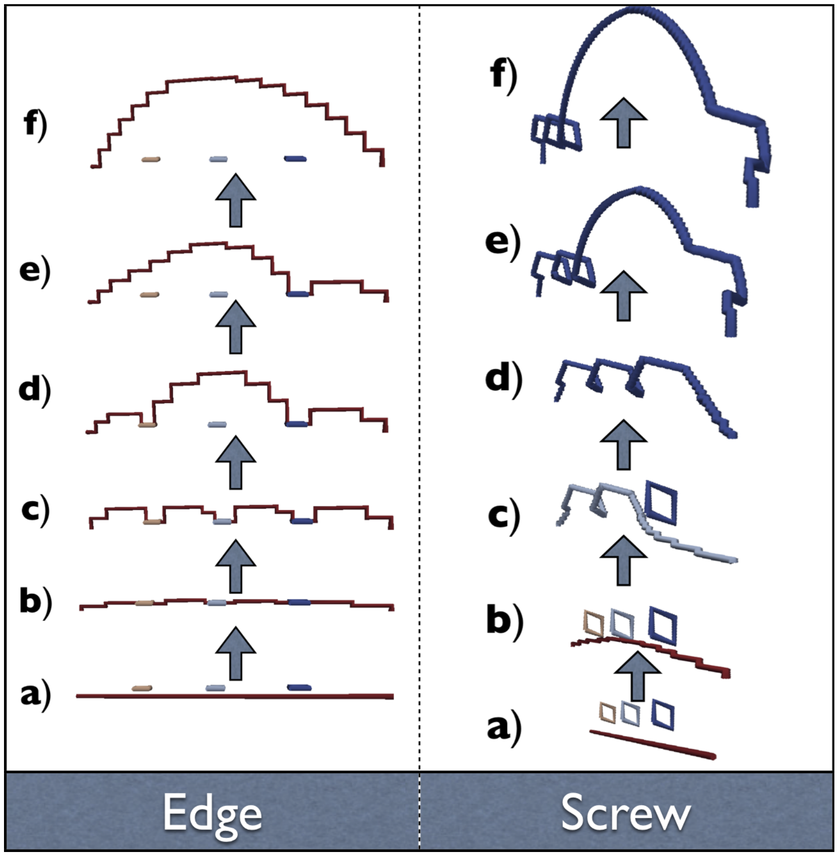


**Figure 4.4** – *Interaction of an Edge dislocation with the loops is shown on the left, and screw dislocation interaction with the loops is shown in the right. The snapshots are to be read from bottom to top. a) represents the initial configuration for edge and screws. b) represents the instantenious configuration when the dislocation contacts the loops. c) With time, the edge dislocation is only blocked by the loops, whereas the screw dislocation absorbs the loops as helical jogs. d) The central loop is bypassed by Orowan bypassing in the edge case, whereas in case of the screw the loops are totally absobed as jogs. e),f)With time (and stress) the edge dislocation bypasses all the loops and bows out. Screw dislocation, on the other hand, bows out pushing the absorbed irradiation loops in to the corners.*

The evolution of edge and screw dislocation in the presence of three irradiation loops having the same Burgers vector as the dislocation themselves is given in figure 4.4. From the simulation corresponding to figure 4.4 it can be seen that

1) In case of an edge dislocation the loops are just sheared but they continue to remain at their location, whereas in case of a screw dislocation, the loops are absorbed as helical jogs, which are then pushed to the ends of the pinning points.

2) Another point to note is the elevator effect shown by screw, loop interactions. The screw dislocation that gets activated after absorbing the helical jogs is on a different plane, at a height proportional to the loop size. The stress-strain plot corresponding to these interactions, is as shown in the figure 4.5.

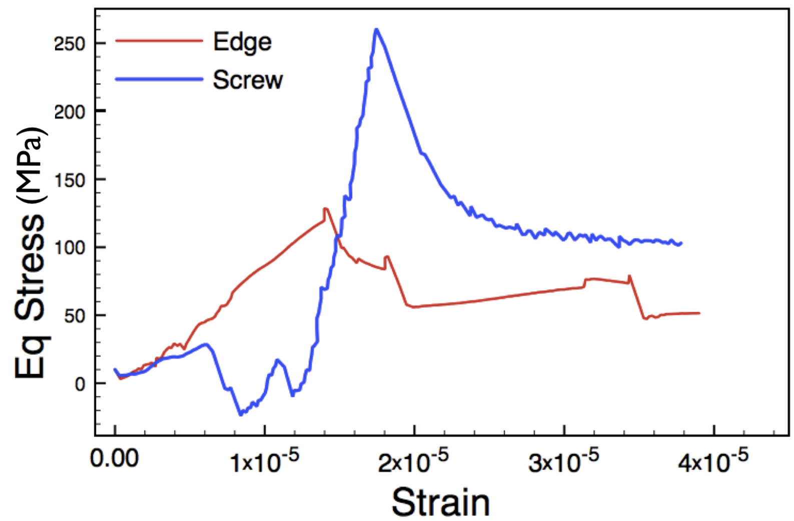


**Figure 4.5** – *Stress-strain plots for the interaction of edge and screw dislocations with the irradiation loop. The blue plot is for screw dislocation and the red plot is for an edge dislocation. These plots correspond to the snapshots given in the figure 4.4.*

3) The stress-strain plot of figure 4.5 shows large excursions and in the case of screw dislocations it is even negative at some places. This is again a consequence of the constant strain rate control employed in these simulations. The attractive character of the screw-loop interaction is refectled in the stress before their contact (corresponding approximately to the snapshot 4.4b on the right, screw). Molecular Dynamics simulation of dislocation interaction with obstacles also revealed similar stress variations [Bacon & Osetsky 2007, Bacon & Osetsky 2009, Bacon *et al.* 2009][1].

4) It can be seen from figure 4.5 that the maximum interaction stress for a screw dislocation (blue line) is almost double that of the edge dislocation (red line). When a screw reacts with a loop, it acquires a helical turn which is the strongest possible obstacle as it spreads along the entire dislocation thanks to the mobility of the superjogs along the dislocation

[1] see also figure 3A of [Fan *et al.* 2013]

line. Edge dislocations on the other hand, need much less stress to shear the irradiation loops (red line).

5) Although screw dislocations require higher stress, they systematically unfault the loops and can therefore clear a glide plane. Edge dislocation can only shear the loops, and cannot aid in the clearing the shear band. These observations are summarized in the table 4.2.

**Table 4.2** – *Summary of screw and edge glide mechanisms in the presence of irradiation loops.*

| **Edge Dislocation** | **Screw Dislocation** |
|---|---|
| Loop shear | Loop absorption as helical turns |
| Drag of helical turns | Gets pinned by helical turns. |
| Glides at moderate stress | Glides only at high stress. |
| Planar glide | Elevator effect. Gets re-emitted in the upper glide plane. |

#### 4.2.1.1 Plastic deformation in the presence of loops: single clear band formation

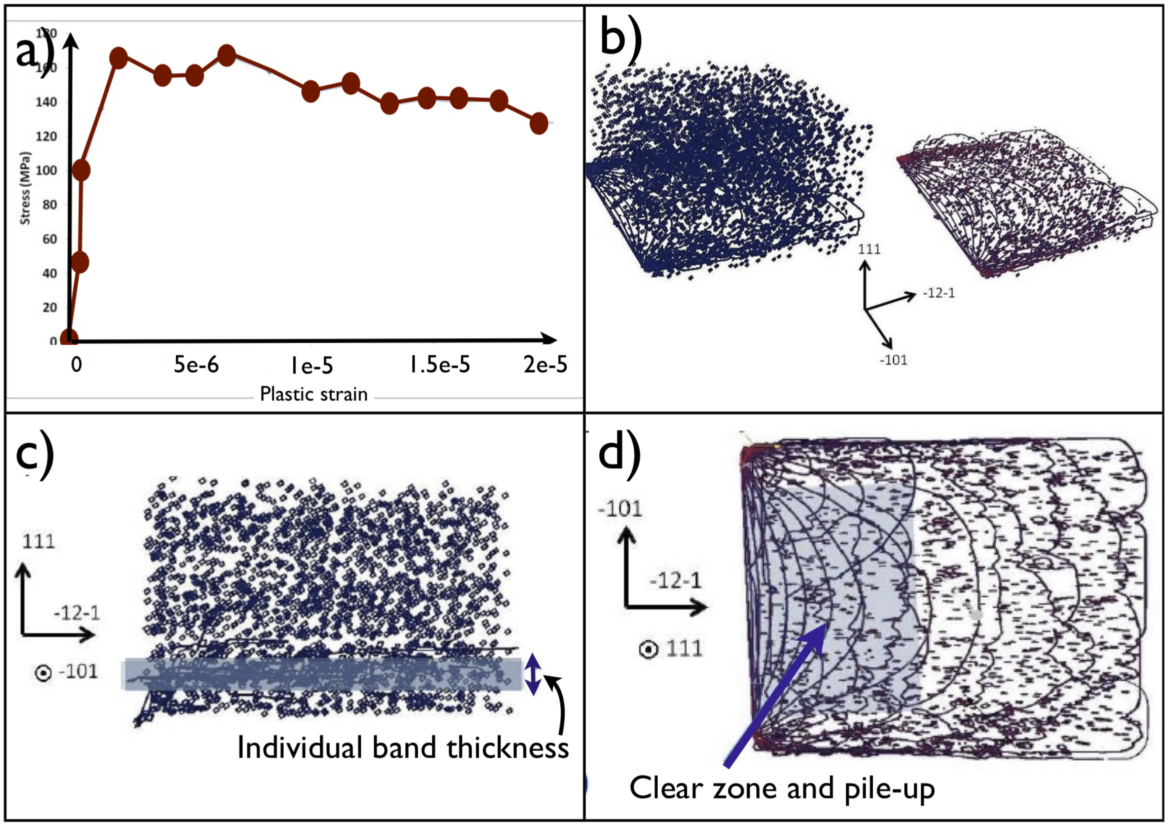


**Figure 4.6** – *Single clear band simulations. a) Stress-strain behavior of the simulation cell. b) Perspective view of the simulation cell after clear band formation, c) cross-section view of a clear band, d) top section view of the same clear band.*

In this section, plastic deformation due to a single screw dislocation source is analyzed. The source emits dislocation(s) through a random population of Frank loops. The nucleation stress is set to $\tau_{nuc} = 90MPa$, i.e. below the critical loop strength for both edge and screw dislocations interaction. Consequently, isolated (or single) dislocations cannot glide through the entire irradiated crystal: dislocation glide is only possible with the help of collective mechanisms. Practically, the first dislocation gets pinned by the helical jogs formed on consecutive prismatic loops. The applied stress then increases and reaches the nucleation stress. A second dislocation is then nucleated, producing a small plastic strain burst, while the applied stress drops. The second dislocation also gets pinned and the applied stress rises again, triggering the nucleation of a third dislocation, etc (see figure 4.6, and figure 6b of [Nogaret *et al.* 2008] for a better illustration).

**Dislocation clearing of irradiation loops** According to [Nogaret *et al.* 2008, Nogaret 2007], two mechanisms are involved in the channel clearing of dislocations, as in figure 4.7:

1. Screw dislocation first unfault the dislocation loops and absorb them as helical turns.

2. The edge dislocations are brushed to the ends of the dislocation line.

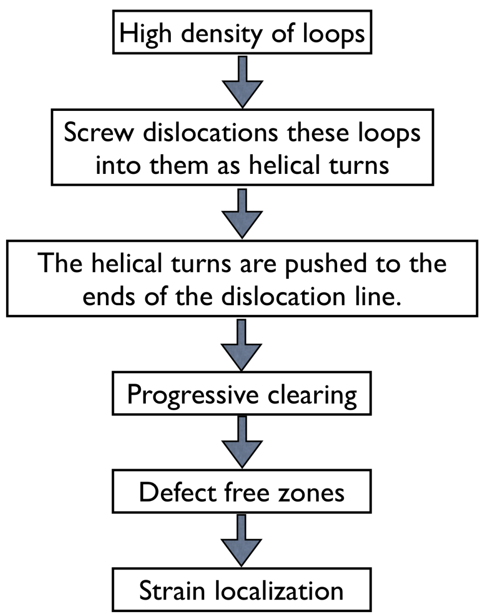


**Figure 4.7** – *Mechanism of channel formation, as per Nogaret.*

Thus, successive and asymmetric action of edge and screw dislocations is responsible for efficient loop removal: It leads to the transformation of a uniformly distributed nanometric sized defects into clusters of large prismatic loops. This results in the localization of deformation in those glide planes which are cleared of their irradiation loops. Another important effect of pile-up development is progressive accumulation of internal stress, in the cross-slip system. Experimentally, new clear bands initiate from existing ones, by germination of secondary channels, in obtuse cross-slip planes (see [Yao 2005]). This means strain spreading into new shear bands is, possibly, a deterministic process, depending on interplay between clear band internal stress and obstacle strength. In an attempt to confirm this idea, internal stress in the vicinity of idealized and realistic pile-ups is investigated in the next two sections.

#### 4.2.1.2 Stress field due to ideal dislocation pile-up

Basic strain spreading mechanisms can be better understood by examining the resolved shear stress field associated with an ideal pile-up, made of N rectilinear screw dislocations. We will examine in detail stress projected in primary and cross-slip systems. In the DD simulation framework, individual dislocations are treated as inclusions in an isotropic elastic medium. The long range stress field due to an infinite screw dislocation along the z-axis, moving along the x-axis has the shear stress components $\sigma_{xz}$ and $\sigma_{yz}$ expressed as

$$\sigma_{xz} = -\frac{Gb}{2\pi(x^2+y^2)}y \tag{4.1}$$

$$\sigma_{yz} = -\frac{Gb}{2\pi(x^2+y^2)}x \tag{4.2}$$

where $(x, y)$ are the coordinates of the evaluation point, assuming the dislocation is located at the origin and G is the shear modulus. The shear stress resolved in the primary slip system is $\tau_{prim} = \sigma_{yz}$. In this framework, the normal to the cross-slip plane is $(-\frac{4}{\sqrt{18}}, \frac{1}{3}, 0)$ so that the shear stress induced by an infinite dislocation in the cross-slip system is

$$\tau_{cs} = \frac{Gb}{2\pi(x^2+y^2)}\left[\frac{2\sqrt{2}y}{3} + \frac{x}{3}\right] \tag{4.3}$$

Note that equation (4.3) now depends on both $x$ and $y$ in a non-equivalent manner that will affect the cross-slip geometry. In the absence of obstacles, such stress distributions favor obtuse over acute cross-slip geometry [Kubin *et al.* 2009].

In the case of a pile up of $N$ infinite screw dislocations, the internal shear stress is given by the superposition of stresses expressed as in equations (4.1 and 4.2), for different values of x. For a given balanced pile-up, each dislocation is located at a null value of the effective stress obtained as the summation of the applied and internal shear stresses. In other words, the internal stress shields off the applied stress acting in the dislocation slip plane, as shown in figure 4.8a.

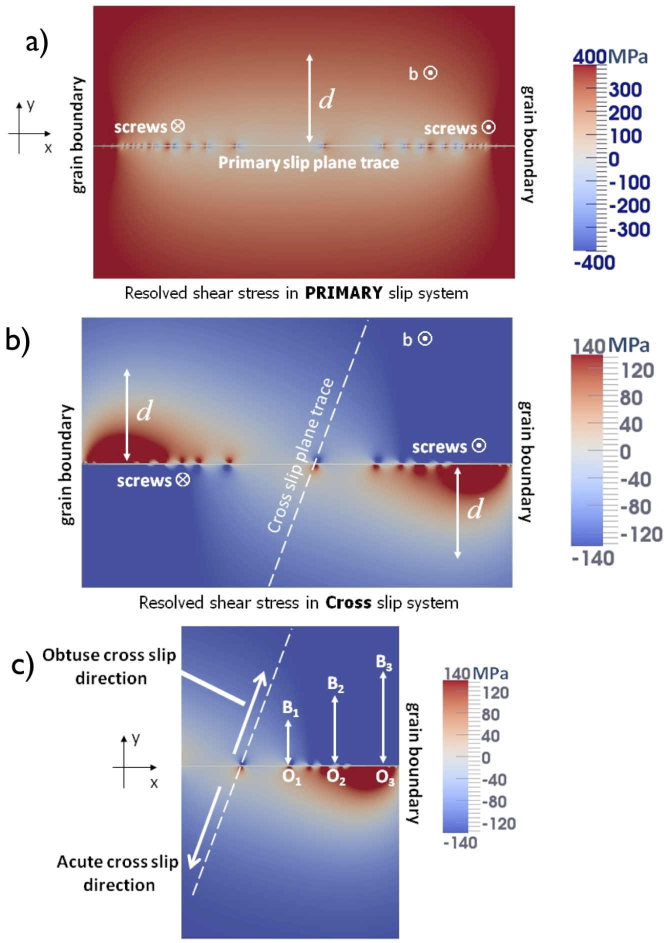


**Figure 4.8** – *Resolved stress field due to a screw dislocation pile-up. The dislocations are pushed against the grain boundary by the applied load $\tau_{applied} = 420MPa$, on both sides of the grain. a) Stress field (internal + applied) resolved in the primary slip system, plotted in plane z = 0. The stress vanished near y = 0 because the applied stress is shielded by the internal stress due to the balanced pile-up. The stress comes back to the applied stress level at a characteristic distance y = d, from the reference glide plane. b) The shear stress field resolved in the cross-slip system, plotted in plane z = 0. Near the pile-up extremities, the stress falls back to zero at the same characteristic distance y = d, from the primary glide plane. c) In the absence of obstacles, the stress-dependent cross-slip probability and characteristic glide range OB depend on the screw dislocation position x, at the time of the glide plane change (ranges $O_1B_1\ldots$ depicted here are arbitrary). The characteristic slip range also depends on the cross-slip direction: it is longer in the obtuse than in the acute direction. In this example, the screw dislocations moved from left to right, before reaching equilibrium.*

In figure 4.8b, the effective (applied+internal) stress profile in the cross-slip plane induced by the equilibrated pileup of screw dislocations is plotted. The sign of $\tau_{cs}$ changes on each side of $y = 0$. This internal stress effect is limited to a small region, mostly concentrated on the pileup extremities. Beyond a certain distance $d$, the effective stress is again, only due to the applied stress. In the case of a pure shear stress imposed in the y-plane, the applied stress resolved in the cross-slip plane is one-third of that resolved in the primary plane.

We have shown that dislocation pile-ups are present in the primary clear band (see figure 4.6). For this reason, secondary channels should initiate at a position $x$ yielding optimal cross-slip conditions. A screw dislocation cross-slipping at a given position will keep on gliding in the new slip plane so long as the driving stress $t_{cs}$ remains strong enough. For instance, the potential glide range **OB** in cross-slip plane is larger if a screw changes its glide plane at position $x = O_3$ (close to pile-up extremities: see figure 4.8c) than at position $x = O_1$ or $O_2$. In other words, it should be possible to predict inter-band spacing according to stress profiles along **OB**.

**Stress field due to a 2D pile-up in a closed grain.** A similar analysis of the local stresses has been conducted in reference [Depres 2004] in the case of a dislocation pile-up in a bulk grain of finite size. The dislocation microstructure was obtained by a single Frank-Read source, located in the center of a cylindrical grain of diameter equal to the height. Figure 4.9 shows the final state when all dislocations achieve their equilibrium positions for a given applied stress magnitude. At the pile-up extremities (near the grain boundaries), the internal shear stress can be described by the following expression

$$\tau_{int}(x, y) = \tau_{app} exp(-k(x)\frac{y}{l}) \tag{4.4}$$

where $y$ is the distance normal to the reference slip plane, $\tau_{app}$ is the applied shear stress magnitude, $l$ is the pile-up length as defined in figure 4.9, and $k(x)$ is a continuous function of $x$. For $\tau(x, y)$ projected in the primary slip system, $k(x)$ is maximal at the pile-up center $x = 0$ and minimal at the pile-up extremities $x = \pm l/2$. The sign of is the same on both sides of the primary slip plane (in both y > 0 and y < 0 regions, c.f. figure 4.8a). For a projection in the cross-slip system however, $k(x)$ is minimal at $x = 0$ and maximal at $x = \pm l/2$, while the sign of in the y > 0 region is opposite to that in the y < 0 region (c.f. figure 4.8b). The negative or $y < 0$ region or branch corresponds to acute cross-slip, while the y > 0 region corresponds to obtuse cross-slip (c.f. figure 4.8c).

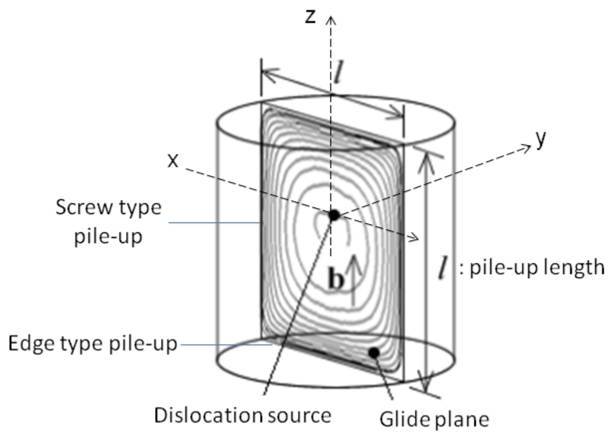


**Figure 4.9** – *Three-dimensional dislocation pile-up developing in a finite-sized grain. The coordinate axis y is perpendicular to the pile-up glide plane. In this case, the pile-up length l is equal to the grain diameter Φ.*

#### 4.2.1.3 Stress field due to realistic clear band arrangement

Realistic clear band simulation was presented in Section 4.2.1.1. The corresponding internal stress distribution can be determined by post-treatment analysis, accounting for the initial defect population and subsequent, deformation-induced dislocation arrangement.

For analysis purpose, a 2D mesh of ($700 \times 700 nm^2$) comprising $200 \times 200$ discrete points is generated parallel to the $(1\bar{1}1)$ cross-slip plane. The mesh is placed in a simulation cell where the internal stress resolved in the cross-slip plane is maximal, which corresponds to a plane containing $A_3$, $O_3$ and $B_3$ as pictured in figure 4.10. The internal resolved shear stress is then calculated at each mesh point. Calculation is done before and after the clear band is generated. Calculation is done before and after deformation, i.e. after clear band is generated. Initially, the stress distribution along direction [121] is due to the loops only (figure 4.10b). For this reason, this stress distribution does not display any particular feature: the number of points with positive stress is comparable to the number of points with negative stress.

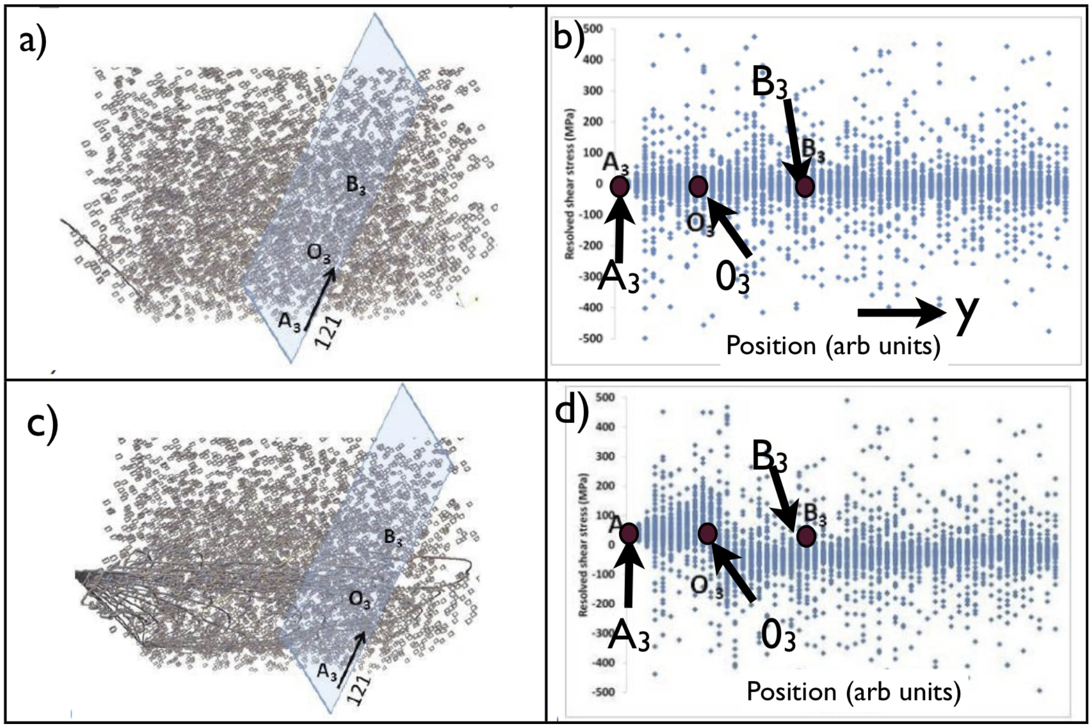


**Figure 4.10** – *Type-I simulation results: stress field in the clear band region. a) Calculation mesh position: parallel to cross-slip plane $(1\bar{1}1)$. b) The resolved shear stress along the 121 cross-slip direction: before clear band formation. The internal stress field is due to the loop population only. c) Calculation mesh position parallel to the cross-slip plane is the same as in a). d) The resolved shear stress along the $\langle 121 \rangle$ cross-slip direction: after the clear band formation. The internal stress field is due to the developing clear band, including dislocation pile-ups, debris, jogs, etc. Note the strain-induced stress distribution modulation, in the AOB region. The simulation volume boundaries are not shown for clarity.*

Once the clear band is formed (see figures 4.10c and 4.10d), the mobile dislocations in the clear channel yield a clear modification of the stress state in the $A_3$ $O_3$ $B_3$ region. The stress polarized region extends over a certain distance on either side of the primary slip plane (point $O_3$ in figure 4.10d). This modulation is a direct consequence of the dislocation structures developing in a finite sized bulk grain. A clearer picture of the deformation-induced changes can be obtained by subtracting the plot of figure 4.10b to that of figure 4.10d. Stress contribution due to the frozen loops is thereby filtered away, as presented in figure 4.11. Between point A and point O, i.e. below the glide plane y = 0, the stress polarity is negative and gradually increases, as $y \rightarrow O$. Between point O and point B, i.e. above the glide plane y = 0, stress polarity is positive and gradually vanishes with increasing distance y > 0.

Interestingly, it is possible to describe the cross-slip stress evolution along direction y using equation (4), taking $t_{app} = 150MPa$ (from figure 4.1a) and $k(x) \approx 5$). This description is consistent with a pile-up length $l = 0.3\mu m$, in good agreement with the results presented in figure 4.1d. The fitting parameters account for realistic and complex dislocation features, including dislocation curvature, super-jogs, debris, etc.

For this reason, stress distribution (along the $[121]$ direction) before deformation includes no particular feature: the number of points with positive stress is comparable to the number of points with negative stress. Stress magnitude extrema correspond to calculation points located close to a dislocation segment, i.e. where the internal stress diverges ($\tau_{CS} > 200MPa$ or $\tau_{CS} < -200MPa$) with $r \rightarrow 0$. This characteristic is a major difficulty for introduction of thermally activated cross-slip in Type-I DD modeling: high stress due to a diverging stress field leads to unrealistically large cross-slip probability, compared to experimental observations [Depres 2004]. In addition, complex stress state in the vicinity of a dislocation segment can change partial dislocation splitting $d_0$ and consequently, affect the cross-slip probability. Type-I model shortcomings are addressed by using Type-II simulations, to be presented in the next Section.

Stress distribution exhibits a clear deformation-induced evolution in **AOB** region (see figure 4.10 and figure 4.11), with respect to un-deformed condition (compare figure 4.10d and figure 4.10b). This change is directly ascribed to dislocation structure development: shear loops, jogs and debris. The stress polarized region extends over a certain distance on either side of position O (see 4.10d). A clearer picture of deformation-induced changes can be obtained by subtracting after/before plots: stress contribution due to fixed loop is then filtered away (see figure 4.11). Between point **A** and point **O**, i.e. below the glide plane $y = 0$, stress polarity is negative and gradually increases, as $y \to O$. Between point **O** and point **B**, i.e. above the glide plane $y = 0$, stress polarity is positive and gradually vanishes with increasing distance $y > 0$. In any case, the positive stress branch ($y > 0$) leads to acute cross-slip, while the negative stress branch ($y < 0$) yields to obtuse cross-slip (see figure 4.8 ). Interestingly, it is possible to fit the overall 1D stress cross-slip stress profile in the cross-slip plane using equation 4.4 with $\tau_{app} = 150MPa$ (from figure 4.6a) and pile-up length $l = 0.4\mu m$.

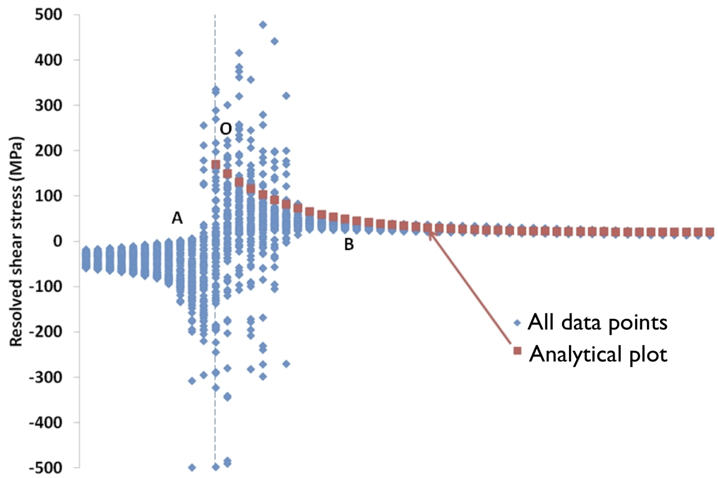


**Figure 4.11** – *Type-I simulation results: internal stress field (without the applied stress contribution) associated with a developing clear band. The average stress evolution between markers O and B can be fitted using equation (4.4).*

## 4.3 Type-II DD simulations: loop defect clusters as facets

### 4.3.1 Simulation setup and dislocation-loop interaction modeling

Note that in the earlier simulations, cross-slip was not implemented, as the cross-slip algorithm for fcc [Robertson *et al.* 2001, C. Robertson 2012] is not appropriate at this length scale ($\sim 0.08b$) and time scale ($5 \times 10^{-14}s$). This implies that the simulation cannot capture the phenomena that are dictated by cross-slip. One way to handle cross-slip is to coarsen the length and timescale of the simulation to those levels where the cross-slip algorithm of [Robertson *et al.* 2001, C. Robertson 2012] is appropriate.

Here, a new modeling scheme will be presented, that will complement the earlier Type-I simulation. In this scheme, an irradiation loop is represented as just a planar facet instead of four connected dislocation lines. These planar facets are of the same size as the irradiation loops, but they don't produce any long range stresses like the irradiation loops. The facets are shearable: that is, a dislocation segment can pass through the facet if the resolved shear stress acting on that dislocation is more than a certain value. The Edge-Screw interaction anisotropy with the loops is implemented through giving different loop strengths for edge and screws. The strength of the shearable facet is higher if the incoming dislocation is a screw, and is much smaller if the interacting dislocation segment is an edge. This is to implement the loop strength anisotropy seen in the earlier DD simulation (see figure 4.5). The algorithm for implementing this "loops-as-facets" scheme is outlined in 4.1 below.

**Algorithm 4.1** Implementing irradiation loops as planar obstacles.

- At every time step, **do**
  - For every facet **do**
    - Check if any dislocation segment is close enough to pierce it in the next time step.
    - If any dislocation segment is found, check if it is an edge or a screw, and also obtain the resolved shear stress acting on it, call it $\sigma_d$.
    - If the incoming dislocation segment is an **edge**:
      - If $\sigma_{\mathbf{d}} > \sigma_{\mathbf{e}}$ the dislocation is allowed to pass through the segment.
      - Otherwise it is blocked in front of the facet.
    - If the incoming dislocation segment is a **screw**:
      - If $\sigma_{\mathbf{d}} > \sigma_{\mathbf{s}}$ the dislocation is allowed to pass through the segment, and **the facet is removed from the simulation.**
      - Otherwise it is blocked in front of the facet.
  - **done**.
- **done**.

Note that if a facet is pierced by a screw dislocation segment ( i.e., if $\sigma_d > \sigma_s$), it is removed from the simulation volume. Or, implementation wise, its strength for incoming screws and edge segments is zeroed, $\sigma_s = \sigma_e = 0$. This is mimicking the loop absorption by a screw dislocation (see right image of figure 4.4). Such loop absorption does not happen on an edge segment hence the loop strength is not zeroed when it is pierced by an edge segment. The loop strength for edge, $\sigma_e$ is set to about half of the loop strength for screw, $\sigma_s$ (see figure 4.5).

By replacing loops with planar obstacles, the length scale of the DD simulations, $XL$, can be increased back to $10b$, rather than $0.08b$ used earlier. Similarly, the timestep of the simulation can also be now increased. This allows for simulating larger simulation sizes and for larger times. This is because, in this implementation, the irradiation loops are not dislocation segments and hence there is no need to reproduce the reaction of the dislocation segment and the irradiation segments.

The planar facets only act as the obstacles to dislocation motion, and cannot reproduce the microscopic reactions like formation of a helical turn when interacting with a screw dislocation etc. The elevator effect, which is a consequence of screw dislocation absorbing a loop as a helical turn is also absent in these simulations. But since the length and timescale of the simulations are typical of DD simulations, the cross-slip algorithm (as presented in [Depres 2004, Shin *et al.* 2003] ) can be implemented. So, a true three dimensional set-up of irradiation loops can be constructed and the dislocations can be allowed to spread over the whole grain, by use of cross-slip. The snapshots for the typical evolution of a FR source in the presence of a 3D spread of irradiation loops is shown in the figure 4.12.

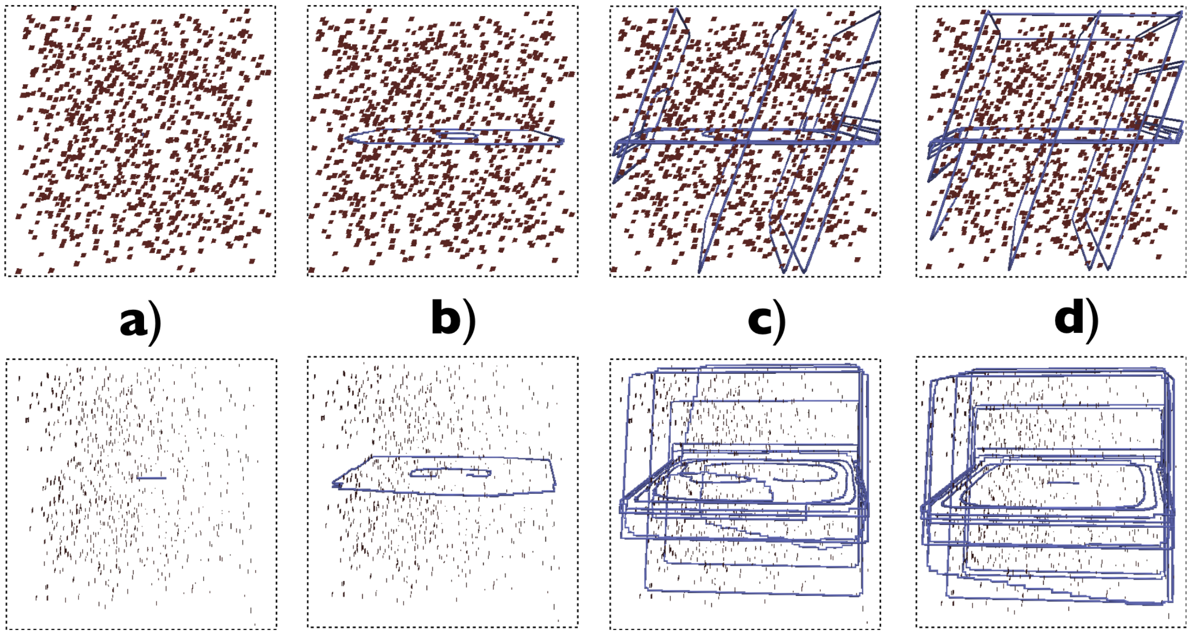


**Figure 4.12** – *Evolution of a FR source in presence of the irradiation loops implemented as shearable facets. The corresponding figures on the top and bottom refer to the same configurations, except that the top figures are viewed along the line direction (Burgers vector of the screw) whereas the figures on the bottom images are viewed along the glide direction of the screw dislocation. The strain spreading in the grain, due to the multiple cross-slips is clearly visible.*

The simulation volume considered in figure 4.12 is of $1\mu^3$, and the initial dislocation length is $100nm$. The simulation volume is populated with $1000$ randomly placed planar obstacles of 10 nm size and whose normal is along the dislocation line direction. Note the cross-slip phenomenon is operational at image c.

**Algorithm 4.2** Generating irradiation loops as facets of different orientations.

Obtain the relevant parameters

1. The simulation box dimensions and orientations: Let they be $l_1$, $l_2$and $l_3$ and $\mathbf{l}_1$, $\mathbf{l}_2$ and $\mathbf{l}_3$ respectively. Note that $\|l_i\| = 1 \forall i = 1..3$
2. The corner of simulation volume, let it be $\mathbf{C}$.
3. The irradiation-loop size and Burgers vector : Let they be $r$ and $\mathbf{b}$ respectively.
4. The number of irradiation loops, $N$.

Now, do the following:
For each $loop = 1..N$ **do**

1. pickup three random numbers $r_1$, $r_2$,$r_3$ $(0 < r_i < 1, i = 1..3)$.
2. Set the center of the loop at $c_{loop} = \sum_{i=1}^{3} r_i l_i \mathbf{l}_i$.
3. The normal to this loop is $\mathbf{b}$, one of the possible Burgers vectors of fcc (See section 5.1). Obtain the two edge directions corresponding to this screw direction, $\mathbf{b}$. Let they be $\mathbf{e_1}$ and $\mathbf{e_2}$. Note that $\mathbf{b}.\mathbf{e}_i = 0, i = 1, 2.$ and $\|e_i\| = 1$
4. Construct the loop with $c_{loop}$ as the center and $\mathbf{e_1}$ and $\mathbf{e_2}$as it sides, of length $r$:

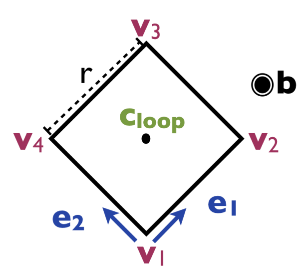


$$\mathbf{v}_1 = c_{loop} - \frac{r}{2}(\mathbf{e}_1 + \mathbf{e}_2)$$
$$\mathbf{v}_2 = c_{loop} + \frac{r}{2}(\mathbf{e}_1 - \mathbf{e}_2)$$
$$\mathbf{v}_3 = c_{loop} + \frac{r}{2}(\mathbf{e}_1 + \mathbf{e}_2)$$
$$\mathbf{v}_4 = c_{loop} - \frac{r}{2}(\mathbf{e}_1 - \mathbf{e}_2)$$

5. Translate these vertices by $\mathbf{C}$, the corner of the simulation volume:
$$\mathbf{v}_i = \mathbf{v}_i + \mathbf{C}, i = 1..3$$
and write these coordinates into a file.
6. Ensure that this facet does not physically overlap with the existing facets. If there is an overlap, discard the entry and repeat from step 1.

**done.**

**Validation of facet description approximation** The same density of loop-facets is introduced in a simulation cell having the same dimensions and boundary conditions as for Type-I simulations. A dislocation source is placed along a border of the cell, using dislocation emission $\tau_{nucl} = 90MPa$ as before, while taking the same applied loading rate ($10^4 s^{-1}$), lattice parameter ($10b$) and time step ($5 \times 10^{-12} s^{-1}$) to be used in Type-II calculations. For the sake of comparison, **dislocation cross-slip is switched off during this first simulation**. Simulation results using facet-loops are shown in figure 4.13b through figure 4.13c. The resulting dislocation structure shown in 4.13b is planar and coarser than the more realistic figure 4.6d case. Since this simplified description takes much fewer dislocation segments, Type-II simulations allow generating larger plastic strain amount and consequently, multiple clear bands in the simulation volume.

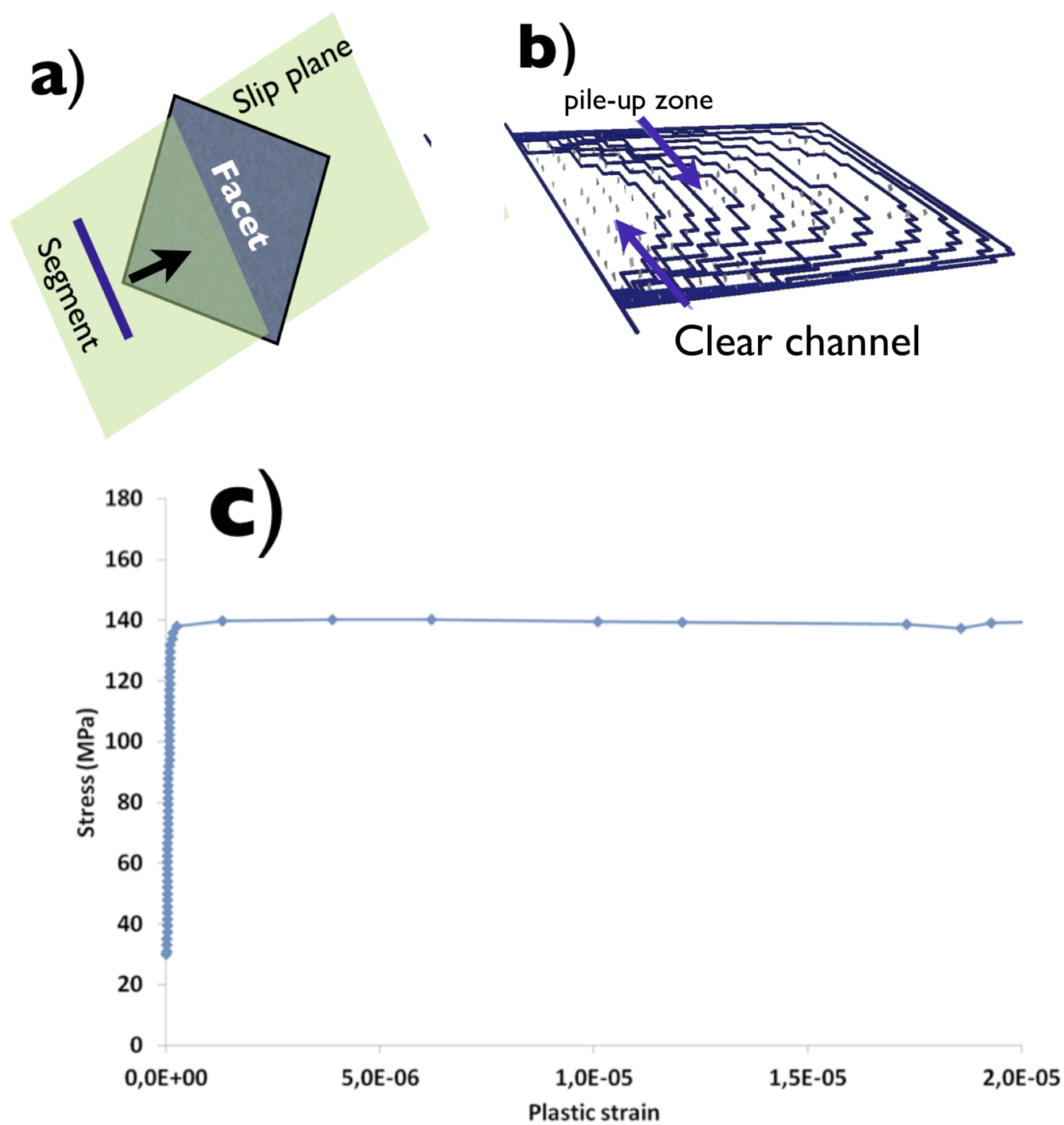


**Figure 4.13** – *Type-II simulation setup. a) Facet-loops are soft obstacles, conditionally traversed depending on the local stress magnitude and the mobile dislocation type, edge or screw. b) Shear band simulation in the presence of facet-loops. The displayed loops are those traversed by mobile screw dislocations (cleared loops) c) Stress-strain plot of simulation shown in b). Pile-up back-stress and associated work hardening are pronounced (unlike in figure 4.8a).*

### 4.3.2 Plastic deformation in presence of loops: multiple shear bands

Unlike the prismatic loops introduced in Type-I simulations, loop-facets introduced here do not produce long range stress. Therefore, there is no stress divergence with $r \rightarrow 0$

for mobile dislocations approaching individual facets. The corresponding, non-diverging stress landscape allows use of a classical thermally activated cross-slip model [Depres 2004, Shin *et al.* 2003], where cross slip probability P over each time step is:

$$P = \beta \frac{l}{L_0} \frac{\Delta t}{t_0} exp(\frac{\tau_d - \tau_{III}}{k_b T} V) \tag{4.5}$$

where $\beta$ is a normalization coefficient ensuring that $0 < P < 1$, $l$ is the length of the considered screw segment, $L_0 = 1\mu m$, $\Delta t$ is the discrete time step, $t_0 = 1s$, $V$ the activation volume, $\tau_d$ the effective resolved shear stress in the cross slip system and $\tau_{III}$ a threshold stress for cross-slip activation, that scales with the stacking fault energy of the simulated fcc crystal through the partial dislocation splitting distance [Robertson *et al.* 2001]. In practice, a random number $N$ between $0$ and $1$ is first generated. Dislocation cross slip occurs only if $N < P$.

Type-II simulations have reduced computational intensity, as compared to Type-I simulations. This is achieved through the use of a much larger discrete lattice parameter (10b) and time step ($\Delta t = 5 \times 10^{-11} s$) than those used in Section 4.2. That coarse gaining procedure allows for generating plastic strain levels corresponding to multiple shear bands, within a reasonable calculation time frame (typically $10^4$ calculation steps). The simulated space geometry is cubic, with grain boundaries as strong, impassable obstacles to dislocation motion (figure 4.14). Tested grain diameters are: $1.0,\ 1.3\ \ and\ \ 5.0\mu m$. Unlike for Type-I simulations, the initial dislocation microstructures consist of a single Frank-Read source; introduced as a 140 nm long pinned dislocation segment in the ½[10-1](111) slip system. The previous dislocation nucleation criterion $t_{nuc}$ is no more used.

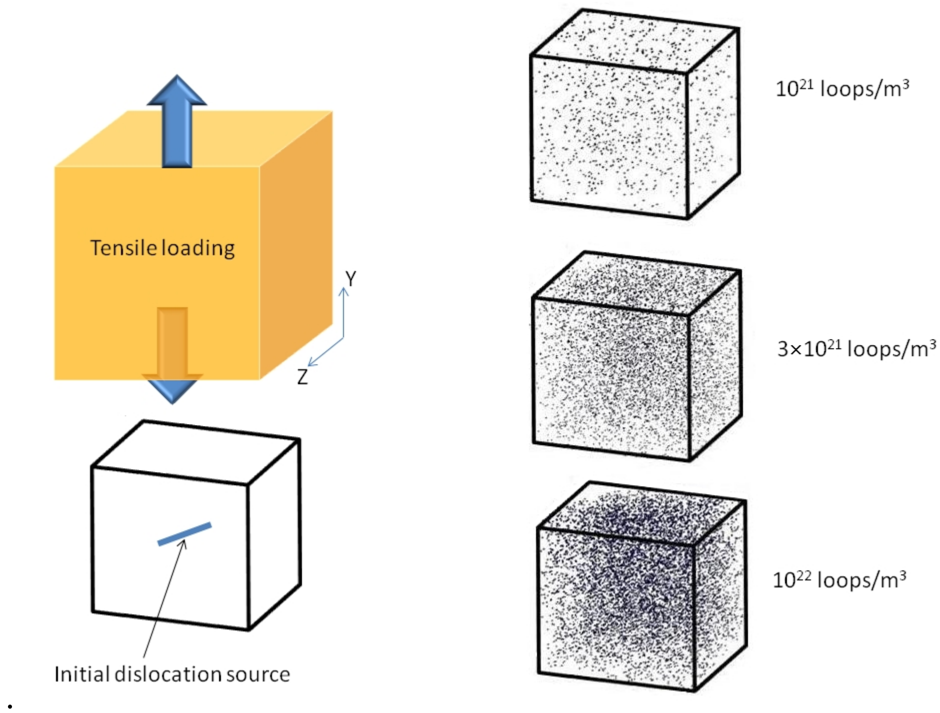


**Figure 4.14** – *Type-II simulations: grain and tensile loading configuration, initial dislocation structure and loop densities.*

The simulated space is submitted to a homogeneous applied stress. All calculations are performed in isothermal conditions, at 300K. A constant plastic strain rate loading condition ($d\epsilon_{yz}/dt = 10^4 s^{-1}$) is achieved using a feedback control loop, based on plastic strain generated during a fixed time interval. Facet-loops are positioned at random locations with the simulated grains. The loop diameter is constant and set to $10nm$. Tested loop densities[2] are $10^{21}$, $3 \times 10^{21}$ and $10^{22}$ $loops/m^3$. When applied loading is switched on, stress augments until the initial, pinned dislocation source starts operating, emitting one shear loop after another, through the Frank-Read mechanism. Mobile dislocations eventually reach the grain boundary, where pile-ups progressively develop. New dislocation sources then form through cross-slip mechanism.

The uni-axial tensile loading is applied along the $\langle 001 \rangle$ direction. All the simulations are analyzed after realization of the same plastic strain amount ($\epsilon_p = 1.4 \times 10^{-2}$). The analyzed

[2] In austenitic steel irradiated at 300-350°C, selected loops densities are achieved for approximately 0.25-0.4 dpa.

features include: dislocation microstructures, cross-slip frequency and grain boundary plastic displacements. The latter information is presented in the form of plastic strain maps. This data is generated by a post treatment method using analytical elastic displacement solutions for finite dislocation segments [Depres *et al.* 2006]. Plastic strain maps in figure 4.15b and figure 4.15d show step-like displacements which contribute to grain boundary damage initiation or development, a) and c) of figure 4.15 show the dislocation spreading in the grain (in figure 4.15c, the irradiation loops are hidden for clarity).

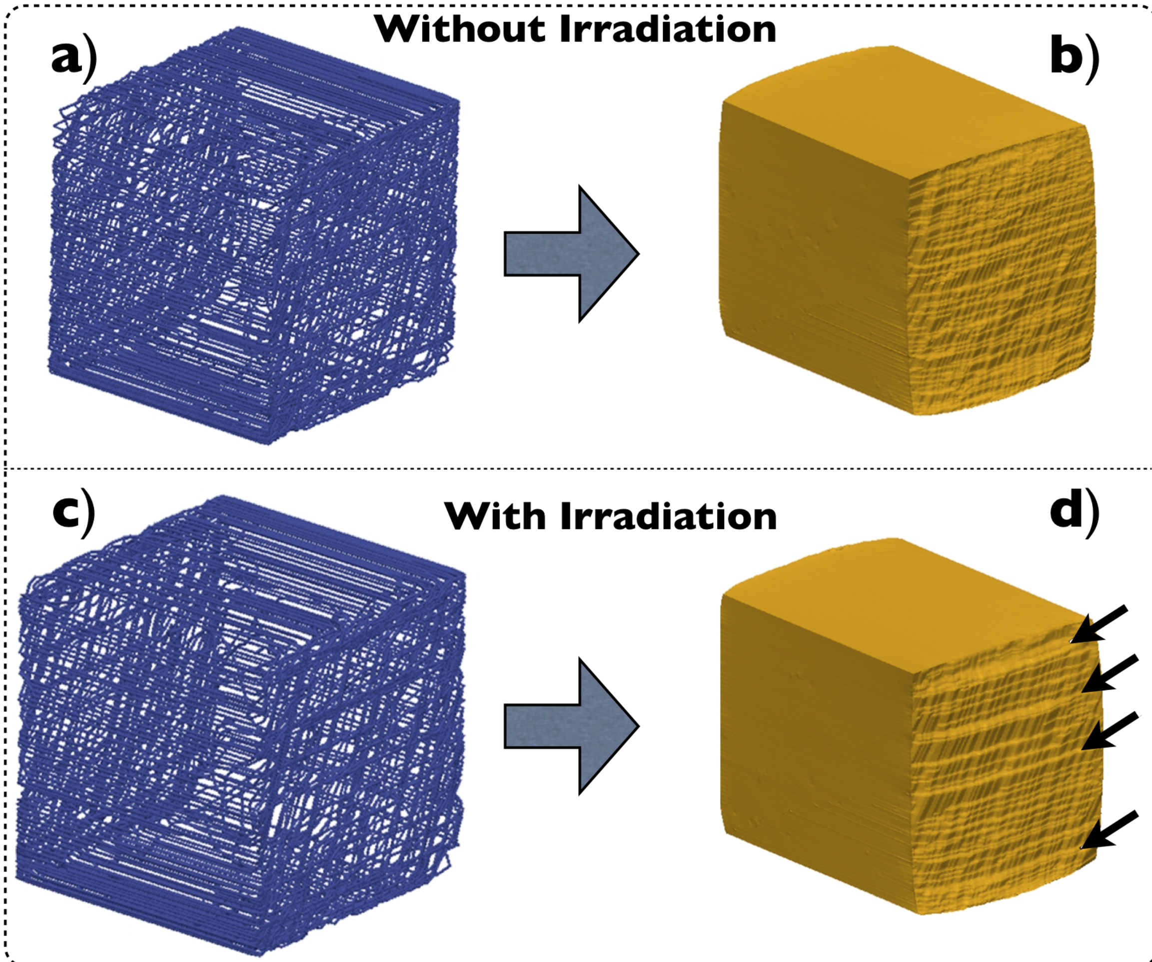


**Figure 4.15** – *Type-II simulation results: dislocation structures and corresponding plastic strain maps of* $1\mu m^3$ *grains stained in uni-axial tension. a) Dislocation structure of the un-irradiated, grain deformed up to* $\epsilon_P = 1.4 \times 10^{-2}$*. b) Plastic strain map of the same un-irradiated deformed grain as in frame-a. c) Dislocation structure in the presence of* $10^{22} loops/m^3$ *. The loops are not shown for clarity. d) Plastic strain map of the irradiated grain, i.e. in presence of* $10^{22} loops/m^3$*. The arrow markers indicate the positions of pronounced slip steps associated with clear bands developing within the grain.*

The tested loop densities correspond to low irradiation doses [Bruemmer *et al.* 1999] and consequently, the irradiation-induced hardening obtained herein is moderate (100 MPa maximum). The strong work-hardening behavior observed in figure 4.16a is a direct consequence of using hard grain (or simulation volume) boundaries, where dislocation pile-ups progressively develop a strong back-stress. In absence of facet-loops, cross-slipping out of and back to parallel primary plane takes place at arbitrary distances from the initial slip band. Since the applied cross-slip stress is higher than $\tau_{III}$ practically everywhere in the grain, the position of each cross-slip event only depends on the stochastic procedure defined by equation 4.5. In the absence of facet-loops, the number of cross-slip events is maximum (see figure 4.16b), generating many new dislocation sources and homogeneous plastic strain (see figure 4.15a). Consequently, the plastic steps induced in the grain boundaries are numerous and small in amplitude (see figure 4.15b). In the presence of facet-loops however, cross-slipping out of and back to the primary plane is partially inhibited due to the numerous interactions with the facet-loops (see figure 4.16b). For this reason, plastic strain localizes into shear bands, yielding higher and more distant surface slip steps in the grain boundaries (see figure 4.15d).

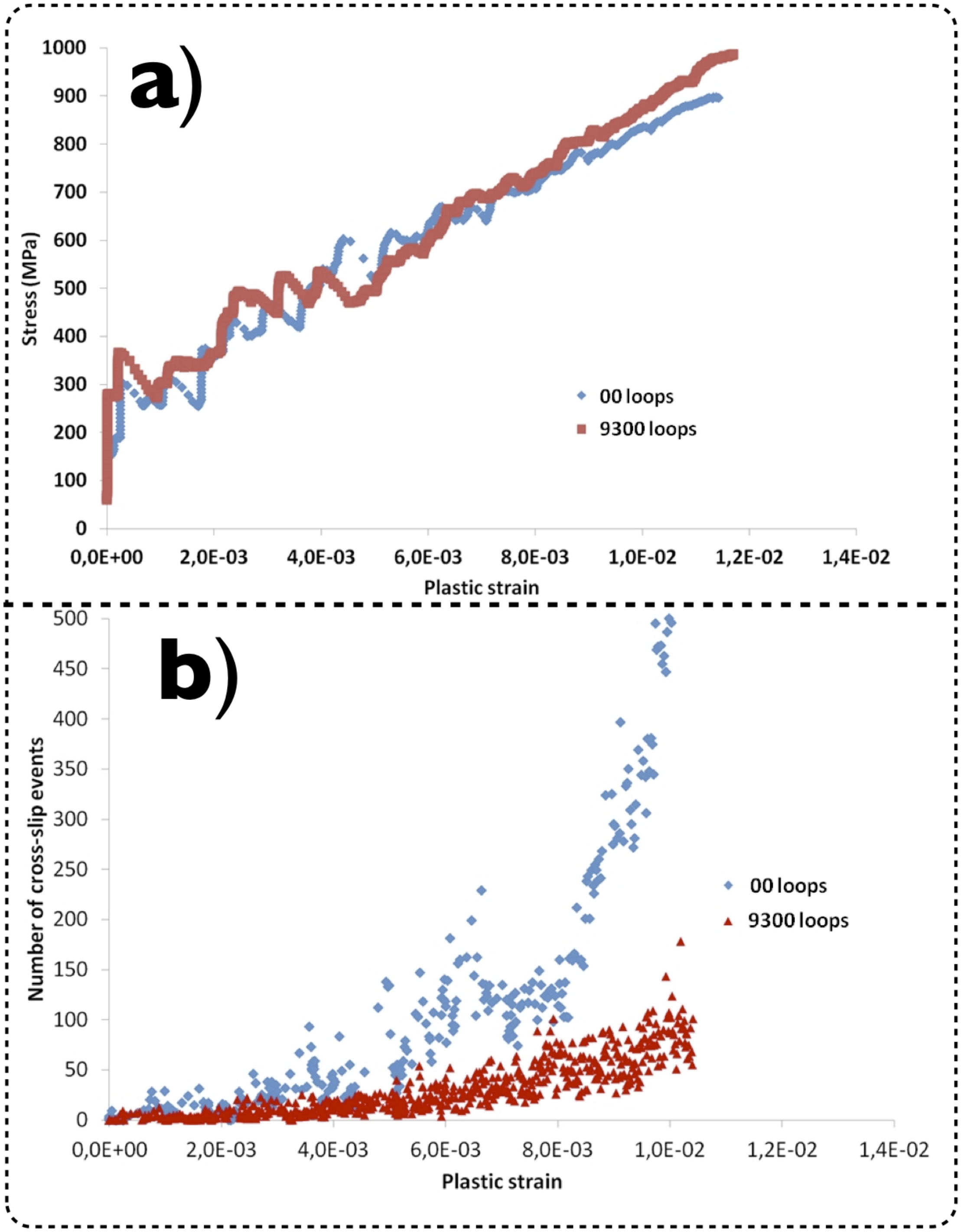


**Figure 4.16** – *Type-II simulation results: plastic strain induced evolutions with and without facet-loops. a) Stress-strain behavior. b) Cross-slip frequency with plastic strain development. Interaction with the loop-obstacles partially inhibit cross-slipping out of and back to primary slip planes.*

The strong work hardening in fcc, shown for example in figure 4.16a, is to be contrasted with bcc where there was no appreciable work hardening, as shown in for example figure 3.7 on page 77.

### 4.3.3 Comparison of Type-I and Type-II simulations

The table consolidates the differences between the two different simulation settings, Type-I and Type-II, used in this work.

**Table 4.3** – *Difference between Type-I and Type-II simulation schemes.*

| Feature | Type-I | Type-II |
|---|---|---|
| **Defect loops** | Prismatic loops | Planar obstacles |
| **Length Scale** | $0.08b$ | $10b$ |
| **Timestep** | $5 \times 10^{-14}$sec | $5 \times 10^{-12}$sec |
| **Cross-slip** | No | Yes |
| **Source Type** | Lathe source | Frank-Read Source |
| **Loop absorption by screws** | Happens by energy criteria. | Implemented through "Loop removal after piercing". |
| **Elevator effect** | Happens naturally | No |
| **Clear channel width** | Yes | No |
| **Multiple clear channels** | No | Yes |

### 4.3.4 Plastic deformation in presence of loops: plastic strain spreading analysis

The formation of new clear bands is related to the ability of mobile dislocations to bypass the facet-loops. This depends on the possibility to change the glide plane multiple times, through cross-slip mechanism. In single slip loading conditions, the effective (i.e. total: applied + internal) stress resolved in the primary slip system is:

$$\tau_{prim}(x, y) = \tau_{app} - \tau_{int,prim} \tag{4.6}$$

where $\tau_{int,prim}$ is the internal stress in the primary slip plane. Similarly, the effective stress resolved in the cross-slip system is

$$\tau_{cs}(x,y) = \frac{1}{3}\tau_{app} \pm \tau_{int,cs} \tag{4.7}$$

where $\tau_{int,cs}$ is the internal stress in the cross-slip plane.

Forming a new clear band requires double cross-slip activation: i.e. a first cross-slip event sending a dislocation out of the primary slip system followed by a second one, driving the dislocation back to the primary slip system. In irradiated crystals, the presence of facet-loops implies multiple elementary double-cross slip activations: at least one for bypassing each obstacle. Cross-slipping back to the primary slip system is most favorable where $\tau_{prim}/\tau_{cs} = \pm 1$. This condition is satisfied at a definite minimal gliding distance from the initial primary slip plane, as shown in figure 4.17a.

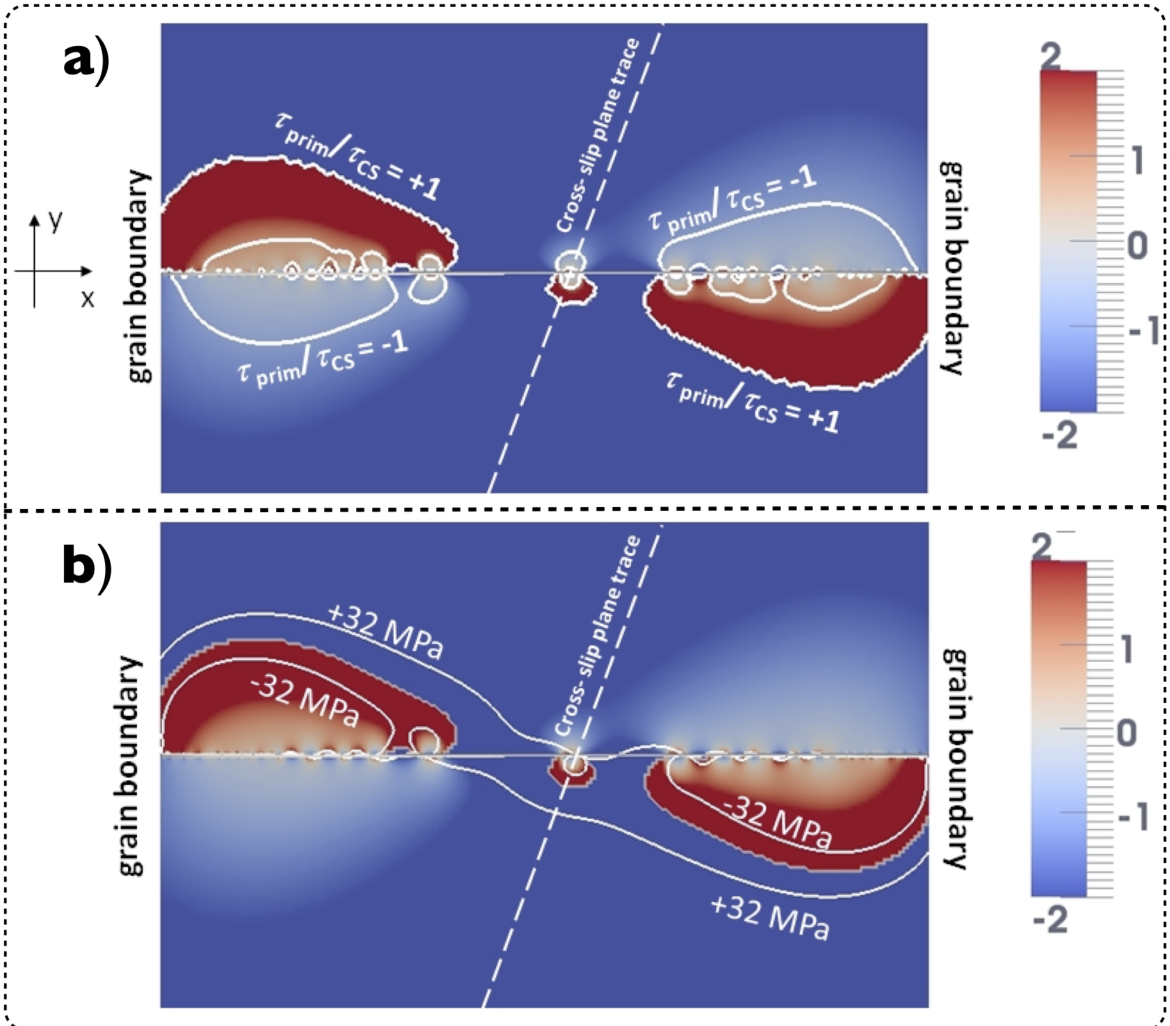


**Figure 4.17** – *The stress ratio R is defined as $\tau_{prim}/\tau_{cs}$. The values of $\tau_{prim}$ and $\tau_{cs}$ used to calculate $R$ are displayed in Fig.4a and 4b, respectively. (a) Iso-values $R = \pm 1$ are marked with a superimposed contour; highlighting a sub-region where a screw dislocation can easily bypass the facet-loops, through multiple cross-slipping. b) The iso- contour $\tau_{cs} = 32MPa$ (i.e. $= \tau_{III}$) is superimposed to the R mapping. The position of iso-contour $\tau_{cs} = 32MPa$ nearly coincides with the position of iso-contour $R = \pm 1$*

In figure 4.17b, it is shown that $\tau_{cs}(x, y) \approx \tau_{III}$ along the iso-value $\tau_{prim}/\tau_{cs} = 1$. Inserting equation (4.4) into equation (4.7) and solving the resulting expression for $\tau_{cs}(x, y) = \tau_{III}$ yields:

$$y \geq \left| \left( \frac{l}{k(x)} \right) ln \left( \frac{\tau_{app}}{\tau_{III} + \frac{1}{3}\tau_{app}} \right) \right| \tag{4.8}$$

Equation (4.8) can therefore be used to predict the minimum distance "$y$" between two adjacent clear bands, assuming that secondary channel preferentially initiate at pile-up extremities. It should be noted that the quantity $t_{app}$ is related to the irradiation conditions through the loop-obstacle strength and the loop density. In other words, $t_{app}$ used in equation (4.8) accounts for an irradiation-induced hardening contribution $\Delta\tau_{irr}$, so that $\tau_{app} \approx (\tau_{YS} + \Delta\tau_{irr}) - \tau_{friction}$, where $\tau_{YS}$ is the material yield stress before irradiation and $\tau_{friction}$ the lattice friction or Peierls stress. The DD simulation results presented in Table-2 show that varying the parameters $\tau_{III}$, $\tau_{app}$ (through the loop density) and pile-up length $l$ (through the grain size) yield an average inter-band spacing in good agreement with equation (4.8). It should be noted that equation (4.8) applies to pure shear loading conditions. In more general tensile loading conditions, the tensile stress level times the Schmid factor acting in the primary slip system must be used instead of $\tau_{app}$ and the tensile stress level times the Schmid factor acting in the cross-slip system, instead of $\frac{1}{3}\tau_{app}$.

**Table 4.4** – *Comparison between Type-2 simulations and model predictions equation (4.8). The values of $\tau_{app}$ inserted in equation (4.8) are taken at the conventional yield point $\epsilon_p = 2 \times 10^{-3}$ of the tensile stress-strain data (as in figure 4.16a, 9300 loops case). The last row refers to the band spacing obtained from the DD simulations, and they are estimated from figure 4.15d for case 1 and 4.18 for Case 2, Case 3 and Case 4.*

| | **Case 1** | **Case 2** | **Case 3** | **Case 4** |
|---|---|---|---|---|
| **Facet-loop density ($m^{-3}$)** | $10^{22}$ | $3 \times 10^{21}$ | $3 \times 10^{21}$ | $3 \times 10^{21}$ |
| $\tau_{app}$ **at yield point** | 420 | 350 | 350 | 350 |
| $\tau_{III}$ | 32 | 32 | 32 | 11 |
| **Pile-Up length (nm)** | 1000 | 1000 | 1300 | 1300 |
| **Min band spacing from equation(4.8)nm** | 180 | 172 | 225 | 265 |
| **Band spacing from DD simulation** | 170-290 | 150-270 | 200-320 | 250-500 |

For instance, it can be seen that the inter-band spacing:

- Augments with the grain size and facet-loop induced hardening,
- Decreases with $\tau_{III}$ (see figure 4.18 and the corresponding caption).

These results are further discussed in the next section.

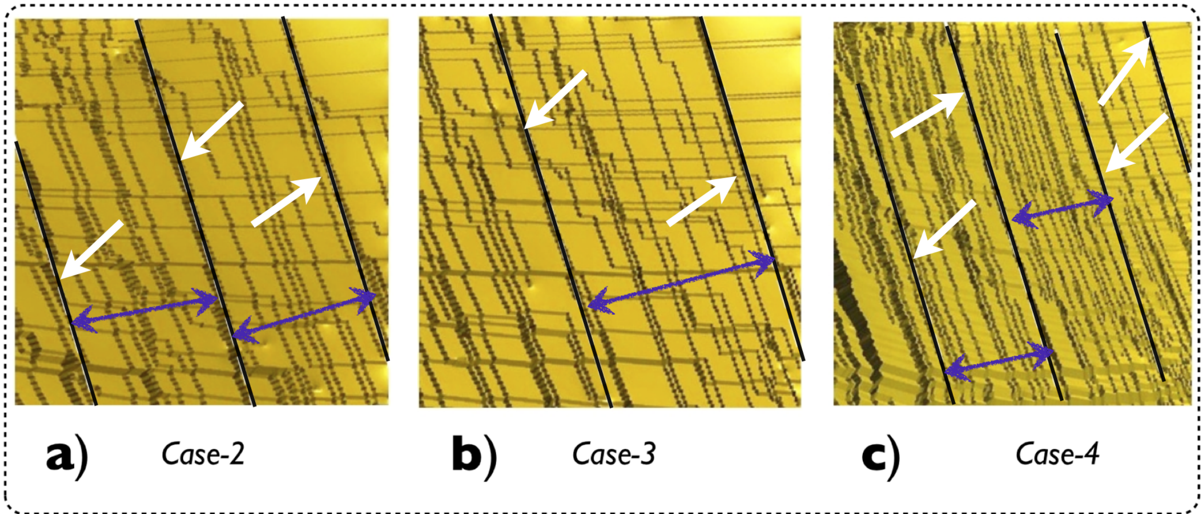


**Figure 4.18** – *Type-II simulation results: effect of material and irradiation condition parameters on clear band distribution in a model fcc metal strained to $\epsilon_p = 1.4 \times 10^{-2}$. The dark lines (pointed at by the white arrows) indicates the steps on the surface make by dislocations coming out of the clear channels. The blue arrows indicate the clear-channel separation. The parameters associated with cases - are listed in Table 4.4. The tested grain sizes ($\leq 1.3\mu m$) and loop densities ($\leq 10^{22} m^{-3}$) are taken as per table 4.4. a) Case 2. b) Case 3 c) Case 4 The clear bands are highlighted by dashed lines superimposed to the plastic strain maps.*

## 4.4 Discussion

The (minimum) shear band inter-spacing according to Eq.(4.8) depends on a few parameters only. Influence of parameters such as $\tau_{III}$ and $\tau_{app}$ can easily be evaluated by comparison with experimental results. For instance, increasing $\tau_{app}$ (with a fixed $\tau_{III}$) means a more pronounced irradiation-induced hardening and therefore stronger strain localization, as shown in Table 4.4 and experimentally observed in [Byun *et al.* 2006, Byun 2003, Pokor *et al.* 2004]. Similarly, lowering the $\tau_{III}$ stress leads to larger shear band spacing, as shown in figure 4.18.

Equation (4.8) predictions are also extrapolated to grain sizes and defect cluster populations representative of various irradiated fcc poly-crystals, for comparison. In [G. Was 2006] for example[3], the applied stress $\tau_{app} = 200MPa$ (at the yield point) and the partial dislocation splitting distance $d_0 = 16nm$. The critical cross-slip stress corresponding to $d_0$ is $t_{III} = 40MPa$, as calculated the using method described in reference [Robertson *et al.* 2001]. Neglecting the Peierls stress and taking a pile-up length $l = 50\mu m$ ($l$ = grain diameter) yields a minimum channel spacing of $y \approx 6\mu m$, in agreement with reference [G. Was 2006]. Good consistency is also obtained by comparison with the experimental data from references [C. Robertson 2012, G. Was 2006, K. Farrell & Hashimoto 2003]. This demonstrates that the analysis proposed in this paper is quite general and applies to grain sizes $1 - 100\mu m$ and irradiation dose ranges $0.5 - 10dpa$, i.e. much larger than the values directly simulated herein (see Section 3.2). Interestingly, the same conclusion also holds for various irradiated fcc materials, including Cu and Ni [Edwards & Singh 2004, Yao 2005]. Eq. (4.8) also shows that the stress distribution generated by a clear band depends very little on jogs or debris (there are no jogs or debris in Type-II simulations). This depends more on the dislocation curvature due to line tension (through the $k(x)$ term), induced by the finite sized grain.

The observed (and simulated) inter-band spacings exhibit a significant variability, nonetheless. For example, the dislocation structure of a particular clear band is not symmetric across the whole deformed grain. This effect is highlighted by displaying side by side the sheared loops, the dislocation microstructure and the corresponding strain map, in figure 4.19. A clear top/down asymmetry is visible thereby: the bottom grain portion includes well-defined channels and much fewer secondary channels. This means the effective pile-up length can significantly differ from the pile-up length $l$ used in equation (4.8). One possible origin of this effect is the pile-up stress field dependence on position $x$, as found in analytical expression (4.3) and depicted in figure 4.8b. This means that secondary channel initiation is more frequent near the grain boundaries.

[3]The data is for alloy H irradiated to 5.5 dpa at $360^oC$, yielding a loop density of $10^{23}m^{-3}$.

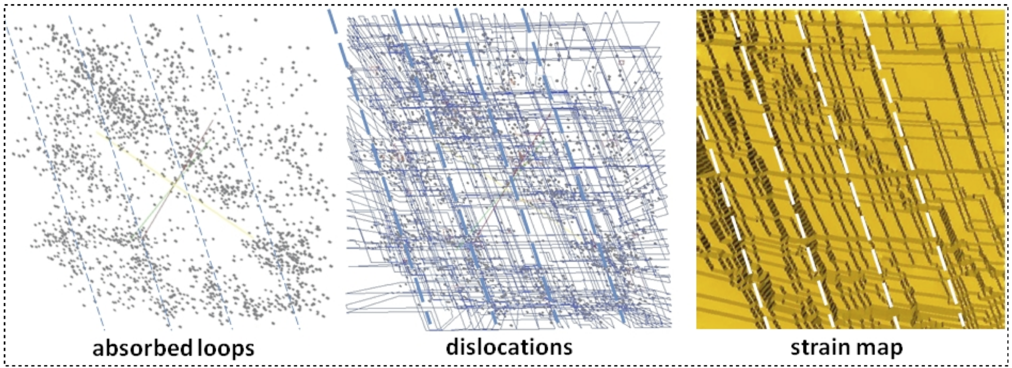


**Figure 4.19** – *Type-II DD simulation results: correspondence between the pronounced surface steps and clear bands developing within the irradiated grain. The superimposed dashed lines indicate the clear band (or channel) positions. Leftmost frame: interacting (or absorbed) facet-loops and corresponding dislocation structures, including primary and secondary channels. Central frame: facet-loops interacting with and possibly absorbed by the mobile screw dislocations. Rightmost frame: plastic strain map of a* $1\mu m^3$ *deformed grain, up to* $\epsilon_p = 1.4 \times 10^{-2}$.

## 4.5 Conclusions

Plastic strain development in post-irradiated fcc grains is investigated by means of three-dimensional dislocation dynamics simulations. In this chapter, 2 different types of simulations were carried out based on their respective, complementary capacities.

In Type-I simulations, loop clusters are treated explicitly and introduced in the simulation cells in the form prismatic dislocation loops. This approach allows for an accurate description of dislocation-loop interaction and internal stress evolutions during the formation of clear bands. It is shown that the stress field developing in the vicinity of a clear band can be described through a simple analytical expression (4.8) accounting for the applied stress magnitude, the grain size and the critical cross-slip stress. This simple description proved adequate even in absence of more complex dislocation features, including: dislocation curvature, super-jogs, and loop debris.

In the present simulation framework, stress magnitude diverges at short distance to the dislocation lines (see equation (4.3) for instance). This is a major difficulty for implementing dislocation cross-slip in Type-I simulations, where the diverging stress field leads to unrealistically large cross-slip stress (and corresponding cross-slip probability) with respect to experimental observations [C. Robertson 2012]. Besides, the complex stress state in the vicinity of a dislocation segment can change the partial dislocation splitting $d_0$ and in turn affect the cross-slip probability.

In Type-II simulations, irradiation-induced loops are treated as planar obstacles made of immobile internal interfaces called facet-loops. These calculations include thermally activated cross-slip mechanism, allowing for plastic strain spreading into the entire grain, in the form of multiple clear bands.

It is shown that the cross-slip stress in the primary slip plane controls the germination of secondary channels, progressively developing in the grain volume, with increasing plastic strain. The stress field acting on the cross-slip system is found to control the spacing between primary channels in presence of facet-loops, through the development of secondary channels. Cross-slip is partially inhibited due to interactions of mobile dislocations with the facet-loops. This effect can explain the experimentally observed augmentation of the surface step spacing, after post-irradiation straining. Various Type-II simulations were carried out, using different simulation parameters (grain, size, loop density and critical cross-slip stress). These calculations show that the inter-band spacing increases with the grain size, while it decreases with the $\tau_{app}/\tau_{III}$ ratio. The results are in good agreement with equation (4.8). The proposed model is validated by comparison with experimental data obtained in various irradiated fcc alloys, for grain sizes $(1 - 100\mu m)$ and irradiation doses (0.5-10 dpa).

# Chapter 5

# Role of Glide and Escaig stresses on dynamics of extended Frank-Read sources

---

*This chapter discusses the results obtained in understanding the role of glide and non-glide stresses on the equilibrium dissociation width of split dislocations in fcc. Nodal based DD code and the Non-singular stress formulation were employed. The dynamics of split FR sources is compared and contrasted to that of perfect FR sources.*

---

## 5.1 Introduction

The dislocation sources used in Chapters 3 and 4 were perfect: that is, their Burgers vectors were shortest lattice vectors of the crystal structure. But, in case of fcc materials, a more realistic description of dislocations is by representing each dislocation in terms of a pair of split dislocations whose Burgers vectors are smaller than the shortest lattice vector and thus enclosing a stacking fault. Now, the resolved shear stresses acting on the two dissociated partials of such a split dislocation is generally different when the crystal is subjected to uniaxial stress, and this will affect the width of the enclosed stacking fault region [Copley & Kear 1968]. In case of austenitic stainless steels, owing to their low stacking fault energy, the effect of external stress on the dissociation width is found to be significant [Kestenbach 1977], being the same order of magnitude as that due to stacking fault energy [Goodchild *et al.* 1970]. Recently, there has been an increased interest in understanding the role of stacking fault energies in the deformation of nano-crystalline materials [Frøseth *et al.* 2004, Van Swygenhoven *et al.* 2004], where the effect of non-glide stresses on the equilibrium dissociation width is studied. Byun [Byun 2003] has derived an expression for separation distance as a function of applied stress and the Burgers vector of the dislocation, within the formalism of linear elastic theory. He has found that, in the case of screw dislocations, the separation between the partials increases with the applied stress and diverges beyond a certain critical stress. This divergence of the dissociation width was the reason attributed to the formation of large faulted regions seen in austenitic steels [Müllner 1997, Meyers *et al.* 1999, Christian & Mahajan 1995, Brooks *et al.* 1979]. When the external stresses were of the range 400-600MPa small $(< 1\mu m)$ isolated regions of stacking faults are found, whereas at stresses greater than 600MPa, large $(> 1\mu m)$ faulted regions were predominant [Byun *et al.* 2003]. In [Baudouin *et al.* 2013], it was shown that the divergence of dislocation dissociation width with the applied external stress is true of dislocations of all line characters and not just for screws as claimed by Byun. In this chapter, the interest is to study the change of the equilibrium stacking fault area enclosed by such a split FR source, under the action of different stress components. Since cross-slip in fcc depends critically on the separation of the partials (see section 6.2.1.2 on page 202), this study will be important in understanding role of different glide and non-glide stresses on the cross-slip of screw dislocations in fcc.

## 5.2 Background

### 5.2.1 Dislocations in fcc

In fcc, the four different sets of $\{111\}$ planes lie parallel to the four faces of the regular tetrahedron, and whose edges are parallel to the $\langle 110\rangle$ slip directions, as shown in the figure 5.1. The corners of this tetrahedron are denoted by ABCD and the corresponding centers of the opposite sites are indicated by $\alpha, \beta, \gamma, \delta$ respectively. In this description, the Burgers vectors are represented, both in magnitude and direction, by the edges of the tetrahedron, AB, BC etc.

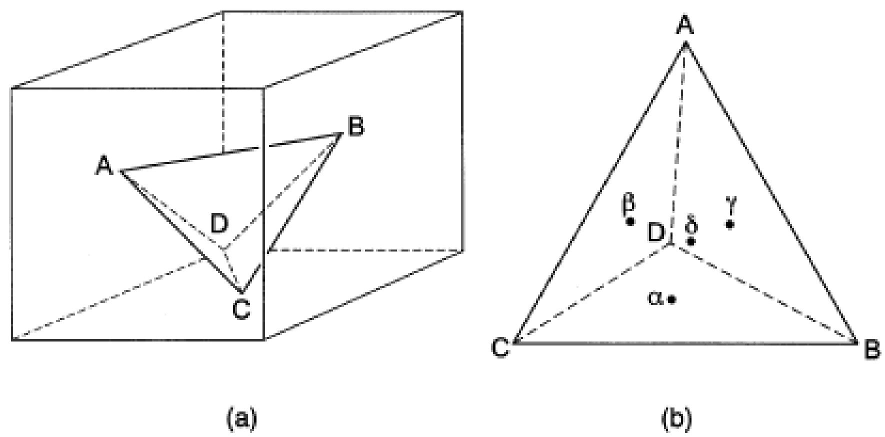


**Figure 5.1** – *Tetrahedron formed by the four nearest neighbors of a face-centered cubic structure. Figure taken from reference [Hull & Bacon 2011].*

The opened-up Thompson's tetrahedron in fcc is given in figure 5.2. From this figure it is clear that there are six screw directions (the edges of Thompson tetrahedron), and corresponding to each screw direction there are two glide planes ( the faces that share the edge). In this way, there are a total of six possible slip systems in fcc. Another way to arrive at this number is to see that there are four faces on the tetrahedron and each face has three possible edge directions, making a total of twelve slip system, as enumerated in table 5.1.

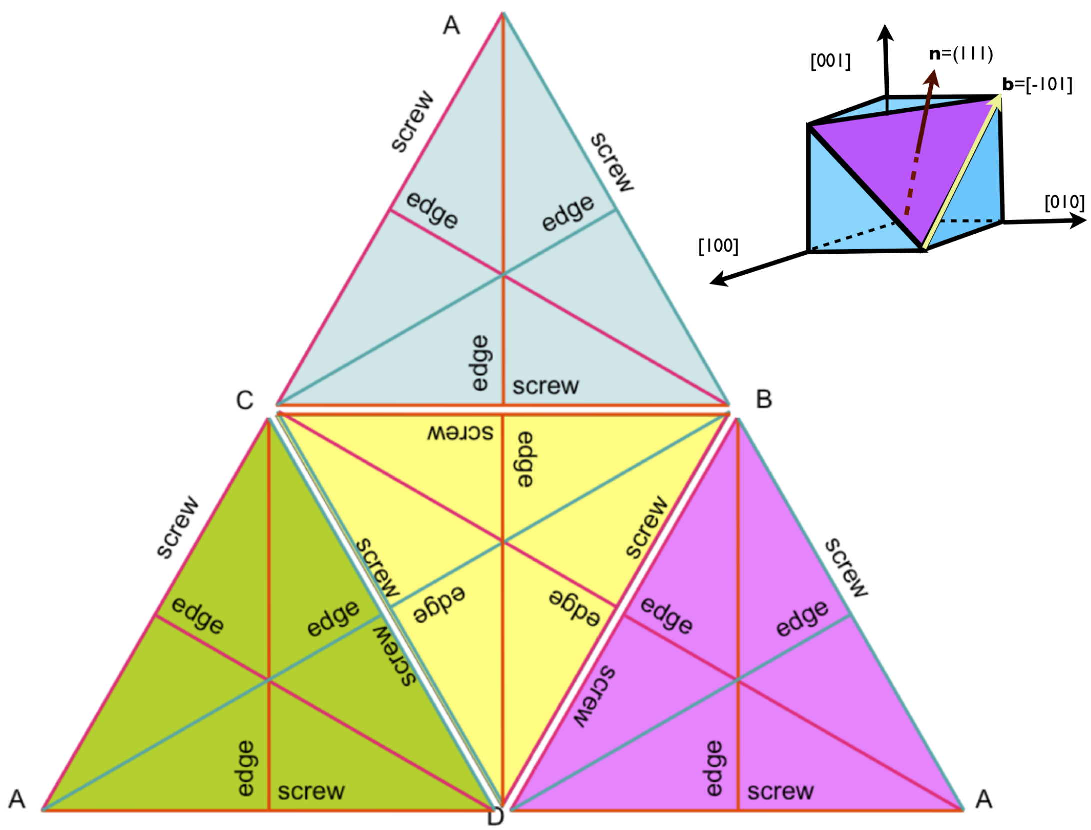


**Figure 5.2** – *Thompson's tetrahedron in fcc.*

**Table 5.1** – *Slip systems in fcc. There are six Burgers vectors (screw directions) making twelve slip systems*

| Slip System Number | Screw | Edge | Normal | Schmidt & Boas Index |
|---|---|---|---|---|
| 1 | $[\bar{1}01]$ | $[\bar{1}2\bar{1}]$ | $(111)$ | B4 |
| 2 | | $[121]$ | $(\bar{1}1\bar{1})$ | D4 |
| 3 | $[011]$ | $[\bar{2}\bar{1}1]$ | $(\bar{1}1\bar{1})$ | D1 |
| 4 | | $[2\bar{1}1]$ | $(\bar{1}\bar{1}1)$ | C1 |
| 5 | $[1\bar{1}0]$ | $[11\bar{2}]$ | $(111)$ | B5 |
| 6 | | $[\bar{1}\bar{1}\bar{2}]$ | $(\bar{1}\bar{1}1)$ | C5 |
| 7 | $[\bar{1}\bar{1}0]$ | $[1\bar{1}\bar{2}]$ | $(\bar{1}1\bar{1})$ | D6 |
| 8 | | $[\bar{1}1\bar{2}]$ | $(1\bar{1}\bar{1})$ | A6 |
| 9 | $[0\bar{1}1]$ | $[2\bar{1}\bar{1}]$ | $(1\bar{1}\bar{1})$ | A2 |
| 10 | | $[211]$ | $(111)$ | B2 |
| 11 | $[101]$ | $[1\bar{2}1]$ | $(\bar{1}\bar{1}1)$ | C3 |
| 12 | | $[12\bar{1}$ | $(1\bar{1}\bar{1})$ | A3 |

The splitting of one perfect dislocations into two partial dislocations can be crudely rationalized within the elementary line energy picture. According to the Frank criteria, the energy per unit length of a dislocation is proportional to the square of its Burgers vector. Hence, it is profitable for a dislocation having a perfect Burgers vector to split into two dislocations whose Burgers vectors are of a smaller magnitude. This energy advantage, of course, comes at a price. The penalty involved in the creation of this split is the formation of the stacking fault in between the two dislocation lines. The energy involved in formation of this stacking fault is given in terms of the Stacking Fault Energy (SFE) which is defined as the energy required for creating a stacking fault of unit area. In materials with low SFE, the partials can move sufficiently away from each other, thereby decreasing the elastic repulsion between the partials, with just a small energy increase due to the increase in the faulted region. The equilibrium separation between the partials is at the distance where there is a balance between the repulsive elastic energy and the attractive stacking fault energy.

Since the energies of fcc and hcp crystal structures have identical first-nearest neighbor interactions and differ only in their next-nearest interactions, it is easy to produce stacking faults in them. A stacking fault in fcc is identical locally to HCP, whereas a stacking fault in HCP would locally resemble the fcc structure.

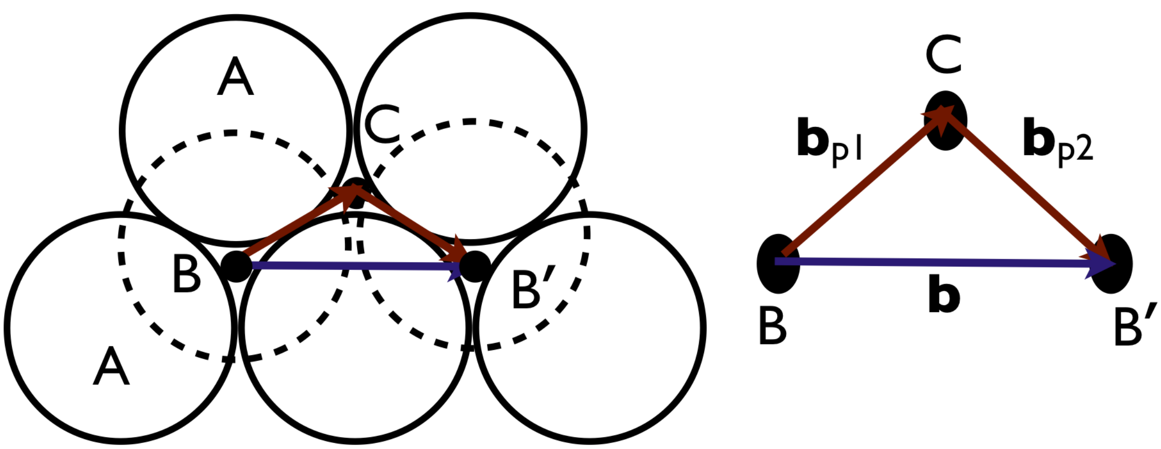


**Figure 5.3** – *Partial dislocations in a fcc stacking. The Burgers vector BB'* $\mathbf{b}$ *can split into two partial Burgers vector* $\mathbf{b}_{p_1}$ *and* $\mathbf{b}_{p_2}$.

Intrinsic stacking faults in fcc occur when a partial shear takes the opposing parts of the crystal on a {111} plane to the nearest interstitial site C from the starting site B over the lower A layer rather than directly to the identity site B that would result in restoration of full order in one step, as shown in figure 5.3. This translation could then be followed by a further partial translation step from site C to B, completing the process and removing the intrinsic stacking fault. This introduces the possibility that dislocations on the {111} planes in fcc with Burgers vectors of type $(a/2)[110]$ type may dissociate into two partial dislocations separated by an intrinsic stacking fault by the following typical dissociation reaction:

$$b = \frac{a}{2}[\bar{1}10] \rightarrow \frac{a}{6}[\bar{2}11] + \frac{a}{6}[\bar{1}2\bar{1}] + SF, \tag{5.1}$$

Since the energy per unit length of a dislocation is proportional to the magnitude of its Burgers vector, this splitting of a dislocation into two partial dislocations is always energetically favorable, except that the creation of a stacking fault consumes energy, and hence the stacking fault energy, i.e., the energy required to create a stacking fault of unit area, $\chi_{SF}$, becomes important in deciding whether it is profitable for a dislocation to split into two partials or remain as one perfect dislocation. The width of the stacking fault is inversely proportional to the $\chi_{SF}$. Hence in materials with low $\chi_{SF}$, the partials tend to remain separated far from each other, thereby reducing their elastic interaction energy. Whereas in materials with high stacking fault energy, the partial dislocations tend to remain close to each other. If the partial separation of the dislocation is of the same order as the core radius, then one need not consider the dislocation as split at all.

The Burgers vector of the Shockley partials is of the form $\frac{1}{6}\langle 112\rangle$, hence it lies on the faces of the tetrahedron and is represented by the line joining the vertex and center of the faces. They are hence of the form, $A\beta, C\delta$ of the figure 5.1. It is readily obvious that if a screw dislocation splits into a pair of partial dislocations, both of them acquire a definite glide plane depending upon the plane in which the dislocation has split, as illustrated in table 5.2.

**Table 5.2** – *Possible planes for a screw dislocations to split into partials.*

| **Screw** | **Normal** | **Partial 1** | **Partial 2** |
|---|---|---|---|
| $\frac{1}{2}[10\bar{1}]$ | $(111)(\delta)$ | $\frac{1}{6}[11\bar{2}]$ | $\frac{1}{6}[2\bar{1}\bar{1}]$ |
| | $(\bar{1}1\bar{1})(\alpha)$ | $\frac{1}{6}[21\bar{1}]$ | $\frac{1}{6}[1\bar{1}\bar{2}]$ |
| $\frac{1}{2}[0\bar{1}\bar{1}]$ | $(\bar{1}1\bar{1})(\alpha)$ | $\frac{1}{6}[\bar{1}\bar{2}\bar{1}]$ | $\frac{1}{6}[1\bar{1}\bar{2}]$ |
| | $(\bar{1}\bar{1}1)(\gamma)$ | $\frac{1}{6}[\bar{1}\bar{1}\bar{2}]$ | $\frac{1}{6}[1\bar{2}\bar{1}]$ |
| $\frac{1}{2}[1\bar{1}0]$ | $(111)(\delta)$ | $\frac{1}{6}[1\bar{2}1]$ | $\frac{1}{6}[2\bar{1}\bar{1}]$ |
| | $(\bar{1}\bar{1}1)(\gamma)$ | $\frac{1}{6}[2\bar{1}1]$ | $\frac{1}{6}[1\bar{2}\bar{1}]$ |
| $\frac{1}{2}[\overline{11}0]$ | $(\bar{1}1\bar{1})(\alpha)$ | $\frac{1}{6}[\bar{1}\bar{2}\bar{1}]$ | $\frac{1}{6}[\bar{2}\bar{1}1]$ |
| | $(1\bar{1}\bar{1})(\beta)$ | $\frac{1}{6}[\bar{2}\bar{1}\bar{1}]$ | $\frac{1}{6}[\bar{1}\bar{2}1]$ |
| $\frac{1}{2}[0\bar{1}1]$ | $(1\bar{1}\bar{1})(\beta)$ | $\frac{1}{6}[1\bar{1}2]$ | $\frac{1}{6}[\bar{1}\bar{2}1]$ |
| | $(111)(\delta)$ | $\frac{1}{6}[1\bar{2}1]$ | $\frac{1}{6}[\bar{1}\bar{1}2]$ |
| $\frac{1}{2}[101]$ | $(\bar{1}\bar{1}1)(\gamma)$ | $\frac{1}{6}[2\bar{1}1]$ | $\frac{1}{6}[112]$ |
| | $(1\bar{1}\bar{1})(\beta)$ | $\frac{1}{6}[1\bar{1}2]$ | $\frac{1}{6}[211]$ |

Since the Shockley partials dislocations have a well-defined glide plane, a dissociated screw dislocation also gains a glide plane: it is the plane into which its Shockley partials have split. Since these split dislocations are also glissile, the whole configuration: two dislocations with partial Burgers vectors and the stacking fault that they enclose evolve under the action of external stress. This chapter presents the difference between the dynamics of split FR source and compares it with a) Parallel Shockley splitting and b) Perfect FR source.

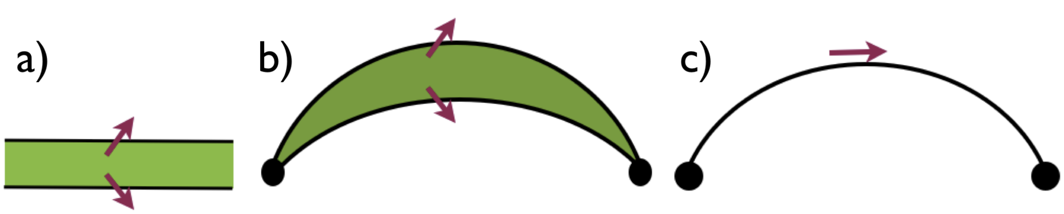


**Figure 5.4** – *Various dislocation configurations referred to in this work. Figure a is a parallel split dislocation; the next image, figure b, is of a split FR source and the right most one, figure c, is a perfect FR source. The region colored green is where the stacking sequence differs from the rest of the crystal. The arrows on each of the partials represent the Burgers vector of that dislocation. It is clear from the line and Burgers vector directions that the dislocation configuration depicted here is a screw dislocation. This cartoon shall be referred to at several places in this and the subsequent chapters.*

The three configurations considered in this work are illustrated in the figure 5.4. The left-most configuration, figure 5.4c, is the split parallel configuration where the two dislocations are parallel to each other and enclose the stacking fault between. The middle figure represents the split FR source where the two partials meet at two common points. The configuration on the right is the usual perfect FR source.

If a screw dislocation splits into a pair of dislocations with the partial Burgers vectors, the whole configuration, i.e., the two dislocation lines and the accompanying stacking fault region shall together be termed as just a "split" screw dislocation, although neither of the two dislocation segments are now pure screws. A "split edge FR source" for example, refers to the configuration containing two dislocations, the vectorial sum of whose Burgers vectors is perpendicular to the line connecting the pinning points. Likewise a "split screw FR source" refers to the configuration where the constituent dislocations have Burgers vectors whose vectorial sum is parallel to the line joining the pinning points. This way, one could construct split FR sources of arbitrary line character.

The Burgers vectors of a split FR source would still lie in the glide plane of the original unsplit dislocation and hence these partial dislocations lines can also glide in the same plane. This way the whole split FR source, together with the enclosing stacking fault, evolves under the action of stress.

### 5.2.2 Dissociation width in the linear elastic theory

The equilibrium dissociation width (also called as the splitting distance) of an extended dislocation can be computed through the force balance, as demonstrated by [Hirth & Lothe 1982, Frøseth *et al.* 2004].

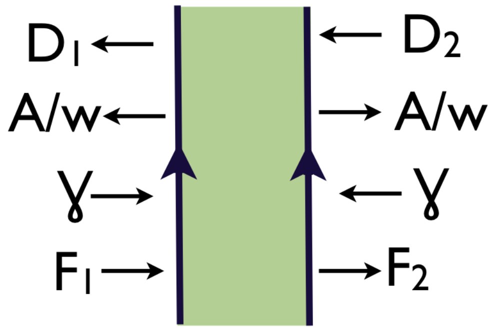


**Figure 5.5** – *Schematic of forces acting on a dissociated dislocation. The applied stress is such that the forces on the partials $F_1$ and $F_2$ act from left to right. $D_1$ and $D_2$ are the damping forces, acting from right to left, $\frac{A}{w}$ is the elastic repulsion acting away from the partials, and the stacking fault force is acting towards the partials.*

Figure 5.5 shows the schematic of free extended dislocation, with the distance between them being $w$. The force balance equation, on each of the partials, then reads:

$$\gamma + F_1 = D_1 + \frac{A}{w} \tag{5.2}$$

and

$$\gamma + D_2 = F_2 + \frac{A}{w} \tag{5.3}$$

where $\gamma$ is the attractive force per unit length exerted by the partials, $\frac{A}{w}$ is the force per unit length due to the internal interactions and $F_i$ is the force per unit length due to any applied stress and $D_i$ is the damping coefficients. Assuming $D_1 = D_2$, the force balance equations can be simplified to $D_1 = D_2 = \frac{F_1+F_2}{2}$ and

$$w = \frac{A}{\gamma + \frac{1}{2}(F_1 - F_2)} \tag{5.4}$$

Now, the interest is getting an expression for $w$ in terms of the applied stress tensor, rather than through the forces. The most generic form of an arbitrary symmetric stress tensor is

$$\overleftrightarrow{\sigma} = \begin{bmatrix} \sigma_{11} & \sigma_{12} & \sigma_{13} \\ \sigma_{12} & \sigma_{22} & \sigma_{23} \\ \sigma_{13} & \sigma_{23} & \sigma_{33} \end{bmatrix} \tag{5.5}$$

Here, we shall consider two types of stresses, the Glide and Escaig stresses and their effect on the dynamics of split dislocation sources.

### 5.2.3 Glide Stress and the dynamics of split dislocations

When one is considering conditions where climb is inhibited, the dislocation motion is confined to a plane that contains both its line direction and its Burgers vector. Such planes are usually the closely packed planes of the crystal and only those stress components are operative which will cause the dislocation to move in such a glide plane. The stresses that satisfy the above requirements are called Glide stresses. Given a stress tensor of the form 5.5, its component that is responsible for the glide of the dislocation is

$$\sigma_{rss} = \overleftrightarrow{\sigma}.\mathbf{n}.\mathbf{b} \tag{5.6}$$

that is, the component of the stress resolved in the glide plane and along the direction of the Burgers vector. All those stress tensors $\sigma$ which yield the same $\sigma_{rss}$ will lead to the same dynamics for the dislocation. Now, if the perfect FR source is split into two dislocations with Burgers vectors $\mathbf{b_1}$ and $\mathbf{b_2}$, such that[1]:

$$\mathbf{b} = \mathbf{b_1}+\mathbf{b_2}, \tag{5.7}$$

these two dislocations will only respond to the resolved shear stresses acting on them via

[1] The vectors $\mathbf{b}_1$and $\mathbf{b}_2$ depends solely on $\mathbf{b}$ and the glide plane (see table 5.2 on page 154).

$$\sigma_{rss}^{b_1} = \sigma.\mathbf{n}.\mathbf{b_1} \;\; and \;\; \sigma_{rss}^{b_2} = \sigma.\mathbf{n}.\mathbf{b_2} \tag{5.8}$$

where $\sigma_{rss}^{b_1}$ is the resolved shear stress acting on the partial having Burgers vector $\mathbf{b_1}$and $\sigma_{rss}^{b_2}$ is resolved shear stress along Burgers vector $\mathbf{b_2}$ and we have

$$\sigma_{rss}^{b} = \sigma_{rss}^{b_1} + \sigma_{rss}^{b_2} \tag{5.9}$$

i.e., the sum of resolved shear stresses acting on the two partial segments is the resolved shear stress acting on the un-split perfect dislocation.

Since $\mathbf{b_1}$ and $\mathbf{b_2}$ make equal angle with $\mathbf{b}$, a resolved shear stress of $\sigma_{rss}^{b}$ is equally split along $\mathbf{b_1}$ and $\mathbf{b_2}$ and hence both partials respond identically to an applied glide stress. If the partial dislocations are parallel to each other (figure 5.4a), then the glide stresses hence have no impact on the width of the the stacking fault region (see equation 5.4, with $F_1 = F_2$). The significant way in which the glide stress component can alter the stacking fault is when the motion of either of the two partials is physically arrested due to some obstacle in the glide path.

### 5.2.4 Escaig Stresses and the dynamics of split dislocations

Consider a perfect FR source having a Burgers vector $\mathbf{b}$. Let a shear stress of magnitude $\sigma$, act on the glide plane of the dislocation $\mathbf{n}_p$ along a direction $\hat{\mathbf{m}}$. The component of this stress which causes the glide of this dislocation is $\sigma cos(\alpha)$ where $\alpha$ is the angle between the vectors $\mathbf{b}$ and $\hat{\mathbf{m}}$[2]. So, a stress acting along a direction $\mathbf{m} = \mathbf{n_p}\times\mathbf{b}$ cannot cause the glide of the dislocation. But if that dislocation splits into partial dislocations having Burgers vector $\mathbf{b_1}$and $\mathbf{b_2}$ such that then the resolved shear stress on each of the partials is $\sigma_{\mathbf{b_1}} = \sigma cos(\alpha_{b_1})$ and $\sigma_{\mathbf{b_2}} = \sigma cos(\alpha_{b_2})$ where $\alpha_{b_1}$ and $\alpha_{b_2}$ are the angles that $\mathbf{m} = \mathbf{n_p}\times\mathbf{b}$ makes with $\mathbf{b_1}$

[2]*Recall that the component of the stress tensor that causes glide in a dislocation is* $\overleftrightarrow{\sigma}.\mathbf{n}.\mathbf{b}$, *where* $\mathbf{n}$ *is the glide plane and* $\mathbf{b}$ *is the Burgers vector*, see section 2.2.6 on page 41.

and $\mathbf{b_2}$ respectively. Since $\mathbf{b}_1$ and $\mathbf{b}_2$ make equal angle with $\mathbf{b}$, the stresses that drive the dislocation are $\sigma_{\mathbf{b_1}} = \frac{\sigma}{2}$ and $\sigma_{\mathbf{b_2}} = -\frac{\sigma}{2}$. This means that a shear along a direction $\mathbf{n_p} \times \mathbf{b}$ causes the partial dislocations to experience equal resolved shear stress but of opposing magnitude, such that the total stress acting on two partials together is zero. Such non-glide stresses are termed Escaig stresses [Escaig 1968]. It should be noted that since the edge components of the partials are parallel to $\mathbf{b_1} - \mathbf{b_2}$, and $\mathbf{n_p} \times \mathbf{b}$ being parallel to $\mathbf{b_1} - \mathbf{b_2}$ (see figure 5.6), the statement that the Escaig stresses act on the edge component of the dislocation is equivalent to the statement that the Escaig stresses act along the $\mathbf{n_p} \times \mathbf{b}$ direction.

Since the Escaig stress acts on each partial in opposite directions, it will directly contribute towards changing the enclosed stacking fault area, and thus the width of the partials. An illustration of direction of glide and Escaig stress is provided in figure 5.6. It is evident that in case of split edges, the Escaig stress acts along the line direction, whereas in case of split screw, the Escaig stress act perpendicular to the direction of the dislocation line.

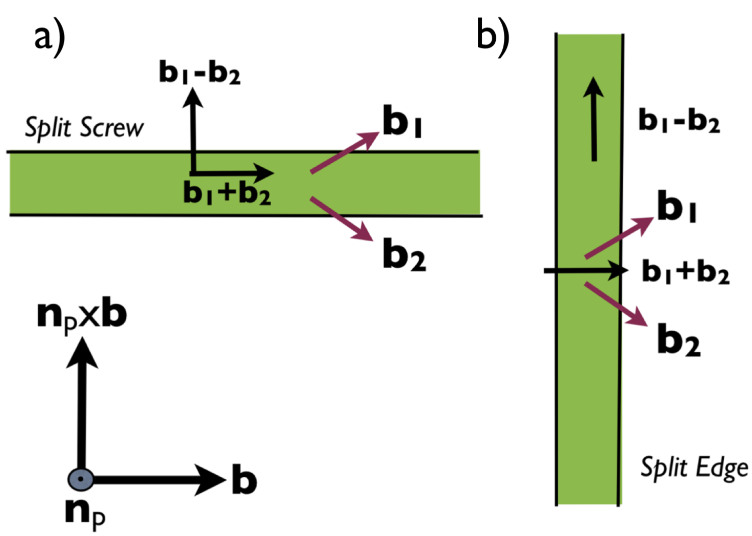


**Figure 5.6** – *Resolution of partial Burgers vectors of a split dislocation, into their edge and screw components. The glide stresses act in the direction of the screw components, whereas the Escaig stress acts along the direction of the edge components of the partial Burgers vector.*

### 5.2.5 Organization of the chapter

The rest of this chapter is organized as follows: section 5.3 lists the materials parameters taken for these simulations. In section 5.4, energy of a dissociated dislocation in the non-singular stress formulation is computed. The actual simulations and discussions start from section 5.5. In section 5.5, we study the energetics of the three configurations presented in figure 5.4. In section 5.6, we study the equilibrium dissociation widths of split parallel dislocations and split FR sources under no applied stress and contrast their dependence on the stacking fault energy of the material. This study is carried out for dislocations of all line characters. In section 5.7, the evolution of a split FR source under the application of glide stress is studied, and compared with that of an un-split perfect FR source. Section 5.8 deals with the response of a split FR source to the Escaig stress acting on it and its dynamics will be compared to the case of split parallel dislocation configuration. The split FR source exhibits a curious behavior under the application of high Escaig stress, which will also be analyzed. Section 5.9 deals with the simultaneous application of Escaig and glide stresses and the response of the split FR source to those stresses. The dissociation width under these stresses, in the case when the motion of the partials is obstructed, is also examined. The next section 5.10 concludes the work, highlighting the major observations and insights.

The simulations in this chapter are carried out in NUMODIS [L. Dupuy & Coulaud 2013], the node based dislocation dynamics software. The algorithm for these simulations is given in section 2.3 on page 49. These studies are carried out in the non-singular elastic theory formalism proposed in [Cai *et al.* 2006] and [Arsenlis *et al.* 2007]. Wherever possible, the difference between the results predicted by the elastic theory and those of the non-singular formalism will be highlighted. The climb and cross-slip phenomenon are suppressed in these simulations, making the study effectively two dimensional, confined to a single closely packed plane.

### 5.2.6 Constructing split dislocations of arbitrary line character

Let $\mathbf{L}$ be the length of the FR source, $\mathbf{n_p}$ be its glide plane, $\mathbf{b}$ the Burgers vector of the unsplit dislocation and let $\mathbf{b_1}$ and $\mathbf{b}_2$ be the Burgers vectors of the partial dislocation lines. Let $\xi$ denote the vector connecting the two pinning points. It is evident that these vectors should satisfy

$$\mathbf{b} = \mathbf{b}_1 + \mathbf{b}_2, \mathbf{n_p}.\mathbf{b} = \mathbf{n_p}.\mathbf{b_1} = \mathbf{n_p}.\mathbf{b_2} = \mathbf{n_p}.\xi = \mathbf{0} \tag{5.10}$$

Let the angle between the line direction $\hat{\xi}$ and the Burgers vector $\mathbf{b}$ be $\theta$. The initial configurations of the Frank-Read sources of different line characters, quantified by $\theta$, are constructed as follows (see figure 5.7)

Let A be one pinning point, with position $\mathbf{r}_A$. The line direction $\hat{\xi}$ is obtained by rotating the unit vector $\hat{\mathbf{b}}$ by an angle $\theta$, about the axis $\mathbf{n_p}$, where $\hat{\mathbf{b}}$ is the unit vector in the direction of $\mathbf{b}$.

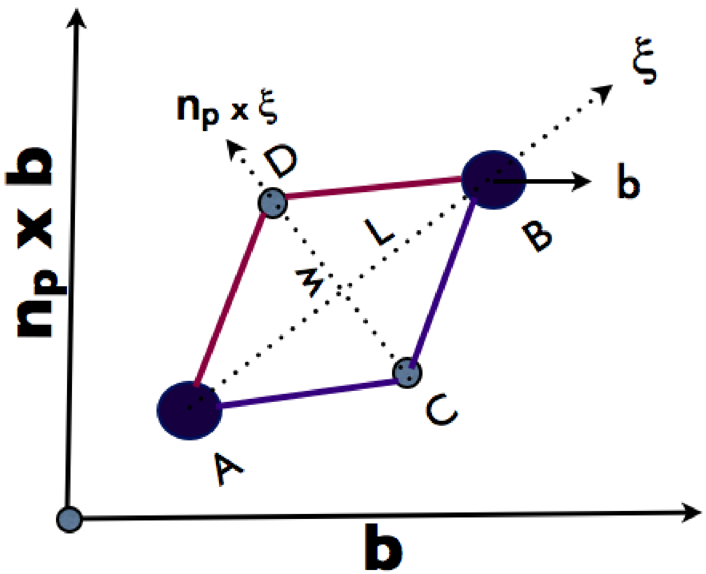


**Figure 5.7** – *Constructing the "Split FR source" of arbitrary line orientation, in a plane whose normal is along $\mathbf{n}_p$. The points A and B, having co-ordinates $\mathbf{r}_A$ and $\mathbf{r}_B$ are the pinning points. The two split dislocations are ADB and ACB. The character of this split dislocation is inferred from the angle $\theta$ that the line orientation $\hat{\xi}$ makes with the Burgers vector $\mathbf{b}$.*

This rotation scheme ensures that the line vector of the dislocation remains confined to a plane whose normal is $\mathbf{n_p}$ and the rotation vector is given by the Rodriguez rotation formula [Koks 2006]:

$$\hat{\xi} = \hat{\mathbf{b}}cos\theta + (\mathbf{n}_p \times \hat{\mathbf{b}})sin\theta + \mathbf{n}_p(\mathbf{n}_p.\hat{\mathbf{b}})(1 - cos\theta).$$

With this line direction, the position of the second pinning point B is:

$$\mathbf{r}_B = \mathbf{r}_A + L\hat{\xi}.$$

These two points are sufficient to construct a perfect FR source, but to construct a split FR source, the two additional points, $\mathbf{r}_C$ and $\mathbf{r}_D$ are needed, as shown in figure 5.7. The center of the dislocation given by

$$\mathbf{c} = \tfrac{\mathbf{r}_A + \mathbf{r}_B}{2}.$$

Let the initial maximum separation between the two partials be $w_m$, The splitting happens in the same plane that contains $\hat{\xi}$ and $\hat{\mathbf{b}}$, that is, the plane $\mathbf{n}_p$ and the direction of maximum separation is perpendicular to the line direction $\hat{\xi}$. Hence, we have

$$\mathbf{r}_C = \mathbf{c} + \tfrac{w_m}{2}(\mathbf{n}_p \times \hat{\xi}) \text{ and } \mathbf{r}_D = \mathbf{c} - \tfrac{w_m}{2}(\mathbf{n}_p \times \hat{\xi}).$$

The construction is now complete. The line segment joining $(A, D, B)$ represents one partial with Burgers vector $\mathbf{b_1}$, the line segment joining $(A, C, B)$ is another partial dislocation with Burgers vector $\mathbf{b_2}$, and the area enclosed within these two line segments is the faulted region.

It should be noted this construction is physically more accurate, in the sense that the Burgers vector remains the same for dislocations of all line orientations $\theta$, whereas the line direction $\hat{\xi}$ is different for lines of different orientation angles. [Byun 2003, Baudouin *et al.* 2013].

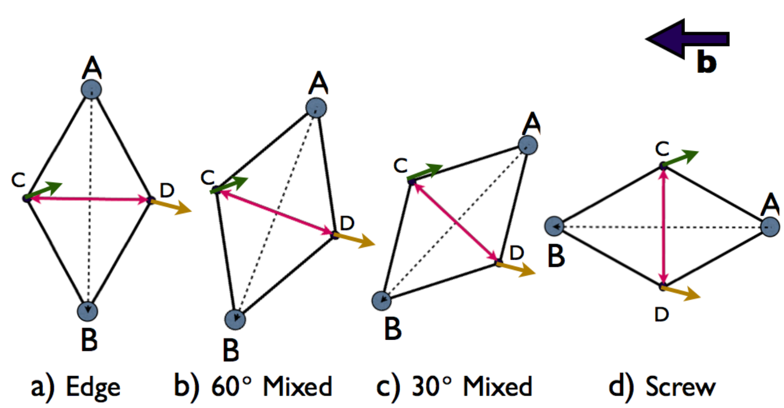


**Figure 5.8** – *Construction of extended FR sources of different line characters. a) An edge dislocation b) a mixed dislocation making 60 deg with $\vec{\mathrm{b}}$ c) a mixed dislocation making 30 deg with **b** and d) a screw dislocation.*

The figure 5.8 indicates the initial structure of four extended FR sources of different line directions. The points A and B represent the pinned points, and C and D represent the points of maximum separation. The segments ACB and ADB represent the dislocation line direction of each of the partials, and the arrows on the lines represent the partial Burgers vector. The dotted line joining the pinning points represents the line direction if the dislocation were un-split. Separation $AB$, the distance between pinning points, is here termed as the "length of the dislocation" although, lengths of each of the partials is more than this distance.

### 5.2.7 Simulating split dislocations of different line characters

Here, the dependence of average width of a split FR on the line character is studied. At $t = 0$, a split FR source of a given length and a line orientation is constructed as discussed above. The initial separation between the partials is taken to be some arbitrary value and the configuration is allowed to evolve for a sufficiently long time $t$. At every instant of the dynamics, the instantaneous stacking fault area $\Delta^t$ and the instantaneous total length $L_{tot}^t$ of the dislocations are recorded. The instantaneous average width is then taken as

$$w^t = \frac{\Delta^t}{\frac{L_{tot}^t}{2}} = \frac{2\Delta^t}{L_{tot}^t} \tag{5.11}$$

The average width is obtained by

$$\bar{w} = \frac{1}{(t_{tot} - t_{eq})} \sum_{t=t_{eq}}^{t=t_{tot}} \frac{2\Delta^t}{L_{tot}^t} \tag{5.12}$$

where $t_{eq}$ is some fraction of total simulation time $t_{tot}$ by which the split dislocation approaches its equilibrium shape.

## 5.3 Material parameters

The materials parameters used for all these simulations (unless otherwise mentioned) are listed in table 5.3. The shear modulus $\mu$, Poisson's ratio $\nu$ and the stacking fault energies are taken according to those given in [Argon 2008].

**Table 5.3** – *Material parameters and dislocation details used in the present simulations. $a$ is the lattice parameter, $\mu$ is the shear modulus, $\nu$ is the Poisson's ratio, $SFE$ is the stacking fault energy, $\mathbf{n}_p$ is the primary glide plane, $\mathbf{b}$ is the Burgers vector of the perfect dislocation, and $\mathbf{b}_1$,$\mathbf{b}_2$ are the Burgers vectors of the partials dislocations. $\mathbf{n}_p$ and $\mathbf{b}$ together uniquely determine the $\mathbf{b}_1$ and $\mathbf{b}_2$. See table 5.2.*

| Material | a($\dot{A}$) | $\mu$(GPa) | $\nu$ | SFE ($mJ/m^2$) | $\mathbf{n}_p$ | $\mathbf{b}$ | $\mathbf{b}_1$ | $\mathbf{b}_2$ |
|---|---|---|---|---|---|---|---|---|
| Cu | 3.661 | 41 | 0.3 | 73 | $(\bar{1}1\bar{1})$ | $\frac{a}{2}[\bar{1}\bar{1}0]$ | $\frac{a}{6}[\bar{1}2\bar{1}]$ | $\frac{a}{6}[\bar{2}\bar{1}1]$ |

## 5.4 Energy of an extended dislocation

Consider a dislocation of length $L$ and Burgers vector $\mathbf{b}$ being dissociated into two straight partial dislocations of length L and Burgers vector $\mathbf{b_1}$ and $\mathbf{b_2}$ respectively. Let these two lines be oriented along the $x$-axis and separated by a distance $r$ along the y-axis. Since both the segments are of equal length $L$, the interaction energy expression equation 2.37 on page 53 simplifies to

$$E_{int} = 2W(r\mathbf{j}) - W(L\mathbf{i} + r\mathbf{j}) - W(-L\mathbf{i} + r\mathbf{j}) \tag{5.13}$$

Substituting for W from equation 2.38 and simplifying leads to

$$\begin{aligned} \frac{E^{int}(L, r, \mathbf{b}_1, \mathbf{b}_2)}{W_0} &= Lln\left[\frac{p+L}{p-L}\right]\gamma \\ &- \frac{(p-q)}{q^2}(\mathbf{b_1}.\mathbf{t})(\mathbf{b_2}.\mathbf{t})\left[(3-\nu)a^2 + (4-2\nu)r^2\right] \end{aligned} \tag{5.14}$$

where

$$\gamma = [(1-\nu)(\mathbf{b_1}.\mathbf{t})(\mathbf{b_2}.\mathbf{t}) + (\mathbf{b_1} \times \mathbf{t}).(\mathbf{b_2} \times \mathbf{t})] \tag{5.15}$$

$$p = \sqrt{L^2 + r^2 + a^2} \tag{5.16}$$

$$q = \sqrt{r^2 + a^2} \tag{5.17}$$

and $W_0$ is same as equation 2.39 on page 54 and $\mathbf{t}$ is the line direction of the partials. This is expression is exact at the moment, although the approximations $L \gg r$ and $L \gg a$ can reasonably made.

The self energy of either of the partials can also be retrieved from equation 5.14 by setting $\mathbf{b}_1 = \mathbf{b}_2$, $r = 0$ and taking half of the obtained interaction energy, which agrees with equation 2.35 on page 52. The total energy of the dissociated dislocation is hence:

$$\begin{aligned} E(L, r, \mathbf{b}_1, \mathbf{b}_2) &= E^{self}(L, \mathbf{b}_1) + E^{core}(L, \mathbf{b}_1) \\ &+ E^{self}(L, \mathbf{b}_2) + E^{core}(L, \mathbf{b}_2) \\ &+ E^{int}(L, r, \mathbf{b}_1, \mathbf{b}_2) + E^{sfe}(L, r) \end{aligned} \tag{5.18}$$

It should be noted that $E^{self}(L, \mathbf{b}_1)$ and $E^{self}(L, \mathbf{b}_2)$ are, in general, not equal since $\mathbf{b}_1$ and $\mathbf{b}_2$ make different angles with the line direction $\mathbf{t}$. If the un-dissociated Burgers vector is $\mathbf{b}$ making an angle $\theta$ with the line vector $\mathbf{t}$, then the Burgers vectors of the partials $\mathbf{b}_1$ and $\mathbf{b}_2$ make an angle $\theta \pm \frac{\pi}{3}$ respectively with $\mathbf{t}$ and have equal magnitude of $\frac{\|\mathbf{b}\|}{\sqrt{3}}$.

The equilibrium dissociation width is the one that minimizes the total energy $E(L, r, \mathbf{b}_1, \mathbf{b}_2)$:

$$\frac{dE(L, r, \mathbf{b}_1, \mathbf{b}_2)}{dr}|_{r=r_{min}} = 0 \quad (5.19)$$

## 5.5 Energy comparison of the three configurations of figure 5.4

The total energy per unit length of the three configurations: the split parallel dislocations, the split Frank-Read and the perfect FR source, for different line orientations and for a given length of $5000A^o$ length is given in figure 5.9.

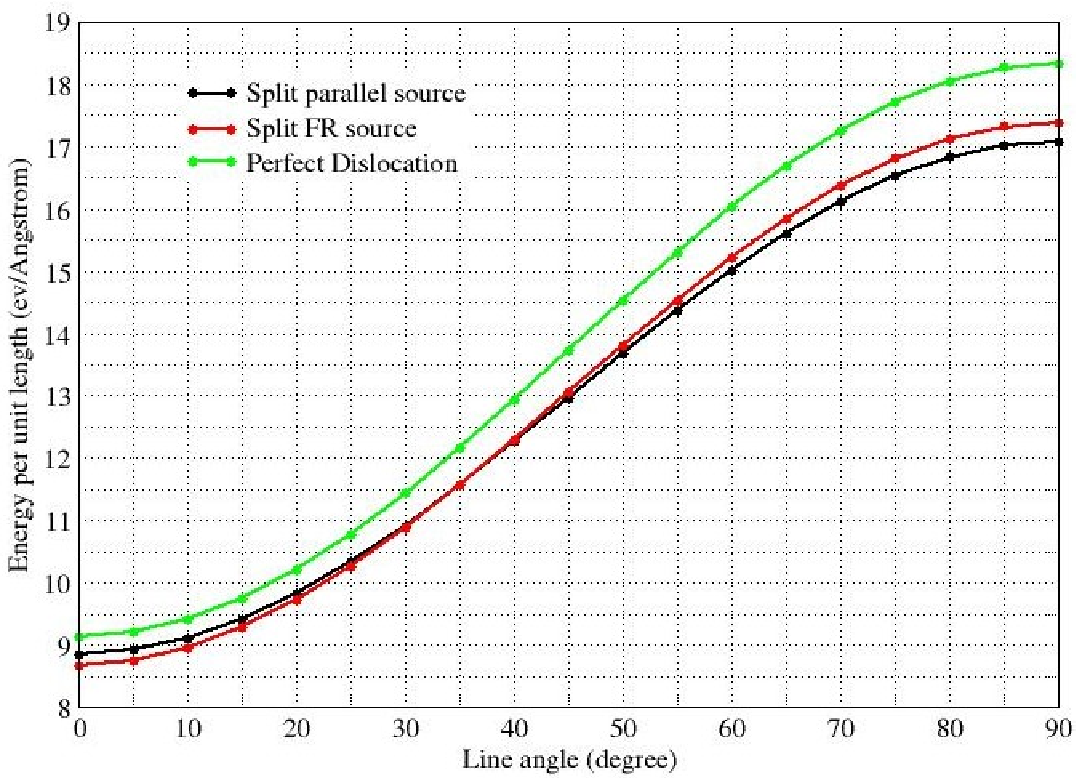


**Figure 5.9** – *The variation of total energy with line angle, for three different configurations. The angle is the angle between the dislocation line direction and its Burgers vector. The Green plot is that of the unsplit dislocation, the black plot is the case of parallel split partials. The curve in red is that of the split FR source.*

The energy of the perfect dislocation for different line characters is obtained by formula (2.3.3). The plot of the parallel split is the minimum of the energy obtained by varying the separation between the parallel partials (see algorithm 5.1). The configuration of split parallel partials and the split FR source have almost identical total energies per unit length, and are lower than the perfect dislocation case. The deviation from the perfect dislocation case increases with increasing angle $\theta$.

## 5.6 Zero stress dissociation widths

Here, the equilibrium dissociation width of the split dislocations under no external stress is studied as a function of material parameters. The widths predicted by elastic theory is compared with that obtained by non-singular stress scheme.

### 5.6.1 Dissociation width of parallel split partials

In the absence of an external stress, the equilibrium separation between parallel partial dislocation lines, under the classical elastic theory of dislocations, is given by [Hirth & Lothe 1982, Baudouin *et al.* 2013]:

$$d = \frac{2+\nu-4\nu cos^2\theta}{24\pi(1-\nu)}\frac{\mu b^2}{\gamma} \tag{5.20}$$

Where $\mu$ and $\nu$ are the shear modulus and Poisson's ratio, respectively, $\gamma$ is the stacking fault energy of the material and $\theta$ is the angle between the line direction $\xi$ and the Burgers direction $\mathbf{b}$. This formula is obtained by setting $A$ of equation 5.4 to the actual value [Daphalapurkar & Ramesh 2012]:

$$A = \frac{\mu}{2\pi}\left(\mathbf{b}_1.\xi\right)\left(\mathbf{b}_2.\xi\right) + \frac{\mu}{2\pi(1-\nu)}\left(\mathbf{b}_1\times\xi\right).\left(\mathbf{b}_2\times\xi\right) \tag{5.21}$$

where $\mathbf{b}_1$ and $\mathbf{b}_2$ are the Burgers vectors of the partials.

Note that the length of the split dislocation does not enter the equation for the separation of partials. As the partial dislocations are parallel to each other, the elastic energy and the stacking fault energy both scale linearly with the dislocation length and hence the distance at which the two forces balance each other, is independent of it.

But in the non-singular stress formulation (see page 50), the self energy of a dislocation does not scale linearly with its length, even after including the core-energy contributions. This brings in a dependence of the dissociation width on the length of the dislocation also.

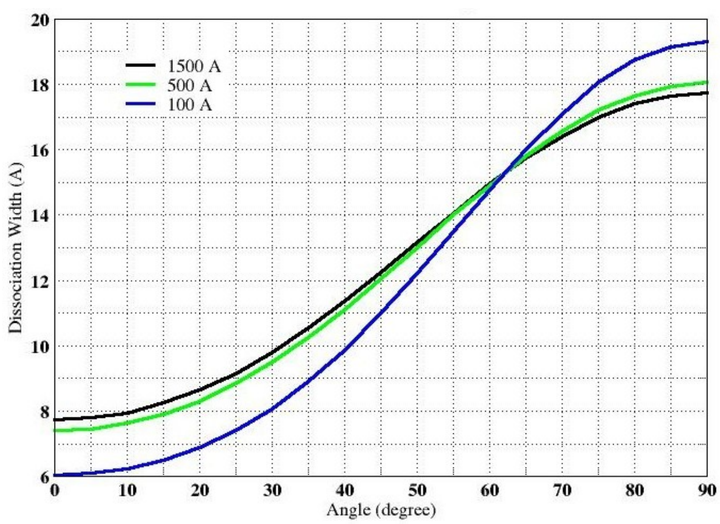


**Figure 5.10** – *Variation of dissociation width with line character for different lengths for parallel split partials, computed using the non-singular stress formulation.*

The variation of dissociation width for various line characters, at three dislocation lengths is given in figure 5.10.

**Algorithm 5.1** Computing the equilibrium separation of the parallel split partials.

1. Construct the parallel split dislocation of the desired line character, and the minimum separation of $d = d_{min}$.
2. Measure the total energy of the system:
$$E_{tot}(d) = E_{elastic} + E_{SF} + E_{core}$$
where $E_{elastic}$ is the sum total of the interaction energy and the self energy of the two partials.
3. Move the partials such that the separation between them is now, $d = d + \Delta d$
4. If $d > d_{max}$ go to step 5, otherwise go to step 2.
5. $d_{equilibrium}$ is the $d$ where $E_{tot}(d)$ is minimum.

For a given dislocation length, the variation of dissociation width with stacking fault energy is given in figure 5.11, along the width predicted by the analytic formula of eq 5.20.

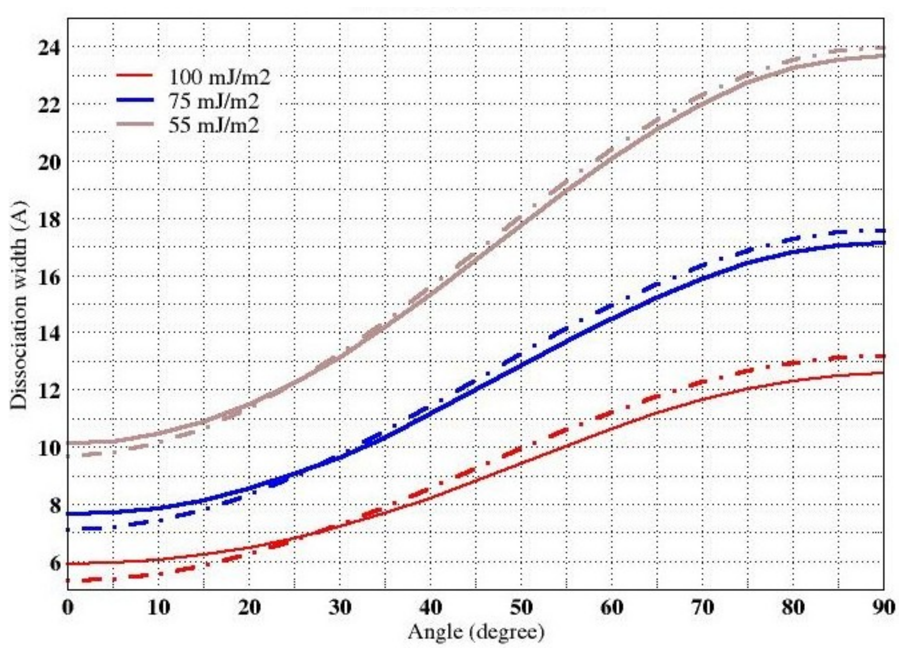


**Figure 5.11** – *Variation of dissociation width with stacking fault energy, for parallel split dislocations. The dotted line is the prediction of eq 5.20, and the solid line is that of the Non-singular stress formulation.*

### 5.6.2 Dissociation width of split FR source

In the case of a split Frank-Read source, the split partials are not parallel to each other along their whole lengths, hence it is useful to talk of the average separation between them defined as the enclosed stacking fault area divided by the half of the total dislocation length. The variation of this average dissociation width under zero stacking fault energy is as shown in Fig 5.12.

It can be seen from the figure 5.12 that the stacking fault area enclosed by the partials remains finite even with 0 SFE. This behavior is to be contrasted with that of the split parallel dislocations, where the partial separation would become infinite (from eq 5.20).

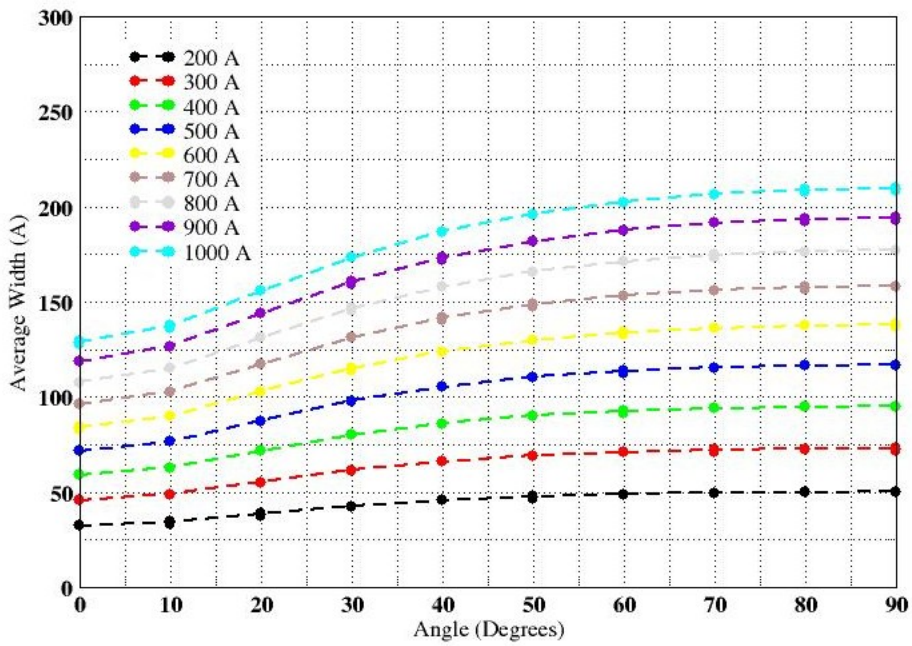


**Figure 5.12** – *Variation of average dissociation width of a split FR source with line character under zero stacking fault energy, for various dislocation lengths, from* $200A$ *to* $1000A$ .

In a split FR source, the partials can reduce their elastic interaction energy by moving away from each other, but this is possible only by bowing away from each other, as they are pinned. Since bowing increases the line energy of the dislocation, it stops when the line energy and elastic energy balance each other. This phenomenon is similar to the curved shape that a FR source takes under a shear stress that is less than the critical stress of activation. The difference is that, in the present case, there is no external stress acting on the dislocation, and the equilibrium shape of the split FR source is dictated only by the internal stress that each partial feels due to the other. This feature is not present in the case of split parallel dislocations as there is no competing energy increase when the partials move away from each other. So, the partial dislocation segments can move indefinitely away from each other and decrease their interaction energy infintely. The effective partial separation is potentially limited only by the grain size.

For a stacking fault energy of $73mJ/m^2$, the average partial separation for a split FR source of length $200\dot{A}$, and for different values of angle between line and Burgers vectors, $\theta$ is given in the table below. The dissociation width for straight, infinitely long dislocations, as given by eq (5.20) is also given for comparison.

**Table 5.4** – *Variation of zero-stress stacking fault width with line orientation. $w$ is the average width of the split FR course, and $d$ is the width predicted by the formula 5.20.*

| $\theta°(degree)$ | $\bar{w}(\dot{A})$ | $d(\dot{A})$ |
|---|---|---|
| 0 | 9.7 | 7.4 |
| 30 | 14.6 | 10.1 |
| 45 | 17.1 | 12.9 |
| 60 | 18.7 | 15.6 |
| 90 | 19.7 | 18.4 |

The dissociation width of split FR source is always greater than the split parallel source. This deviation is found to increase with the dislocation length, up to a certain length.

### 5.6.3 Change of average dissociation width with stacking fault energy

The dependence of average dissociation width of a split FR source on the material's stacking fault energy is obtained by running a series of simulations for different dislocation lengths. The variation is as shown in the figure 5.13. The average dissociation width falls inversely with the stacking fault energy, as in the case of the parallel partials case. The dependence of the dissociation width on the dislocation length (distance between the pinning points) is greater in case of low stacking fault energy.

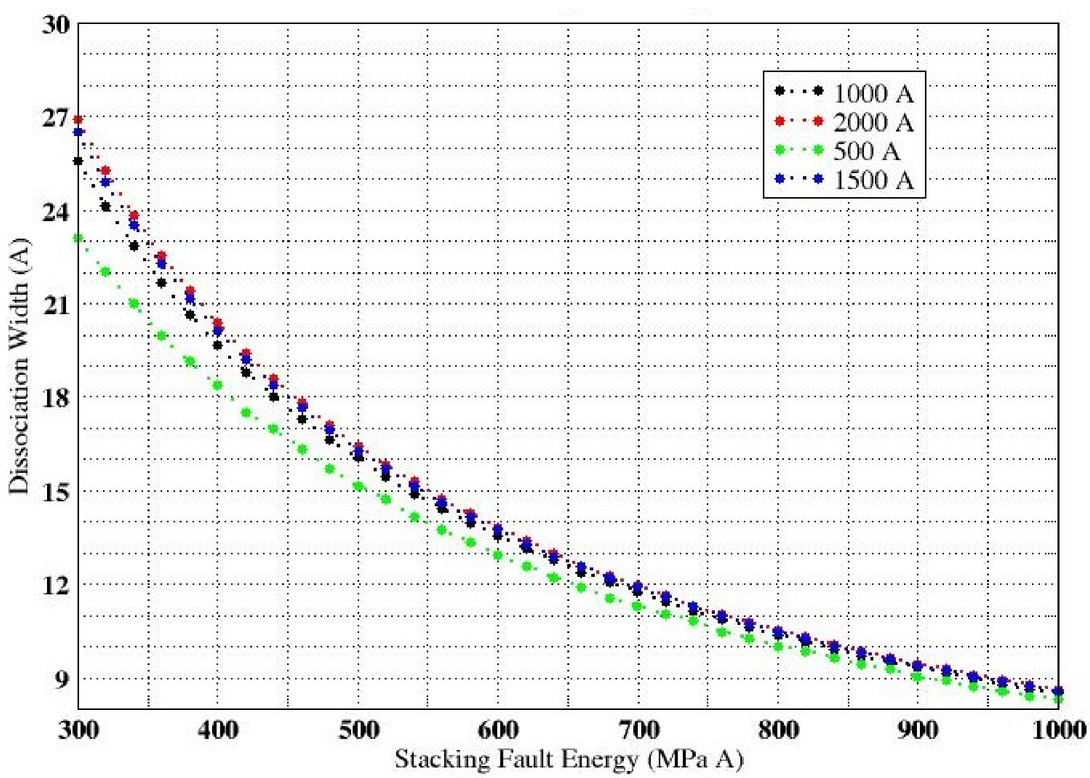


**Figure 5.13** – *Variation of dissociation width with stacking fault energy, for four dislocation lengths, from* $500\dot{A}$ *to* $2000\dot{A}$

The width-vs-SFE data fitted to a function of the form $w = a/x^b + c$ , where $w$ is the dissociation width and $x$, the stacking fault energy gives the coefficients $a, b$ and $c$ as $b = -1$, and $c = 11A$ is the average dissociation width under zero stacking fault energy.

### 5.6.4 Discussion

The equilibrium width of a split FR source, is found to be greater than that predicted for infinitely long parallel partial dislocations for all line directions. Also, the disagreement between $\bar{w}(\theta)$ and $d(\theta)$ seems to be minimum for screw ($\theta = 0$) and edge ($\theta = 90^o$) orientations and approaches a maximum for $\theta = 45^o$. Also, the equilibrium width of a screw FR is much lower than that an edge source.

## 5.7 Evolution of a split FR source under glide Stress

Under the application of a shear stress, a dislocation that is pinned at its two end points would bow into an arc such that the increased line tension force balances the component of Peach-Kohler force on to the glide plane. The radius of curvature of the arc would decrease with the increasing applied stress, until a threshold stress called activation stress is reached. Once the stress exceeds the activation stress, the radius of curvature falls below the distance between the pinning points and hence the dislocation's length would irreversibly increase emitting the dislocation loops which close on to themselves. This multiplication of dislocations is a primary source of strain spreading in crystals. The line tension approximation gives the approximation of this nucleation stress as [Hirth & Lothe 1982]

$$\sigma = \alpha \frac{\mu b}{L} \tag{5.22}$$

where $L$ is the distance between the pinning points, $\mu$ the shear modulus, $b$ the magnitude of Burgers vector, and $\alpha$ a prefactor that differs between the edge and screw type of dislocations.

The above formula is under the assumption that the equilibrium shape of the bowed out dislocation is an arc of a circle, which is true only when the Poisson's ratio is zero. Otherwise the shape is more an arc of an ellipse, owing to the differences between the mobilities and stresses produced by the edge and screw components of a bowed out dislocation. The Frank-Read multiplication mechanism in case of extended dislocation sources is being pursued only recently[Shimokawa & Kitada 2014, Min-Sheng *et al.* 2014].

The algorithm for obtaining the nucleation stress from dislocation dynamics simulations was presented in [Shishvan *et al.* 2008]. Since here the intent is limited to contrast the activation behavior of split FR source vis-a-vis a perfect FR source, a simple method will be adapted to estimate the activation stress. A shear stress of magnitude $\sigma$ is applied in the glide plane $\mathbf{n}_p$ in the direction of the Burgers vector $\mathbf{b}$. The magnitude of stress $\sigma$ is varied with time as shown in figure 5.14.

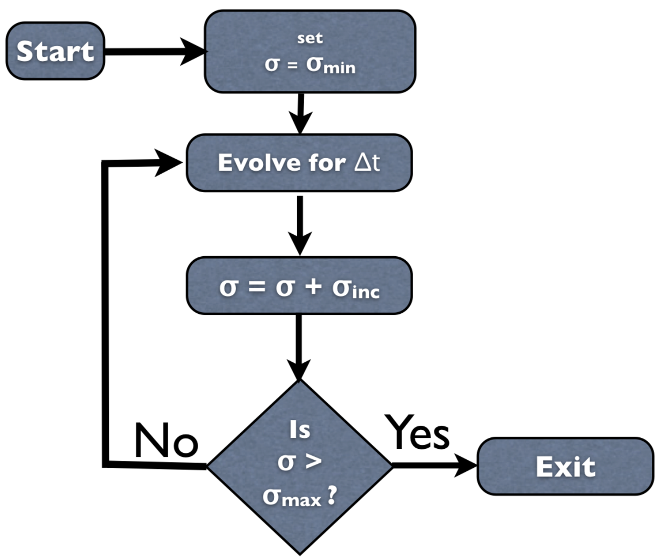


**Figure 5.14** – *Flowchart for the stress variation employed in simulations discussed in sections 5.7 and 5.8.1. The $\sigma$ refers to the magnitude of stress.*

At the end of this scheme, the dislocation length as a function of time is obtained, which can be readily converted to a function of stress. At stresses less than the activation stress, the dislocation length tends to a constant which depends on the applied stress. Once the stress exceeds the threshold stress, the length of the dislocation increases without limit, as there is no equilibrium shape for the dislocation. Hence by observing the dislocation length vs stress plot the nucleation stress can be assigned the minimum stress window where the dislocation length continues to increase without saturating to a constant value. The accuracy of this technique is limited by the fineness of $\delta\sigma$.

Although the current method is less efficient than the algorithm of [Shishvan *et al.* 2008], it is employed here as the aim is not to accurately determine the activation stress but only to compare the activation behavior of a perfect FR source and the split FR source for different shear stresses.

For a dislocation of length 1000A, and with the material parameters given in 5.3, the variation of instantaneous dislocation length with applied stress is as follows:

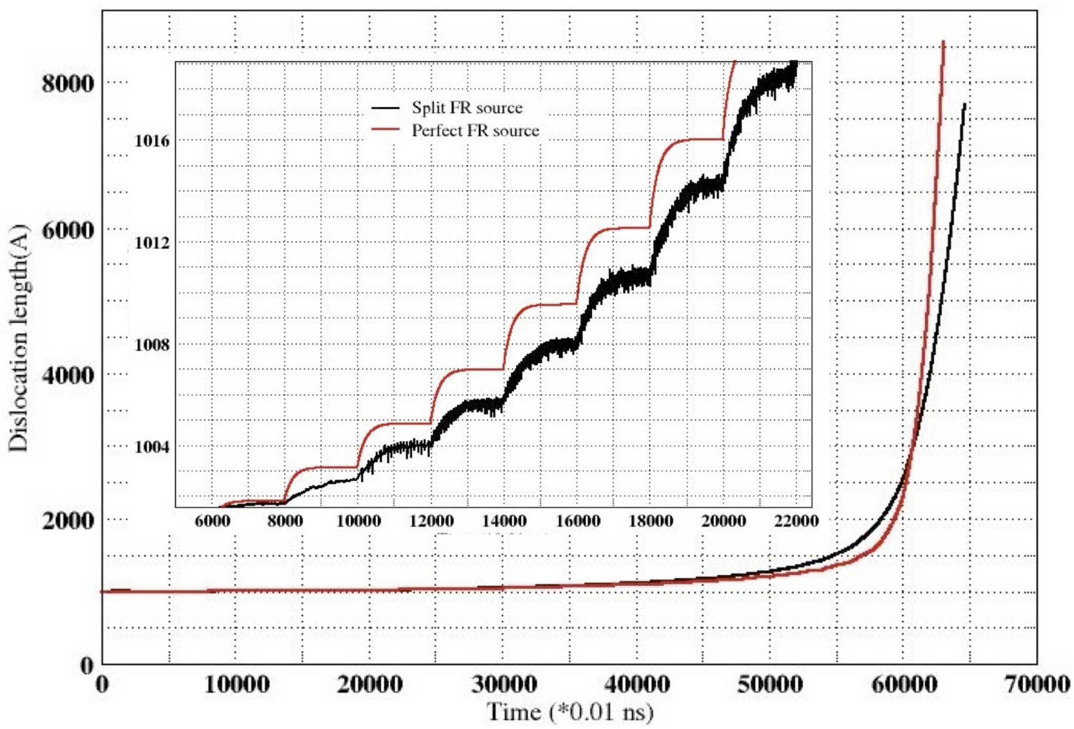


**Figure 5.15** – *Time evolution of instantaneous dislocation length under quasi-static glide stress, for a perfect FR source (red) and a split dislocation source (black). The inset shows a zoomed version of a smaller window of time.*

In the case of the split FR source, the instantaneous dislocation length is taken as the average of the lengths of the two partials. As can be seen, the total lengths of both perfect

FR and split FR follow each other at all Escaig stresses, and even the activation stress is almost identical for both.

# 5.8 Evolution of a split FR source under Escaig Stress

## 5.8.1 Average dissociation width under applied Escaig stress

The stress variation scheme is the same as shown in the figure 5.14. But the stress $\sigma$ is along the shear direction $\mathbf{n}_p \times \mathbf{b}$. During the course of this, the average partial separation is recorded at every $\delta t$ ($\delta t << \Delta t$) time-step. The numerical values of the parameters is as given in table 5.5.

**Table 5.5** – *The parameters used in the simulation.*

| $\sigma_{min}$(MPa) | $\sigma_{min}$(MPa) | $\sigma_{inc}$(MPa) | $\Delta t$ (ns) | $\delta t$ (ns) | Length (A) |
|---|---|---|---|---|---|
| 0 | 300 | 20 | 5 | 0.01 | 1000 |

The time-evolution of the stacking fault area enclosed by the partials is as given in figure 5.16:

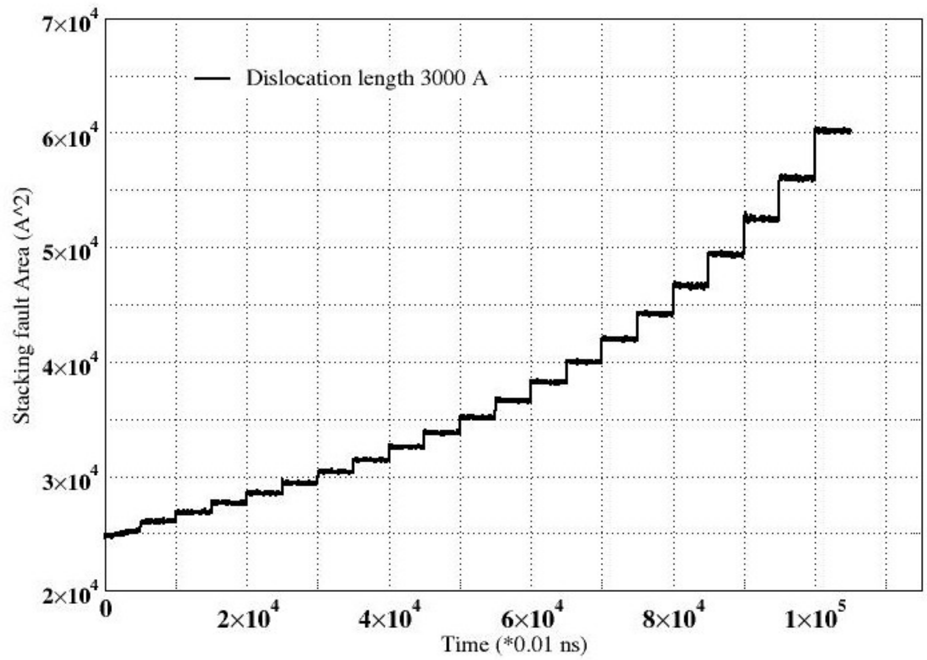


**Figure 5.16** – *Variation of the instantaneous stacking fault area as a function of time, where the Escaig stress is varied incrementally from -300 MPa to 300 MPa, in steps of 30MPa.*

The points at which the dissociation width changes by a considerable magnitude correspond to the times when the applied stress is incremented. In the time window when the stress is held constant, the dissociation width attains an equilibrium value corresponding to that stress. The instantaneous total dislocation length also shows a similar variation with time. Hence, the dissociation width can be extracted from these time variations and plotted as a function of applied Escaig stress, as in figure 5.17.

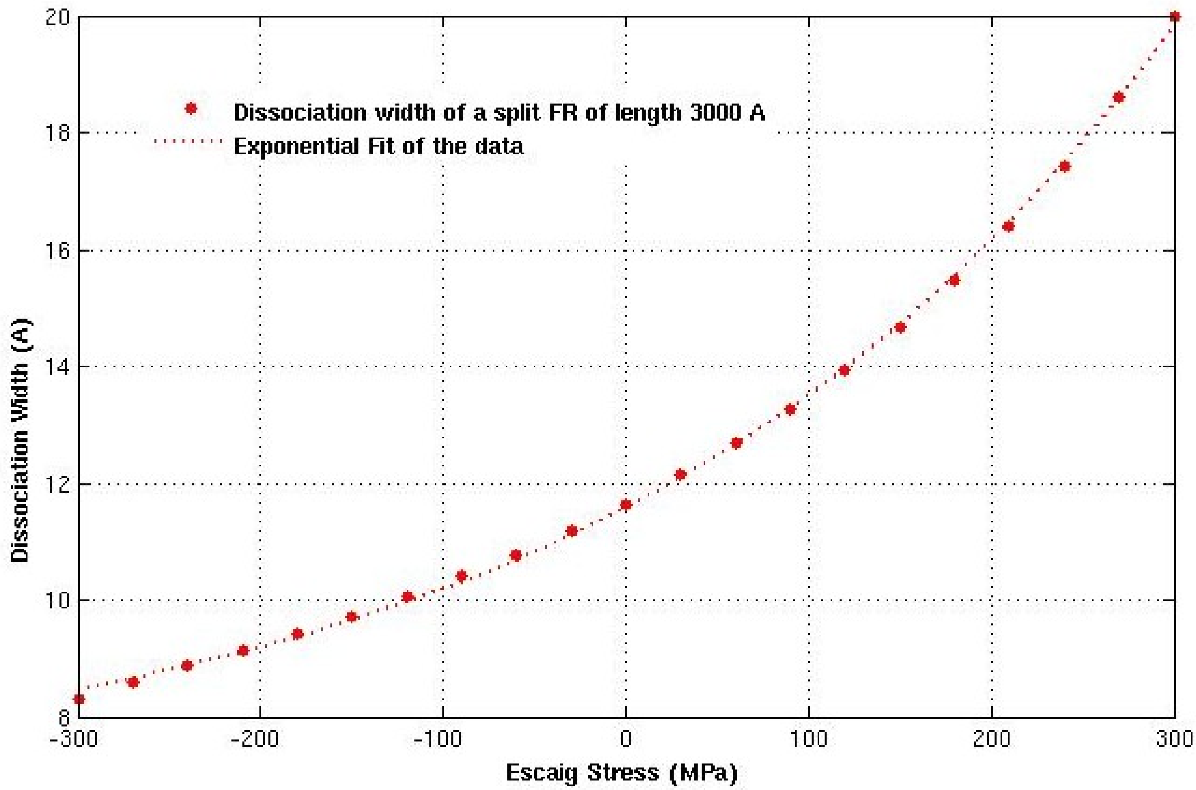


**Figure 5.17** – *Variation of the dissociation width with the applied Escaig stress, for a split FR source of 3000 A length. The dots represent the actual data and the dotted line is the data fitted to an exponential relation. The data for this plot is obtained from that of graph in figure 5.16.*

### 5.8.2 Average dissociation width under simultaneous variation of stacking fault energy and applied Escaig stresses

In the case of parallel, infinitely long split dislocations, the dependence of partial width on the Escaig stress is given in [Baudouin *et al.* 2013] as

$$d = \frac{2 + \nu - 4\nu cos^2\theta}{24\pi(1-\nu)} \frac{Gb^2}{\gamma - \frac{b}{2\sqrt{3}}\sigma_{\mathbf{n_p}\times\mathbf{b}}} \tag{5.23}$$

where $b$ is the magnitude of the Burgers vector and the rest of the terms are as defined for the equation 5.20. The difference between equation 5.20 and 5.23 is that $\gamma$ in the denominator of $Gb^2$ in the RHS of 5.20 is replaced by $\gamma - \frac{b}{2\sqrt{3}}\sigma_{\mathbf{n_p}\times\mathbf{b}}$. It is hence evident that the Escaig stress directly couples to the stacking fault energy and determines the stacking fault separation, in the same way that the stacking fault energy does.

The dependence of dissociation width on the stacking fault energy for split FR sources was studied in section 5.6.3. To understand the interplay of stacking fault energy and the Escaig stress in determining the stacking fault width, we have performed a series of dislocation dynamics simulations under different SFEs and Escaig stresses. The variation of the stacking fault width with SFE and Escaig stress is as shown in the figure 5.18. The x-axis is the stacking fault energy measured in units of $MPa.\dot{A}$, and the y-axis is the product of magnitude of Escaig stress times the magnitude of the Burgers vector, measured in $MPa.\dot{A}$. The z-axis is the computed average stacking fault width, averaged over the time of simulation. The contours lines projected on the $x-y$ plane are those $(x, y)$ points which yield the same stacking fault width. These contours are all fairly linear and are parallel to each other, indicating that the stacking fault energy and the applied Escaig stress couple linearly even in the case of the extended FR sources.

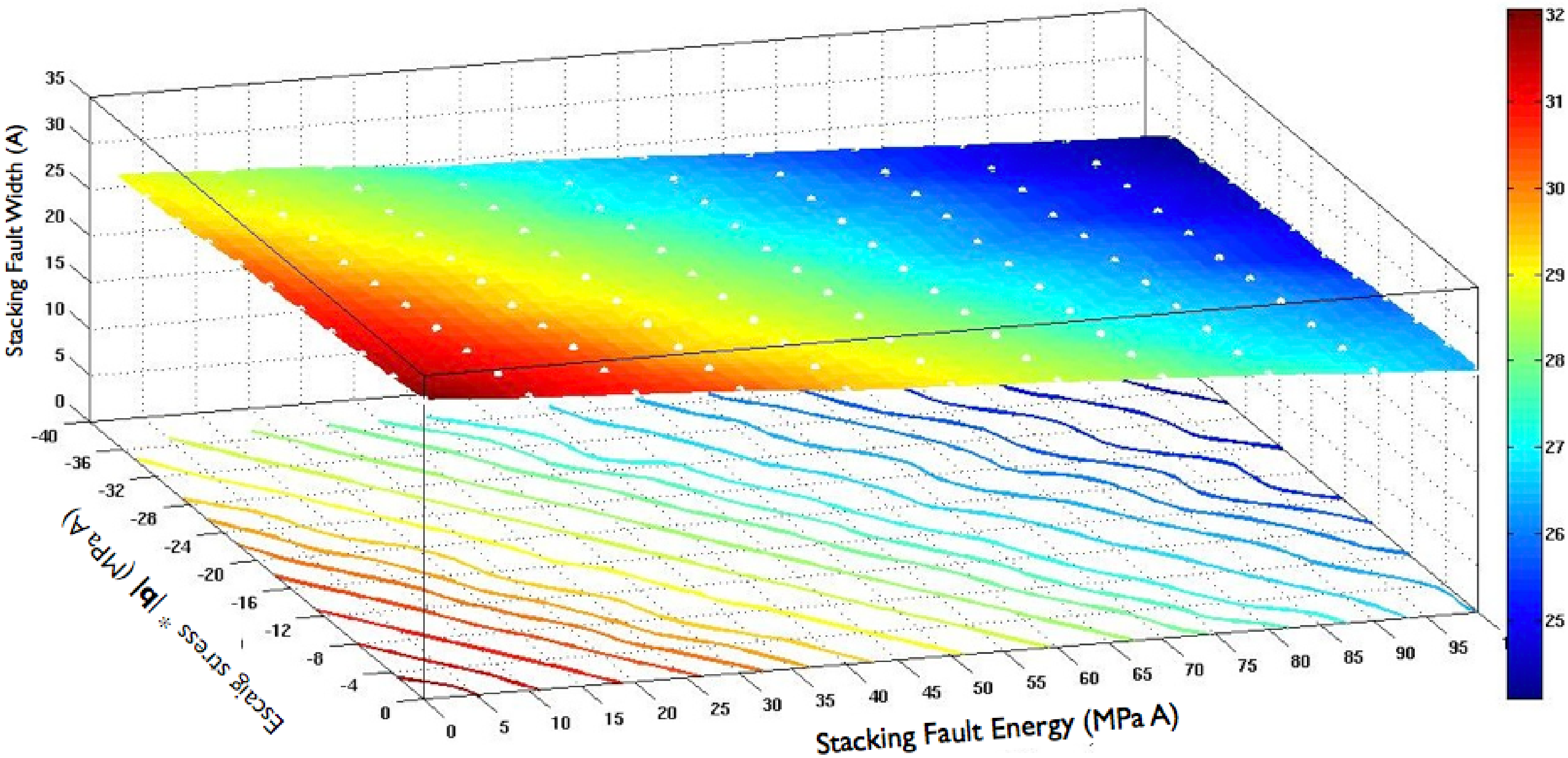


**Figure 5.18** – *The width of the stacking fault, at different values of the stacking fault energies and at various Escaig stresses. The contours indicates the regions of same width values.*

### 5.8.3 Escaig stress induced activation

A curious phenomenon that manifests only in the case of the split FR source (fig 5.4b) and is absent in both parallel split dislocation (fig 5.4a) and perfect FR source (5.4c) is the activation of each segment under high Escaig stress. If the Escaig stress is beyond a certain threshold, the partials of the split FR source bow out in opposite directions such that the radius of curvature of each of the partials exceeds half of the length of the dislocation, as shown in the figure 5.19.

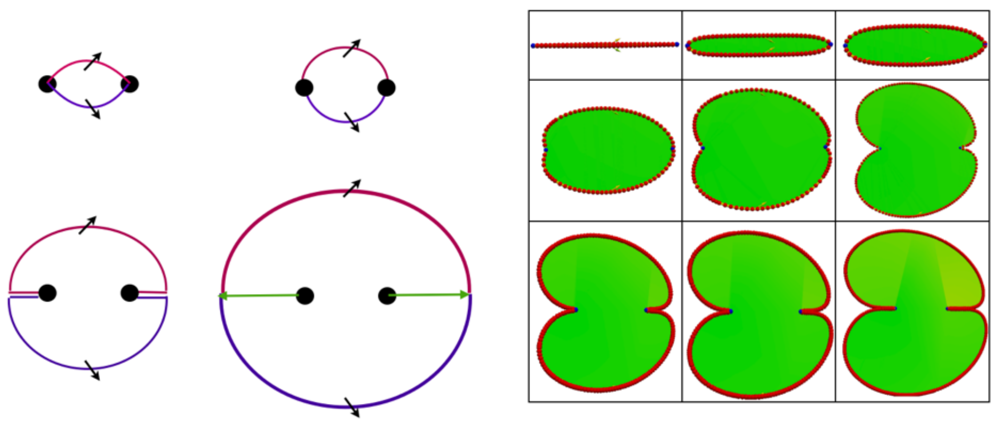

**Figure 5.19** – *The image on the left is a schematic of Escaig induced loop growth, and the images on the right are snapshots of DD simulations. The red circles are the dislocation nodes, and the area in green is the stacking fault area.*

At this point, those segments of partials that are aligned along the line joining the pinning points will tend to attract each-other as their line directions are now the reverse of their original line directions. If this attraction is strong enough, each of the two pairs of segments beyond each of the pinning points may coalesce into a perfect screw dislocation, and the rest of the loop may continue to grow indefinitely, increasing the length of the two perfect dislocations which connect the pinning points with the circumference of the growing loop.

Since the recombination process of split partials into a single perfect dislocation under the action of Escaig stress is not implemented in our present DD code, one way to verify whether the two half-loops would grow indefinitely is to do a simulation where the pinning points and the two partial dislocations are connected by two perfect dislocations. The initial configuration for such a simulation is as shown in figure 5.20.

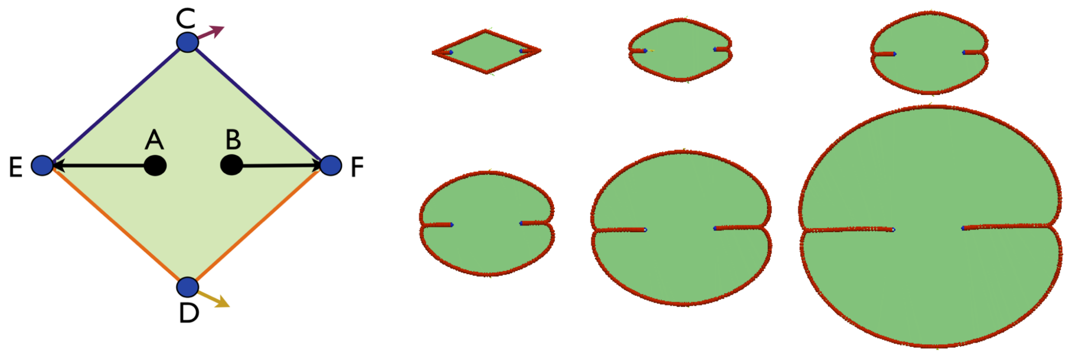


**Figure 5.20** – *The initial configuration for demonstrating the Escaig stress induced dislocation activation, and its evolution in the dislocation dynamics simulations. The points A and B represent the pinning points of the split FR source. C and D are the points of maximum separation. The dislocation segments AE and BF are the perfect dislocation, whereas the dislocation segments EDF and ECF represent the initial partial dislocation segments. The arrows at nodes C and D indicates the Burgers vector of the partial dislocations. The nodes E and F are two points at which three dislocations (two partial dislocations and one perfect dislocation) meet. Compare this figure with the FR multiplication figure 2.17 on page 58.*

The nodes E and F of the figure 5.20 are shared by all three dislocations and hence have a restricted degree of freedom. Their motion is confined to the line joining the pinning points AB. Note that this configuration is supposed to mimic the case where the arms of the two oppositely activated partials meet along the line joining the pinning points AB and merge into two perfect dislocations on either side of the pinning points. The dislocations AE and BF represent those two perfect dislocations. As the stress acting is a pure Escaig stress, it does cause the evolution of the two perfect segments AE and BF, and hence they always remain straight. If the stresses are not sufficient for the coalescence of the two partials dislocations into a perfect dislocation, the nodes E and F would collapse into the pinning points A and B respectively, in which case the there are no perfect dislocations in the simulation any more.

The above simulation was carried out under a constant Escaig stress of magnitude 1500 MPa, and the dislocation length is 1000 A. The stacking fault energy and other parameters are as given in table 5.3. One could estimate the activation stress for this Escaig assisted FR mechanism in a similar way as discussed in section 5.7 . It is found that it is easier to activate this mechanism in longer split FR sources than in shorter ones, which is intuitive.

This Escaig assisted FR like mechanism does not lead to continuous emission of dislocation loops as in the FR mechanism because one-half of the loop has a different Burgers vector from the other half and hence there is no possibility of annihilation of opposing segments.

In the conventional FR multiplication of split dislocations (see, for example figure 2.17 on page 58) the stacking fault also moves along with the partials including it, whereas in the present mechanism, the stacking fault spreads as the partials move away from each other. The Frank-Read evolution is possible for both pinned perfect dislocation source and pinned split dislocation source, whereas this Escaig stress induced loop growth is only possible for pinned split dislocation.

In the case of infinitely long parallel partial dislocations, recall that the dissociation width is given by the formula 5.23, and as discussed in [Byun 2003, Baudouin *et al.* 2013], the dissociation width approaches infinity at a critical Escaig stress of $\sigma^{c}_{\mathbf{n_p}\times\mathbf{b}} = \frac{\gamma}{b}$, where $\gamma$ is the stacking fault energy per unit area and $b$, the magnitude of the un-dissociated Burgers vector.

## 5.9 Dissociation width under simultaneous application of glide and Escaig stresses

### 5.9.1 Stress variation scheme:

If the shear direction $\mathbf{m}$ makes an angle other than $0$ or $\pi/2$ with the direction of the Burgers vector $\mathbf{b}$, the split dislocation will see both glide and Escaig stresses acting on it, and by systematically varying the direction of shear, one can control the glide and non-glide component of the stress.

The shear plane is kept at $\mathbf{n_p}$, but the shear direction is taken along

$$\mathbf{m} = \mathbf{b}cos\theta + (\mathbf{n_p} \times \mathbf{b})sin\theta \tag{5.24}$$

The angle $\theta$ defines the angle between the shear direction $\mathbf{m}$ and the Burgers vector $\mathbf{b}$. If the magnitude of the shear stress is $\sigma$, the resolved shear stress in the shear plane along the Burgers vector, indicated as $\sigma_{\mathbf{b}}$, is $\sigma cos\theta$ and the Escaig stress along the direction $\mathbf{n_p} \times \mathbf{b}$ , $\sigma_{\mathbf{n_p}\times\mathbf{b}}$, is $\sigma sin\theta$. As $\theta$ is varied from $0$ to $\frac{\pi}{2}$, the shear stress along the screw direction, $\sigma_{\mathbf{b}}$ decreases from $\sigma$ to $0$, whereas $\sigma_{\mathbf{n_p}\times\mathbf{b}}$ increases from $0$ to $\sigma$.

If the dislocation under consideration is a perfect screw, the component of stress along the perpendicular to the line direction, i.e., $\sigma_{\mathbf{n_p}\times\mathbf{b}}$ has no effect on its glide. Whereas, if the dislocation is a split screw dislocation, its partial dislocations have mixed character, and hence both $\sigma_{\mathbf{b}}$ and $\sigma_{\mathbf{n_p}\times\mathbf{b}}$ affect the dynamics of the partial dislocation segments.

Now, the simulation is carried out as follows:

A screw dislocation of length $L_{tot}$ is taken, and, at time $t = 0$, with $\mathbf{n_p}$ as the shear plane. The schematic flowchart for stress variation is given in figure 5.21

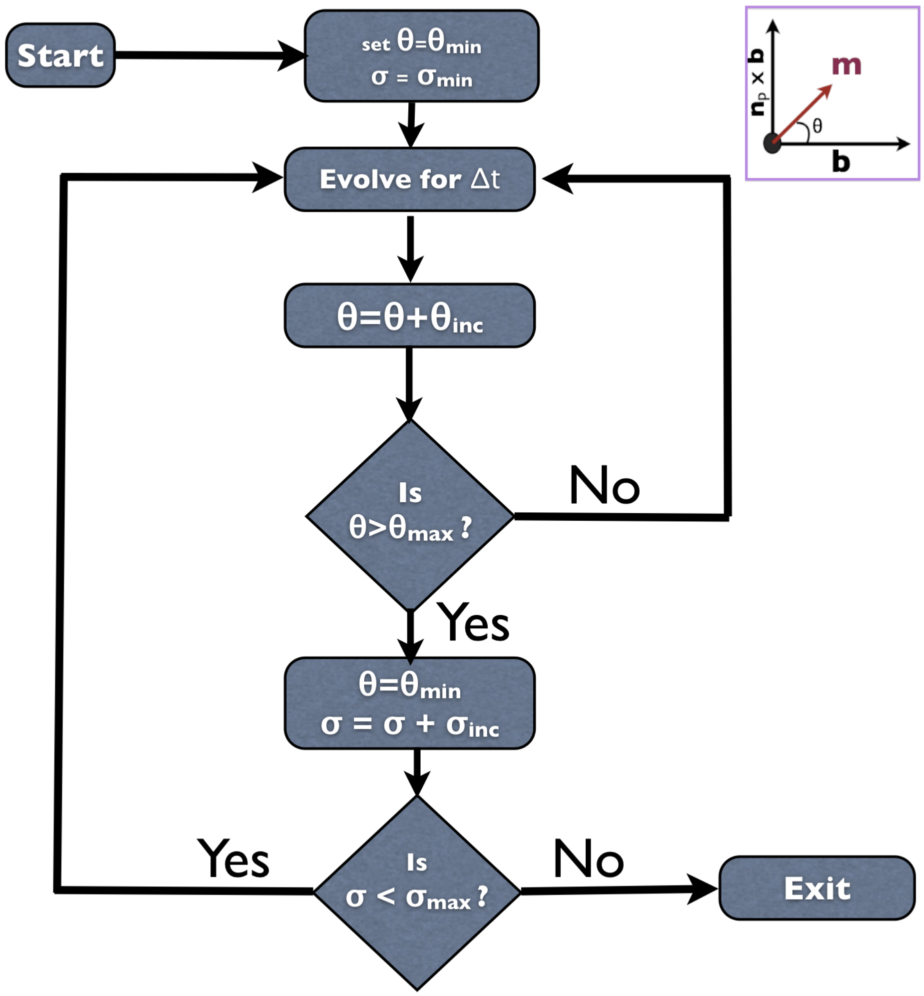


**Figure 5.21** – *Flow chart for the stress variation adopted in section 5.9. $\sigma$ is the stress magnitude and $\theta$ is the angle between the shear direction **m** and the Burgers vector **b**, as shown in the top right inset. At $\theta = 0^o$, the stress is pure glide stress whereas at $\theta = 90^o$, the stress is pure Escaig stress.*

The total simulation time is, hence

$$\Delta T = ((\theta_{max} - \theta_{min})/\theta_{inc} + 1)((\sigma_{max} - \sigma_{min})/\sigma_{inc} + 1)) \times \Delta t \tag{5.25}$$

The values used for these parameters are given in table 5.6.

**Table 5.6** – *Input parameters used in the simulation discussed in section 5.9*

| $L_{tot}(A)$ | $\theta_{min}$ | $\theta_{max}$ | $\theta_{inc}$ | $\sigma_{min}(MPa)$ | $\sigma_{max}(MPa)$ | $\sigma_{inc}(MPa)$ | $\Delta t$ (ns) |
|---|---|---|---|---|---|---|---|
| 500 | 0 | 360 | 10 | 0 | 300 | 30 | 2 |

The maximum shear stress $\sigma_{max}$ is less than the activation stress, so the dynamics of the dislocation remains completely irreversible. Also, the simulation time interval at each of the stress angle pair should be sufficiently long enough such that the dislocation has enough time to respond to the new stress amplitude and direction. The figure 5.22 shows the variation of glide and non-glide stresses acting on the system as a function of time.

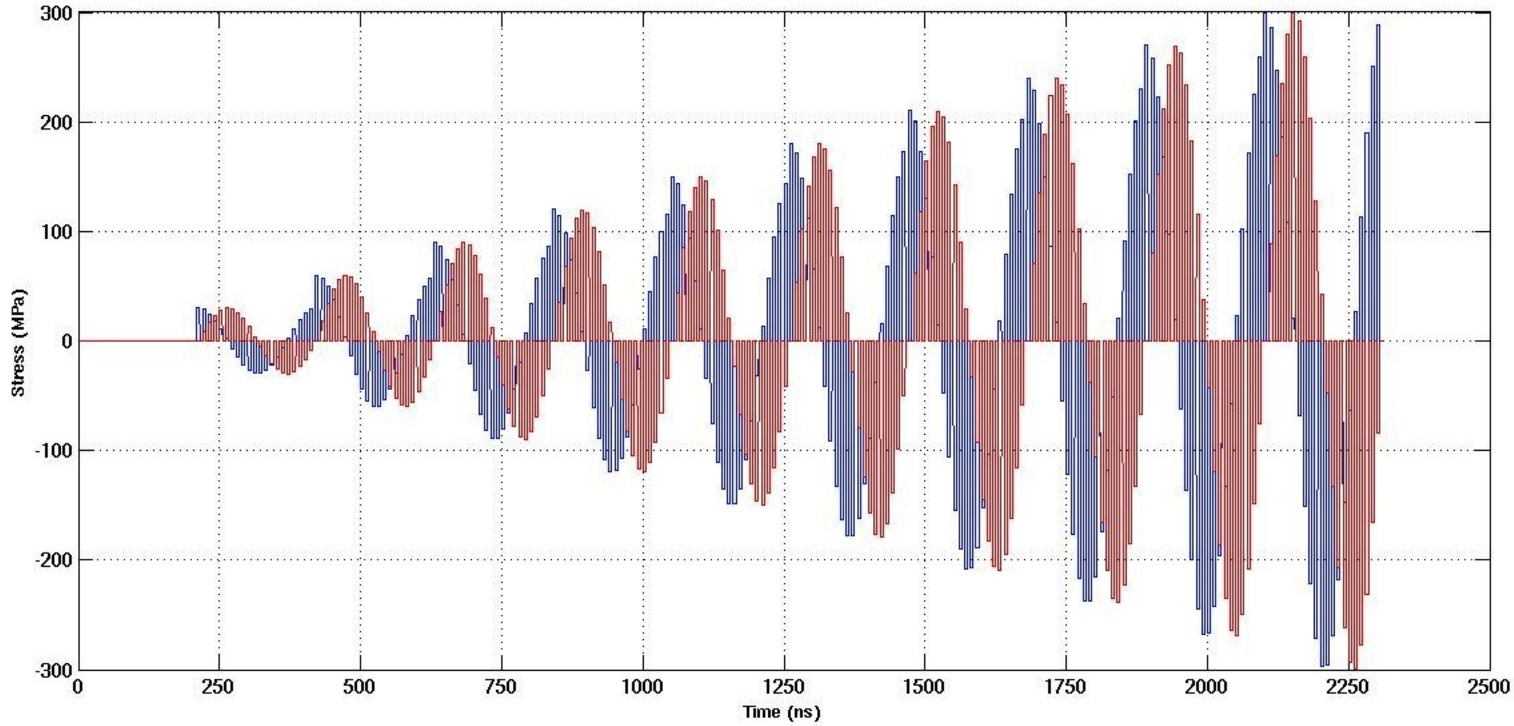


**Figure 5.22** – *Variation of glide and Escaig stresses as a function of time, when the angle $\theta$ and the stress amplitude $\sigma$ are progressively varied, according to the scheme given in figure 5.21. The two stresses, when nonzero, are out of phase with each-other and the amplitude of each of them is progressively varied from 0 to 300 MPa.*

Here, the glide and non-glide stresses are out of phase when non-zero. After performing simulations at every angle, the applied stress on the system is released such the system relaxes to its original state.

### 5.9.2 Results

The interest is to study the evolution of average separation between the partial dislocation under the action of glide and non-glide stresses. The operational rule for getting the average separation between the partials is explained earlier.

For a dislocation of length 1000 A, the variation of average separation is shown in figure 5.23.

Where the x-axis is the glide stress in MPa and the y-axis is the non-glide stress in MPa, and the color-coded data is the equilibrium stacking fault width at those stresses. It is evident that, in case of an FR source, the average stacking fault width depends on both the glide stress and the Escaig stress. The dependence of average width on the glide stress is due to the pinning of the partials, and is absent in the case of parallel split. It is readily visible from the above plot that the two partials are maximally separated when the glide stress is zero and the non-glide stress is at its positive maximum.

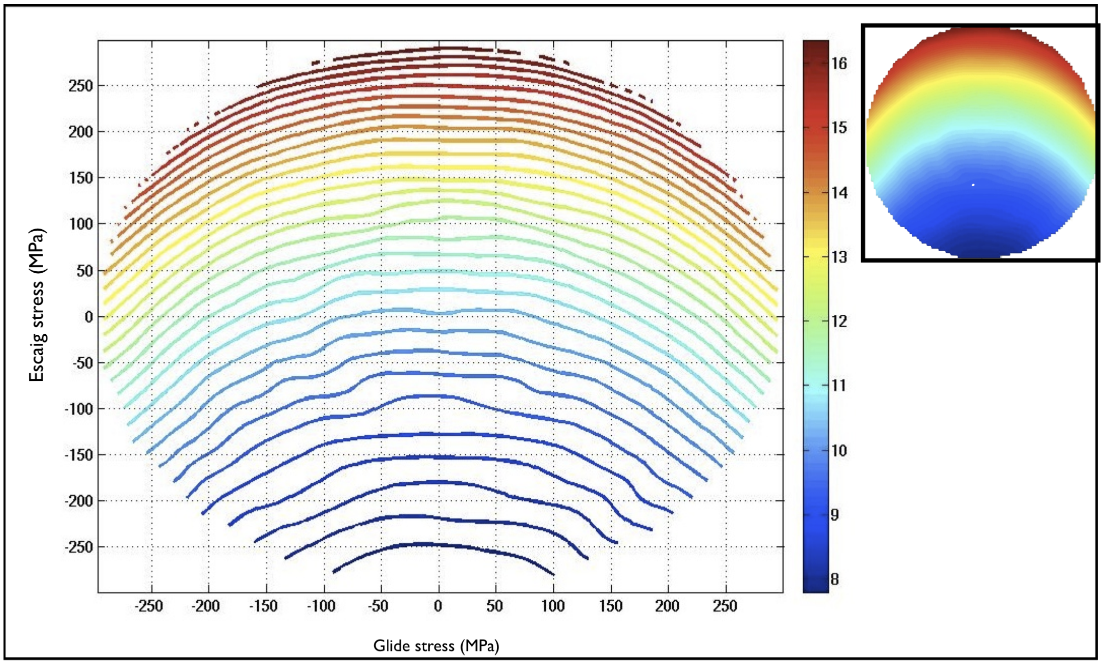


**Figure 5.23** – *Plot of dissociation width, color-coded as a function of Escaig and Glide stresses. The inset on the top right is the actual color-coded interpolated 2D plot of dissociation width, from which the main contour plot is obtained. The contours are those Escaig and Glide stresses which yield the same dissociation width. 30 contour lines are plotted here, color coded with their dissociated width. The units of the color code is Angstrom.*

It should be noted that the plot in figure 5.23 is symmetric about the vertical axis, but not about the horizontal axis. This is because a positive Escaig stress causes the dislocations to move away from each other and negative Escaig stress pulls them towards each other, whereas the glide stress will act identically on the two dislocations irrespective of its sign. It appears that all the contours can be easily approximated as the arc of circles. These circles are concentric, with the common center lying on the x=0 axis, at a negative Escaig stress, and zero glide stress. This means that if the Escaig stress is positive, to get the same width but at zero Escaig stress, the glide stress has to be higher in magnitude than the Escaig stress, and vice-versa. The whole plot itself is disc shaped, and this is just because of the stress variation scheme employed.

This is more visible in the plot 5.24. The blue plot in this figure gives the instantaneous dissociation width under the action of the glide and Escaig stresses acting at that point of time. This is normalized to its value under the absence of the stresses. The simulation time under each window of stresses is long enough such that the dissociation width attains a constant value. The width returns back to its zero stress value as soon as the stresses acting on the system are withdrawn. At a stress amplitude of 150 MPa, the largest dissociation width is about 25% more than the no-stresses width, whereas the smallest dissociation width is about 20% less than the no-stresses value. These maximum and minimum dissociation widths both occur when the glide stress is zero and the Escaig stress is at its positive and negative amplitude respectively.

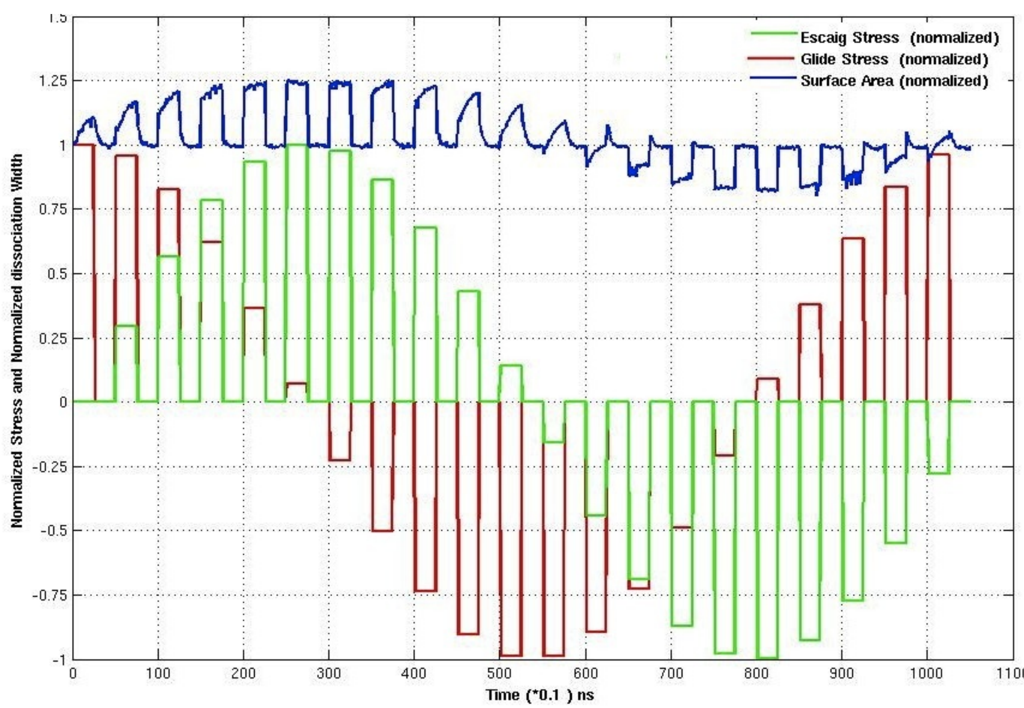


**Figure 5.24** – *Variation of dissociation width with normalized stresses. Each of the stresses is normalized to its maximum value and the dissociation width is normalized with its value in the absence of any external stresses. The green plot indicates the Escaig stress and the red plot is the variation of glide stress. These stresses correspond to one particular amplitude of $\sigma = 150$ MPa and the $\theta$ varied from $0$ to $2\pi$.*

It will be more instructive to trace the average dissociation width as a function of the angle $\theta$ of equation 5.24. Towards that end, a split screw FR source of length $300A$ is considered and a shear stress of a fixed amplitude is applied on its glide plane $\mathbf{n}_p$ but along different directions $\mathbf{m}$, varied with time. At every $\theta$, the dislocations are allowed to evolve for a period of $100ns$, and the instantaneous dislocations length and the stacking fault area is recorded at every 0.01ns. Note that the applied stress is not set back to zero between each angle increment as in the previous case corresponding to figure 5.24.

The average dislocation length and the average stacking fault area enclosed by the partials, as a function of $\theta$ (of equation ( 5.24 on page 185)) is shown in the figure 5.25, for a stress amplitude of 250 MPa. Here, the total dislocation length and the stacking fault area are plotted separately for the purpose of clarity.

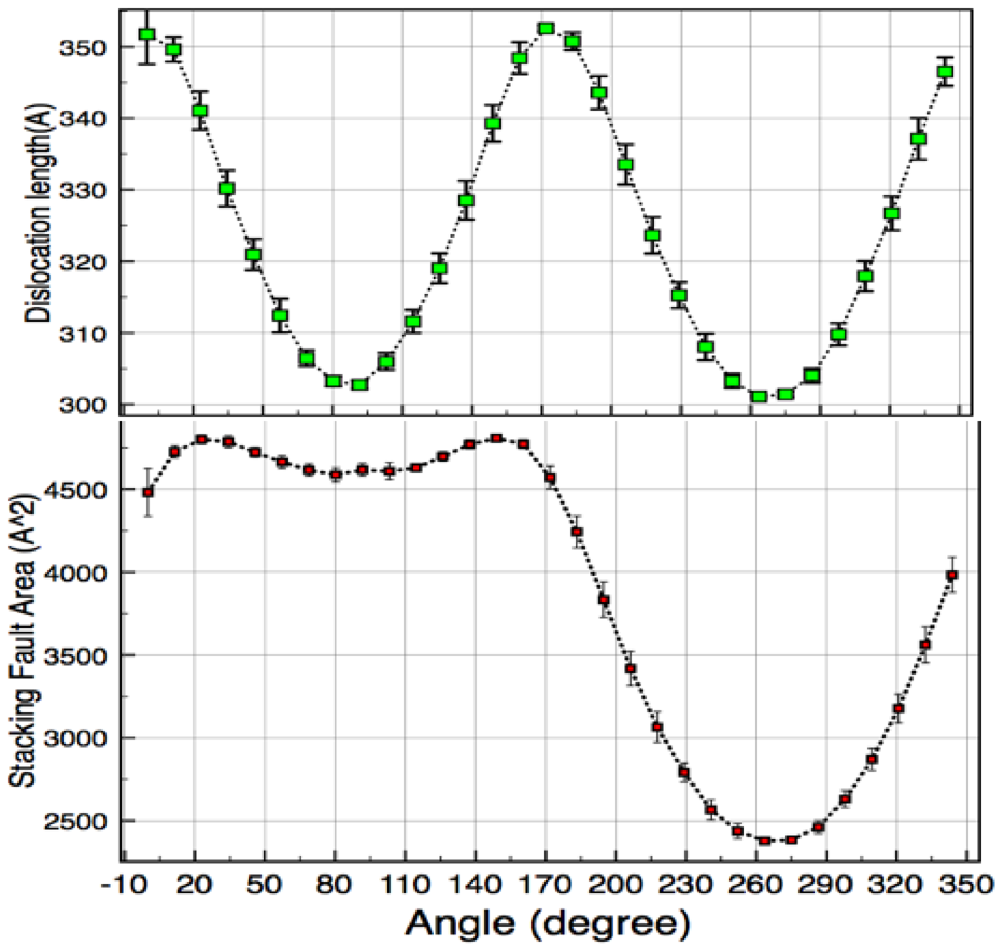


**Figure 5.25** – *Change of dislocation length and the stacking fault area at different angles of shearing. The dots represent the mean of the values recorded at the different times, and the error bars are the standard deviation of these quantities.*

Referring to the figure 5.25, the average dislocation length (defined as the half of the sum of the lengths two partials) is maximum when the angle is $0$ or $180$, and minimum at $\theta = 90^o$ and $\theta = 270^o$. The minimum value is very close to the distance between the pinning points ($300A$). The average dissociation width is the ratio of the stacking fault area and the average dislocation length. The variation of this dissociation width is shown in figure below, along with similar plots at every stress amplitudes is shown in figure 5.26.

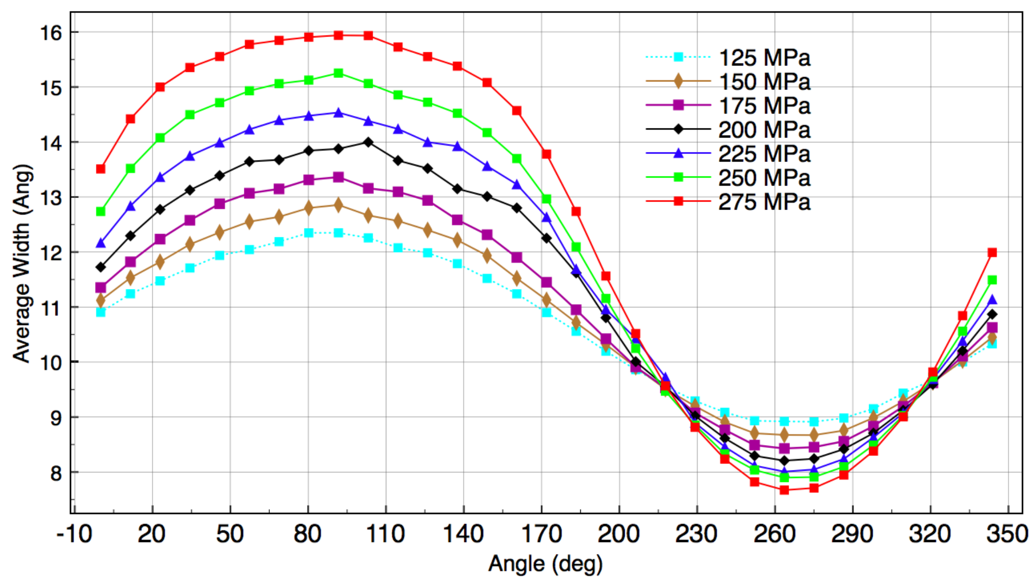


**Figure 5.26** – *Variation of dissociation width with the angle between the glide direction* $\mathbf{m}$ *and Burgers vector* $\mathbf{b}$*. Seven different stress amplitudes were considered.*

From the plot of 5.26, it is clear that the dissociation width is maximum for $\theta = 90^o$, that is, when the glide component is zero, and all the stress is along $\mathbf{n}_p \times \mathbf{b}$ direction (positive Escaig stress). The minimum of the width falls at about $\theta = 270^o$, which also means that the glide component of the stress is zero and all the stress is along the $\mathbf{b}\times\mathbf{n}_p$direction (Negative Escaig stress). This trend is also visible from the plot 5.23, where the minimum and maximum dissociation widths falls on the $\sigma_\mathbf{b}$ $=0$ axis. It should also be noted that the average dissociation width becomes independent of the applied stress, if the angle $\theta = 210°$ or $\theta = 330°$.

### Dissociation width in presence of obstacles in the glide plane

The glide stress will have a greater impact on the partial width if the motion of the leading partial is arrested due to the presence of any impenetrable barrier in its glide path. Once the leading partial is immobilized, the trailing partial gets pushed towards it and hence the stacking fault width decreases with increasing glide stress. A split FR source is considered, with two planar facets placed at a distance of 10 A, whose lengths are parallel to the dislocation line and whose normal are along the glide direction of the dislocation. The variation of stacking fault width in such an arrangement is shown in figure 5.27.

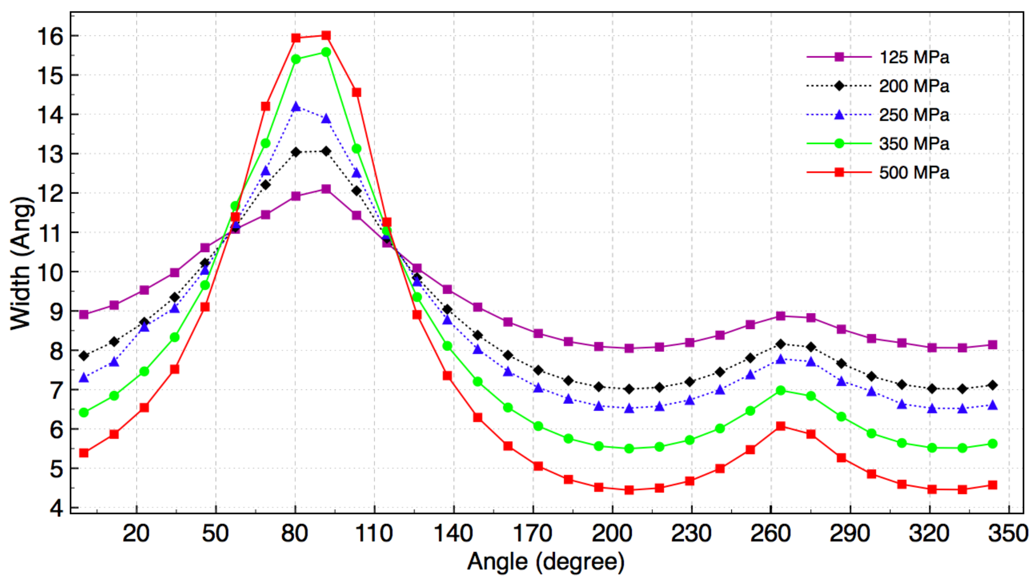


**Figure 5.27** – *Variation of dissociation width as a function of the angle between the shear direction* $\mathbf{m}$ *and the Burgers vector* $\mathbf{b}$*, in the presence of an impenetrable barrier along the glide direction of the dislocation, at a very close distance to it. Different lines correspond to different stress magnitudes, applied on the* $\mathbf{n}_p$ *plane along the direction* $\mathbf{m}$ *given in eq 5.24*

The plot 5.27 is to be compared to the plot 5.26, to understand the effect of an obstacle on the dissociation width. In the presence of an obstacle along the glide direction, although the maximum dissociation width continues to be at $\theta = 90°$, the minimum is no longer at $\theta = 270°$. In fact, the point $\theta = 270°$ is a local maxima. Also, the dissociation width is independent of the applied stress when the angle is about $90° \pm 30°$. The qualitative effect of the obstacle is more visible in plot 5.28, which shows the two widths for a particular stress amplitude of $250MPa$.

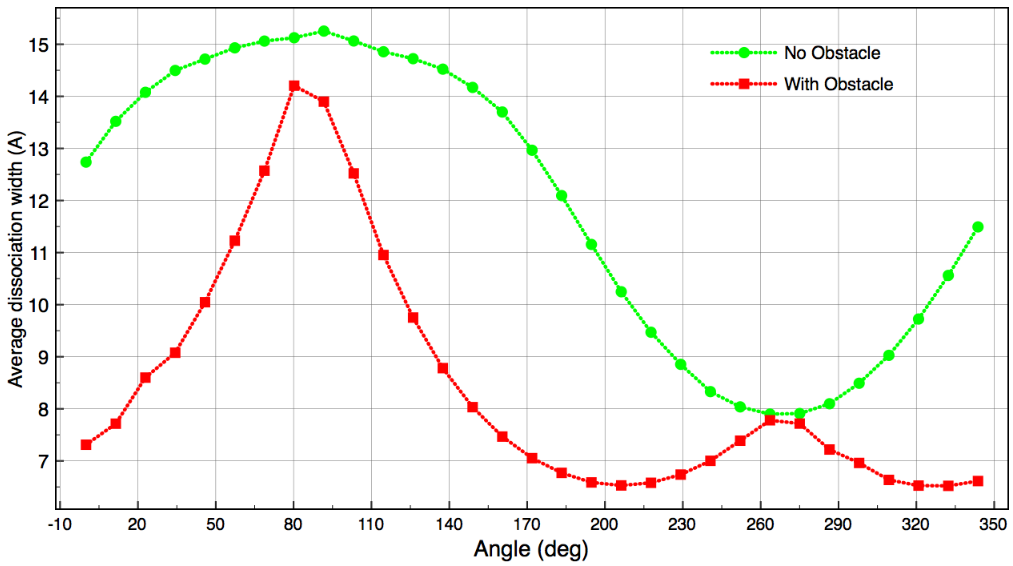


**Figure 5.28** – *Comparison of plots 5.26 and 5.27, at one particular stress amplitude of 250 MPa.*

From figure 5.28, it can be seen that the average dissociation width is the same in presence and absence of the obstacles only at $\theta = 270°$ and at all other angles the presence of obstacle reduces the average dissociation width. The variation of dissociation width with angle, in the presence of obstacles is more steeper and attains a minimum at $\theta = 210°$ and at $\theta = 330°$, that is $\theta = 270° \pm 60°$. These two points are identical to the angles where the dissociation width becomes independent of the amplitude of the applied stress in no obstacle case (refer to figure 5.26).

## 5.10 Conclusions

The Evolution of extended Frank-Read source is studied under non-singular stress formulation and contrasted with that of perfect FR source and the parallel split dislocations.

1. The split FR source is found to be energetically favorable compared to a perfect FR source, for dislocations of all line characters.

2. The equilibrium stacking fault width of a split parallel dislocation computed in the non-singular stress formalism, is almost equal to that predicted by the classical elastic theory.

3. It is found that the average dissociation width increases as the line character is varied from screw to edge.

4. It is also found that the average dissociation width decreases with increasing stacking fault energy for the pinned FR sources of all line characters.

The role of glide and non-glide stresses on the average dissociation width of a dissociated FR source is investigated here for the first time. The salient observations are:

1. Under the application of pure glide stress, the dynamics of a split FR source is almost identical to that of the perfect FR source, with respect to the plastic deformation that is induced.

2. The inclusion of Escaig stresses, however, causes the dynamics of a split FR source to differ significantly from that of a perfect FR source which does not respond to Escaig stresses at all.

3. It is demonstrated that once the applied Escaig stress reaches a critical threshold, the two arms of the split FR source get activated away from each other such that the fault region increases continuously, but without emission of loops. This feature cannot be expected in a perfect FR source, which does not get influenced by the Escaig stresses, and parallel split dislocations where the parallels are not pinned, and the partials arms cannot get activated.

4. This Escaig assisted FR like mechanism does not lead to continuous emission of dislocation loops as in the FR mechanism because one-half of the loop has a different Burgers vector from the other half and hence there is no possibility of annihilation of opposing segments.

5. The dynamics of a split FR source under controlled simultaneous application of Escaig and glide stresses is studied and it was found that, in the absence of the obstructions on the glide plane, the stacking fault width is more sensitive to the Escaig stress than to the glide stress.

6. If the leading partial dislocation is blocked in its glide plane, the glide stress component more significantly influences the dissociation width than the Escaig stress.

# Chapter 6

# Dynamics of a Frank-Read source with constrictions

---

*A pinned split screw dislocation with pre-existing constrictions is considered, and its dynamics is studied under a systematic variation of the glide and Escaig stresses acting on its primary and cross-slip planes. These results are compared and contrasted with that of pinned but perfect screw on one hand and unpinned parallel split screw on the other.*

---

## 6.1 Introduction

In Chapter 5, the dynamics of a split FR source was studied under controlled variation of glide and non-glide stresses. There the focus was to understand the role of these stresses on the enclosed stacking fault and hence on the average dissociation width of the split FR sources. The study was appropriate for dislocations of all line characters. In the present chapter, we study the role of these glide and Escaig stresses on the cross-slip of the dissociated screw dislocation.

Cross-slip is a phenomenon whereby a screw dislocation leaves its glide plane and begins to glide in the corresponding conjugate glide plane (Two planes are conjugate to each other with-respect to a dislocation if they share its Burgers vector). At temperatures where climb is inhibited, the only way that the strain can spread itself across the grain and homogenize itself is by cross-slipping of the screw dislocations, as seen in the earlier chapters (Chapter 3 and Chapter 4).

Cross-slip is an activated phenomenon, and the parameters governing its rates are not yet fully understood [Püschl 2002]. Cross-slip in fcc is a more involved problem as the dislocations in fcc are known to exist as a pair of Shockley partials, which enclose a stacking fault between them [Kelly & Knowles 2012]. It is now understood that cross-slip rate depends sensitively on the local stresses acting on the partials constituting the split screw dislocation. Cross-slip activation parameters have been studied through the elastic theory of dislocations [Escaig 1968, Duesbery *et al.* 1992, Saada 1991] as well as molecular dynamics simulations [Rao *et al.* 2009].

Here our focus shall be confined to a screw dislocation, constructed such that a fraction of its length has already cross-slipped and can glide in its corresponding glide-plane, which is conjugate to the glide-plane of the original un-slipped section. The evolution of this *composite* screw dislocation under the various Glide and Escaig stresses shall be the focus of this study. This study, hence, bypasses the questions about nucleation of constriction points, and their subsequent motion away from each other. These questions are, in-fact, beyond the scope of the dislocation dynamics scheme, as this technique is applicable only beyond a certain length-scale, whereas mechanisms that govern cross-slip operate at a much smaller time scale.

## 6.2 Background

### 6.2.1 Modeling cross-slip mechanism in fcc

The Shoeck and Seeger (SS) model [Schoeck & Seeger 1955, Wolf 1960] was one of the first models for cross-slip. It postulates that for cross-slip to occur the dissociated partials in the primary plane should recombine over a certain length, and then bow out in the cross-slip plane. There is a critical configuration for the bowed-out configuration of the cross-slip segment, beyond which the cross-slip is successful, see figure 6.1a and b. Friedel modified this mechanism by observing that the dislocation segment in the cross-slip plane can split into partials, and reduce the energy, as in figure 6.1c. The Friedel-Escaig (FE) model enhances the Friedel model by postulating that the cross-slip segment can split into partials as soon as the constrictions can occur, as shown in figure 6.1d and 6.1e.

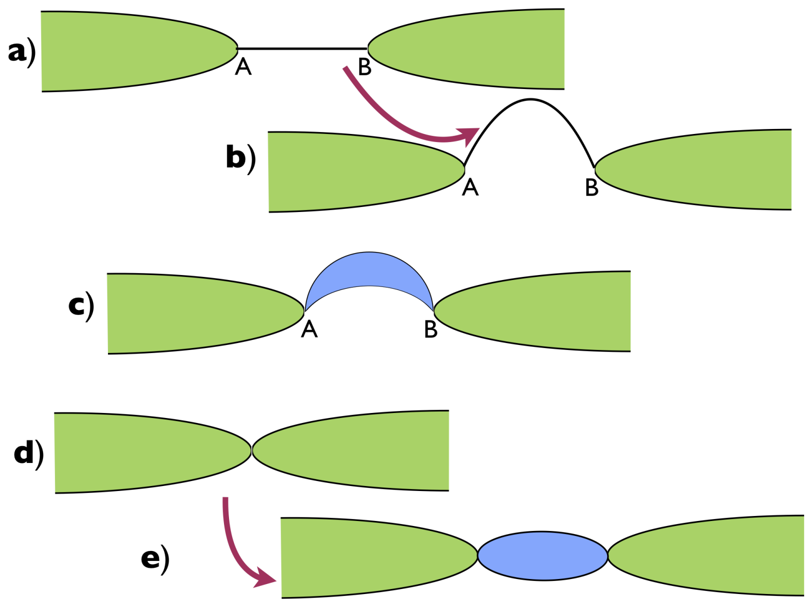


**Figure 6.1** – *Proposed cross-slip mechanisms: a,b) the Schoek-Seeger mechanism. c) The Friedel mechanism. d,e) The Friedel/Escaig mechanism. The regions in green are the stacking faults in the primary plane and the blue regions are the faulted regions on the corresponding cross-slip plane.*

#### 6.2.1.1 Fleischer mechanism

This is an alternate mechanism for cross-slip where there is no requirement for formation of constriction. The model is explained below:

Let $(11\bar{1})$ and $(1\bar{1}\bar{1})$ be the primary and cross-slip planes. In the FE mechanism, the dissociation proceeds as

$$\frac{a}{6}[112] + \frac{a}{6}[2\bar{1}1] \rightarrow \frac{a}{2}[101] \tag{6.1}$$

and

$$\frac{a}{2}[101] \rightarrow \frac{a}{6}[1\bar{1}2] + \frac{a}{6}[211] \tag{6.2}$$

That is, the dissociated screw first recombines in the primary plane and then splits in the cross-slip plane. The activation energy for this reaction is equal to the energy required for recombination reaction, eq 6.1. Fleischer proposed [Fleischer 1959] an alternative mechanism that does not require the recombination of the partials for cross-slip to take place. According to this alternate mechanism, cross-slip can occur when the leading partial, say $\frac{a}{6}[2\bar{1}1]$, dissociates into two partials one of which glides on the cross-slip planes and other remains sessile on the intersection of the two planes.

$$\frac{a}{6}[2\bar{1}1] \rightarrow \frac{a}{6}[211] + \frac{a}{3}[0\bar{1}0] \tag{6.3}$$

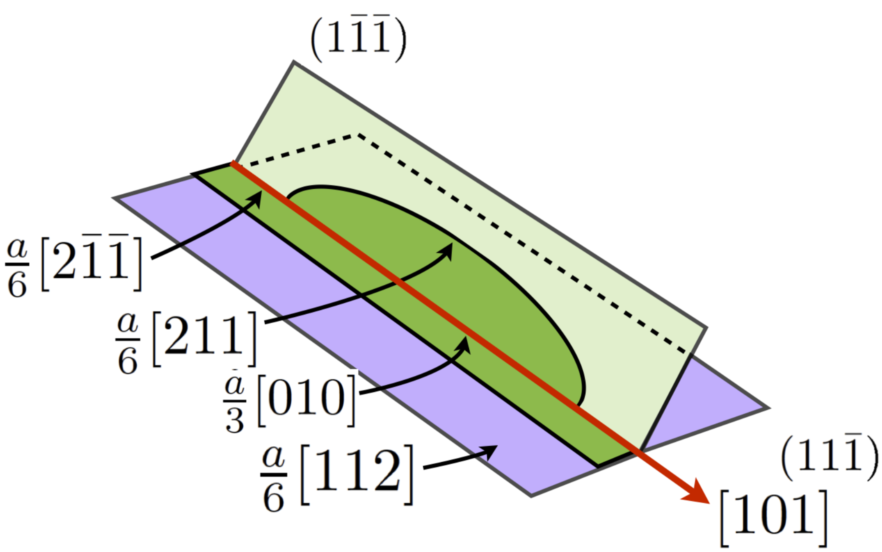


**Figure 6.2** – *Cross-slip, according to Fleischer mechanism.*

The dislocation with Burgers vector $\frac{a}{6}[211]$ is glissile on the cross-slip plane $(1\bar{1}\bar{1})$, so the partial glides on the cross-slip plane whereas the partial with Burgers vector $\frac{a}{3}[0\bar{1}0]$ remains sessile at the intersection of the primary and cross-slip planes. Now, the second partial of the original split dislocation combines with this $\frac{a}{3}[0\bar{1}0]$ and generates the second partial on the cross-slip plane.

$$\frac{a}{6}[112] + \frac{a}{3}[0\bar{1}0] \rightarrow \frac{a}{6}[1\bar{1}2] \tag{6.4}$$

This mechanism of cross-slip, however, was shown to require too much activation energy and is observed only under high stresses. The next section, hence details the FE mechanism introduced earlier.

Since the interest in this chapter is in examining cross-slip through the Friedel-Escaig mechanism of 6.1e, this model is explained in the section 6.2.1.2.

#### 6.2.1.2 Friedel-Escaig mechanism

In the FR model, cross-slip proceeds as follows: (see figure 6.3)

**Step 1:** Formation of a point constriction on a dissociated screw segment, C (figure 6.3b).

**Step 2:** Under stress, this point constriction splits into two constrictions, which are split in the cross-slip planes (figure 6.3c).

**Step 3:** If the length of the cross-slipped segment reaches a critical value, the whole dislocation irreversibly spreads into the cross-slip plane (figure 6.3d).

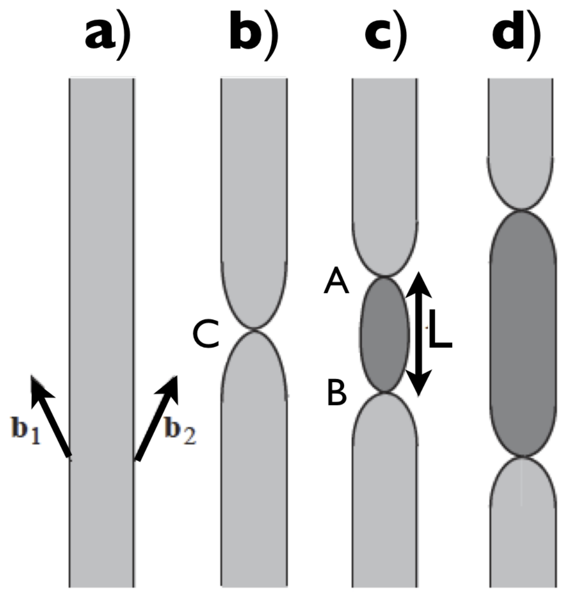


**Figure 6.3** – *Friedel-Escaig mechanism of cross-slip.*

Consider the Thompson's tetrahedron in fcc (see section 5.2 on page 151). Recollect that the edge of this tetrahedron represent the possible Burgers vectors in fcc. Consider one such side of the tetrahedron, represented by the vector $\mathbf{b}$ in the figure 6.4. Now, let the two faces of the tetrahedron that share this side be $\mathbf{n}_p$ and $\mathbf{n}_{cs}$. A screw with this Burgers vector can hence, glide on either of the two glide planes $\mathbf{n}_p$ and $\mathbf{n}_{cs}$. This screw dislocation can also split into two partial dislocations which are glissile in one of these two planes. For concreteness, we choose the glide plane and Burgers vector as shown in the table given along with the figure 6.4.

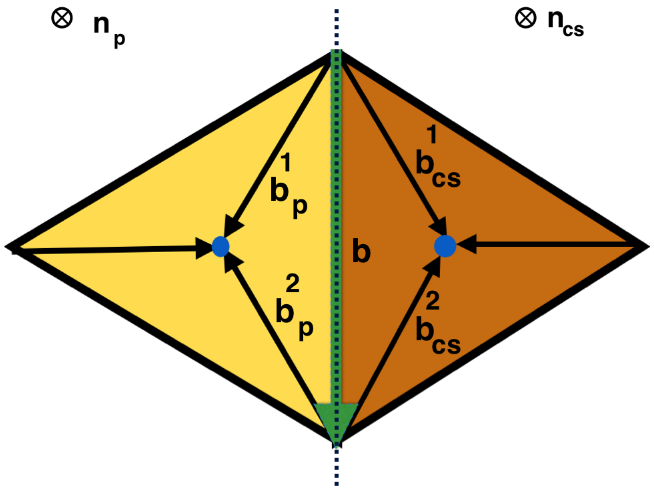


| Normal | Burgers Vector | First partial | Second Partial |
|---|---|---|---|
| $\mathbf{n}_p = (\bar{1}1\bar{1})$ | $\mathbf{b} = \frac{a}{2}[\bar{1}\bar{1}0]$ | $\mathbf{b}_p^1 = \frac{a}{6}[\bar{1}\bar{2}\bar{1}]$ | $\mathbf{b}_p^2 = \frac{a}{6}[\bar{2}\bar{1}1]$ |
| $\mathbf{n}_{cs} = (1\bar{1}\bar{1})$ | | $\mathbf{b}_{cs}^1 = \frac{a}{6}[\bar{2}\bar{1}\bar{1}]$ | $\mathbf{b}_{cs}^2 = \frac{a}{6}[\bar{1}\bar{2}1]$ |

**Figure 6.4** – *The section of the Thompson's tetrahedron that is of interest to this work. A screw dislocation with Burgers vector* $\mathbf{b}$ *lies along the side common to both the faces,* $\mathbf{n}_p$*and* $\mathbf{n}_{cs}$*. This dislocation can hence split to partials on either of the planes. The table here shows the possible Burgers vectors for splitting in* $\mathbf{n}_p$ *and* $\mathbf{n}_{cs}$*. See table 5.2 on page 154 for more information.*

These vectors satisfy these requirements

| |
|---|
| $\mathbf{b} = \mathbf{b}_p^1 + \mathbf{b}_p^2 = \mathbf{b}_{cs}^1 + \mathbf{b}_{cs}^2$ |
| $\mathbf{n_p}.\mathbf{b} = \mathbf{0} \qquad and \qquad \mathbf{n_{cs}}.\mathbf{b} = \mathbf{0}$ |
| $\mathbf{n_p} \times \mathbf{n_{cs}} = \mathbf{b}$ |
| $\mathbf{n_p}.\mathbf{b_p^i} = \mathbf{0}, i = 1,2 \qquad and \qquad \mathbf{n_{cs}}.\mathbf{b_{cs}^i} = \mathbf{0}, i = 1,2$ |
| $\mathbf{n_p}.\mathbf{b_{cs}^i} \neq \mathbf{0}, i = 1,2 \qquad and \qquad \mathbf{n_{cs}}.\mathbf{b_p^i} \neq \mathbf{0}, i = 1,2$ |

Now, a general stress tensor acting on the composite screw dislocation couples to both the planes and the four partial Burgers vector. Given a general stress tensor of the form,

$$\overleftrightarrow{\sigma} = \begin{bmatrix} \sigma_{11} & \sigma_{12} & \sigma_{13} \\ \sigma_{12} & \sigma_{22} & \sigma_{23} \\ \sigma_{13} & \sigma_{23} & \sigma_{33} \end{bmatrix}$$

The projection of this stress in the primary and cross-slip planes is $\overleftrightarrow{\sigma}.\mathbf{n}_p$ and $\overleftrightarrow{\sigma}.\mathbf{n}_{cs}$. The component of the applied stress that is actually responsible for the glide of the dislocation is the stress resolved in the glide plane, along the direction of the Burgers vector. If the dislocation is perfect with a Burgers vector $\mathbf{b}$, the glide components of stress in the primary and cross-slip planes are $\overleftrightarrow{\sigma}.\mathbf{n_p}.\mathbf{b}$ and $\overleftrightarrow{\sigma}.\mathbf{n_{cs}}.\mathbf{b}$ [1]. These stresses are responsible for the overall glide of the dislocation in the primary and cross-slip plane. If the dislocation is now split in the primary and cross-slip plane, then apart from these two stresses, there are another component acting on the primary and cross-slip planes but along the edge directions in those planes given by $\overleftrightarrow{\sigma}.\mathbf{n_p}.(\mathbf{n_p} \times \mathbf{b})$ and $\overleftrightarrow{\sigma}.\mathbf{n_{cs}}.(\mathbf{n_{cs}} \times \mathbf{b})$. The aim of this chapter is to understand the dynamics of the composite screw Frank-Read source under different glide and Escaig stress values in the primary and cross-slip planes.

A possible instantaneous configuration of a composite perfect FR source of length $L_p + L_{cs}$ under an action of an arbitrary stress is shown in figure 6.5. The section of the screw of the length $L_p$ from the left glides in the primary plane $\mathbf{n}_p$ and the rest of the screw has the glide plane $L_{cs}$. Since the Schmid factor need not be same on $\mathbf{n}_p$ and $\mathbf{n}_{cs}$, the bowing out of these segments will be different. Here, we examine the role of glide and Escaig stresses acting on $\mathbf{n}_p$ and $\mathbf{n}_{cs}$ on the dynamics of such a composite configuration.

[1]see section 2.2.6 on page 41.

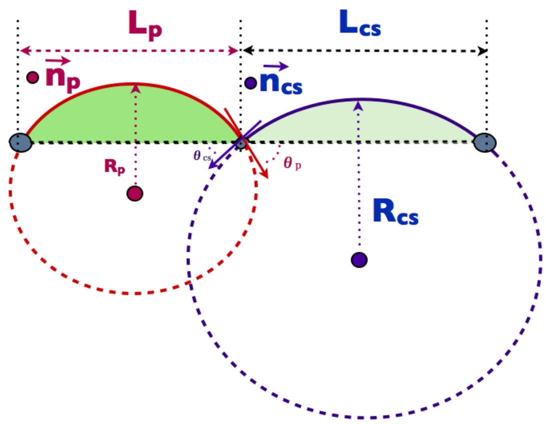


**Figure 6.5** – *Instantaneous configuration of a partially cross-sliped perfect composite screw FR source of total length $L_p + L_{cs}$. A segment of length $L_p$ from the left end (colored in red) glides in one plane $\mathbf{n}_p$ and the rest of the segment of length $L_{cs}$ (colored in blue) glides in another equivalent plane $\mathbf{n}_{cs}$. The arrows at the common point indicates the direction of the line tension. The segment bowing out in the primary plane is an arc whose radius of curvature is $R_p$ and similarly $R_{cs}$ is the radius of curvature of the segment bowing out in the cross-slip plane.*

## 6.3 Computational Details

These simulations are carried out in NUMODIS [L. Dupuy & Coulaud 2013], the node based dislocation dynamics software. The algorithm for these simulations is given in section 2.3 on page 49. These studies are carried out in the non-singular elastic theory formalism proposed in reference [Cai *et al.* 2006].

### 6.3.1 Material parameters

The materials parameters used for all these simulations (unless otherwise mentioned) are listed in table 6.1. The shear modulus $\mu$, Poisson's ratio $\nu$ and the stacking fault energies are taken according to those given in [Argon 2008].

| Material | a ($\dot{A}$) | $\mu$(GPa) | $\nu$ | SFE $mJ/m^2$ | Primary Slip System | Cross-slip Slip System |
|---|---|---|---|---|---|---|
| Cu | 3.661 | 41 | 0.3 | 73 | $(\bar{1}1\bar{1})[\bar{1}\bar{1}0]$ | $(1\bar{1}\bar{1})[\bar{1}\bar{1}0]$ |

**Table 6.1** – *Material parameters used in this simulation.*

### 6.3.2 Simulation details:

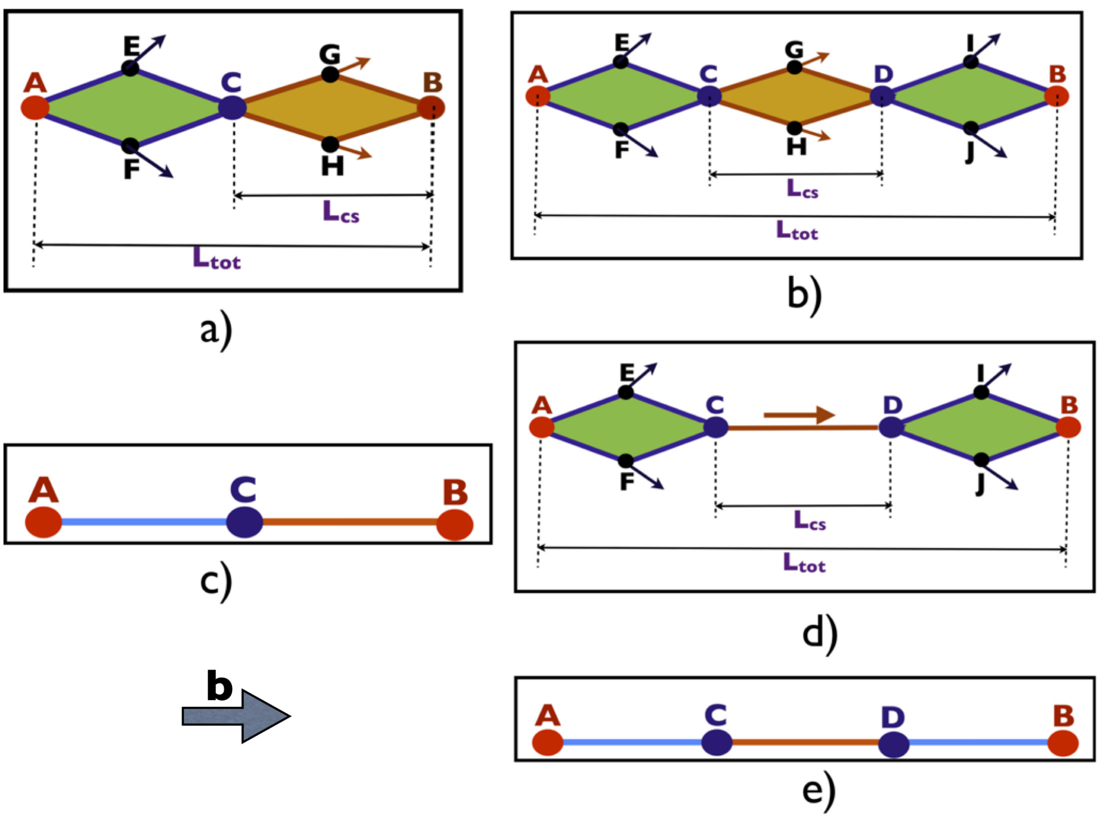


**Figure 6.6** – *The dislocation configurations used in these simulations. See text for description.*

The figure 6.6 shows the configurations used in these simulations. (Section 5.2.6 on page 161 details the initial construction procedure for split dislocation of arbitrary line character).

The nodes A and B are the pinning points of the FR source. The images c) and e) represent the composite FR source constructed from perfect dislocations. Consider first figure c. It consists of two dislocation segments: section AC and section CB. They both are screw dislocations, having the same Burgers vector, but differ in their glide plane. AC glides in the plane $\mathbf{n_p}$, whereas CB glides in the plane $\mathbf{n}_{cs}$. The figure e is similar, except that the segment that glides on the cross-slip plane originates at the central regions instead of the right end as in "c". AC and DB are dislocations gliding on the primary glide plane and the section CD glides on the cross-slip plane. Now, figure 6.6a represents a composite split FR source corresponding to the case 6.6c. The dislocation segment AC of figure 6.6c is now split into two partial dislocations AEC and AFC. This splitting takes place in the glide plane of that dislocation, i.e., $\mathbf{n}_p$. The arrows on the points E and F indicate the direction of the Burgers vector of these dislocations. Similarly, the segment CB of figure 6.6c is split into CGB and CHB, but now the splitting happens in the glide plane of the section CB i.e., in the plane $\mathbf{n}_{cs}$. The arrows on G and H indicate the Burgers vectors of these partials and they are different from the Burgers vectors of the partials AEC and AFC. Now, consider image 6.6b. It is also identically constructed as in 6.6a, except that the cross-slipped section originates from the central region, rather than from the right. The left and right segments of this configuration glide on the primary plane, whereas the central split dislocations glide on the cross-slip glide plane. The image 6.6d, represents a configuration where the central segment is not split into partials dislocations as in figure 6.6b, but is of perfect Burgers vector.

The nodes A and B are pinned and hence they don't evolve with time. The points C and D are the points where more than two dislocations with different Burgers vectors meet. Hence, compared to the other nodes, these "*physical* nodes" have lesser degree of freedom as their motion needs to be confined to the common axis of the two conjugate planes in which the split, partially cross-slipped dislocation evolves. The motion of these nodes, hence, happens only along the direction given by the Burgers vector of the un-split dislocation. If these nodes move away from each other, the dislocation length in the cross-slip segment increases, and if the nodes move toward to each other, the dislocation length in the cross-slip plane decreases. The distance between the pinning points, $L_{total}$ remains constant all through the dynamics. The nodes **A** and **B** have no degrees of freedom, nodes **C** and **D** have one degree of freedom and the nodes **E**,**F**,**G**,**H**,**I** and **J** have two degrees of freedom.

Now, consider figure 6.6a and 6.6c. Here the cross-slip segment is assumed to be originating from the right end of the screw dislocation and hence there is only one common node **C,** which will move along the common-axis of the two planes, i.e., along the Burgers vector direction of the un-dissociated screw. This common node **C**, hence can move either towards the left node **A**, thereby increasing the length of the cross-slip segment or move towards the right node **B**, thereby decreasing the length of the cross-slip segment. At some point in time, the common node will get annihilated by recombining either at **A** or **B**, thereby making the glide-plane of the screw dislocation to be either totally primary or totally cross-slip. So, in each of the simulation the distance of the common node with the left pinning point is monitored. If the distance between them is less than $100\dot{A}$, The simulation is terminated, and the result of the simulation is recorded as success. (Success, in the sense that the cross-slipped segment has encompassed the whole dislocation line). Similarly, if the distance between the common node and the left node is greater than $90\%$ of the total dislocation length, the program is terminated and the result of the simulation is recorded as a failure. This way, for each pair of primary and cross-slip stress, a result of +1 (success) or -1 (failure) is obtained. Examining this map will hence give an indication of which $(\sigma_p, \sigma_{cs})$ combination is conducive for cross-slip and which aren't.

Similarly, consider the figure 6.6b, 6.6d and 6.6e. Here the nodes C and D can only glide along the line AB. Under the application of certain stresses, if these nodes move towards each other, this implies that the length of the central cross-slipped section decreases whereas the motion of C and D nodes away from each other indicates that the applied external stress is favorable for the cross-slip process. So the distance between the nodes C and D vis-a-vis the distance between the pinning points A and B, gives a good estimate on the favorability or otherwise of the applied stress for cross-slip.

The aim of this study is to obtain such maps whose two axes are the control parameters like primary and cross-slip stresses and the third axis is the result of the simulation (success or failure) at the corresponding control parameters.

Although the code is fully capable of demonstrating total node annihilation, the program is terminated when the length of the cross-slipped segment is either greater than 90% of the total dislocation length or less than $100\ Angstroms$. This is to reduce the computational load. Now, the only requirement is that the total simulation time $t_{max}$ is sufficiently large enough for either of the above two cases to be satisfied. It is also possible that the distance of the common node neither reaches the left node (complete-cross-slip ) nor does it reach the (annihilation of the cross-slip segment) within any given time. This implies that for a pair of lengths $(L_{tot}, L_{cs})$ and those stresses $(\sigma_p, \sigma_{cs})$, the equilibrium configuration is the one with co-existing primary and cross-slip segments. The locus of such stress pairs hence demarcate the the stresses map into regions where cross-slip is conducive and those where cross-slip is not. The algorithm is briefly described in 6.1.

**Algorithm 6.1** Algorithm for understanding cross-slip favorability of different stresses for a partially cross-slipped 2 segment screw dislocation ( of type 6.6a and c).

1. At time t=0, Select the initial lengths $L^0_{tot}$, $L^0_{cs}$, $L^0_{prim} = L^0_{tot} - L^0_{cs}$, and initials stresses acting on the dislocations.
2. Evolve the system for certain time at a constant applied stress.
3. At every time-step, measure the distance between the common node C and the left pinned node A (refer to 6.6a or c) , $L_{prim}$
   (a) If the distance $CA < 100$ , output +1 and go to step 4.
   (b) If $CA > 0.9 \times AB$, output -1 and go to step 4.
4. Update the external stress and return to step 2.

Instead of having the cross-slip segment originate from the right end of the dislocation, one could construct the cross-slip segment to lie on the middle of the dislocation, and this will lead to three dislocation segments with two common nodes connecting those segments. For such dislocations, the distance $d_{common}$ between those two common nodes is taken as the criteria. The result of a simulation is termed success if $d_{common} > 0.9L_{tot}$ and failure if $d_{common} < 100$ .

In-fact, this 3-segment situation is experimentally more physical (see figure (6.3)) but now the primary and the cross-slip segments are not on equal footing. The two segments that glide in the primary plane have one pinned node each, whereas the segment that glides on the cross-slip plane has no pinned nodes. As shall be seen further, this feature alone produces a different stress map for the 3-segment case than the 2-segment case, although the lengths and other physical parameters are kept the same.

### 6.3.3 Simulation Parameters:

The simulation parameters common to all the simulations are given below:

**Table 6.2** – *Simulation parameters used in this work.*

| Core-radius a (Ang) | time-step (ns) | discretization length (Ang) | $B_e(Pa.s)$ | $B_s(Pa.s)$ |
|---|---|---|---|---|
| 3.661 | 0.001 | 10 | $9.82 \times 10^{-6}$ | $2.31 \times 10^{-6}$ |

## 6.4 Energy analysis of the composite FR source

Consider a split 3-segment Frank-Read source. The stability of this configuration will first be analyzed zero external stresses. As the non-singular stress formulation is self-consistent [Cai *et al.* 2006], the forces acting at a nodal point of a dislocation configuration can be obtained by taking the negative of gradient of the total energy of the dislocation at that nodal position.

The total energy of a dislocation is given by the sum of elastic energy, core energy and the stacking fault energy (see 2.3.3 on page 52).The stacking fault energy is obtained by multiplying the stacking fault energy per unit area with the total stacking fault enclosed by the partial dislocations. The variation of the total energy of a dislocation, as a function of the length of the cross-slipped segment is shown in the figure 6.7.

These simulations are carried out by constructing the desired composite dislocations and allowing the computational nodes to relax under their mutual interactions. The mobility of the physical nodes is not permitted so that the length of the cross-slip segment does not change under the dynamics. In this sense, these simulations are the “restrained dislocation dynamics” simulations, as the evolution of the system is allowed but a few degrees of freedom are not allowed to evolve.

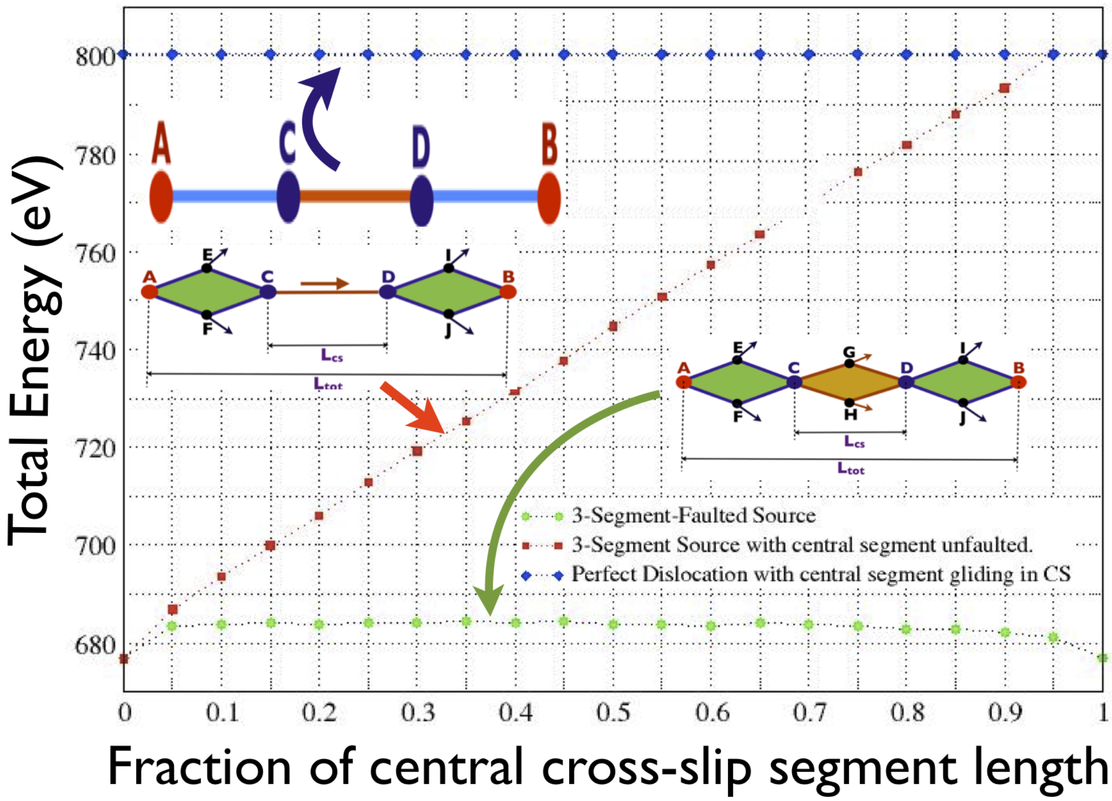


**Figure 6.7** – *Energies of the configuration, as a function of the length of cross-slip segment. The y-axis represents the total energy (in eV) and the x-axis represent the fraction of the dislocation length that has cross-slipped. The plot in green corresponds to the configuration 6.6b. The plot in red corresponding to configuration given in figure 6.6d, and the plot in blue corresponding to figure 6.6e. The configurations are also depicted within the graph for quick reference.*

The y-axis of figure 6.7 is the total energy of the dislocation configuration and the x-axis is the fraction of the total length taken up by the cross-slipped segment. Consider first, the green plot, which corresponds to figure 6.6b. It is evident from this plot that the total energy of the 3-segment configuration is slightly higher than the non-composite configurations ( those configurations corresponding to the data points at $x = 0$ and $x = 1$) but otherwise it is independent of the length of the cross-slip segment. That is, the existence of a cross-slip segment increases the total energy, but once a cross-slip segment is introduced, its total energy is practically independent of the length of that cross-slipped segment. So there is no energy incentive for the cross-slipped segment either to spontaneously shrink or spread along the original dislocation line. But if the central segment is constructed as a perfect dislocation (as in figure 6.6d) , then the energy increases linearly with the length of the central cross-slip segment, as seen in the red plot of the above figure. The blue plot corresponds to the 3-segment perfect dislocation case, and its total energy is independent of the length of the central dislocation. Hence here, under no external stress, there is no force between the common nodes.

## 6.5 Evolution under different stresses

### 6.5.1 Scheme-I

Consider the applied stress of the form:

$$\overleftrightarrow{\sigma} = \begin{bmatrix} 0 & 0 & \sigma_{13} \\ 0 & \sigma_{22} & 0 \\ \sigma_{13} & 0 & 0 \end{bmatrix} \tag{6.5}$$

That is, all stress components, except for $\sigma_{13}$ and $\sigma_{22}$, are zero. Now if the components $\sigma_{13}$ and $\sigma_{22}$ are

$$\sigma_{13} = \frac{\sqrt{6}}{2}(\sigma_p + \sigma_{cs}) \tag{6.6}$$

and

$$\sigma_{22} = \frac{\sqrt{6}}{2}(\sigma_p - \sigma_{cs}) \tag{6.7}$$

then one gets $\overleftrightarrow{\sigma}.\mathbf{n_p}.\mathbf{b} = \sigma_p$, and $\overleftrightarrow{\sigma}.\mathbf{n_{cs}}.\mathbf{b} = \sigma_{cs}$, where $\sigma_p$ and $\sigma_{cs}$ are the required resolved shear stress on primary and cross-slip planes. So, by a suitable choice of $\sigma_{13}$ and $\sigma_{22}$ one can independently control the shear stresses responsible for glide in the primary and cross-slip planes.

Consider a dislocation of the form shown in the figure 6.6a or figure 6.6c. Suppose the stress resolved in the primary plane defined by $(\mathbf{n}_p, \mathbf{b})$ is $\tau_p$ and similarly, stress resolved in the cross-slip plane defined by $(\mathbf{n_{cs}}, \mathbf{b})$ be $\tau_{cs}$. Assume that both $\tau_p$ and $\tau_{cs}$ are both less than the critical nucleation stress. Now, under the application of these two independent stresses, the common node tends to move along an axis that is common to both $\mathbf{n}_p$ and $\mathbf{n}_{cs}$, that is, along the direction $\mathbf{b}$, which is the direction of the original dislocation line. Our interest is in understanding the dynamics of this common node, which will control the extent of the dislocation evolution in the primary and cross-slip plane. As the end-points of the total dislocation are pinned, the motion of the common node towards the left end point indicates that the length of the cross-slipped segment is increasing at the expense of the length in the primary segment and vice versa, as discussed earlier. At the first look, it appears as if the dynamics of the common node is governed by the initial lengths in the primary and the cross-slip planes and the stresses acting on those planes, i.e., the dynamics is determined by the four parameters given by $(L_{tot}, L_{cs}, \tau_p, \tau_{cs})$.

#### 6.5.1.1 Configuration details

Consider a composite Frank-Read source of total length $L_{tot}$ of which, a section of length $L_{cs}$ glides in the cross-slip plane and the rest glides in the primary slip plane. We perform several set of simulations, with each set composing of several independent simulations with different stresses acting on this screw dislocation segment. The stress tensor is of the form shown earlier (Eq 6.5, Eq 6.6 and Eq 6.7), where $\sigma_p$ is drawn from an array of $(\sigma_{p,min} : \sigma_{p,inc} : \sigma_{p,max})$ and similarly $\sigma_{cs}$ is drawn from $(\sigma_{cs,min} : \sigma_{cs,inc} : \sigma_{cs,max})$. Hence the total number of independent simulations in each trail is $((\sigma_{p,max} - \sigma_{p,min})/\sigma_{p,inc} + 1) \times ((\sigma_{cs,max} - \sigma_{cs,min})/\sigma_{cs,inc} + 1)$. Each of these simulations is carried out for a specific time, $t_{max}$.

The results of each of these simulations are a series of triplet of numbers $(\sigma_p, \sigma_{cs}, \pm 1)$ where +1 indicates that under the primary and cross-slip stresses of $\sigma_p$ and $\sigma_{cs}$, the cross-slip length tends to the total length, $L_{cs} \rightarrow L_{tot}$ and the length of the primary segment $L_{prim} \rightarrow 0$. Similarly, a value of -1 indicates that $L_{cs} \rightarrow 0$ and $L_{prim} \rightarrow L_{tot}$.

As an example, consider a split composite 3-segment FR (of type 6.6b). If the stress acting on the composite FR sources are not favorable for cross-slip, the central cross-slipped segment annihilates and the subsequently the whole dislocation glide on the primary glide plane as shown in the figure 6.8.

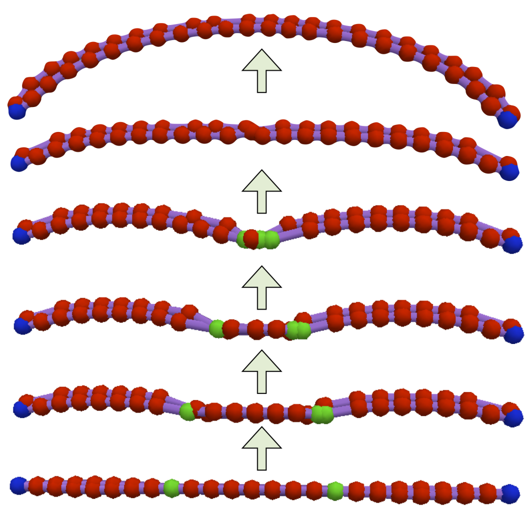

**Figure 6.8** – *The evolution of a three segment split composite FR source of the form shown in the figure 6.6b. The figures from top-left to bottom-right illustrate the annihilation of the central cross-slipped section.*

On the other hand, if the stresses acting are favorable for the cross-slip segment, its length grows at the expense of the length of the primary segment and soon the whole dislocation starts gliding in the cross-slip plane, as shown in the figure 6.9.

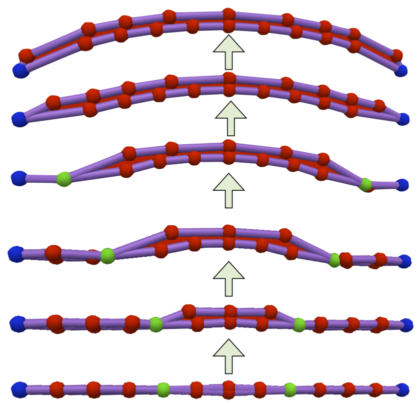

**Figure 6.9** – *The evolution of a three segment split composite FR source of the form shown in the figure 6.6b. The figures from top to bottom illustrate the cross-slip segment spreading over the whole dislocation length.*

The sets of simulations performed under this stress variation scheme are shown in the table 6.3. Each set of simulations corresponds to a particular initial configuration of dislocations, described by one of the figures of 6.6.

**Table 6.3** – *The list of all simulations that are carried out in this stress variation scheme.*

| | Config | $\sigma_{p,min}$ $(MPa)$ | $\sigma_{p,max}$ $(MPa)$ | $\sigma_{p,inc}$ $(MPa)$ | $\sigma_{cs,min}$ $(MPa)$ | $\sigma_{cs,max}$ $(MPa)$ | $\sigma_{cs,inc}$ $(MPa)$ | # of runs |
|---|---|---|---|---|---|---|---|---|
| **Set 1** | 6.6c | -250 | 250 | 50 | -250 | 250 | 50 | 121 |
| **Set 2** | 6.6c | -250 | 250 | 50 | -250 | 250 | 50 | 121 |
| **Set 3** | 6.6c | -250 | 250 | 50 | -250 | 250 | 50 | 121 |
| **Set 4** | 6.6a | -250 | 250 | 50 | -250 | 250 | 50 | 121 |
| **Set 5** | 6.6e | -150 | 150 | 20 | -150 | 150 | 20 | 256 |
| **Set 6** | 6.6e | -150 | 150 | 20 | -150 | 150 | 20 | 256 |
| **Set 7** | 6.6e | -150 | 150 | 20 | -150 | 150 | 20 | 256 |
| **Set 8** | 6.6e (Wall) | -150 | 150 | 20 | -150 | 150 | 20 | 256 |
| **Set 9** | 6.6c(Bent) | -150 | 150 | 20 | -150 | 150 | 20 | 256 |

| | $L_{tot}$ $(\dot{A})$ | $L_{cs}$ $(\dot{A})$ |
|---|---|---|
| **Set 1** | 1000 | 300 |
| **Set 2** | 1000 | 500 |
| **Set 3** | 1000 | 700 |
| **Set 4** | 1000 | 500 |
| **Set 5** | 900 | 300 |
| **Set 6** | 900 | 150 |
| **Set 7** | 900 | 450 |
| **Set 8** | 900 | 150 |
| **Set 9** | 900 | 150 |

#### 6.5.1.2 Results

**Results for Sets 1,2 and 3 of table 6.3:**

The results for the first three sets of runs given in table 6.3 is given in the figure 6.10. Figure 6.10a corresponds to the case when the primary and cross-slip segments are of equal length. Figure 6.10b and 6.10c corresponds to the case when the cross-slip segment length is less and greater than the primary segment length respectively.

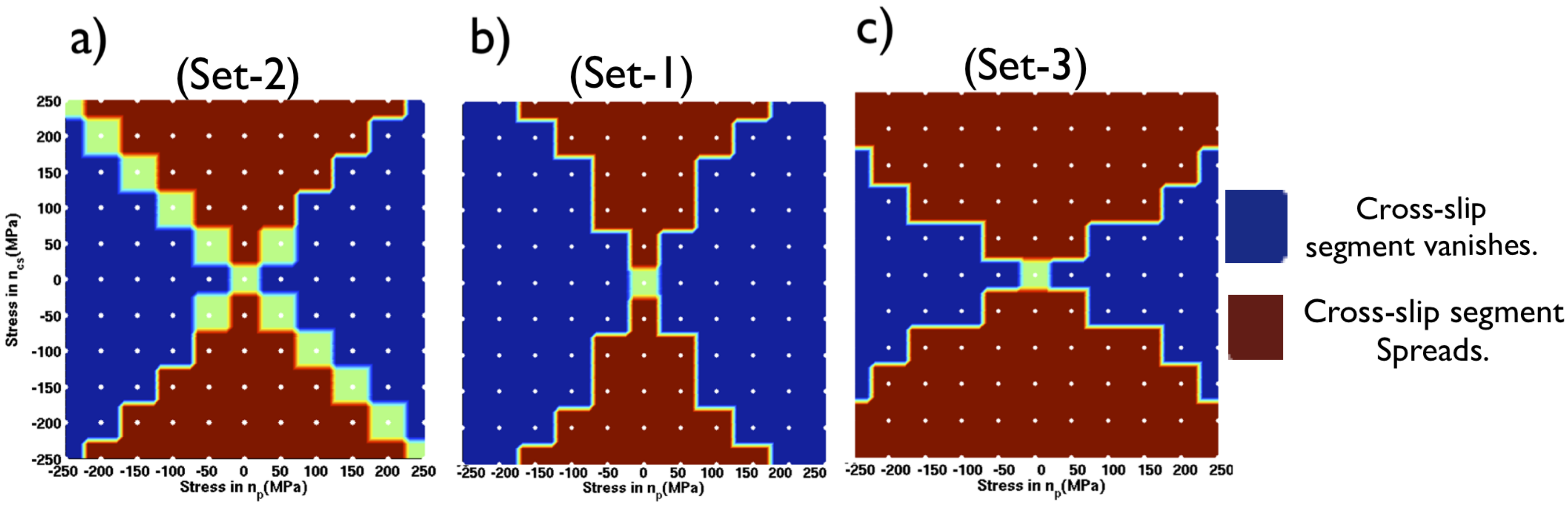


**Figure 6.10** – *The stress zone obtained in the first three cases discussed in table 6.3. The x-axis refers to the stress acting on the primary slip system, $\sigma_p = \overleftrightarrow{\sigma}.\mathbf{n}_p.\mathbf{b}$, and y-axis is the stress resolved in the cross-slip plane, $\sigma_{cs} = \overleftrightarrow{\sigma}.\mathbf{n}_{cs}.\mathbf{b}$. The regions in red indicate the $(\sigma_p, \sigma_{cs})$ combination that leads to the cross-slip spreading the whole dislocation length, and region in blue indicates the $(\sigma_p, \sigma_{cs})$ combination that leads to the length of the cross-slip going to zero. The regions in green indicate the $(\sigma_p, \sigma_{cs})$ values where the composite configuration neither glides totally into cross-slip plane nor glides totally in the primary plane. Plot a corresponds to set 2, plot b corresponds to set 1, and Plot c corresponding to set 3 of the table 6.3.*

One feature common to all these simulations is that at $(\sigma_p = 0, \sigma_{cs} = 0)$, lengths of the primary and cross-slip segments tend to remain constant. There is no spontaneous annihilation or spread of the cross-slipped segment, irrespective of its initial length and the total length of the dislocation.

The color-coded stresses plot corresponding to set 4 of table 6.3 is found to be almost identical to that of set 1. This indicates that splitting of each of the two dislocations into pairs of partials have no appreciable effect on the possibility of cross-slip.

**Results for Sets 5, 6 and 7 of table 6.3:**

The runs in set 5, 6 and 7 of 6.3 are carried out with the dislocation configuration of figure 6.6b. The color-coded plots for these sets of simulations are shown in the figure 6.11.

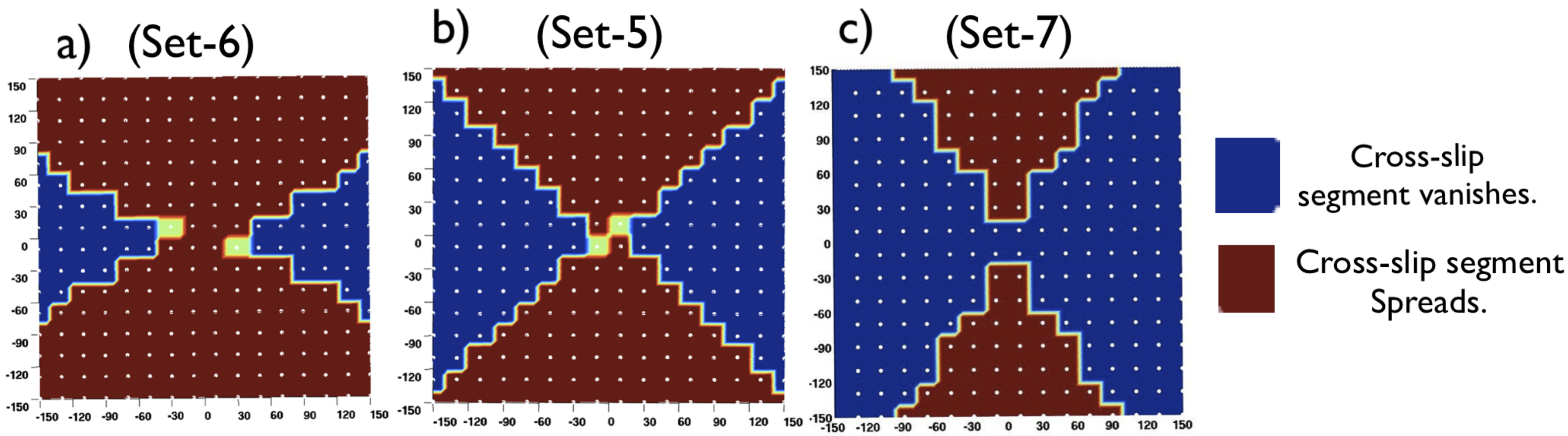


**Figure 6.11** – *The stress zone obtained in simulations set 5,6 and 7 of table 6.3. The x-axis refers to the stress acting on the primary slip system, $\sigma_p = \overleftrightarrow{\sigma}.\mathbf{n}_p.\mathbf{b}$ in MPa and y-axis is the stress resolved in the cross-slip plane, $\sigma_{cs} = \overleftrightarrow{\sigma}.\mathbf{n}_{cs}.\mathbf{b}$ in MPa The regions in red indicate the $(\sigma_p, \sigma_{cs})$ combination that leads to the cross-slip spreading the whole dislocation length, and region in blue indicates the $(\sigma_p, \sigma_{cs})$ combination that leads to the length of the cross-slip going to zero. The regions in green indicate the $(\sigma_p, \sigma_{cs})$ values where the composite configuration neither glides totally into cross-slip plane nor glides totally in the primary plane. Plot a corresponds to set 6, plot b corresponds to set 5, and Plot c corresponding to set 7 of the table 6.3.*

Note that the three plots of figure 6.11 are corresponding to the case of figure 6.6e, where the composite FR source has two common-nodes connecting the primary and cross-slip planes. Figure 6.11b corresponds to the case when the length of the cross-slip segment is one-third the distance between the pinning points. Figure 6.11a and 6.11c corresponds to the case when cross-slip segment length is less and greater than the one-third of the total length respectively.

**Results for Set 8 of table 6.3:**

In simulations of set 8 of table 6.3, the dislocation evolution in the primary plane is arrested due to the presence of a barrier at a distance of $10\ Ang$ placed perpendicular to the glide direction of the dislocation. The color-coded plot for the cross-slip occurrence in this configuration is given in figure 6.12.

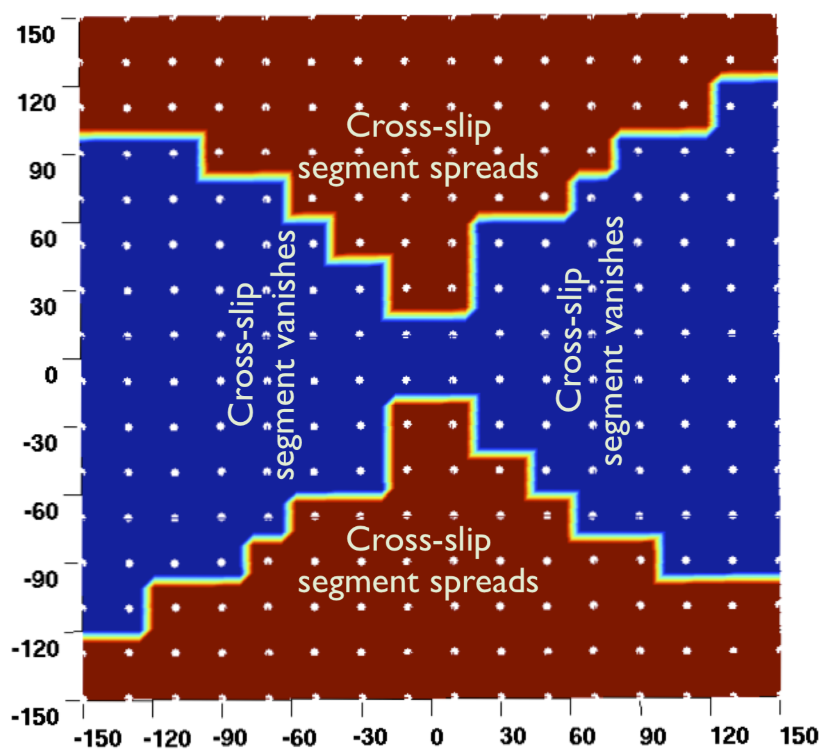


**Figure 6.12** – *Color-Coded plot corresponding to set 8 of table 6.3. In these simulations, the segment length in the cross-slip plane is only $\frac{1}{6}^{th}$ of the total length, but the glide of the dislocation in the primary plane is arrested but inserted an impenetrable obstacle.*

**Results for Set 9 of table 6.3:**

The set 9 corresponds to the case of figure 6.6e, but here the cross-slip segment is not along the line joining the pinning point but is displaced parallel to it by a distance of $5\ nm$, as shown in the figure 6.13. The corresponding color-coded plot for the cross-slip occurrence also shown along with.

Consider top image of figure 6.13. Here, the points A and B are the pinning points, and the dislocation line is now ACDB. The sections AC and DB, by construction are of mixed character, whereas the section CD is a perfect screw dislocation. This configuration corresponds to the case where the screw dislocation is not along the line joining the pinning points but is parallel to it, separated by a distance ($5\ nm$ in this case). The sections AC and DB glide on the primary glide plane, whereas CD is allowed to glide on the cross-slip plane. The points C and D have just one degree of freedom, along the line length CD. The cross-slip is considered success if the distance between these nodes C and D becomes equal to the distance between the pinning points A and B, and is considered failure if length CD tends to zero.

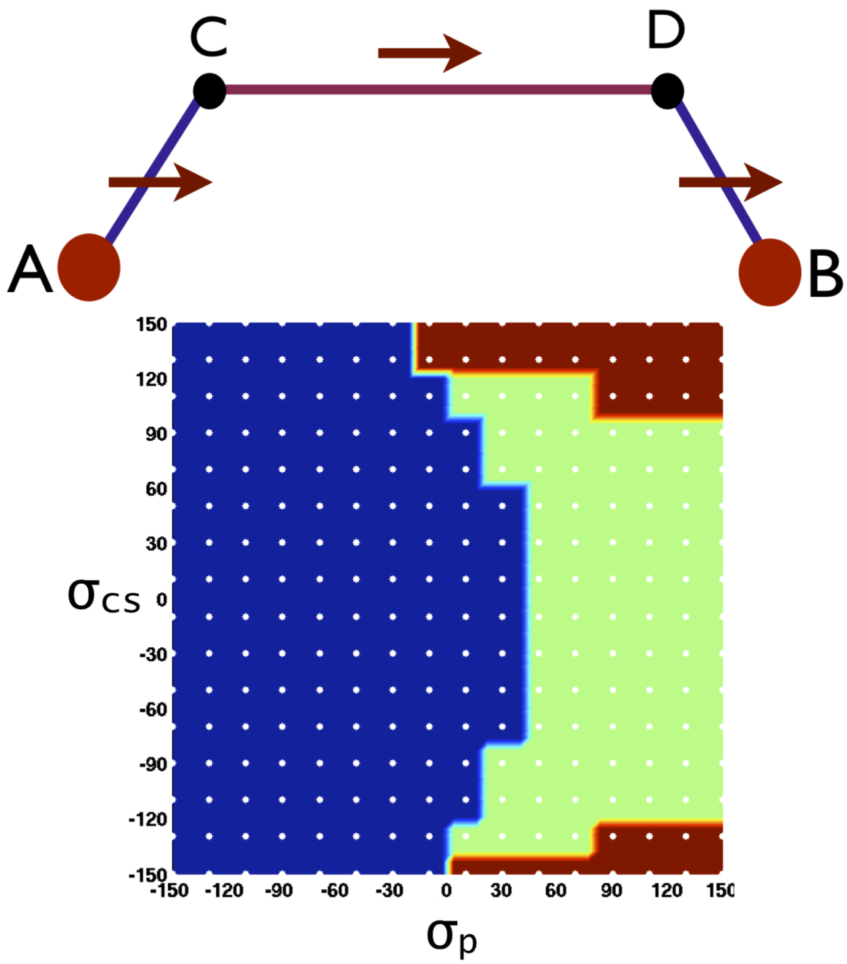


**Figure 6.13** – *The set-up and result corresponding to the set 9 of the table 6.3. The image on the left is explained in the text. The image on the right corresponds to the result of primary and cross-slip stress acting on this configuration. The x-axis refers to the stress acting on the primary slip system, $\sigma_p = \overleftrightarrow{\sigma}.\mathbf{n}_p.\mathbf{b}$ in MPa and y-axis is the stress resolved in the cross-slip plane, $\sigma_{cs} = \overleftrightarrow{\sigma}.\mathbf{n}_{cs}.\mathbf{b}$ in MPa The regions in red indicate the $(\sigma_p, \sigma_{cs})$ combination that makes the length CD equal to AB, and region in blue indicates the $(\sigma_p, \sigma_{cs})$ combination that makes the length CD tend to zero. The regions in green indicate the $(\sigma_p, \sigma_{cs})$ values where the length of cross-slip segment CD neither goes to 0 nor equals distance between pinning points AB.*

The bottom image of figure 6.13 marks the regions on the $(\sigma_p, \sigma_{cs})$ plane favorable for cross-slip. It can be seen that the cross-slip is not possible for all cases where $\sigma_p < 0$ independent of the cross-slip stress $\sigma_{cs}$. Due to the presence of an impenetrable obstacle along CD, an application of positive $\sigma_p$ will not lead to any glide along the primary plane.

Cross-slip in this configuration appears to be possible only when $|\sigma_{cs}| > 120\ MPa$ and $|\sigma_p| > 0$.

### 6.5.2 Scheme-II

In this stress variation scheme, the applied stress is of the form:

$$\overleftrightarrow{\sigma} = \begin{bmatrix} 0 & \sigma_{12} & \sigma_{13} \\ \sigma_{12} & 0 & 0 \\ \sigma_{13} & 0 & 0 \end{bmatrix} \tag{6.8}$$

That is, all stress components except for $\sigma_{12}$ and $\sigma_{13}$ are zero. If the components $\sigma_{12}$ and $\sigma_{13}$ are

$$\sigma_{12} = \frac{\sqrt{18}}{4}(\sigma_{ep} - \sigma_{ecs}) \quad \sigma_{13} = -\frac{\sqrt{18}}{2}(\sigma_{ep} + \sigma_{ecs}) \tag{6.9}$$

then one gets $\overleftrightarrow{\sigma}.\mathbf{n_p}.(\mathbf{n_p} \times \mathbf{b}) = \sigma_{ep}$, and $\overleftrightarrow{\sigma}.\mathbf{n_{cs}}.(\mathbf{n_{cs}} \times \mathbf{b}) = \sigma_{ecs}$, where $\sigma_{ep}$ and $\sigma_{ecs}$ are the Escaig stress acting on the primary and cross-slip planes respectively. This stress scheme allows for independent control of the Escaig stresses acting on the primary and cross-slip planes, $\sigma_{ep}$ and $\sigma_{ecs}$, by varying $\sigma_{12}$ and $\sigma_{13}$ according to Eq 6.9.

Now, if the only non-zero stress components are $\sigma_{12}$ and $\sigma_{13}$, then the stresses acting on the primary and the cross-slip planes are both equal to $\sigma_{13}$. So, under this stress variation scheme, one can independently vary the $\sigma_{ep}$ and $\sigma_{ecs}$, keeping the glide stress on primary plane and glide stress on cross-slip plane equal.

#### 6.5.2.1 Simulated cases

A composite split FR source of the form shown in figure 6.6a is considered. The total length of the dislocation is $100\,nm$, of which a section of length $50\,nm$ can glide on the cross-slip plane. Four different simulations were carried out corresponding to different combinations of $(\sigma_{ep}, \sigma_{ecs})$ as shown in table 6.4.

**Table 6.4** – *Primary and Cross-slip Escaig stresses considered for this study.*

| | $\sigma_{ep}$ (MPa) | $\sigma_{ecs}$ (MPa) |
|---|---|---|
| Simulation 1 | 0 | -100 |
| Simulation 2 | 0 | 100 |
| Simulation 3 | -100 | 0 |
| Simulation 4 | 100 | 0 |

#### 6.5.2.2 Results and Discussion

Each of the 4 simulations referred to in table 6.4 is independently carried out for a total time of 10 ns. The runs are determined within this time if the length of the cross-slipped segment either increases to more than 90% of the total dislocation length or decreases to less than the 10% of the total dislocation length. Since these simulations are carried out with the initial dislocation configuration of figure 6.6a, there is only one node common to the primary and cross-slip segment.

The plot of length of cross-slip segment (distance between the common node and the other pinned end) as a function of time, for these four configuration is shown in the figure 6.14.

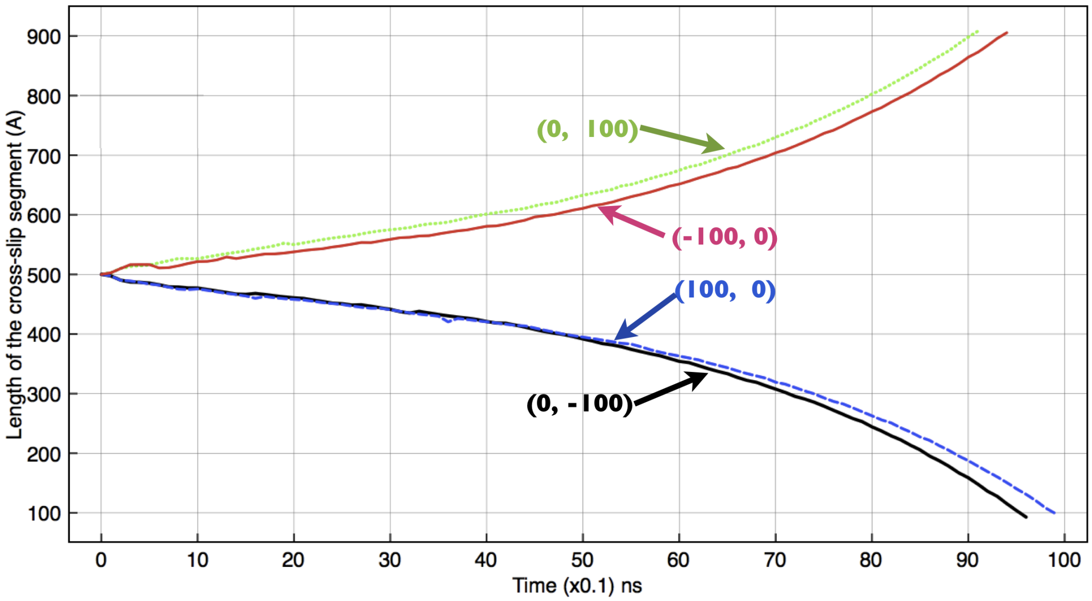


**Figure 6.14** – *Evolution of length of the cross-slip segment as a function of time, under the action of various Escaig stresses* $(\sigma_{ep}, \sigma_{ecs})$ *as discussed in Scheme-III. The plot in red corresponds to* $(-100, 0)$*, plot in blue corresponds to* $(100, 0)$*. The plot in green corresponds to* $(0, -100)$ *and the plot in black corresponds to the* $(0, 100)$*. The stresses are given in MPa.*

The first observation from the plot of figure 6.14 is that the dynamics of the composite FR source is not symmetric in sign of Escaig stresses. The dynamics under the primary Escaig stress of magnitude $100\ MPa$, for example, is markedly different from that of $-100\ MPa$. This has to be compared with the dynamics under the application of glide stress, discussed in section 6.5.1. There the probability for cross-slip to succeed or fail depended only on the magnitude of the glide stresses on the primary and cross-slip plane and not on their sign.

A positive Escaig stress acts so as to move the two partials away from each other, whereas a negative Escaig stress acts towards pulling the dislocations towards each other. Whereas the positive and negative glide stress both would keep the two partial dislocations together.

It is well-known [Hirth & Lothe 1982, Byun 2003, Baudouin *et al.* 2013] that the negative of Escaig stresses couple linearly with the stacking fault energy. This implies that applying a positive Escaig stress is equivalent to a corresponding reduction in the stacking fault energy and the effect of a negative Escaig stress is akin to a corresponding increase in the stacking fault energy.

Consider first, the case when there is no Escaig stress in the cross-slip plane. This corresponds to the simulations $3$ and $4$ of table 6.4. Since an application of positive $\sigma_{ep}$ leads to a reduction in the stacking fault energy for the partial dislocation segments lying in the primary slip plane. Hence it is more energetically favorable for the composite FR source to completely glide in the primary glide plane, as the effective stacking fault energy there is less when compared with that in the cross-slip glide plane. Thus a positive primary Escaig stress to an initially composite FR source leads to shrinking and eventual disappearance of the cross-slip segment. This explains the blue plot of figure 6.14, which corresponds to an Escaig stresses $(100, 0)$. The y-axis marks the length of the cross-slip segment and hence it shows that the cross-slip segment eventually shrinks to zero under an application of a positive Escaig stress acting in the primary slip plane.

Similarly, a negative Escaig stress in the primary $\sigma_{ep}$ would increase the effective stacking fault energy and hence the whole composite dislocation would glide in the cross-slip plane where the effective stacking fault energy is less. So, under the application of a stress of the form $(-100, 0)$, the length of the cross-slip segments increases with time to encompass the whole dislocation line, as shown in the red plot of figure 6.14.

The other two plots of the figure 6.14, corresponding to the simulation 1 and 2 of figure 6.4 can also be understood with similar arguments.

In-fact, the observations of these 4 simulations are extended to the $(\sigma_{ep}, \sigma_{ecs})$ cases as tabulated in the figure 6.5, along with the result obtained in those simulations.

**Table 6.5** – *Overview of the dynamics of a split composite FR source under the application of different Escaig stresses in its primary and cross-slip planes.*

| Case | Sign of $\sigma_{ep}$ | Sign of $\sigma_{ecs}$ | Condition | Result |
|---|---|---|---|---|
| 1 | $+$ | $+$ | $\|\sigma_{ep}\|<\|\sigma_{ecs}\|$ | FAIL |
| 2 | $+$ | $+$ | $\|\sigma_{ep}\|>\|\sigma_{ecs}\|$ | SUCCESS |
| 3 | $+$ | $-$ | $\|\sigma_{ep}\|<\|\sigma_{ecs}\|$ | FAIL |
| 4 | $+$ | $-$ | $\|\sigma_{ep}\|>\|\sigma_{ecs}\|$ | FAIL |
| 5 | $-$ | $+$ | $\|\sigma_{ep}\|<\|\sigma_{ecs}\|$ | SUCCESS |
| 6 | $-$ | $+$ | $\|\sigma_{ep}\|>\|\sigma_{ecs}\|$ | SUCCESS |
| 7 | $-$ | $-$ | $\|\sigma_{ep}\|<\|\sigma_{ecs}\|$ | SUCCESS |
| 8 | $-$ | $-$ | $\|\sigma_{ep}\|>\|\sigma_{ecs}\|$ | FAIL |

From table 6.5, it can be seen that the composite screw dislocation glides on the cross-slip plane when $\sigma_{ecs} > \sigma_p$, whereas it glides in the primary plane when $\sigma_{ecs} < \sigma_p$.

### 6.5.3 Scheme-III

In Scheme-I, the role of shear stresses acting on the primary and cross-slip segments was examined, and in Scheme-II, the role of Escaig stress acting on the partials of the primary and cross-slip planes was examined. In this scheme-III, we study stress schemes where both glide stress and non-glide Escaig stresses are acting simultaneously on the split FR dislocation. Here the stress variation is achieved by progressively changing the plane of the shear-stress and the direction of shear stress.

Given $\mathbf{n_p}$ and $\mathbf{b}$ from the table 6.1, the shear plane in this scheme is taken of the form:

$$\mathbf{n} = \mathbf{n_p} cos\theta_n + (\mathbf{n_p} \times \mathbf{b}) sin\theta_n \tag{6.10}$$

so that as $\theta_n$ is varied from $0$ to $2\pi$, the shear plane gets rotated in a plane whose normal is $\mathbf{b}$. Note that the shear plane $\mathbf{n}$ remains perpendicular to $\mathbf{b}$ for all values of $\theta_n$. Now, for a given $\mathbf{n}$, the shear plane $\mathbf{m}$ is taken as

$$\mathbf{m} = \mathbf{b}cos\theta_m + (\mathbf{n} \times \mathbf{b})sin\theta_m \tag{6.11}$$

The angle variations are illustrated in figure 6.15.

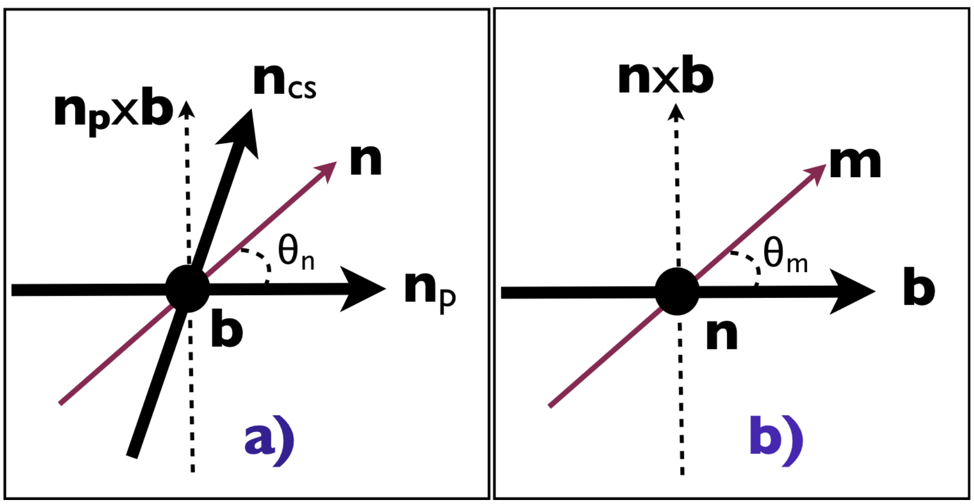


**Figure 6.15** – *Definitions of $\theta_n$ and $\theta_m$ used in this scheme. Figure a) is the variation of angle $\theta_n$, which is the angle between the shear plane $\mathbf{n}$ and the primary glide plane $\mathbf{n_p}$. Figure b) is the variation of angle $\theta_m$ which is the angle between the shear direction $\mathbf{m}$ and the Burgers vector $\mathbf{b}$. In figure a the plane of the figure has the normal as $\mathbf{b}$, whereas in figure b the plane of the paper has the normal $\mathbf{n}$.*

As $\theta_m$ is varied from $0$ to $2\pi$, the shear direction $\mathbf{m}$ gets rotated in a plane whose normal is $\mathbf{n}$. Hence the shear direction is always orthogonal to the shear plane, although the shear plane itself is being rotated in a plane defined by the Burgers vector $\mathbf{b}$.

#### 6.5.3.1 Simulated cases

The sets of simulations that were carried out in this scheme is shown in table 6.6. Each of these 6 sets of runs consists of 625 independent simulations, corresponding to each pair of angles $(\theta_m, \theta_n)$.

**Table 6.6** – *Simulation sets considered in the Scheme-III.*

| Set | Configuration | $L_{tot}$ | $L_{cs}$ | $\theta_{m,inc}$ | $\theta_{n,inc}$ | Remarks |
|---|---|---|---|---|---|---|
| 1 | 2-seg-Perfect | 1000 | 500 | 15 | 15 | The primary and cross-slip segments are of equal length. |
| 2 | 2-seg-Perfect | 1000 | 150 | 15 | 15 | The cross-slip segment is smaller than the primary segment. |
| 3 | 2-seg-Split | 1000 | 500 | 15 | 15 | Same as set 1, except that the dislocations gliding in primary and cross-slip planes are split into partials. |
| 4 | 3-seg-Perfect | 900 | 300 | 15 | 15 | The CS segment originates from the center of the dislocation, and is one-third of the total length. |

#### 6.5.3.2 Results and Discussion

In this stress variation scheme, the changing of angles that shear direction and shear plane make with $\mathbf{n_p}$ and $\mathbf{b}$. The results expected in these simulations are of the form $(\theta_m, \theta_n, \pm 1)$, where, again, $+1$ indicates the cross-slipped segment spreads over the whole dislocation and $-1$ indicates that its length has shrunk to zero.

The color-coded plot for the case of set 1 in table 6.6, is shown in the figure 6.16.

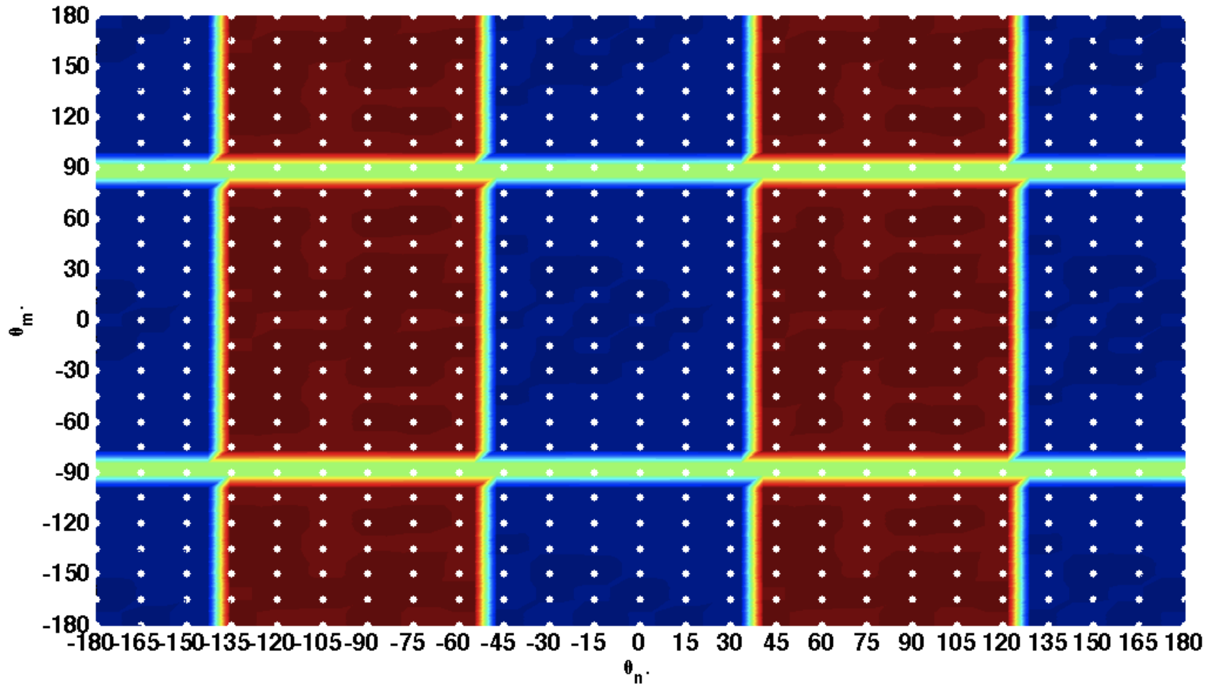


**Figure 6.16** – *Color-coded plot, obtained for the simulation set 1 of 6.6. The x-axis is the angle $\theta_n$ (in degree) between the shear plane $\mathbf{n}$ and primary glide plane $\mathbf{n}_p$. The y-axis is angle $\theta_m$ (again in degrees) between the shear direction $\mathbf{m}$ and the glide direction $\mathbf{b}$. The white dots are the data points where the simulations are performed. The color-coding is obtained by extrapolating the results at these data points. The regions in red indicates the regions in the $(\theta_n, \theta_m)$ where the cross-slip segment spreads over the full dislocation length, and the regions in blue indicates those $(\theta_n, \theta_m)$ values where it gets annihilated. The regions in green corresponds to the dislocation neither growing nor annihilating.*

From this plot, it is visible that the occurrence of complete cross-slip or annihilation is independent on the angle $\theta_m$.

Now, the variation of cross-slip probability with the angle $\theta_n$ can be understood as follows: This angle is the angle that the shear plane makes with the primary glide plane. Now, the acute angle included between the primary glide plane $\mathbf{n_p}$ and cross-slip glide plane $\mathbf{n_{cs}}$ is $70.53°$, and the obtuse angle is $109.47°$. So, if the angle $\theta_n$ is in the window $(-109.47°/2, 70.53°/2)$ the component of the applied stress is more in the primary glide plane compared to the cross-slip plane, so under these $\theta_n$, the cross-slip segment will get annihilated as the stress on the primary slip system is more. For $\theta_n$ in the window $(70.53°/2, 180° - (109.47°/2))$ the stress in the cross-slip plane is more than that in the primary plane, and hence the cross-slip segment spreads over the whole dislocation line. Since the Burgers vector of the dislocation segment in primary and cross-slip plane is identical, the effect of the variation in the shear direction i.e., the variation of $\theta_m$ has no impact on the cross-slip tendency. The dependence on $\theta_m$ is present only when the shear direction becomes parallel to $\mathbf{n} \times \mathbf{b}$ and hence the component of applied stress along $\mathbf{b}$ becomes $0$. If the composite Frank-Read source is composed of perfect dislocations, this shear stress does not lead to any glide in either of the two planes.

$$\overleftrightarrow{\sigma}.\mathbf{n}.\mathbf{m} = 0 \quad if \quad \theta_m = 0 \,\forall\, \theta_n \tag{6.12}$$

Now consider the case of set 2 of table 6.6. Here the cross-slip segment of smaller length compared to the primary. The color-coded plot corresponding to this configuration is as shown in figure 6.17. This figure is to be compared with the figure 6.16, which corresponds to the case where cross-slip segment is of the same length as the primary. Compared to that, the angles $(\theta_n, \theta_m)$ at which the cross-slip succeeds is now much reduced. Again, the dependence of cross-slip occurrence on $\theta_m$is almost nonexistent.

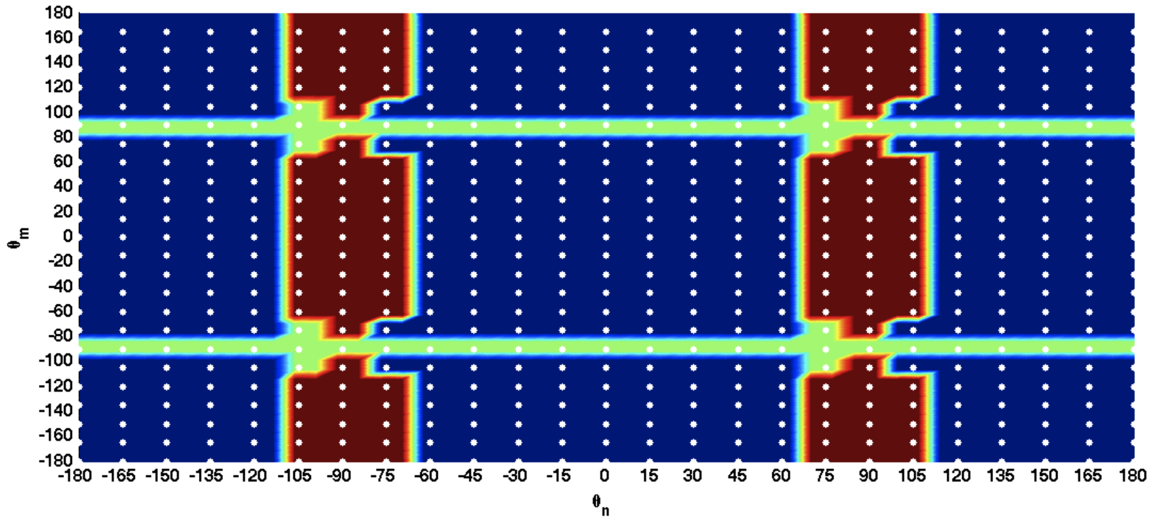


**Figure 6.17** – *Color-coded plot corresponding to the simulation set 2 of table 6.6. Here the length of the cross-slip segment is less than the length of the primary segment. The x-axis is the angle $\theta_n$ (in degree) between the shear plane $\mathbf{n}$ and primary glide plane $\mathbf{n}_p$. The y-axis is angle $\theta_m$ (again in degrees) between the shear direction $\mathbf{m}$ and the glide direction $\mathbf{b}$. The white dots are the data points where the simulations are performed. The color-coding is obtained by extrapolating the results at these data points. The regions in red indicates the regions in the $(\theta_n, \theta_m)$ where the cross-slip segment spreads over the full dislocation length, and the regions in blue indicates those $(\theta_n, \theta_m)$values where it gets annihilated. The regions in green corresponds to the dislocation neither growing nor annihilating.* .

It was found that the results corresponding to the set 3 of table 6.6 are also identical to set 1 of 6.6 (Results not shown here). This shows that the cross-slip occurrence in this scheme does not depend on the where the dislocations are split or not.

Now, in set 4 of the table 6.6 , the cross-slip segment originates from the center of the primary segment. The color-coded map for this case, shown in figure 6.18, is identical to that of set 1 of table 6.6 shown in figure 6.16. It is to be noted that the length of the cross-slip segment is one-third of the total length in the set 3, where as in set 1 it is exactly half of the total length. This is consistent with what is seen in the earlier stress variation schemes also.

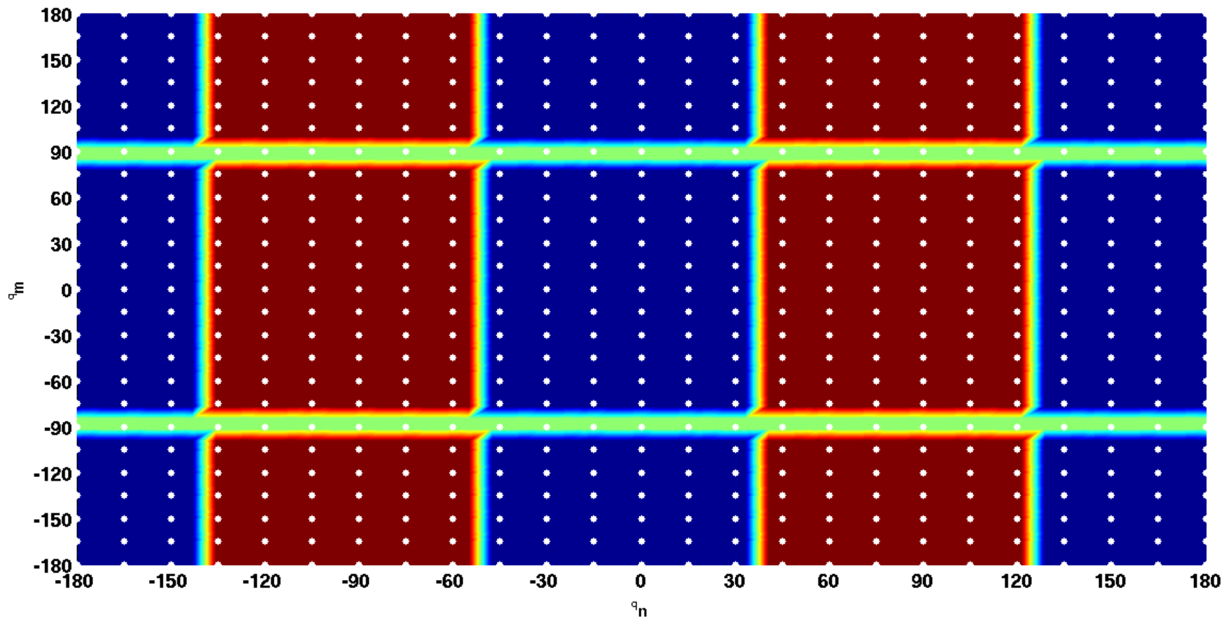


**Figure 6.18** – *Color-coded plot corresponding to the simulation set 4 of table 6.6. The x-axis is the angle $\theta_n$ (in degree) between the shear plane $\mathbf{n}$ and primary glide plane $\mathbf{n}_p$. The y-axis is angle $\theta_m$ (again in degrees) between the shear direction $\mathbf{m}$ and the glide direction $\mathbf{b}$. The white dots are the data points where the simulations are performed. The color-coding is obtained by extrapolating the results at these data points. The regions in red indicates the regions in the $(\theta_n, \theta_m)$ where the cross-slip segment spreads over the full dislocation length, and the regions in blue indicates those $(\theta_n, \theta_m)$values where it gets annihilated. The regions in green corresponds to the case where the central dislocation segment neither growing nor annihilating.*

From these schemes of stress variation it appears that it is more likely for cross-slip to succeed if the cross-slip segment originates from the center of the original screw rather then the one of the pinning points.

## 6.6 Conclusions

DD simulations of a Frank-Read screw source, a part of which has its glide plane different from the rest of its length is undertaken. Energetically, it is found that the configuration where the cross-slip segment is also split into partials is more favorable compared to the configuration where the central segment is perfect.

The response of such a “Composite FR source” to different glide and non-glide stresses in primary and cross-slip stresses is then studied. The important observations are as follows

1. Under the application of stress tensors of a certain form, it is found that the behavior of these “Composite FR sources” is different if the dislocations are composed of perfect dislocations and partial dislocations.

2. It is found that the propensity of the cross-slipped segment to spread over the full length of the source is predominantly dependent on the glide stresses acting on the primary and cross-slip planes, and does not significantly depend on the non-glide stresses acting on those plane.

# Chapter 7

# Summary & Conclusions

Plastic deformation, manifesting at macroscopic length and time scales, has its origins primarily in the dynamics of dislocations, their mutual interactions, and their interactions with other defects and impurities embedded in the matrix. Accurate modelling of these interactions is hence crucial for understanding the microscopic origins of macroscopic plastic deformation. Three dimensional Dislocation Dynamics (3D-DD) is a powerful computational tool that complements the more popular computational tools like Molecular Dynamics and Finite Element Methods in understanding the dislocation evolution across different length and timescales. This thesis employed the 3D-DD formalism, particularly for examining the following four issues:

1. The **evolution of dislocations in ferritic steels** in presence of irradiation induced prismatic loops and oxide-dispersions.

2. Understanding the role of stresses on the primary and cross-slip planes on the features of **multiple clear channels formed in austenitic stainless steels**.

3. Study the variation of the equilibrium stacking fault width of a split FR source under the **simultaneous application of glide and Escaig stresses** acting in its glide plane.

4. Study the **role of glide and Escaig stresses** acting on the primary and cross-slip planes **in the cross-slip of a pinned screw dislocation.**

The scale and features implemented in each of the results chapters is given in table 7.1.

**Table 7.1** – *Features implemented in each of the chapters of this thesis.*

| Feature\Chapter | 3 on page 61 | 4 on page 110 | 5 on page 148 | 6 on page 198 |
|---|---|---|---|---|
| **Crystallography** | BCC | fcc | | |
| **Dislocations** | Perfect | | Split | |
| **Scale** | Grain | | Single dislocation | |
| **DD Technique** | Edge-Screw based dislocation dynamics | | Nodal based dislocation dynamics | |
| **Stress variation** | Feedback based constant strain-rate controlled | | Peicewise constant stress | |
| **Software** | TRIDIS | | NUMODIS | |

From table 7.1, it is visible that the almost half of the thesis dealt with the macroscopic three dimensional dislocation interactions, in presence irradiation induced obstacles, with glide and cross-slip features implemented. The second half of the thesis deals with more elementary phenomena concerned with a single dislocation source, but in more detail involving nodal representation, and accomodating the stacking faults.

For the present thesis, the software for performing Edge-Screw based Dislocation Dynamics, TRIDIS, was enhanced with new functionalities for handling interaction of dislocations with irradiation induced dislocation loops. These interactions rules were devised based on results of molecular dynamics simulations available in the literature. With these interaction rules in place, the initial dislocations are evolved under constant strain rate and the resulting dislocation microstructure is analyzed using various post-processing tools.

More accurate and realistic modeling of cross-slip in fcc materials requires going beyond the edge-screw model employed in TRIDIS. Dislocations in fcc are split into partials and enclose a stacking fault between them, and at the moment TRIDIS is insufficient to handle these features. NUMODIS is a nodal based DD code, currently under development, that is capable of handling partial dislocations and stacking faults.

Since the partials have Burgers vector different from the original unsplit dislocation, they respond to non-glide components of the external applied stress tensor. A significant part of the thesis dealt with understand the dynamics of a single pair of split dislocations under the action of different glide and non-glide components. Various stress variation schemes were devised for controlled variation of the glide and Escaig stresses and the equilibrium dissociation width is examined under those stresses. NUMODIS was extended with new modules written in object-oriented C++ , for carrying out these simulations and post processing of the results.

## 7.1 Highlights of the thesis

Significant observations coming out of the present thesis are as follows:

1. The mobility rules and cross-slip algorithm employed for studying the plastic deformation in dispersion-strengthened ferritic steels are found to be well capable to reproduce all well-known characteristics of dislocations in bcc structure like pensile glide etc. The dislocation microstructure obtained using 3D dislocation dynamics is comparable to those seen in TEM micrographs.

2. It was found that cross-slip is a important factor that controls the strain localization. In the case of irradiated ODS steels, the Orawon loops formed around the dispersoids due to the dislocation glide, enhance the cross-slip probability and hence provide greater strain spreading than in irradiated steel devoid of these dispersoids.

3. The loop-induced hardening in case of irradiated RPV ferritic steels, is significant and stable. Its magnitude is weakly influenced by deformation temperature and loop density in the range of $100K - 300K$ and $5 \times 10^{20} - 5 \times 10^{21}$ range respectively. Also, interacting loop population is directly proportional to loop strength, at least up to a loop strength of 300 MPa.

4. In the studies of clear channel formation in austenitic steels, it is shown that the stress field developing in the vicinity of a clear band can be described through a simple analytical expression accounting for the applied stress magnitude, the grain size and the critical cross-slip stress. This simple description proved adequate even in absence of more complex dislocation features like super-jogs and loop-debris.

5. The separation of clear channels is function of the grain size, irradiation dose as well as the stacking fault energy (SFE). It is found that the shear band spacing increases with decreasing SFE.

6. It is also found that cross-slip stress field in primary plane controls germination of secondary channels whereas the cross-slip stress in crossslip plane also controls the extent (length) of secondary channel and therefore, the spacing between primary channels in presence of facet-loops.

7. The stress field acting on the cross-slip system is found to control the spacing between primary channels in presence of facet-loops, through the development of secondary channels. Cross-slip is partially inhibited due to interactions of mobile dislocations with the facet-loops. This effect explains the experimentally observed augmentation of the surface step spacing, after post-irradiation straining.

8. In the nodal based studies of split FR sources using NUMODIS, it was found that the presence of Escaig stresses directly affects the equilibrium dissociation width, and hence impacts the cross-slip probability of a screw dislocation.

9. It is found that under the application of Escaig stress of a suitable magnitude can activate the two arms of a split FR source away from each other indefinitely, in a Frank-Read like phenomenon. This can explain the presence of large stacking faults seen in some low stacking fault energy materials.

10. Under the application of stress tensors of a certain form, it is found that the behavior of the screw dislocations with constrictions is different if the dislocation segments are composed of perfect dislocations and partial dislocations. The role of glide and non-glide stresses acting on the primary and cross-slip stresses is markedly different for pinned composite sources vis-à-vis the parallel composite source. The propensity for the cross-slipped segment to spread over its full length is seen predominantly dependent on the glide stresses acting on the primary and cross-slip planes.

11. The cross-slip possibility increases greatly if the motion of leading partial segments in the primary glide plane is blocked due to presence of any obstacles.

12. Cross-slip is found to be more likely if the cross-slipped section originates from the centre of the FR source rather than its pinned ends.

## 7.2 Future Directions

The simulations in Chapter 3 and 4 concern primarily about the evolution (through glide and cross-slip) of dislocations in the presence of obstacles. It should be noted that the stress-strain plots obtained through these simulations do not exactly match those obtained by experiments on bulk samples. The simulation-produced stress-strain plots hence only aid in comparing the hardening etc of different simulation cases. This is because, in simulations the tensile loading is carried out on a single grain, and at a high strain rate, where-as the bulk sample are polycrystalline, in general. The dislocation micro-structure obtained from the simulations is, on the other hand, is comparable with the experimental TEM micrograph. Another point to note is that the simulations reported in chapters 3 and 4 are carried out without incorporating climb. Implementing the mechanism of climb in these DD simulation can have interesting consequences as now the dislocations can bypass the obstacles not just through cross-slip of screw segments but also by climb of their edge segments. The dependence of size of the ODS precipitates on the irradiation induced hardening, particularly with realistic particle sizes is another issued which need to be undertaken.

The mechanisms seen in chapter 5 and chapter 6 indicate that the Escaig stresses in primary and cross-slip planes can have important consequences in the cross-slip phenomena. These observations, coupled with more elementary observations coming from atomistic simulations of cross-slip can lead to a more realistic cross-slip scheme to be constructed. This cross-slip scheme needs to be sensitive to the local stresses, and hence must be applicable even in presence of irradiation defects like Frank-loops etc. On the computation front, the software NUMODIS needs to be parallelized so that the large-scale dislocation defects interactions can be analyzed, incorporating new cross-slip rules.

# Bibliography


[Alamo *et al.* 2004] A Alamo, V Lambard, X Averty and MH Mathon. *Assessment of ODS-14% Cr ferritic alloy for high temperature applications*. Journal of nuclear materials, vol. 329, pages 333–337, 2004. 71, 93

[Amodeo & Ghoniem 1990] RJ Amodeo and NM Ghoniem. *Dislocation dynamics. I. A proposed methodology for deformation micromechanics*. Physical Review B, vol. 41, no. 10, page 6958, 1990. 22

[Argon 2008] Ali S Argon. Strengthening mechanisms in crystal plasticity. Numeéro 4. Oxford University Press Oxford, 2008. 52, 165, 206

[Arsenlis *et al.* 2007] Athanasios Arsenlis, Wei Cai, Meijie Tang, Moono Rhee, Tomas Oppelstrup, Gregg Hommes, Tom G Pierce and Vasily V Bulatov. *Enabling strain hardening simulations with dislocation dynamics*. Modelling and Simulation in Materials Science and Engineering, vol. 15, no. 6, page 553, 2007. 160

[Bacon & Osetsky 2007] DJ Bacon and Yu N Osetsky. *The atomic-scale modeling of dislocation-obstacle interactions in irradiated metals*. JOM, vol. 59, no. 4, pages 40–45, 2007. 116

[Bacon & Osetsky 2009] David J Bacon and Yuri N Osetsky. *Dislocation Obstacle Interactions at Atomic Level in Irradiated Metals*. Mathematics and Mechanics of Solids, vol. 14, no. 1-2, pages 270–283, 2009. 116

[Bacon *et al.* 1973] DJ Bacon, UF Kocks and RO Scattergood. *The effect of dislocation self-interaction on the Orowan stress*. Philosophical Magazine, vol. 28, no. 6, pages 1241–1263, 1973. 81

[Bacon *et al.* 2009] DJ Bacon, Yu N Osetsky and D Rodney. *Dislocation obstacle interactions at the atomic level*. Dislocations in solids, vol. 15, pages 1–90, 2009. 116

[Bako *et al.* 2007] B Bako, D Weygand, M Samaras, J Chen, MA Pouchon, P Gumbsch and W Hoffelner. *Discrete dislocation dynamics simulations of dislocation interactions with*

*Y 2 O 3 particles in PM2000 single crystals*. Philosophical Magazine, vol. 87, no. 24, pages 3645–3656, 2007. 71

[Bakó *et al.* 2008] B Bakó, D Weygand, M Samaras, W Hoffelner and M Zaiser. *Dislocation depinning transition in a dispersion-strengthened steel*. Physical Review B, vol. 78, no. 14, page 144104, 2008. 7, 8, 71, 83

[Bakó *et al.* 2009] B Bakó, M Samaras, D Weygand, J Chen, P Gumbsch and W Hoffelner. *The influence of Helium bubbles on the critical resolved shear stress of dispersion strengthened alloys*. Journal of Nuclear Materials, vol. 386, pages 112–114, 2009. 71

[Baluc *et al.* 2004] N Baluc, R Schäublin, P Spätig and M Victoria. *On the potentiality of using ferritic/martensitic steels as structural materials for fusion reactors*. Nuclear fusion, vol. 44, no. 1, page 56, 2004. 71

[Baluc *et al.* 2007] N Baluc, DS Gelles, S Jitsukawa, A Kimura, RL Klueh, GR Odette, B Van der Schaaf and Jinnan Yu. *Status of reduced activation ferritic/martensitic steel development*. Journal of Nuclear Materials, vol. 367, pages 33–41, 2007. 87

[Barnett 1985] DM Barnett. *The displacement field of a triangular dislocation loop*. Philosophical Magazine A, vol. 51, no. 3, pages 383–387, 1985. xv, 46

[Baudouin *et al.* 2013] Jean-Baptiste Baudouin, Ghiath Monnet, Michel Perez, Christophe Domain and Akiyoshi Nomoto. *Effect of the applied stress and the friction stress on the dislocation dissociation in face centered cubic metals*. Materials Letters, vol. 97, pages 93–96, 2013. 149, 163, 168, 179, 184, 227

[Brooks *et al.* 1979] JW Brooks, MH Loretto and RE Smallman. *< i> In situ</i> observations of the formation of martensite in stainless steel*. Acta Metallurgica, vol. 27, no. 12, pages 1829–1838, 1979. 149

[Brown 1964] LM Brown. *The self-stress of dislocations and the shape of extended nodes*. Philosophical Magazine, vol. 10, no. 105, pages 441–466, 1964. 28

[Bruemmer *et al.* 1999] Stephen M Bruemmer, Edward P Simonen, Peter M Scott, Peter L Andresen, Gary S Was and James L Nelson. *Radiation-induced material changes and susceptibility to intergranular failure of light-water-reactor core internals*. Journal of Nuclear Materials, vol. 274, no. 3, pages 299–314, 1999. 137

[Bulatov & Cai 2006] Vasily Bulatov and Wei Cai. Computer simulations of dislocations, volume 3. Oxford University Press, 2006. xiv, 40

[Byun *et al.* 2003] TS Byun, EH Lee and JD Hunn. *Plastic deformation in 316LN stainless steel–characterization of deformation microstructures*. Journal of nuclear materials, vol. 321, no. 1, pages 29–39, 2003. 149

[Byun *et al.* 2006] TS Byun, N Hashimoto and K Farrell. *Deformation mode map of irradiated 316 stainless steel in true stress–dose space*. Journal of nuclear materials, vol. 351, no. 1, pages 303–315, 2006. 144

[Byun 2003] TS Byun. *On the stress dependence of partial dislocation separation and deformation microstructure in austenitic stainless steels*. Acta Materialia, vol. 51, no. 11, pages 3063–3071, 2003. 144, 149, 163, 184, 227

[C. Robertson 2010] E. Meslin C. Robertson. *Experimental analysis of the plastic behavior of ion-irradiated bainitic RPV steel.* Rapport technique, Deliverable PERFORM60 D1-2.2, 2010. xxvii, 98

[C. Robertson 2012] J. Man C. Robertson L. Dupuy. *Plasticity Mechanisms in Irradiated Austenitic Stainless Steels: mesoscale modelisation of cross-slip,*. In PAMELA Workshop, Mol, Belgium, 2012. 127, 128, 145, 147

[Cai *et al.* 2006] Wei Cai, Athanasios Arsenlis, Christopher R Weinberger and Vasily V Bulatov. *A non-singular continuum theory of dislocations*. Journal of the Mechanics and Physics of Solids, vol. 54, no. 3, pages 561–587, 2006. 51, 53, 54, 55, 160, 206, 211

[Caillard *et al.* 2003] D Caillard, JL Martin*et al.* Thermally activated mechanisms in crystal plasticity. Cambridge Univ Press, 2003. 63, 76

[Canova & Kubin 1991] G Canova and LP Kubin. *Dislocation microstructures and plastic flow: a three dimensional simulation*. Continuum models and discrete systems, vol. 2, pages 93–101, 1991. 28

[Chang *et al.* 2010] Hyung-Jun Chang, Marc Fivel, David Rodney and Marc Verdier. *Multiscale modelling of indentation in FCC metals: From atomic to continuum*. Comptes Rendus Physique, vol. 11, no. 3, pages 285–292, 2010. 24

[Chaussidon *et al.* 2008] Julien Chaussidon, Christian Robertson, David Rodney and Marc Fivel. *Dislocation dynamics simulations of plasticity in Fe laths at low temperature*. Acta Materialia, vol. 56, no. 19, pages 5466–5476, 2008. 67, 69, 79

[Chaussidon *et al.* 2010] Julien Chaussidon, Christian Robertson, Marc Fivel and Bernard Marini. *Internal stress evolution in Fe laths deformed at low temperature analysed by* *dislocation dynamics simulations*. Modelling and Simulation in Materials Science and Engineering, vol. 18, no. 2, page 025003, 2010. 23, 70

[Chen *et al.* 2008] J Chen, P Jung, W Hoffelner and H Ullmaier. *Dislocation loops and bubbles in oxide dispersion strengthened ferritic steel after helium implantation under stress*. Acta Materialia, vol. 56, no. 2, pages 250–258, 2008. 87

[Chevy *et al.* 2012] Juliette Chevy, François Louchet, Paul Duval and Marc Fivel. *Creep behaviour of ice single crystals loaded in torsion explained by dislocation cross-slip*. Philosophical Magazine Letters, vol. 92, no. 6, pages 262–269, 2012. 23

[Christian & Mahajan 1995] John Wyrill Christian and Subhash Mahajan. *Deformation twinning*. Progress in Materials Science, vol. 39, no. 1, pages 1–157, 1995. 149

[Copley & Kear 1968] SM Copley and BH Kear. *The dependence of the width of a dissociated dislocation on dislocation velocity*. Acta Metallurgica, vol. 16, no. 2, pages 227–231, 1968. 148

[Daphalapurkar & Ramesh 2012] Nitin P Daphalapurkar and KT Ramesh. *Orientation dependence of the nucleation and growth of partial dislocations and possible twinning mechanisms in aluminum*. Journal of the Mechanics and Physics of Solids, vol. 60, no. 2, pages 277–294, 2012. 168

[De Carlan *et al.* 2009] Y De Carlan, J-L Bechade, Ph Dubuisson, J-L Seran, Ph Billot, A Bougault, T Cozzika, S Doriot, D Hamon, J Henry*et al.* *CEA developments of new ferritic ODS alloys for nuclear applications*. Journal of Nuclear Materials, vol. 386, pages 430–432, 2009. 71

[De Castro *et al.* 2007] V De Castro, T Leguey, A Munoz, MA Monge, P Fernández, AM Lancha and R Pareja. *Mechanical and microstructural behaviour of Y< sub> 2</sub> O< sub> 3</sub> ODS EUROFER 97*. Journal of Nuclear Materials, vol. 367, pages 196–201, 2007. 5

[Depres *et al.* 2004] Christophe Depres, CF Robertson* and MC Fivel. *Low-strain fatigue in AISI 316L steel surface grains: a three-dimensional discrete dislocation dynamics modelling of the early cycles I. Dislocation microstructures and mechanical behaviour*. Philosophical Magazine, vol. 84, no. 22, pages 2257–2275, 2004. 77, 91

[Depres *et al.* 2006] Christophe Depres, CF Robertson and MC Fivel. *Low-strain fatigue in 316L steel surface grains: a three dimension discrete dislocation dynamics modelling of the early cycles. Part 2: Persistent slip markings and micro-crack nucleation*. Philosophical Magazine, vol. 86, no. 1, pages 79–97, 2006. 23, 136

[Depres 2004] Depres. *Modelisation des stades precurseurs de l'endommagement en fatigue dans l'acier 316L*. PhD thesis, INPG, 2004. 91, 123, 126, 129, 134

[Devincre 1995] B Devincre. *Three dimensional stress field expressions for straight dislocation segments*. Solid state communications, vol. 93, no. 11, pages 875–878, 1995. 35

[Doan *et al.* 2010] Dinh Phuong Doan, Tran BaoTrung Tran, Van An Nguyen, Anh Tu Phan*et al.* *Microstructural evolution and some mechanical properties of nanosized yttrium oxide dispersion strengthened 13Cr steel*. Advances in Natural Sciences: Nanoscience and Nanotechnology, vol. 1, no. 3, page 035009, 2010. 5

[Duesbery *et al.* 1992] MS Duesbery, NP Louat and K Sadananda. *The mechanics and energetics of cross-slip*. Acta metallurgica et materialia, vol. 40, no. 1, pages 149–158, 1992. 199

[Dunlop *et al.* 2007] JW Dunlop, YJM Bréchet, Laurent Legras and Y Estrin. *Dislocation density-based modelling of plastic deformation of Zircaloy-4*. Materials Science and Engineering: A, vol. 443, no. 1, pages 77–86, 2007. 49

[Edwards & Singh 2004] DJ Edwards and BN Singh. *Evolution of cleared channels in neutron-irradiated pure copper as a function of tensile strain*. Journal of nuclear materials, vol. 329, pages 1072–1077, 2004. 145

[Edwards *et al.* 2005] Danny J Edwards, Bachu N Singh and JB Bilde-Sørensen. *Initiation and propagation of cleared channels in neutron-irradiated pure copper and a precipitation hardened CuCrZr alloy*. Journal of nuclear materials, vol. 342, no. 1, pages 164–178, 2005. xiii, 8, 9

[Escaig 1968] B Escaig. *Sur le glissement dévié des dislocations dans la structure cubique à faces centrées*. Journal de Physique, vol. 29, no. 2-3, pages 225–239, 1968. 159, 199

[Fan *et al.* 2013] Yue Fan, Yuri N Osetskiy, Sidney Yip and Bilge Yildiz. *Mapping strain rate dependence of dislocation-defect interactions by atomistic simulations*. Proceedings of the National Academy of Sciences, vol. 110, no. 44, pages 17756–17761, 2013. 49, 116

[Fivel *et al.* 1997] M Fivel, M Verdier and G Canova. *3D simulation of a nanoindentation test at a mesoscopic scale*. Materials Science and Engineering: A, vol. 234, pages 923–926, 1997. 23

[Fleischer 1959] RL Fleischer. *Cross slip of extended dislocations*. Acta Metallurgica, vol. 7, no. 2, pages 134–135, 1959. 201

[Foreman & Makin 1966] AJE Foreman and MJ Makin. *Dislocation movement through random arrays of obstacles*. Philosophical magazine, vol. 14, no. 131, pages 911–924, 1966. 28

[Foreman 1967] AJE Foreman. *The bowing of a dislocation segment*. Philosophical magazine, vol. 15, no. 137, pages 1011–1021, 1967. 38

[Frøseth *et al.* 2004] AG Frøseth, PM Derlet and H Van Swygenhoven. *Dislocations emitted from nanocrystalline grain boundaries: nucleation and splitting distance*. Acta Materialia, vol. 52, no. 20, pages 5863–5870, 2004. 149, 155

[G. Monnet 2011] L. Vincent G. Monnet B. Devincre. *Deliverable D1-2.9 Crystal plasticity constitutive law for irradiated RPV steel.* Rapport technique, PERFORM60, 2011. 95, 96, 104, 107

[G. Was 2006] Z. Jiao G. Was J. Busby. *The Use of Proton Irradiation to Determine IASCC Mechanisms in Light Water Reactors - Phase 3: Deformation Studies.* Rapport technique, EPRI, Palo Alto, CA, 2006. 3, 144, 145

[Garcia-Rodriguez 2011a] D. Garcia-Rodriguez. PhD thesis, INPG, 2011. 70

[Garcia-Rodriguez 2011b] Daniel Garcia-Rodriguez. *Optimization d'un code de dynamique des dislocations pour l'e'tude de la plasticite des aciers ferritiques*. PhD thesis, INPG, 2011. 64

[Ghoniem *et al.* 2000] NM Ghoniem, BN Singh, LZ Sun and T Diaz de la Rubia. *Interaction and accumulation of glissile defect clusters near dislocations*. Journal of nuclear materials, vol. 276, no. 1, pages 166–177, 2000. 28

[Goodchild *et al.* 1970] D Goodchild, WT Roberts and DV Wilson. *Plastic deformation and phase transformation in textured austenitic stainless steel*. Acta Metallurgica, vol. 18, no. 11, pages 1137–1145, 1970. 149

[Gruner 1988] G Gruner. *The dynamics of charge-density waves*. Reviews of Modern Physics, vol. 60, no. 4, page 1129, 1988. 7

[Hatano & Matsui 2005] Takahiro Hatano and Hideki Matsui. *Molecular dynamics investigation of dislocation pinning by a nanovoid in copper*. Physical Review B, vol. 72, no. 9, page 094105, 2005. 49

[Hernandez-Mayoral & Gomew-Briceno 2010] Hernandez-Mayoral and Gomew-Briceno. 2010. xxvii, 98

[Hirth & Kubin 2009] John P Hirth and Ladislas Kubin. Dislocations in solids, volume 15. Elsevier, 2009. 42

[Hirth & Lothe 1982] John P Hirth and Jens Lothe. *Theory of dislocations*. 1982. 41, 46, 63, 90, 155, 168, 174, 227

[Hull & Bacon 2011] Derek Hull and David J Bacon. Introduction to dislocations, volume 37. Elsevier, 2011. xxi, 150

[Humphreys & Hirsch 1970] FJ Humphreys and PB Hirsch. *The Deformation of Single Crystals of Copper and Copper-Zinc Alloys Containing Alumina Particles. II. Microstructure and Dislocation-Particle Interactions*. Proceedings of the Royal Society of London. Series A, Mathematical and Physical Sciences, pages 73–92, 1970. 12

[Jackson 1985] PJ Jackson. *Dislocation modelling of shear in fcc crystals*. Progress in materials science, vol. 29, no. 1, pages 139–175, 1985. 12

[Jenkins *et al.* 2009] ML Jenkins, Z Yao, M Hernandez-Mayoral and MA Kirk. *Dynamic observations of heavy-ion damage in Fe and Fe–Cr alloys*. Journal of Nuclear Materials, vol. 389, no. 2, pages 197–202, 2009. 73

[Ji & Robbins 1992] Hong Ji and Mark O Robbins. *Percolative, self-affine, and faceted domain growth in random three-dimensional magnets*. Physical Review B, vol. 46, no. 22, page 14519, 1992. 7

[K. Farrell & Hashimoto 2003] T. S. Byun K. Farrell and N. Hashimoto. *Mapping flowow localization process in deformation of irradiated reactor structural alloys- final report,*. Rapport technique, Nuclear Energy Research initiative Program No. MSF99-0072, ORNL/TM-2003/63., 2003. xiii, 6, 8, 145

[K. Gururaj 2010] C. Robertson K. Gururaj. *Communication to 2nd Asian Nuclear Prospect Conference*. 2010. 73

[Kelly & Knowles 2012] Anthony A Kelly and Kevin M Knowles. Crystallography and crystal defects. John Wiley & Sons, 2012. xiv, 42, 199

[Kestenbach 1977] H-J Kestenbach. *The effect of applied stress on partial dislocation separation and dislocation substructure in austenitic stainless steel*. Philosophical Magazine, vol. 36, no. 6, pages 1509–1515, 1977. 149

[Kimura 2007] A. Kimura. Rapport technique, 2007. 71

[Kiritani 1997] M Kiritani. *Story of stacking fault tetrahedra*. Materials chemistry and physics, vol. 50, no. 2, pages 133–138, 1997. 58

[Kishimoto *et al.* 2006] Hirotatsu Kishimoto, Kentaro Yutani, Ryuta Kasada and Akihiko Kimura. *Helium cavity formation research on oxide dispersed strengthening (ODS) ferritic steels utilizing dual-ion irradiation facility*. Fusion engineering and design, vol. 81, no. 8, pages 1045–1049, 2006. 87

[Kocks *et al.* 1975] UF Kocks, AS Argon and MF Ashby. *Thermodynamics and kinetics of slip*. Progress in Materials Science, vol. 19, 1975. 7, 63

[Kohyama *et al.* 1994] Akira Kohyama, Yutaka Kohno, Kentaro Asakura and Hideo Kayano. *R&D of low activation ferritic steels for fusion in Japanese universities*. Journal of nuclear materials, vol. 212, pages 684–689, 1994. 87

[Koks 2006] Don Koks. Explorations in mathematical physics. Springer, 2006. 162

[Kubena *et al.* 2012] Ivo Kubena, Benjamin Fournier and Tomas Kruml. *Effect of microstructure on low cycle fatigue properties of ODS steels*. Journal of Nuclear Materials, vol. 424, no. 1, pages 101–108, 2012. xiii, 7, 21, 22

[Kubin *et al.* 1992] Ladislas P Kubin, G Canova, M Condat, Benoit Devincre, V Pontikis and Yves Bréchet. *Dislocation microstructures and plastic flow: a 3D simulation*. Solid State Phenomena, vol. 23, pages 455–472, 1992. 23

[Kubin *et al.* 2009] L Kubin, T Hoc and B Devincre. *Dynamic recovery and its orientation dependence in face-centered cubic crystals*. Acta Materialia, vol. 57, no. 8, pages 2567–2575, 2009. 121

[Kubin 2013] Ladislas Kubin. Dislocations, mesoscale simulations and plastic flow, volume 5. Oxford University Press, 2013. 12

[L. Dupuy & Coulaud 2013] M. Fivel E. Ferrié A. Etcheverry L. Dupuy M. Blétry and O. Coulaud. www.numodis.com, 2013. Developed under the supervision of Laurent DUPUY, CEA, Saclay, in collaboration with CNRS Paris XIII and Grenoble INP. 26, 56, 160, 206

[Lagow *et al.* 2001] BW Lagow, IM Robertson, M Jouiad, DH Lassila, TC Lee and HK Birnbaum. *Observation of dislocation dynamics in the electron microscope*. Materials Science and Engineering: A, vol. 309, pages 445–450, 2001. 76

[Larkin & Ovchinnikov 1973] AI Larkin and Iun Ovchinnikov. *Electrodynamics of inhomogeneous Type II superconductors*. Zhurnal Eksperimental'noi i Teoreticheskoi Fiziki, vol. 65, pages 1704–1714, 1973. 7

[Lepinoux & Kubin 1987] J Lepinoux and LP Kubin. *The dynamic organization of dislocation structures: a simulation*. Scripta metallurgica, vol. 21, no. 6, pages 833–838, 1987. 28

[Libert 2007] M Libert. PhD thesis, Ecole Centrale de Paris, SRMA/CEA/Saclay, 2007. 63

[Liu *et al.* 2008] Z.L. Liu, X.C. You and Z. Zhuang. *A mesoscale investigation of strain rate effect on dynamic deformation of single-crystal copper*. International Journal of Solids and Structures, vol. 45, no. 13, pages 3674 – 3687, 2008. Special Issue Honoring K.C. Hwang Fracture, Plasticity, Micro- and Nanomechanics Special Issue Honoring K.C. Hwang. 49

[Louchet & Saka 2003] Francois Louchet and Hiroyasu Saka. *Comments on the paper: observation of dislocation dynamics in the electron microscope, by BW Lagow et al.* Materials Science and Engineering: A, vol. 352, no. 1, pages 71–75, 2003. 76, 77

[Marian *et al.* 2002] Jaime Marian, Brian D Wirth and J Manuel Perlado. *Mechanism of formation and growth of< 100> interstitial loops in ferritic materials*. Physical review letters, vol. 88, no. 25, page 255507, 2002. 73

[Martinez *et al.* 2008] E Martinez, Jaime Marian, A Arsenlis, M Victoria and JM Perlado. *Atomistically informed dislocation dynamics in fcc crystals*. Journal of the Mechanics and Physics of Solids, vol. 56, no. 3, pages 869–895, 2008. 54

[Matijasevic *et al.* 2008] Milena Matijasevic, Enrico Lucon and Abderrahim Almazouzi. *Behavior of ferritic/martensitic steels after n-irradiation at 200 and 300 C*. Journal of Nuclear Materials, vol. 377, no. 1, pages 101–108, 2008. 87, 104

[McClintock *et al.* 2009] David A McClintock, Mikhail A Sokolov, David T Hoelzer and Randy K Nanstad. *Mechanical properties of irradiated ODS-EUROFER and nanocluster strengthened 14YWT*. Journal of Nuclear Materials, vol. 392, no. 2, pages 353–359, 2009. 71, 93

[Meyers *et al.* 1999] MA Meyers, O Voehringer, YJ Chen, S Ankem and CS Pande. *Advances in Twinning*. Publication of TMS, Pennsylvania, page 43, 1999. 149

[Miller *et al.* 2009] Michael K Miller, AA Chernobaeva, Ya I Shtrombakh, KF Russell, RK Nanstad, D Yu Erak and OO Zabusov. *Evolution of the nanostructure of VVER-1000 RPV materials under neutron irradiation and post irradiation annealing*. Journal of Nuclear Materials, vol. 385, no. 3, pages 615–622, 2009. 87, 104

[Min-Sheng *et al.* 2014] Huang Min-Sheng, Zhu Ya-Xin and Li Zhen-Huan. *Dislocation Dissociation Strongly Influences on Frank-Read Source Nucleation and Microplasticy of*

*Materials with Low Stacking Fault Energy*. Chinese Physics Letters, vol. 31, no. 4, page 046102, 2014. 175

[Müllner 1997] Peter Müllner. *On the ductile to brittle transition in austenitic steel*. Materials Science and Engineering: A, vol. 234, pages 94–97, 1997. 149

[Nakada & Keh 1968] Y Nakada and AS Keh. *Solid solution strengthening in Fe-N single crystals*. Acta Metallurgica, vol. 16, no. 7, pages 903–914, 1968. 80

[Nishioka *et al.* 2008] Hiromasa Nishioka, Koji Fukuya, Katsuhiko FUJJI and Yuji Kitsunai. *Deformation structure in highly irradiated stainless steels*. Journal of Nuclear Science and Technology, vol. 45, no. 4, pages 274–287, 2008. xiii, 9, 11

[Nogaret *et al.* 2007] Th Nogaret, Ch Robertson and D Rodney. *Atomic-scale plasticity in the presence of Frank loops*. Philosophical Magazine, vol. 87, no. 6, pages 945–966, 2007. 18, 111, 113

[Nogaret *et al.* 2008] Thomas Nogaret, David Rodney, Marc Fivel and Christian Robertson. *Clear band formation simulated by dislocation dynamics: Role of helical turns and pile-ups*. Journal of Nuclear Materials, vol. 380, no. 1, pages 22–29, 2008. 23, 87, 110, 119

[Nogaret 2007] Th Nogaret. *Approche Multiechelle Des Mechanismes De Plasticite Dans les Aciers Austenitiques Irradies*. PhD thesis, INPG, 2007. xiv, 18, 19, 21, 119

[Odette *et al.* 2008] GR Odette, MJ Alinger and BD Wirth. *Recent developments in irradiation-resistant steels*. Annu. Rev. Mater. Res., vol. 38, pages 471–503, 2008. 1, 5

[Oksiuta *et al.* 2009] Z Oksiuta, P Olier, Y De Carlan and N Baluc. *Development and characterisation of a new ODS ferritic steel for fusion reactor application*. Journal of Nuclear Materials, vol. 393, no. 1, pages 114–119, 2009. 71

[Onimus & Béchade 2009] Fabien Onimus and Jean-Luc Béchade. *A polycrystalline modeling of the mechanical behavior of neutron irradiated zirconium alloys*. Journal of Nuclear Materials, vol. 384, no. 2, pages 163–174, 2009. 49

[Onimus *et al.* 2004] Fabien Onimus, Isabelle Monnet, JL Béchade, Claude Prioul and Philippe Pilvin. *A statistical TEM investigation of dislocation channeling mechanism in neutron irradiated zirconium alloys*. Journal of nuclear materials, vol. 328, no. 2, pages 165–179, 2004. 49

[Osetskiy & Stoller 2011] Y. N. Osetskiy and R. E. Stoller. *Molecular Dynamics Modeling of Dislocation-Obstacle Interactions and Mechanisms of Hardening and Strengthening in Irradiated Metals*. Rapport technique, Oak Ridge National Laboratory, 2011. xiii, 15

[Osterstock *et al.* 2010] Stéphane Osterstock, Christian Robertson, Maxime Sauzay, Véronique Aubin and Suzanne Degallaix. *Stage I surface crack formation in thermal fatigue: a predictive multi-scale approach*. Materials Science and Engineering: A, vol. 528, no. 1, pages 379–390, 2010. 23

[Pokor *et al.* 2004] C Pokor, Y Brechet, Ph Dubuisson, J-P Massoud and A Barbu. *Irradiation damage in 304 and 316 stainless steels: experimental investigation and modeling. Part I: Evolution of the microstructure*. Journal of nuclear materials, vol. 326, no. 1, pages 19–29, 2004. 113, 144

[Porollo *et al.* 1998] SI Porollo, AM Dvoriashin, AN Vorobyev and Yu V Konobeev. *The microstructure and tensile properties of Fe–Cr alloys after neutron irradiation at 400° C to 5.5–7.1 dpa*. Journal of nuclear materials, vol. 256, no. 2, pages 247–253, 1998. 84

[Püschl 2002] W Püschl. *Models for dislocation cross-slip in close-packed crystal structures: a critical review*. Progress in materials science, vol. 47, no. 4, pages 415–461, 2002. 26, 199

[Ramar *et al.* 2007] A Ramar, N Baluc and R Schäublin. *Effect of irradiation on the microstructure and the mechanical properties of oxide dispersion strengthened low activation ferritic/martensitic steel*. Journal of Nuclear Materials, vol. 367, pages 217–221, 2007. 71

[Rao *et al.* 2009] SI Rao, DM Dimiduk, JA El-Awady, TA Parthasarathy, MD Uchic and C Woodward. *Atomistic simulations of cross-slip nucleation at screw dislocation intersections in face-centered cubic nickel*. Philosophical Magazine, vol. 89, no. 34-36, pages 3351–3369, 2009. 199

[Robach *et al.* 2003] JS Robach, IM Robertson, BD Wirth and A Arsenlis. *In-situ transmission electron microscopy observations and molecular dynamics simulations of dislocation-defect interactions in ion-irradiated copper*. Philosophical Magazine, vol. 83, no. 8, pages 955–967, 2003. 9

[Robertson & Fivel 1999] CF Robertson and MC Fivel. *A study of the submicron indent-induced plastic deformation*. Journal of materials research, vol. 14, no. 06, pages 2251–2258, 1999. 23

[Robertson *et al.* 2001] C Robertson, MC Fivel and A Fissolo. *Dislocation substructure in 316L stainless steel under thermal fatigue up to 650 K*. Materials Science and Engineering: A, vol. 315, no. 1, pages 47–57, 2001. 127, 128, 134, 145

[Saada 1991] G Saada. *Cross-slip and work hardening of fcc crystals*. Materials Science and Engineering: A, vol. 137, pages 177–183, 1991. 199

[Sauzay & Kubin 2011] M Sauzay and LP Kubin. *Scaling laws for dislocation microstructures in monotonic and cyclic deformation of fcc metals*. Progress in Materials Science, vol. 56, no. 6, pages 725–784, 2011. 12

[Schaeublin *et al.* 2002] R Schaeublin, T Leguey, P Spätig, N Baluc and M Victoria. *Microstructure and mechanical properties of two ODS ferritic/martensitic steels*. Journal of nuclear materials, vol. 307, pages 778–782, 2002. 71, 93

[Schäublin *et al.* 2008] Robin Schäublin, Jean Henry and Yong Dai. *Helium and point defect accumulation:(i) microstructure and mechanical behaviour*. Comptes Rendus Physique, vol. 9, no. 3, pages 389–400, 2008. 71

[Schoeck & Seeger 1955] G. Schoeck and A. Seeger. In Pg. 340 Phys Soc London (1955)., 1955. 199

[Schwarz 1999] KW Schwarz. *Simulation of dislocations on the mesoscopic scale. I. Methods and examples*. Journal of Applied Physics, vol. 85, no. 1, pages 108–119, 1999. 28

[Shenoy *et al.* 2000] VB Shenoy, RV Kukta and R Phillips. *Mesoscopic analysis of structure and strength of dislocation junctions in fcc metals*. Physical Review Letters, vol. 84, no. 7, page 1491, 2000. 28, 45

[Shimokawa & Kitada 2014] Tomotsugu Shimokawa and Soya Kitada. *Dislocation Multiplication from the Frank-Read Source in Atomic Models*. Materials transactions, vol. 55, no. 1, pages 58–63, 2014. 175

[Shin *et al.* 2001] CS Shin, MC Fivel, D Rodney, R Phillips, VB Shenoy and L Dupuy. *Formation and strength of dislocation junctions in FCC metals: A study by dislocation dynamics and atomistic simulations*. Le Journal de Physique IV, vol. 11, no. PR5, pages Pr5–19, 2001. 45

[Shin *et al.* 2003] CS Shin, MC Fivel, M Verdier and KH Oh. *Dislocation–impenetrable precipitate interaction: a three-dimensional discrete dislocation dynamics analysis*. Philosophical Magazine, vol. 83, no. 31-34, pages 3691–3704, 2003. 129, 134

[Shin *et al.* 2005] CS Shin, MC Fivel, M Verdier and C Robertson. *Dislocation dynamics simulations of fatigue of precipitation-hardened materials*. Materials Science and Engineering: A, vol. 400, pages 166–169, 2005. 23, 82

[Shin *et al.* 2007] Chan Sun Shin, CF Robertson and MC Fivel. *Fatigue in precipitation hardened materials: a three-dimensional discrete dislocation dynamics modelling of the early cycles*. Philosophical Magazine, vol. 87, no. 24, pages 3657–3669, 2007. 82, 87

[Shin 2004] C. Shin. PhD thesis, INPG, 2004. xv, 35, 38, 44, 46

[Shishvan *et al.* 2008] S Soleymani Shishvan, S Mohammadi and M Rahimian. *A dislocation-dynamics-based derivation of the Frank–Read source characteristics for discrete dislocation plasticity*. Modelling and Simulation in Materials Science and Engineering, vol. 16, no. 7, page 075002, 2008. 53, 175, 176

[Takahashi *et al.* 2011] Akiyuki Takahashi, Zhengzheng Chen, Nasr Ghoniem and Nicholas Kioussis. *Atomistic-continuum modeling of dislocation interaction with Y< sub> 2</sub> O< sub> 3</sub> particles in iron*. Journal of Nuclear Materials, vol. 417, no. 1, pages 1098–1101, 2011. 22

[Terentyev *et al.* 2008] Dmitry Terentyev, P Grammatikopoulos, DJ Bacon and Yu N Osetsky. *Simulation of the interaction between an edge dislocation and a< 100> interstitial dislocation loop in $\alpha$-iron*. Acta Materialia, vol. 56, no. 18, pages 5034–5046, 2008. xiii, 16, 73, 84

[Terentyev *et al.* 2010] Dmitry Terentyev, David J Bacon and Yu N Osetsky. *Reactions between a 1/2< 111> screw dislocation and< 100> interstitial dislocation loops in alpha-iron modelled at atomic scale*. Philosophical Magazine, vol. 90, no. 7-8, pages 1019–1033, 2010. xiii, 16, 17, 73, 83, 84

[Urabe & Weertman 1975] Namio Urabe and J Weertman. *Dislocation mobility in potassium and iron single crystals*. Materials Science and Engineering, vol. 18, no. 1, pages 41–49, 1975. 65

[Van Swygenhoven *et al.* 2004] H Van Swygenhoven, PM Derlet and AG Frøseth. *Stacking fault energies and slip in nanocrystalline metals*. Nature Materials, vol. 3, no. 6, pages 399–403, 2004. 149

[Verdier *et al.* 1998] M Verdier, M Fivel and In Groma. *Mesoscopic scale simulation of dislocation dynamics in fcc metals: principles and applications*. Modelling and Simulation in Materials Science and Engineering, vol. 6, no. 6, page 755, 1998. 23, 24, 62, 71, 111

[Waltar & Todd 2011] AE Waltar and DR Todd. *Tsvetkov. Fast Spectrum Reactors*, 2011. 1

[Weygand *et al.* 2001] D Weygand, LH Friedman, E Van der Giessen and A Needleman. *Discrete dislocation modeling in three-dimensional confined volumes*. Materials Science and Engineering: A, vol. 309, pages 420–424, 2001. 28

[Wolf 1960] H Wolf. *The activation energy for cross slip of a dissociated screw-dislocation*. Z. Naturforsch. A (Astrophysik, Physik und Physikalische Chemie), 15a (3), pages 180–193, 1960. 199

[Yao 2005] Z. Yao. *The relationship between the irradiation-induced damage and the mechanical properties of single crystal Ni*. PhD thesis, EPFL, 2005. 119, 145

[Zbib *et al.* 2000] Hussein M Zbib, Tomas Diaz de la Rubia, Moono Rhee and John P Hirth. *3D dislocation dynamics: stress–strain behavior and hardening mechanisms in fcc and bcc metals*. Journal of Nuclear Materials, vol. 276, no. 1, pages 154–165, 2000. 49